

Crystallographic studies of clean and alkali covered metal and semiconductor surfaces

Anders Mikkelsen

September 2001

Contents

1	Introduction	7
1.1	Preface	7
1.2	List of publications	8
1.3	Introduction	10
1.4	Alkali adsorption on metal surfaces.	13
1.5	Surface alloy formation on close packed Al surfaces	15
1.6	Aluminum - lithium alloying	16
1.7	Clean and alkali covered semiconductor surfaces	18
1.8	Experiments with Low energy electrons	21
1.8.1	Low Energy Electron Diffraction (LEED)	21
1.8.2	Core Electron Spectroscopy	22
1.9	Surface Science list of acronyms	25
1.9.1	Experimental	25
1.9.2	Theoretical	26
2	Experimental and theoretical methods	27
2.1	The LEED experiment	27
2.1.1	Experimental setup	27
2.1.2	The Digital LEED System	29
2.1.3	Analyzing the data	33
2.1.4	Experimental procedures used for alkali-metal systems	41
2.2	Theory of LEED	42
2.2.1	The LEED pattern	42
2.2.2	Multiple scattering theory of LEED	44
2.2.3	Including thermal atomic vibrations	50
2.2.4	The Average T-matrix Approximation (ATA)	52
2.2.5	Recent developments in LEED theory	54
2.3	Application of LEED theory to actual crystal structures	56
2.3.1	Computation of I(V) curves	56
2.3.2	R-factor analysis of experimental and theoretical spectra	56
2.3.3	Structural refinement	58

2.4	HRCLS experiments and analysis	60
2.4.1	Beamlines I311 at the MAXII storage ring and SGM-1 at the ASTRID storage ring	60
2.4.2	Experimental chambers	60
2.4.3	Numerical analysis of Core-level Spectra	61
2.4.4	Interpretation of core-level shift	62
3	Structure and dynamics of unreconstructed metal surface systems	65
3.1	Introduction	65
3.2	Clean Al(100)	66
3.3	Al(110): Temp. dependence of structural and dynamical parameters	67
3.3.1	Introduction	67
3.3.2	LEED experiment and calculations	69
3.3.3	Structural results	73
3.3.4	Surface thermal expansion coefficients	77
3.3.5	Anisotropic and isotropic vibrations	79
3.3.6	Bulk vibrational parameters	80
3.4	Cu(100)	80
3.5	Cu(100)-c(2 × 2)-Na	83
3.5.1	Introduction	83
3.5.2	LEED experiment and calculations	83
3.5.3	Discussion	86
4	Single layer Li and Na surface alloys on Al	87
4.1	Introduction	87
4.2	Structure of Al(100)-c(2 × 2)-Li	89
4.2.1	LEED measurements and structural determination	89
4.2.2	Structural parameters	91
4.2.3	Surface structure vs. bulk alloy	91
4.2.4	Comparison to theoretical calculations	91
4.3	Structure of Al(100)-($\sqrt{5} \times \sqrt{5}$)R27°-Na	93
4.3.1	LEED measurements and structural analysis	93
4.3.2	Theoretical calculations and discussion	96
4.3.3	HRCLS and LEED measurements of the order/disorder phase transition	98
4.4	Structure of Al(110)-c(2 × 2)-Li	103
4.4.1	LEED measurements and structural analysis	103
4.4.2	Substitutional adsorption and Al-Li alloy formation	104
4.5	Structure of Al(110)-c(2 × 2)-Na	105
4.5.1	LEED measurements and structural analysis	105
4.6	Comparison of the c(2 × 2) Na and Li structures on Al(110)	109

4.7	Evolution of the surface structure with Li and Na coverage on Al(110)	110
4.7.1	CLS reference spectra	110
4.7.2	Evolution of the surface structure with Li and Na coverage	112
4.7.3	Summary and discussion	116
5	Substrate relaxation induced by superstructure formation	119
5.1	Introduction	119
5.2	The PIFB electrostatic model	121
5.3	Applications of the PIFB model to clean metal surfaces	122
5.4	Extending the model to reconstructions and adsorbate structures	127
5.4.1	Ir, Au, Pt(110)-(1x2) missing row reconstruction	129
5.4.2	Al(110)-c(2x2)-Na and Al(110)-c(2x2)-Li	130
5.4.3	Al(111)-(2x2)-Rb	132
5.4.4	Al(111)-($\sqrt{3} \times \sqrt{3}$)R30° -K, Rb, Cs	134
5.5	Limitations of the LF-PIFB model	134
5.6	Summary and discussion	135
6	Al-Li multilayer surface alloys	137
6.1	An unusual Al(100)-c(2x2)-2Li multilayer alloy	137
6.1.1	Introduction	137
6.1.2	LEED measurements and structural determination	138
6.1.3	DFT calculations	141
6.1.4	Discussion	141
6.2	Al(110)-Li multi layer structures	143
6.2.1	Introduction	143
6.2.2	CLS and LEED pattern observations of multi layer structures	144
6.2.3	Segregation on Al _{81.3} Li _{12.7} (110) versus adsorption of Li on Al(110)	146
7	Na multilayer surface structures on Al(110)	147
7.1	Introduction	147
7.2	Structure of Al(110)-(4x1)-Na.	148
7.2.1	LEED measurements and structural determination	148
7.2.2	CLS measurements for the c(2x2)-Na and (4x1)-Na phases	154
7.3	Evolution of the surface structure with Na coverage	156
7.3.1	LEED Patterns	156
7.3.2	CLS measurements	156
7.3.3	Discussion	159

8	Silicon and germanium surface structures	161
8.1	Introduction	161
8.2	Structural determination of Si(100)-(2 × 1)	163
8.2.1	Preparation of the Si(100) surface	163
8.2.2	LEED experiment and structural determination	166
8.3	Structural determination of Ge(100)-c(4 × 2)	171
8.3.1	Introduction	171
8.3.2	LEED experiment and structural determination	172
8.4	Na adsorption on Si(100) and Ge(100)	176
8.4.1	Introduction	176
8.4.2	LEED experiment and structural determination	177
9	Summary and conclusion	185

Chapter 1

Introduction

1.1 Preface

This thesis has been submitted to the Faculty of Natural Science, University of Aarhus, in order to fulfil the requirements for the Ph.D. degree in physics. As the reader will soon learn, the main part of the work has centered around the construction and application of a state-of-the-art Low Energy Electron Diffraction (LEED) experimental setup, designed with the specific purpose of obtaining precise (in the $\frac{1}{100}$ Ångstrom range) crystallographic information about surface crystal structures. The work was carried out in a four year period from September 1997 to July 2001. All LEED measurements mentioned in this thesis were carried out at the new LEED experimental setup at Institute of Physics and Astronomy (IFA), University of Aarhus. High resolution core-level experiments were done at the ASTRID storage ring situated also at IFA, and at the MAXII storage ring at MAXLAB in Lund, Sweden.

During my Ph.D. study I was so fortunate as to travel several times abroad to work in other labs. First I would like to thank Professor Wolfgang Moritz, Institut für Mineralogie und Kristallografie, LMU, Munich for giving me the opportunity to work at his very fine laboratory. It was a great pleasure to familiarize myself with SPA-LEED and SXRD, and to apply these techniques to such complex systems as for example quasi-crystals. I should also like to thank Wolfgang Moritz personally for sharing his great knowledge of surface crystallography, and many other things. The laboratory in Munich was also filled with many pleasant people from Germany and Spain, and I should especially like to thank Martin Gierer, with whom I had the pleasure of collaborating.

I should also like to thank Professor! Jesper N. Andersen, Institute of Physics, Lund University for his great hospitality and many interesting discussion during several stays at his state-of-the-art surface science beamline at MAXII. In Lund

I also had the pleasure of spending countless productive hours at beamline I311 with Mikael Borg and Maria Wiklund, on top of that they are both great people. Mikael Borg is further acknowledged for our very successful collaboration, combining our LEED structural determinations and his DFT calculations for the Al(100)-c(2 × 2)-2Li and the Al(100)-($\sqrt{5} \times \sqrt{5}$)R27°-Na systems.

During my four years as a Ph.D. student at IFA I have had the great pleasure of working together with many different people. I have received help and advice from many physicists and technicians at our institute.

I would especially like to thank my supervisor David Adams, for sharing his great understanding of both surface science and science in general. David has spent so many hours on my account, explaining and discussing all kinds of interesting topics, that I might as well take up smoking.

Experimental work is never done by one person and I have indeed collaborated with a number of people at our institute, thanks to all of you for many good hours in the laboratories beneath our institute. The LEED studies of Na on Al(110) and Li on Al(100) presented in this thesis were preceded by very thorough and reliable core-level spectroscopy and qualitative LEED measurements done by Søren V. Hoffmann (SVH) and Jakob H. Petersen (JHP) respectively. New core-level measurements of the Al(110) Li and Na systems were done by JHP, SVH and myself. LEED measurements of the Al(100)-c(2 × 2)-Li system were performed by JHP and myself. Jarek Jiruse from Brno, the Czech Republic, visited us during a period of several months and he collaborated in the experimental LEED work on the Al(110) Li and Na structures. I also had the opportunity to work together with Zheshen Li on the interesting Si(100) - Ba system, which is not discussed in this thesis. All the LEED calculations presented here were carried out by me and David Adams.

Professor Niels E. Christensen, IFA is gratefully acknowledged for calculating new Si and Ge potentials, and for many interesting discussions.

Arne N. Larsen, IFA is acknowledged for generously supplying the Si crystals used in this work, and interesting discussion about Si and Ge.

I would also like to use this occasion to thank my family, my friends and especially my beautiful girlfriend Trine, for everything. Finally I would like to thank my wonderful new born daughters Maria and Nanna, although they did not exactly help in finishing this thesis, they have certainly helped to put surface science in perspective.

1.2 List of publications

Publications *not* included in this thesis have been marked by a *.

- ("Temperature dependence of the Al(110) surface structure",
A.Mikkelsen and D.L. Adams, in preparation, 2001)
- ("Surface structure of Ge(100)-c(4 × 2): A LEED analysis",
A.Mikkelsen, W. Moritz and D.L.Adams, in preparation , 2001)
- ("Structure and formation of the Al(100)-($\sqrt{5} \times \sqrt{5}$)R27°-Na phase",
M. Borg, A. Mikkelsen, J. N. Andersen, and D.L.Adams, in preparation ,
2001)
- ("Substrate reconstruction induced by superstructure formation",
A.Mikkelsen and D.L.Adams, in preparation , 2001)
- "The surface structures formed by Na adsorption on Al(110)",
A.Mikkelsen, J.H.Petersen, J.Jiruse, S.V.Hoffmann, and D.L.Adams, Surf.
Sci., 2001, accepted for pub.
- "Unusual Al(100)-c(2 × 2)-2Li multilayer surface alloy",
A. Mikkelsen, M. Borg, J. N. Andersen, J.H.Petersen, and D.L.Adams,
Phys. Rev. Lett., Vol. 87 (2001), 096102
- "Structure and formation of Al-Li surface alloys on Al(110) by Li adsorp-
tion.",
A.Mikkelsen, J.H.Petersen, S.V.Hoffmann, J.Jiruse and D.L.Adams, Surf.
Sci., Vol. 487 (2001), 28
- "Surface reconstruction and relaxation of Al(110)-c(2 × 2)-Na",
A.Mikkelsen, S.V.Hoffmann,J.Jiruse and D.L.Adams, Phys. Rev. B, Vol.
61 (2000), 13988
- * "Quasicrystalline surface order on decagonal Al_{72.1} Ni_{11.5} Co_{16.4}: An in-
vestigation with spot profile analysis LEED",
M. Gierer, A.Mikkelsen, M.Gräber, P. Gille and W. Moritz, Surf. Sci. and
Lett., Vol. 463 (2000), L654
- "Structure and dynamics of the Al(110) surface",
A.Mikkelsen, J.Jiruse and D.L. Adams, Phys. Rev. B, Vol. 60 (1999), 7796
- "Structure of Al(100)-c(2 × 2)-Li: A binary surface alloy",
J.H.Petersen, A. Mikkelsen, M.M.Nielsen and D.L.Adams, Phys. Rev. B,
Vol. 60 (1999), 5963
- * "Surface alloy formation by adsorption of Li on Al(100): studied by high-
resolution core-level spectroscopy and low energy electron diffraction",

J.H Petersen, C. Søndergård, S.V. Hoffmann, A. Mikkelsen, D.L. Adams, Surf. Sci., Vol. 437 (1999), 317

- "Surface structure of Cu(100)-c(2 × 2)-Na: A LEED analysis", A.Mikkelsen and D.L.Adams, Phys. Rev. B, Vol. 60 (1999), 2040

1.3 Introduction

Crystallography plays an important part in all the natural sciences as was quite evident at the most recent European Crystallography Meeting (ECM-19), where more than 2000 scientists discussed many diverse topics such as, designing drugs using crystallography, the structure of enzymes in beer, Gbar pressure metal-insulator alkali phase transitions and the structure of concrete. This is only natural as any study of physical, biological or geological systems often starts with the fundamental question: "What does it look like?" Although crystallography in the strictest sense only deals with long range periodic structures, the structures encountered in this perfect world will also be realized many places in our disordered reality. Carefully drawing up maps of hundreds, thousands, even tens of thousands of simple and complex structures might seem a little tedious, but such catalogs are the starting point for a better understanding of nature.

Surface crystallography was of course also represented at the ECM-19, but compared to for example structural biology, surface crystallography has a long way to go. While our colleagues in biology have determined tens of thousands of complex molecular structures consisting of hundreds of atoms, surface scientists have determined perhaps a few thousand very simple structures with some 20 individual atoms in the most complex cases. This lack of insight might seem astounding as the surface is the place of interaction between a solid and the outside world, making the bulk properties of a material quite unimportant for many purposes compared to the surface properties.

Although surface crystallography has attracted much attention, progress has been inhibited by the inherently 2D nature of the surface, which presents a number of difficult challenges. Most importantly the X-ray methods, which are the main reason for the great successes in other fields of crystallography, have been very difficult to apply in surface science. Because X-rays only interact weakly with matter, they will always penetrate deeply into the crystal. Even at grazing incidence a huge bulk contribution will be visible, while the surface will contribute only a miserably small signal.

Electrons with kinetic energy between $\sim 50\text{eV}$ and $\sim 500\text{eV}$, called low energy electrons are, in contrast to X-rays, very surface sensitive, because the electron inelastic mean free path is of the order of $5\text{-}10\text{\AA}$ in this low energy range

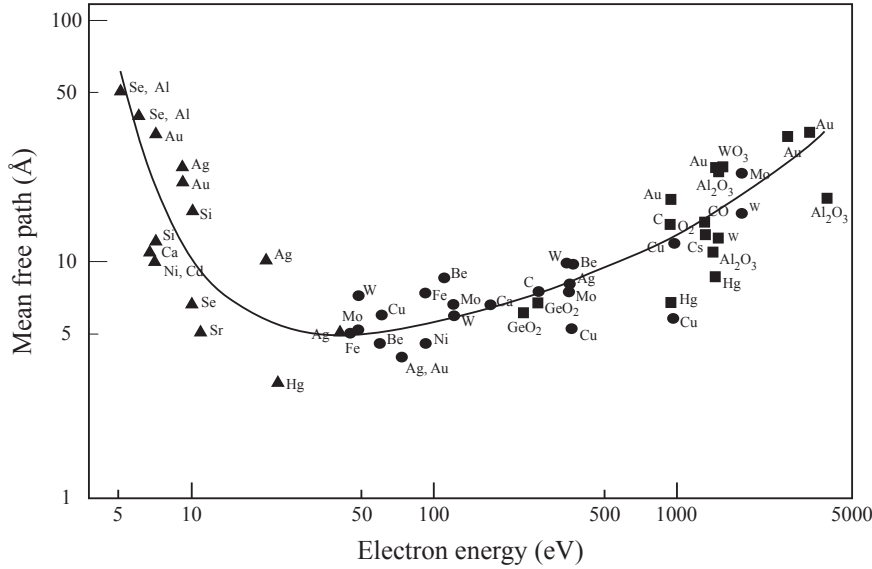


Figure 1.1: Universal curve of electron inelastic mean free path[1], the minima is mainly given by the strong interaction with plasmons for low energy electrons

for all common materials as depicted on Fig. 1.1 The short inelastic mean free path ensures that if only elastically scattered electrons are considered, the main contribution will be from electrons back-scattered by the first few layers of the surface.

Low energy electrons are also an excellent choice for acquiring information about the crystal structure by diffraction experiments, because they have a De Broglie wavelength $\lambda_e = \frac{12.3}{\sqrt{E_{eV}}} \text{Å}$, which is less than or equal to the lattice constants of solid materials.

All the work presented in this thesis and indeed much of the work done in surface science uses the properties of low energy electrons in one way or the other. Unfortunately the strong interaction of the electrons with matter comes with a price, namely that the single scattering approximation which makes interpretation of diffraction experiments much simpler is not very good for low energy electrons. This is the main reason that low energy electron diffraction (LEED) has not been as successful as X-ray diffraction where single scattering is the underlying approximation of all interpretation. This being said, LEED has been very successful in determining surface structures, and plays a very important part in forming our understanding of surface structure and dynamics.

LEED is well suited for the study of metal surfaces and by far the greatest bulk

of structural work has been done for clean and adsorbate covered metal systems. These studies have shown that a wealth of structures and phase transitions exists, many of which can only occur at the surface. The solid metal surface can also change the rate of a chemical reaction between adsorbates. For example, reactions which occur only very slowly (or not at all) in the gas phase can speed up when the constituents are adsorbed on a metal surface. Heterogeneous catalysis, as this process is called, is the basis of a billion euro industry, used for example to produce artificial fertilizer (ammonia) from nitrogen and hydrogen, to refine raw oil and to clean your car exhaust.

Catalysis have been an important motivation for the study of alkali metals on metal surfaces, as it has been found that alkalis can act as promoters on catalytically active metals, speeding up the catalytic reaction further. However the main reason for studying alkali adsorption on metal surfaces in recent years has been that the alkalis constitute a very nice and simple model system for theoreticians due to their single valence electron. Experimentally alkalis are also a favorable choice as very clean and well defined sources exists in the form of getters. If one wants to go to the simplest of the simple model systems one could choose a free electron metal like aluminum as the adsorption substrate for the alkali. A large number of structural studies have indeed been performed on alkali-Al systems during recent years, and no matter where people have looked, new and surprising structures and phase transitions have been found, making any notion that simple elements make simple adsorption systems seem ridiculous.

The work presented in this thesis centers around the construction and application of a new digital LEED system. After the initial construction period which lasted approximately one half year, efforts have focused on the following three main subjects of interest. Precision measurements of structural and dynamical parameters have been made as a function of temperature for simple systems. Ongoing investigations of alkali-aluminum systems have been continued, taking on more complex systems on more open surfaces. Finally we have ventured into the area of semiconductor surfaces, and alkali adsorption on semiconductor surfaces. While each of these three themes could perhaps be the focus of a thesis, it has been the desire of the author to try out many different surface systems during the four years of Ph.D. work, especially as the new LEED experimental setup should be tried out on a number of different challenges.

In the remainder of this chapter a short introduction to alkali adsorption in general, and Al-Li alloying in particular, is followed by a section on semiconductor surfaces. Finally an introductory discussion of the experimental techniques used in this work is presented.

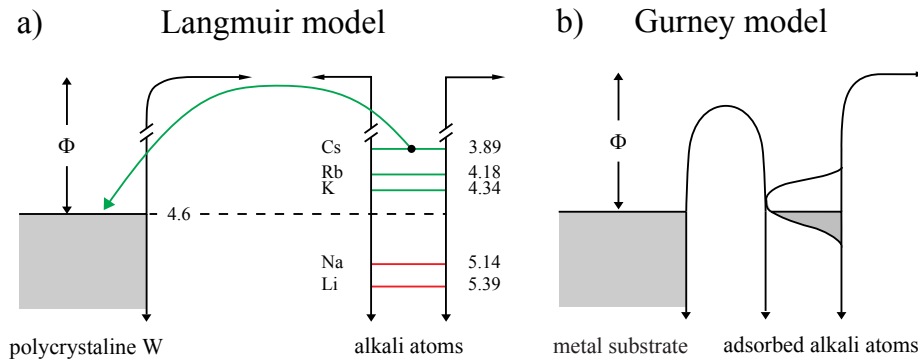


Figure 1.2: a) Langmuir and b) Gurney models of of alkali adsorption explaining the work function decrease at low coverage.

1.4 Alkali adsorption on metal surfaces.

Historically, the main subject of interest for many years was the behavior of the substrate work function Φ (defined as the energy needed to move an electron from the Fermi level into the vacuum) as a function of alkali coverage Θ_{alkali} . In the first studies by Langmuir and co-workers[2, 3], it was found that Cs adsorption on W leads to a steep decrease of the work function of W at low coverages, and that the Cs atoms could be desorbed from the surface in the form of positive ions. As is shown in Fig. 1.2a, this was explained by arguing that the ionization potential of the 6s electron of Cs is considerably smaller than the work function of W. Thus a charge transfer of the 6s valence electron to the metal would be favorable, resulting in the formation of a positive-outward surface dipole and hence a decrease in the work function. The decrease in slope or even slight increase of the work function found at higher alkali coverages, was also explained within this model as being due to depolarization of the surface dipoles with increasing surface density[4]. These early models turned out to be too simplistic as similar work function behavior was found for alkali adsorption systems where the ionization potential of the alkali valence electrons is larger than the work function of the substrate metal. A refined model shown in Fig. 1.2b was proposed by Gurney[5] in which the valence levels of the alkali are broadened and shifted in the presence of the surface allowing a charge transfer to the metal to be energetically favorable. This would lead to partly ionic bonding, and one is essentially back to the dipole model of Langmuir. The decrease in dipole moment at higher alkali coverage was explained by Gurney as a downward shift and hence greater occupation of ionization levels of the alkali, leading to a more neutral, metallic bonding. This

model qualitatively explains the behavior of the work function changes due to alkali metals.

More rigorous, self-consistent, theoretical calculations were performed by Lang and Williams[6], which confirmed the Gurney picture. Lang and Williams assumed a jellium model of the substrate, in which ions are represented by a positive uniform background that ends abruptly at the surface, while extending infinitely into the bulk. The electron density was allowed to vary subject to the limiting conditions of zero charge at infinite distance from the surface in the vacuum region and charge neutrality of the whole system. A jellium model of the surface was thought to be quite adequate as it was believed that alkalis in general adsorbed in high symmetry sites on an unreconstructed surface, although very few structural studies had been published at the time.

In recent years it has been found that this simple picture of alkali adsorption is not correct. Alkali atoms often adsorb in the less symmetric bridge, on-top sites. Strong perturbations of the substrate also occur, in the most extreme cases resulting in surface alloying of alkali atoms. This modern revolution in the understanding of alkali adsorption on metals was primarily due to a large number of studies of alkali adsorption on Al surfaces. Although the very first on-top alkali structure was found for Cu(111)-(2 × 2)-Cs [7], it was quite unexpectedly found that the Al(111)-(√3 × √3)R30°-Li, Na, K, Rb phases and the Al(111)-(2 × 2)-Na phases formed by adsorption at room temperature, involve rather complex *reconstructions* of the substrate, and formation of surface alloys[8, 9]. This is perhaps even more surprising in that Al is bulk immiscible with Na, K, Rb and Cs. Reconstructive adsorption was later found for the Au(110)-c(2 × 2)-K, Cu(110)-(2 × 1)-Li, and Au(110)-c(2 × 2)-Na phases[10–12] formed by adsorption at room temperature. Reconstructive adsorption involving major rearrangement of the substrate atoms is however not the general rule. Recent examples of simple chemisorption, involving at most perturbations of the substrate atoms from their original positions, include the Al(111)-(√3 × √3)R30°-K, Rb, and Cs phases and the Al(100)-c(2 × 2)-Na phase[8, 9, 13, 14] formed by adsorption at 100K, along with for example the Ni(100)-c(4 × 2)-K, Ni(100)-c(2 × 2)-Na, Ni(111)-(2 × 2)-K, Pd(100)-K, and Ru(0001)-(2 × 2)-Cs phases formed by adsorption at room temperature [15–19]. Further examples of alkali adsorption on metals surfaces can be found in the comprehensive review by Diehl and McGrath [20].

The limitations of the Langmuir-Gurney picture due to structural effects can best be illustrated by comparing work function measurements of Na adsorbed on Al(111) at T=140K and at T=300K as shown in fig 1.3. It has been found that Na chemisorbs at T=140K, while several substitutional structures are formed by adsorption at T=300K. Comparison of the two curves indicates that although the L-G picture has some merit at low coverages, surface structures play an important role for $\Theta_{Na} > 0.1\text{ML}$. C. Stampfl and M. Scheffler[21] have confirmed by

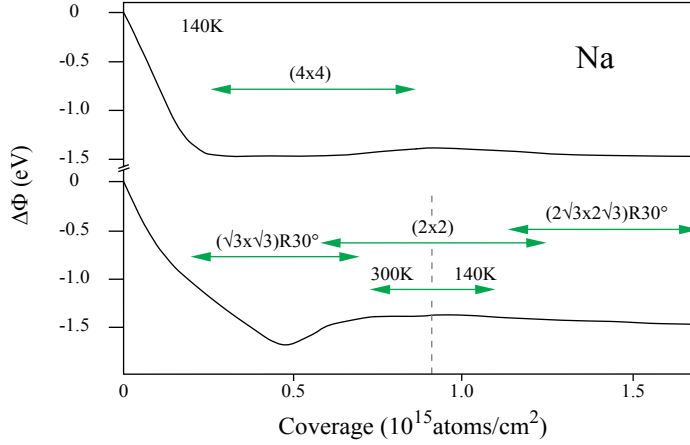
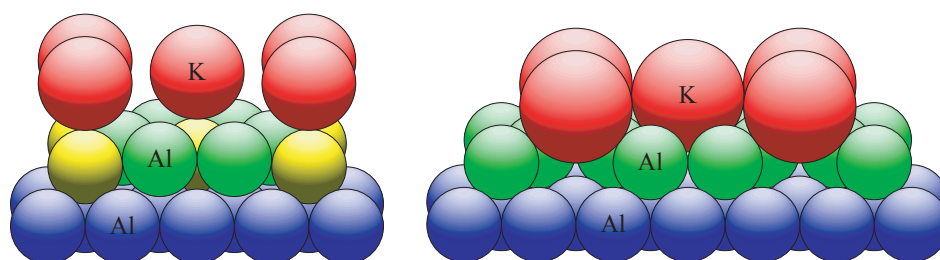


Figure 1.3: Change in work function by adsorption of Na on Al(111) at 140K and 300K, adapted from Hohlfeld and Horn[23]. Note that while the work function behavior is quite similar at very low coverages, at higher coverages it is influenced by the surface structures.

ab-initio calculations that it can be necessary to take into account the structure of the surface to explain the work function behavior for alkali coverages above a few tenths of a monolayer. Further more it has been found that alkali island formation can occur at coverages even as low as 0.06ML[22] which contradicts the dipole picture of Langmuir and Gurney where a strong repulsive force should exist between the alkalis.

1.5 Surface alloy formation on close packed Al surfaces

The alkali-aluminum studies presented in this thesis were partially motivated by the peculiar surface alloy structures and phase transitions found on the close packed Al(111) surface in previous work[8]. Surface alloy formation was especially surprising for the heavier alkalis Na, K, Rb and Cs as they are immiscible with Al. The first such alloy to be discovered was the room temperature Al(111)- $(\sqrt{3} \times \sqrt{3})R30^\circ$ -Na phase where SEXAFS measurements indicated that Na atoms are adsorbed in 6-fold coordinated substitutional sites[24]. $(\sqrt{3} \times \sqrt{3})R30^\circ$ LEED patterns are also found after adsorption of 0.33ML K or Rb both at $T=100K$ and $T=300K$, but as is quite evident by comparison of core-level spectra or LEED I(V) curves[8, 25], the structures formed by adsorption at room temperature and low temperature are quite different. It is also found that this structural phase transition



100K: K in on-top site on rumpled Al layer

300K: K in substitutional site

Figure 1.4: Al(111)-($\sqrt{3} \times \sqrt{3}$)R30°-K structures forms after adsorption of 0.33ML K both at T=300K and T=100K. However, while a substitutional structure forms at room temperature, an on-top structure forms at 100K

is irreversible, in that upon annealing the structure formed at 100K to room temperature, the structure found at room temperature persists after cooling to 100K again. Analysis of the measured LEED I(V) curves indicated very clearly that after adsorption at 100K all the alkali was positioned in on-top positions, while adsorption at room temperature led to the formation of substitutional alkali-Al alloys. The different structures formed at 100K and 300K are shown in fig 1.4 for the case of K. While this is more or less the end of the story for K and Rb adsorption at room temperature, it was found by several methods[26] that for Na an even more complex Al(111)-(2 × 2)-Na multilayer alloy could be formed by adsorption of 0.5ML Na. This structure, depicted in Fig. 1.5, consists of an Al layer sandwiched by two Na layers, where the lowest lying Na layer is substitutionally embedded into the surface.

Theoretical attempts at describing the alkali-metal adsorption systems have also had some success. M. Scheffler and co-workers[24, 27] using DFT together with the local density approximation (LDA) and ab initio pseudopotentials were able to correctly predict the surprising reconstructive adsorption of the $\sqrt{3}$ -Na system on Al(111), but they could not predict the correct structures for the heavier alkalis. While the Al(111)-(2 × 2)-Na sandwich model was originally based on HRCLS measurements, the quantitative structure was first determined by DFT calculations[28], which were then confirmed by a LEED analysis of the same system[26].

1.6 Aluminum - lithium alloying

Al-Li alloys are of significant technological and fundamental interest because of their rather unusual mechanical properties and the fact that Li is the only alkali

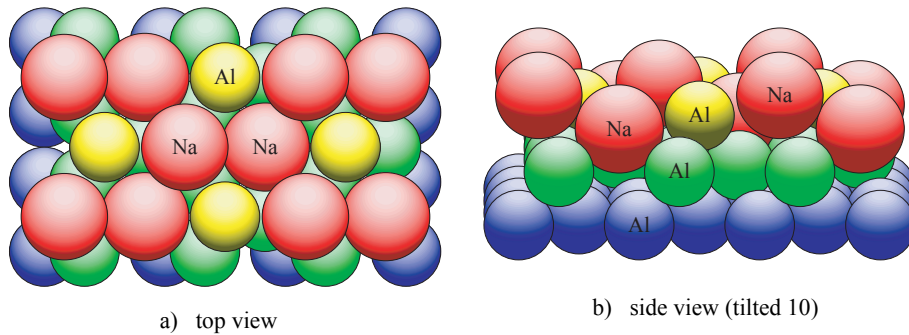


Figure 1.5: The Al(111)-(2 × 2)-Na multilayer alloy formed by adsorption of 0.25ML Na in three-fold hollow sites, 0.25ML Na in substitutional sites, and 0.25ML Al in between.

which alloys with aluminum. Al-rich Al-Li alloys are used in the aerospace industry because of their high strength and low density compared to other Al binary alloys[29, 30]. These alloys have also been proposed as new materials for high-intensity pulsed photocathodes[31], in which regeneration of the active surface layers by Li segregation to the surface plays an important role.

The bulk phase diagram for Al-Li contains a single, stable crystalline phase, namely the AlLi phase with bcc-like NaTi structure. However, a metastable Al₃Li phase is also found, which has an fcc-like Cu₃Au structure. This phase forms as microcrystallite precipitates which can occupy up to 50% of the crystal volume. Al₃Li precipitates are thought to play an important role in establishing the stiffness of Al-rich alloys, both by pinning down defects and by their own high Young's modulus. The bulk precipitation of the Al₃Li phase is of current interest[32], and it is conceivable that studies of surface alloy formation have implications for the studies of precipitation of Al₃Li at defects.

The main features of the experimental phase diagram have been confirmed by a number of theoretical studies. In particular, Freeman and co-workers[34, 35] have shown that the Al₃Li alloy is stable at 0° K, but metastable at room temperature. These workers have also shown that the Cu₃Au-type structure of Al₃Li has a lower energy than alternative possibilities with the same stoichiometry. However the Al₃Ti-type structure, discussed in chapter 6, was apparently not considered. It was concluded that the bonding in Al₃Li involves donation of the Li valence electron to strengthen the Al bonds.

It is interesting to note that the surface properties of Al-Li alloys are also of considerable importance. Segregation of Li to the surface under oxidizing conditions is a serious problem. Since it does not appear to be possible to grow macroscopic single-crystals of Al-Li alloys, the present work can be seen in part as an attempt to characterize the surface properties of alloys formed by adsorption

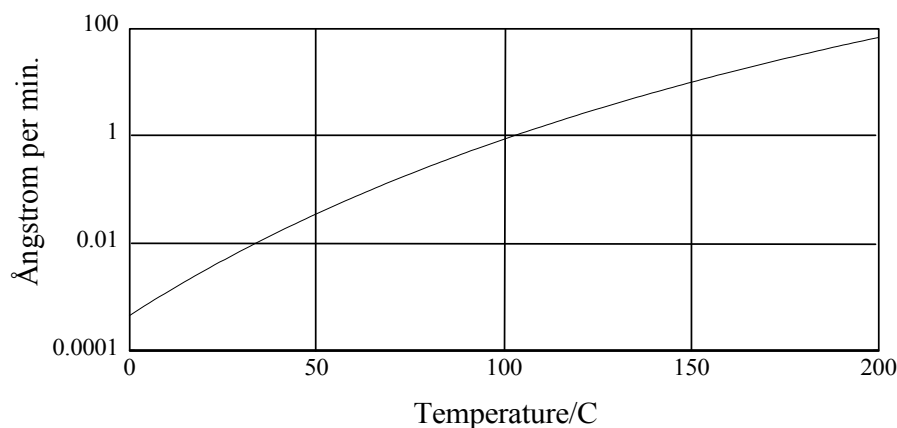


Figure 1.6: Mean diffusion length per minute for Li diffusion[33] in bulk Al as a function of temperature.

of Li on a single-crystal Al surface. Adsorption as a tool for formation of multi-layer surface alloys might seem unusual, but for materials where only dilute single crystal alloys have been made (≤ 14 at % of Li in Al), this method represents a simple way to obtain ordered structures which, in contrast to bulk precipitates, are easy to study.

As is shown in the work presented in this thesis and in previous work for alkali adsorption on Al(111), the structures formed by adsorption of Li at low coverage are similar to the structures formed by the heavier alkalis. However, the ability of Li to form bulk alloys with Al leads to the expectation that multilayer alloy formation may occur at higher coverages of Li. The diffusion coefficient $D_{Li}(Al)$ of Li in Al as a function of temperature has been experimentally determined[33], and the mean diffusion length per minute ($\sqrt{D_{Li}(Al) * t}$, $t = 1$ min.) is shown in Fig 1.6. The most interesting temperature regime from a surface science point of view seems to be room temperature to a few 100 degrees celsius. In this temperature range, Li diffusion into the subsurface will be appreciable on a time scale of minutes, while it is still not so fast that Li will disappear into the bulk much quicker than it can be adsorbed on the surface.

1.7 Clean and alkali covered semiconductor surfaces

Semiconductors (especially silicon) are the most important building blocks of all the chip technology found throughout modern society. Electronic circuits are printed on semiconductor *surfaces*, where properties in the first few layers can play an important role both in growth and in electronic properties of the finished design. This is especially true as the on going work to miniaturize such devices

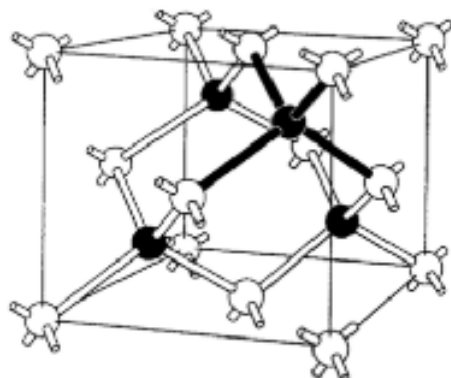


Figure 1.7: Model of the zincblende atomic geometry, which can be used as a basic model for many important semiconductor materials (Si, Ge, GaAs etc.). In the case of Si (or Ge) both open and closed circles on the drawing represents Si (or Ge), which yields the diamond structure.

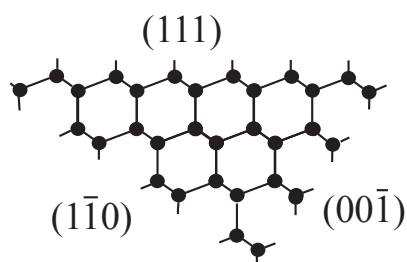


Figure 1.8: Dangling bonds on several Si faces associated with the bulk termination.

will eventually results in circuitry on the Ångstrom length scale.

In the 1950s germanium was actually the major semiconductor material, but germanium proved to be unstable in many applications because Ge devices exhibited high leakage currents at only moderately elevated temperatures. Moreover germanium oxide is water soluble and unsuited for device fabrication [36]. Silicon has become the preferred substitute since the 1960s, and so most research has focussed on Si. However as SiGe hetero-structures have become of increasing interest in recent years, due to for example their possible applications as optoelectronic components[37], research in pure germanium has also become more popular. Another reason for studying Ge is that it shares many properties with Si, while it is much easier to prepare for surface science experiments, which makes Ge interesting as a model system for Si.

Semiconductor surfaces are a most popular study in surface science as even a limited survey of the literature will soon reveal. From looking closer at some of

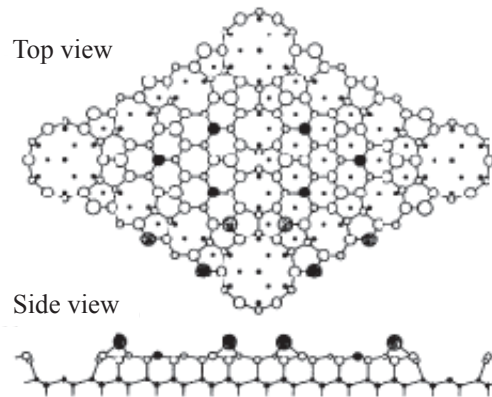


Figure 1.9: The Si(7×7) reconstruction Adapted from ref.[38]

the many hundreds of published papers it becomes evident that although a huge number of experiments have been conducted and a great deal of theoretical work has been published, a large number of issues remains unresolved. Surface crystallography of semiconductor surfaces also has a long way to go, and even clean single element semiconductor surfaces have not been mapped out with the same accuracy and confidence as the clean metal surfaces. To understand why it almost inevitably must be like this, one needs to take a look at the semiconductor chemistry. The semiconductors Si and Ge, discussed in this work, are held together by covalent bonds in a diamond structure as shown in Fig. 1.7. In a rough model, tetrahedrally coordinated semiconductors are bound together by tetrahedral nearest-neighbor bonds, each of which contains two spin-paired electrons. At a surface which exhibits the bulk geometry, some of the bonds will be broken and the surface atoms will have an unpaired electron. These 'dangling' bonds indicated on Fig. 1.8, make the surface rather unstable. To accommodate the dangling bonds, the semiconductor surfaces can strongly relax, forming new bonds between Si atoms at the surface. One famous example of such a reconstruction is the Si(111)-(7×7) reconstruction[38], shown in Fig. 1.9. The Si surface can of course also easily react with various gases. For example, a thick amorphous SiO₂ film will form in the presence of oxygen.

Alkali adsorption on semiconductor surfaces has been studied for a number of reasons. As was found on metal surfaces, alkalis can act to lower the work function of semiconductors[39] which, as on metal surfaces, can be used for a number of industrial purposes. Alkalis act as promoters to speed up oxidation processes and have also been used in the creation of negative affinity photocathodes. In recent years, alkali adsorption on semiconductor surfaces has been used as a model system of the metal-semiconductor interface[40]. Especially the Schottky barrier

in a metal-semiconductor interface can be studied using alkalis, because alkali metal-semiconductor interfaces are not very reactive (making prolonged studies experimental possible) and alkalis tend to form 1D or 2D structures and not 3D islands. Thus the formation of the Schottky barrier can be studied by slow deposition of alkalis.

1.8 Experiments with Low energy electrons

1.8.1 Low Energy Electron Diffraction (LEED)

LEED is a very old technique. The very first LEED experiments were carried out by Davisson and Germer in 1927[41–43]. They found that the angular distribution (of the intensity) of $\sim 100\text{eV}$ elastically scattered electrons from a Ni single crystal differed from that of a polycrystalline sample. The single crystal displayed a highly structured pattern which was interpreted as a result of electron diffraction. This result was a very important confirmation of the wave properties of the electron predicted by quantum mechanics, and the Nobel price was later awarded to Davisson for this work (back then the Professor often got all the credit, today it is more accepted that Post Docs and even Ph.D. students sometimes get their own ideas). The notion that these low energy electrons could also be used as a basis for the development of a surface sensitive structural tool was not put into practice until the 60's, when it became possible to construct the ultra high vacuum (UHV) chambers needed to keep surfaces clean over extended periods of time. Today almost all surface science experimental setups are equipped with a LEED optics, which in most cases is used as a diagnostic tool for determining the surface unit cell and estimating surface disorder.

The LEED experiment is depicted schematically in Fig. 1.10. A well defined electron plane wave \mathbf{k}_i is scattered on a crystal, and as will be shown later, the back-scattered wave field at the detector (usually a fluorescent screen with a retarding-grid high pass filter), will consist of a number of plane waves \mathbf{k}_s . $|\mathbf{k}_i| = |\mathbf{k}_s| = k$, because inelastically scattered electrons are removed by the retarding grids. The components of the \mathbf{k}_s vectors parallel to the surface are equal to the parallel component of \mathbf{k}_i plus a crystal reciprocal lattice vector \mathbf{g}_{hk} parallel with the surface. At normal incidence, as shown in Fig. 1.10b, $\mathbf{k}_{s\parallel} = \mathbf{g}_{hk}$, and one can further deduce that $d_{hk} = R \sin(\Theta_{hk}) = \frac{R}{k} g_{hk}$. Thus the LEED pattern on the fluorescent screen is a map of the 2D reciprocal lattice of the surface. Furthermore, by varying the energy ($k \propto \sqrt{E}$) or the angle of the incoming electrons, the intensity variation of the back-scattered plane waves can be used to obtain detailed information about the structure and dynamics of the crystal surface.

Unfortunately, the use of low energy electrons also presents serious difficul-

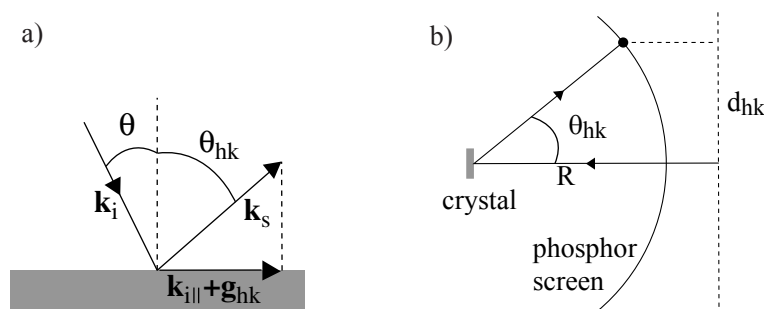


Figure 1.10: a) Schematic drawing of the basic LEED scattering situation. b) Basics of the LEED experiment for $\Theta_i = 0$.

ties, since they scatter so strongly off the atoms in the solid. This implies that the kinematic approximation, of only one scattering event prior to the scattered wave reaching the detector, works very poorly, making the direct methods used in X-ray diffraction difficult or even impossible to apply in LEED. The electron-electron interactions between the incoming electrons and the electrons of the solid are a further complication. Hence the Schrödinger equation we have to solve is a coupled many-body equation which is very difficult to deal with. This problem is overcome in the same way as in theoretical band-structure calculations (LEED calculations are actually based on the Greens function or KKR method [44]), by using a mean-field approximation in which the electron-electron interaction is represented by an average potential. In this way the complicated many-electron problem can be reduced to solving a one-particle Schrödinger equation. In the next chapter, a quantum-mechanical multiple scattering theory taking scattering of all orders into account will be discussed, which quite accurately describes the LEED experiment. Even though the kinematic approximation is not sufficient for structure determination by LEED, the single scattering picture can be very convenient for understanding the basic physics of the scattering process, and is also often used for interpreting effects due to disorder which are difficult (or even impossible) to address using the full theory.

1.8.2 Core Electron Spectroscopy

Instead of probing the surface directly with low energy electrons the surface atoms can be excited using photons or electrons and any emitted low energy electrons can be detected. These electrons may then reveal the abundance and the chemical surroundings of the emitting atom.

As described in ref.[45], the phenomenon of photoemission was first detected by Hertz back in 1887, and explained in 1905 by Einstein, who suggested that light propagates in fixed quanta - photons. The first photoemission spectroscopy

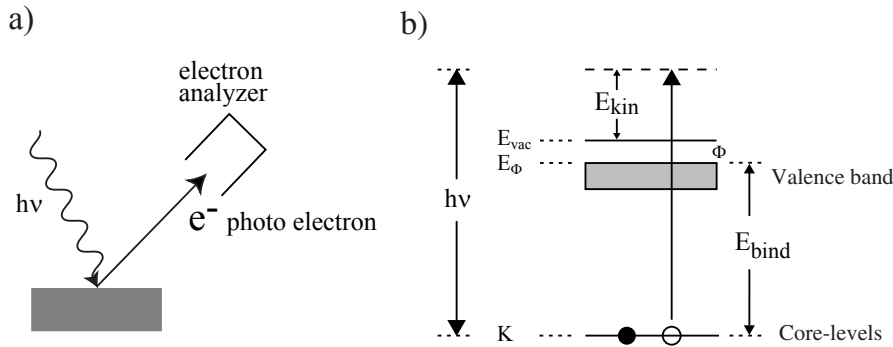


Figure 1.11: a) The Photo emission experiment b) Electron excitation in the PES experiment.

(PES) experiments were performed at around the time when the first LEED experiment was carried out by Davisson and Germer. Light monochromatized by a prism spectrograph was focused onto the surface of Na or K in a vacuum tube. The maximum kinetic energy of the liberated electrons was then measured by determining the voltage required to suppress the current across the vacuum vessel. By performing such experiments, both the work function ϕ and the relationship \hbar/e could be determined.

The basic principles of more recent photoemission spectroscopy (PES), as depicted in Fig. 1.11, are quite simple, although the actual equipment used can be very complicated. A monochromatized light source (in this work a synchrotron radiation (SR) source which is monochromatized by an arrangement of gratings and slits) illuminates a surface. If the photon energy is high enough, electrons can be emitted from the surface and subsequently detected using an electrostatic analyzer in which both angle and kinetic energy of the electrons can be determined. While the delocalized electrons of the valence band are also interesting to study, this work primarily uses the core electrons which are more localized around a single atom. Thus using core electrons one can focus on a single atomic species. As shown schematically on Fig. 1.11 A photon of energy $h\nu$, high enough to excite for example a core-level electron, leads to the emission of an electron with kinetic energy $E_{kin} = h\nu - \Phi - E_B$ where E_B is the binding energy of the core electron and Φ is the work function of the surface.

High resolution core level spectroscopy

While the electron core-level binding energy is roughly equal to the value found for neutral free atoms, it was established in the 60's [46] that the exact value will depend on the chemical surroundings of the emitting atom. This effect is utilized in high resolution core-level spectroscopy (HRCLS) experiments, where the HR

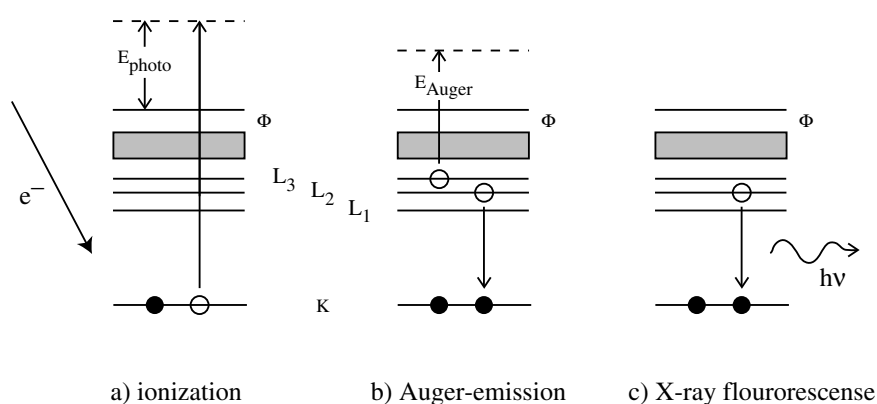


Figure 1.12: Upon the ionization process a), the solid can relax by b) a Auger process or c) x-ray fluorescence

in HRCLS is obtained by exploiting the phenomenal qualities of synchrotron radiation light sources and advanced high resolution electron analyzers. High resolution is important because the core level shifts due to the surroundings of an atom are usually quite small at surfaces ($\sim 100\text{meV}$). Although some simple 'rules of thumb' exist for estimating the chemical shifts, it is by no means a simple task to predict these values with a reasonable precision. In recent years some progress has been made especially using *ab initio* DFT calculations, but usually comparison to known model systems has yielded the most convincing results.

The intensity of emitted electrons with a specific energy and angle will depend on a number of factors. The number of electrons emitted from specific types of atoms must be proportional to the number of atoms of this type, this can be used to get a relative measure of the abundance. The probability of a core-level excitation will vary with both atomic element and the atomic level. For example the intensity of the $\text{Al}2p_{1/2}$ is roughly half of the intensity of the $\text{Al}2p_{3/2}$. The intensity of the emitted electrons also depends on the path out of the material and into the vacuum, which can be used to probe the position of a given atom with respect to the surface-vacuum interface. Later on we will present measurements at various exit angles, which can be used to probe the depth profile of a species. To sum up, the abundance, surroundings and depth profile of a specific atomic species can be probed by core-level spectroscopy.

Auger electron spectroscopy

Instead of looking at the excited core electron as in HRCLS we now turn our attention to the process of filling up the core hole. The basic Auger process is depicted

in Fig. 1.12. Electrons or photons can be utilized in Auger electron spectroscopy (AES) to excite core-level electrons. The hole left behind by the removal of a core electron will be filled up by an electron from a higher level, and the remaining kinetic energy is then released as either photons, or transmitted to another electron in a so-called Auger process. One might think that this is a very indirect approach, but it turns out that for most materials Auger electrons are emitted with energies in the low energy range, making them well suited for surface studies. It can also be noted that the probability of electron emission is high enough for all common elements that abundances as low as 0.01 ML can be detected with fairly inexpensive equipment. Finally it is substantially easier to measure an electron energy spectrum, compared to a photon energy spectrum. The same considerations of the influence of an atom chemical environment, as for photon-excited core-level spectroscopy are relevant for AES, but as the Auger levels of interest often involve the valence band, the level will be rather broad, and so AES is mostly used for determining the abundance of various elements on the surface or the depth profile of the elements. In the studies presented below AES has been used to monitor impurities on the surface.

1.9 Surface Science list of acronyms

It is probably safe to say that no other part of materials science uses quite the same number of acronyms, due to the multitude of experimental and theoretical approaches applied to the problems at hand. The development of all these techniques can be seen as a testament to the great challenges of dealing with and understanding surfaces. Here is a short list of the techniques mentioned in this thesis.

1.9.1 Experimental

- AES - Auger Electron Spectroscopy
- AFM - Atomic Force Microscopy
- CLS - Core Level Spectroscopy
- HAS - Helium Atom Scattering
- HEIS - High Energy Ion Scattering
- HRCLS - High Resolution Core Level Spectroscopy
- LEED - Low Energy Electron Diffraction

- LEIS - Low Energy Ion Scattering
- MEIS - Medium Energy Ion Scattering
- PES - Photo Electron Spectroscopy
- PhD - Photoelectron Diffraction
- STM - Scanning Tunnelling Microscopy
- SEXAFS - Surface Extended X-ray Absorption Fine Structure
- SXRD - Surface X-Ray Diffraction
- TEM - Transmission Electron Microscopy

1.9.2 Theoretical

- ATA - Average T-matrix Approximation
- CPA - Coherent Potential Approximation
- DFT - Density Functional Theory
- GGA - Generalized Gradient Approximation
- KKR method - Korringa, Kohn and Rostock method
- LDA - Local Density Approximation
- QHA - QuasiHarmonic Approximation

Chapter 2

Experimental and theoretical methods

2.1 The LEED experiment

2.1.1 Experimental setup

The chamber

A new experimental ultra high vacuum (UHV) chamber dedicated to quantitative LEED I(V) experiments was acquired from Vacuum Generators (VG) in September 1997. The spherical chamber is made of a special alloy called μ -metal (a mixture of Ni, Fe, Cu and Cr), which effectively reduces the penetration of outside magnetic fields into the chamber, resulting in fields of ≤ 10 mGauss inside the chamber. To obtain UHV, the chamber is equipped with a Turbo-V300HT Varian Turbo pump for both initial reduction of pressure and maintenance of $< 1 * 10^{-10}$ torr pressure. A Varian VacIon 300 ion pump used for pressure reduction in the low pressure region is also installed and inside the ion pump a titanium sublimation pump is used to give extra pumping capacity. The combined pumping power of these three different pumps is enough to achieve a pressure in the 10^{-11} torr region, but because of the outgassing of the new metal walls of the system, and normal operation (annealing, sputtering, measurements) the base pressure is usually $\sim 1 * 10^{-10}$ torr. Residual gases were mostly H_2 with small traces of H_2O , CO and CO_2 . A gas dosing system with its own ion pump, designed at our lab, can be used to admit various gases into the chamber in a controlled fashion ($1 * 10^{-10}$ torr - $1 * 10^{-5}$ torr and seconds in reaction time). It is also used to feed the sputtering gun with Argon. The ion pumps in the main chamber and in the gas dosing system can be closed off to allow large gas pressures of e.g. Ar in the system.

Sample preparation and characterization

The chamber is equipped with an HTP manipulator from VG, allowing positioning to within 0.1° around all three axis of the crystal. The tilt (δ) angle is restricted to a maximum change of 7° . X-Y-Z translation is allowed to within 0.1mm over a length of 200mm for the z-axis (up/down) and 20mm in X/Y directions. The temperature of the crystal is measured with an N-type thermocouple. Electron bombardment from a filament positioned behind the crystal and liquid N_2 cooling, allow for temperature changes from 100K to 1500K, the upper limit determined by the N-type thermocouple used. The temperature can be regulated to within a few degrees (constant value or linear ramping) using a Eurotherm 2408 temperature controller, recently installed. The sample can be sputtered by a differentially pumped VG sputter gun using Ar^+ ions accelerated to 0.5-2.5 keV. Alkali metals can be evaporated on to the crystal from a SAES getter[47] source by applying a direct current of 5-7A. The alkali sources are mounted on a linear translator, which allows the sources to be positioned ~ 1 cm from the crystal. The getters are always thoroughly degassed before use, and taken to temperatures (currents) considerably above the final evaporation temperature in order to open the sources. During actual evaporation, the chamber pressure never rose more than $5 * 10^{-11}$ torr . Metal crystals were cut from single-crystal rods and aligned to within 0.1° of the desired crystal plane orientation by mechanical polishing. The rectangular metal crystals with a thickness of ~ 2 mm are mounted between two tungsten pins, and orientated so that the tilt angle of $\delta = 0^\circ$ and a polar angle of $\theta = 90^\circ$ on the manipulator will be as close to normal incidence of the electron beam as possible. Si and Ge crystals were cut from wafers (see details in chapter 8) with a thickness of 0.4mm and aligned to $<0.5^\circ$ of the specified crystal plane. They were mounted on a Mo plate and strapped down by Ta foil. The crystals were indirectly heated by heating the Mo plate. Recently we have positioned a shielding/focusing Mo cylinder around the electron-bombardment filament in order to reduce desorption of adsorbed gases from the immediate surroundings of the crystal, during annealing of the crystal. This is especially relevant for Si and Ge where pressure during the final steps of the annealing should not rise too much.

Analytical facilities of the chamber

The pressure in the chamber was measured with a standard ion gauge, and the composition of the residual gas could be checked with a VG quadrupole mass spectrometer. Surface composition and contamination was investigated by AES using a hemispherical electron analyzer (VX100) with a radius of 10cm, and using the LEED electron gun as source of the 2500eV electrons. The LEED measurements were carried out using an Omicron NG reverse view LEED optics and

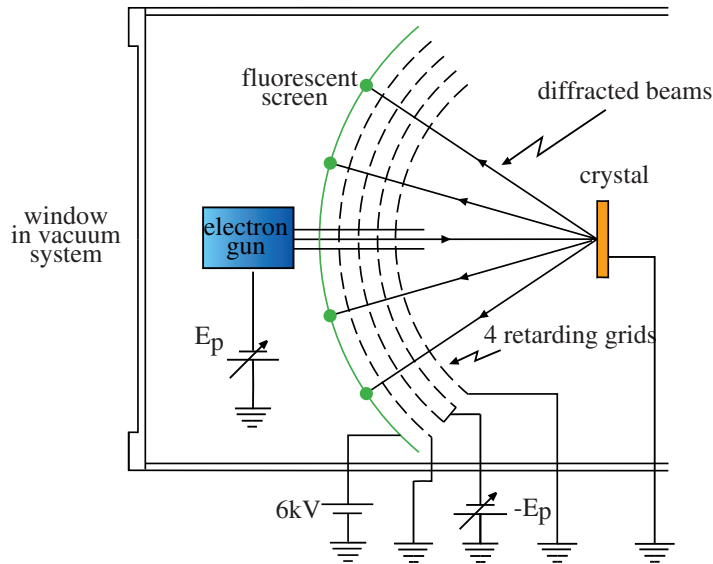


Figure 2.1: The four grid LEED optics.

electron gun.

2.1.2 The Digital LEED System

The LEED apparatus

A schematic drawing of a four-grid LEED optics is given in Fig. 2.1. Electrons are created by a LaB_6 filament heated by a current of ~ 1 A. The electrons are accelerated to the desired energy towards the anode of the electron gun (the filament being the cathode), and are focussed by 4 electrostatic lenses, to give a beam diameter of ~ 0.5 mm at the crystal. The inelastically back-scattered electrons are removed by a high pass filter made out of four spherical grids. This is accomplished by applying the voltages to the four grids as depicted in Fig. 2.1. Setting the first grid to the ground of the crystal and chamber ensures that the volume between the crystal and the retarding grids is free of significant electrostatic fields. The electrons are decelerated between the first and the second grid, and optimally only the elastically scattered electrons are allowed through by setting the potential on the second grid to 100% of the elastic electrons kinetic energy. However due to the strong lensing effects of the grid holes, the potential has to be $\leq 90\%$ of the elastic electron energy, to avoid broadening of the diffraction spots. In order to obtain a more well-defined retarding potential, the third grid is held

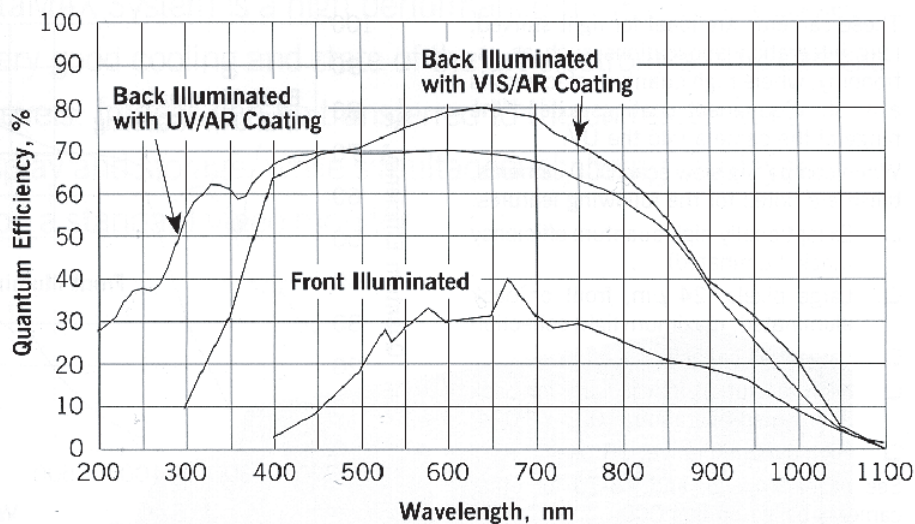


Figure 2.2: CCD efficiency according to Princeton Instruments

at the same potential as the second, which is believed to decrease the number of inelastic electrons allowed through. The fourth grid is again grounded, in order to screen the effect of the 6kV potential on the fluorescent screen. Finally the electrons are pulled on to the fluorescent screen by the large voltage on the screen (6kV), where they light up the screen resulting in a beautiful diffraction pattern (well sometimes).

The Princeton 16bit CCD camera

The heart of our new digital LEED system is a slow-scan 16 bit Charge-Coupled Device (CCD) camera. The scientific grade CCD in the camera has several features which makes it a very powerful tool for LEED experiments. Most significant is the large 16 bit dynamic range of the camera, because of the large well capacity of each pixel (~ 330000 electrons) and low read-out-noise of about 5 electrons per pixel per second. Later in this section, beam intensities are given in terms of the 65K gray tones corresponding to the 16-bit dynamic range of the CCD. A large dynamic range is important because the intensity of the various beams can vary quite dramatically. In general, the intensities of the accessible beams in the typical energy range of 50-450eV (and even at the same energy) can vary a factor of about 1000-4000, ie. $\sim 10 - 12$ bits.

The CCD also has a high quantum efficiency (a large percentage of the pho-

tons hitting the CCD create electron-hole pairs in the pixels), because it is back-illuminated. On an ordinary CCD the readout contacts are in front of the absorption array. However on a back-illuminated CCD the adsorbing Si back of the crystal has been coated with a thin antireflecting film and can now be exposed directly to light, which causes a quite dramatic improvement in the efficiency as can be seen from Fig. 2.2.

The number of defect pixels on the CCD were virtually zero. Noise produced by thermally generated electron-hole pairs, called dark currents, are minimized to 1 electron $\text{s}^{-1}\text{pixel}^{-1}$ by Peltier cooling the chip to -40°C . Response non-uniformity across the CCD is $\leq 1\%$ measured with a LabSphere uniform light source, which is of the order of accuracy of the light source itself. Geometric distortion is virtually non-existent. Linearity of the 16bit dynamic range has been tested by Princeton Instruments and was found to be better than 1.5%.

All these features combine to give extremely high quality images, with exposure times of 0.1-0.6s for even very faint LEED patterns. In fact *only one series of images is necessary in order to obtain high quality resolution of all beams* in contrast to the old video-LEED system[48] where 10 or more spectra were averaged. The camera is positioned on a Manfrotto camera base which can rotate the camera around all three axis. Furthermore the camera can be translated quite freely in the X-Y-Z directions. The lens used for obtaining images of the full screen is a high quality Nikkor f/2 28mm lens. For close-up photos a Nikkor 85mm lens can be used.

System control and data acquisition

The main task in the LEED I(V) experiment is to obtain the intensities of the diffracted beams as a function of electron energy. In contrast to the old LEED I(V) system [48], where analysis and recording of images was performed in real time, this task has been split into two separate parts. First, images of the LEED beams are recorded and stored on the hard disk. Then a lengthy analysis of the images can be performed later by a separate program. This simplifies the recording procedure considerably, and a more sophisticated and careful analysis of data can be performed. A schematic diagram of the acquisition process is depicted in Fig. 2.3. Two separate memory buffers are used in parallel, which has the advantage that an image can be stored on the hard disk while a new one is being read out of the CCD chip to the computer memory. The time consuming part of this process is the read-out from the CCD chip which takes $\sim 2\text{s}$ per image, when the camera runs in 16 bit mode (a $\times 10$ faster 12bit mode is available). Because of the high quantum efficiency of the CCD, and the fast lens, the exposure time of the CCD is usually between 0.1-0.6s. Since a series of images usually consists of 400 images total recording time is $\sim 20\text{min}$.

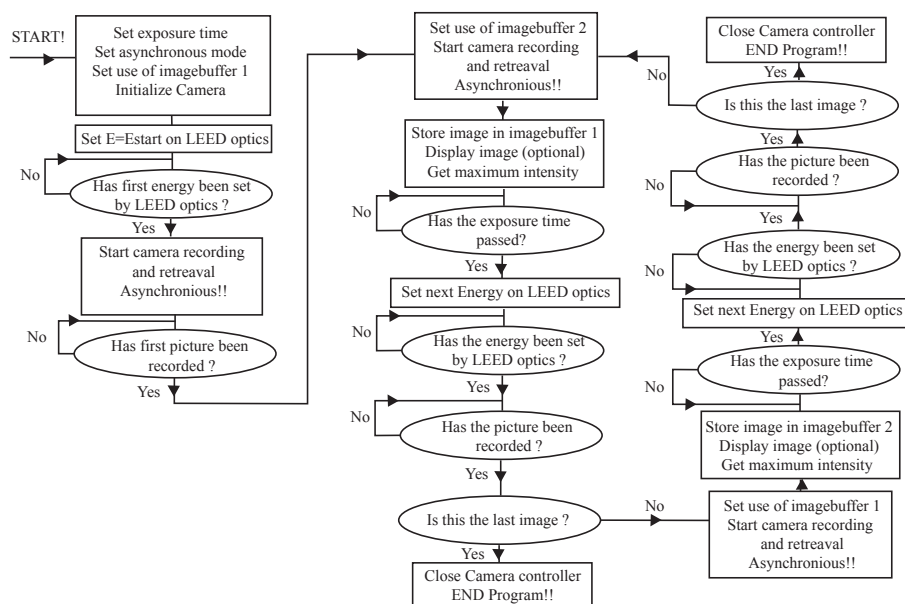


Figure 2.3: This is a schematic drawing of our recording program for the PC used to obtain series of ~ 400 images of the LEED fluorescent screen as a function of energy.

The control and analysis computer is a Pentium Pro with 64MB ram and two 16 GB hard disks (one exchangeable). Computer control and monitoring of the LEED optics is accomplished via a 16 bit A/D converter connected through a home built DAC isolation amplifier. The control program is written in Microsoft Visual Basic, using dynamic link libraries supplied by Princeton Instruments (for the CCD camera) and National Instruments (the A/D converter). A whole series of images requires 200MB storage, so even using the capacity of several hard disks, the images are stored on CD-ROMs after having been compressed using the commercial program WinZip.

It was possible to record a series of images at variable temperatures up to 550K although an electron bombardment filament was used for heating. This was accomplished by monitoring the filament current and recording images only when the filament was turned off. As no voltage between crystal and filament could be allowed for and there had to be reasonable intervals where the filament was off, this method could only be used up to a temperature of about 550K. For variable temperature measurements below room temperature, the efficiency of the cooling system could simply be regulated by submersing the coil with a continuous flow of N_2 used for cooling more or less in liquid nitrogen, and stable temperatures between 100K and 300K were obtained.

2.1.3 Analyzing the data

The purpose of the data analysis is to extract the integrated intensities of each LEED beam from the recorded images. This process has the following steps:

- Locating the beams on the images
- Integrating spot intensities of all available beams and removing the background. Ideally, this process would involve fitting the experimental spot profiles with functions describing the separate contributions of elastically and inelastically scattered electrons. In practice this is difficult for reasons discussed below.
- Repetition of these processes for all electron energies
- Averaging of the $I(V)$ curves of symmetry-equivalent beams which in principle are identical due to the symmetry of the crystal. In the averaging process the difference between symmetry beams will constitute a measure of the uncertainty of the $I(V)$ curves.
- Normalizing of the $I(V)$ curves at each energy due to the change in incoming electron beam current. Intensity is assumed to be proportional to the current of the incoming electron beam.

The final result is $I(V)$ curves for a number of symmetry-averaged beams which will be compared with theoretical calculations. The process, which is both robust and quite accurate, will be described in detail below.

Calculation of beam positions and corrections due to camera/optics geometry.

In order to acquire the integral intensity of a diffracted beam it is necessary to know the position of the beam on the LEED screen. Since the structure of the substrate crystal is always known and the surface unit cell usually can be inferred (we have included a large database with many possible structures to ease the process), the direction of the outgoing beams can be calculated for a given energy and angle of incidence of the electron beam. However, we still have to take the geometry of the optics into account. In the subsequent discussion, the camera is assumed to be positioned so that the LEED optics is centered around the center of the camera image plane, which simplifies the calculations somewhat. This optimal position of the camera can easily be obtained during the alignment of the camera, but it must be noted that the LEED program takes any deviations of the camera from this optimal position into account. A schematic drawing of the optics geometry is given in Fig. 2.4. The problem of finding the beam position is in fact

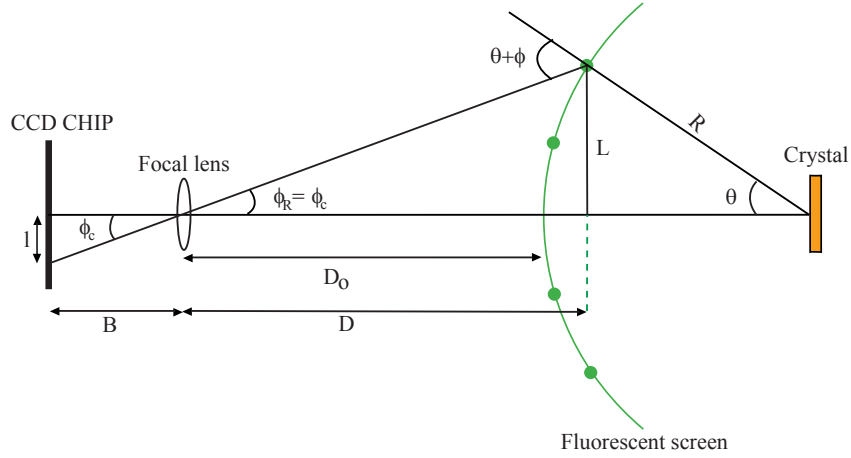


Figure 2.4: Schematic drawing of CCD chip in LEED optics geometry

over-determined because B , D , D_0 , L , θ defined on Fig. 2.4 and the length of a CCD pixel $l_p = 24\mu\text{m}$ are all known. Since

$$\phi_c = \phi_R \Rightarrow \tan(\phi_c) = \tan(\phi_R) \Rightarrow \frac{B}{l \cdot l_p} = \frac{D}{L}$$

it should be quite easy to find the beam position l in pixels. The only problem is that the uncertainties in B and l_p will have a large effect on this expression, but since the screen radius in pixels from the recorded images is known it can be used to eliminate these factors from the expression.

$$\frac{B}{l_{sr} \cdot l_p} = \frac{D_{SR}}{L_{SR}} \Rightarrow l = \frac{D_{SR} l_{SR} L}{L_{SR} D}$$

D_{SR}, l_{SR}, L_{SR} denotes values of D, l, L for $\theta = 51^\circ$ the angle of the screen circumference. $D = D_0 + R(1 - \cos(\theta))$ and $L = R \sin(\theta)$. Denoting $\theta_M = 51^\circ$ as the θ angle of the screen circumference the formula for l is:

$$l = \frac{R \sin(\theta) \{D_0 + R_{SR}(1 - \cos(\theta_M))\} l_{SR}}{\{D_0 + R(1 - \cos(\theta))\} R_{SR} \sin(\theta_M)}$$

the only parameter not known with good accuracy is D_0 , but it can be seen from the preceding formula, that the uncertainty in this quantity will not have great influence on the value for l . D_0 can be found by using the focal length (when focussing the camera, the point where the fluorescent screen terminates is used as focus point), or by simple measurements of the distance from the camera lens to the LEED optics. Similar values are found using the two methods (~ 30 cm), but even changes of several centimeters of this value have no great influence on

the calculated beam position. Using this method, the positions of the individual beams can be obtained within 1-4 pixels. The final positions are obtained by a simple search for the strongest pixel within a small area around the calculated position. In obtaining the intensity in a given diffracted beam the fact that different positions on the LEED screen have different relative distances to the CCD in the camera must be taken into account, which gives the Lambert's Law correction proportional to D^2 . The solid angle as seen from the camera also varies with the position of the spot. These two corrections are found to influence the intensity of a given beam $I_{initial}$ as[49]:

$$I_{final} = I_{initial} * \left(\frac{r}{D_0 + B}\right)^2 \frac{1}{\cos(\theta + \phi)}$$

where r is the distance from a given point on the LEED optics to the CCD image plane and the other quantities are given in Fig. 2.4. Before acquiring the $I(V)$ curves, a table of this correction to each pixel on the CCD is created, and subsequently used. Independent checks of the formulas and assumptions made above are difficult, however it should be mentioned that the fact that the position of all beams can be calculated to within a few pixels over an energy range of 50-500eV and at various angles indicates that this approximation is valid. The corrections to the intensity have been checked previously by the Århus LEED group[49].

Alignment of the camera and crystal

The camera can be aligned parallel with the electron gun using the fact[50] that the electron gun lies on the axis of the LEED fluorescent screen to within $\sim 0.1^\circ$. The circular back of the gun, and the circular radius of the screen must have the same center when the camera is aligned. This is used to align the camera by iteratively varying the X, Z positions and angles of the camera. Having the center of the LEED optics in the center of the image plane is considered the optimal position and can be set to within a few pixels of the CCD. After this alignment of the camera, the crystal is initially aligned by optimization between the calculated positions of the LEED beams and the positions observed. By doing this at several energies an initial lineup of $0.5^\circ - 0.3^\circ$ can be reached. Full alignment consists of setting the polar $\theta = \pm 0.1^\circ$ and tilt $\delta = \pm 0.1^\circ$ angle by minimizing the R-factor defined in section 2.3.2 for the comparison of $I(V)$ spectra for symmetry-equivalent beams as a function of these two angles. The precision of the geometry at off-normal incidence $\theta \neq 0^\circ$, which involved setting the azimuthal angle $\phi = 0^\circ$ by aligning a close-packed direction in the LEED pattern with the horizontal, is less certain due to possible errors in the mutual alignment of the crystal goniometer and the LEED optics. However, subsequent comparisons of experimental and

calculated $I(V)$ spectra as a function of θ indicated that the precision of the incidence geometry was also of the order of $\pm 0.1^\circ$ for $\theta = 10^\circ$. The condition $\phi = 0^\circ$ was chosen to preserve mirror-plane symmetry for measurements at $\theta \neq 0^\circ$.

Spot analysis / spot profile

As mentioned above, an important part of the analysis process is the determination of the intensities in the LEED spots, as corrected for the (some times large) background in the LEED pattern. This process is subject to some uncertainty because of various factors discussed below. When the LEED beams reach the phosphor/tin-oxide coated glass fluorescent screen they have a finite width and shape determined by a number of physical effects. Upon leaving the electron gun the electron beam is believed to have an energy spread $\leq 0.15\text{eV}$ due to the LaB_6 filament and an angular distribution of Gaussian shape with Lorentzian like tails[51–53] with a divergence $\leq 0.25^\circ$.

The fact that the surface is not a perfect single crystal, but consists of domains of varying size with various kinds of defects on them results in a further broadening of the LEED beams. While a perfect single crystal scatters into beams with delta function shape, the imperfect crystal scatters into beams with a finite non-zero width. The actual shape of the beams is determined by the type and distribution of domains and defects on the surface. Thus the beam profile can be used to determine the distribution of steps and kinks on the surface.

The influence of surface imperfections in a conventional LEED optics such as ours is quite small compared to instrumental effects for well-ordered surfaces, making only small-scale disordering visible. The limits to the length scale possible for observing defects is called the coherence length, and is defined by Pendry [54] as the length scale within which the incoming (and outgoing) beams can be considered as single plane waves. Two waves outside the coherence length will have independent phase factors due to instrumental effects, and in a steady state scattering situation, information about their interaction on the surface will be impossible to obtain, because the relation between the two phases is unknown. This is a highly intuitive explanation and definition, which can be quantified somewhat in terms of an instrument response function[53], but no matter which view has been taken on this effect by various authors[52–54], all agree that the coherence length of a normal LEED optics is around 100-500Å. One example from this work where the surface roughness influences the beam profiles is shown in Fig. 2.5a for Al(110), where the diffracted beams are elongated along the [100] direction at a few low energies due to surface disorder.

The retarding grids will introduce a further broadening of the beams due to the lensing effect of the grids. An analysis of images taken with the 85 mm lens suggests that the beam profiles are significantly influenced by the lensing effect

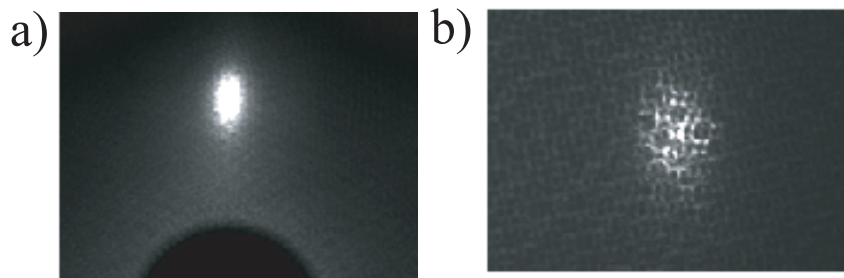


Figure 2.5: a) Al(110) spots are elongated at 68 eV which is attributed to surface disorder in the [100] direction. b) Image of a LEED beam taken with 85 mm lens. Notice the Moirré pattern

of the grids of the LEED optics. It is conceivable that the grids might be partially responsible for the weak, long-range tails of the very intense spots. These tails are most likely a mixture of elastic and inelastically scattered electrons, where the composition gradually shifts towards a high concentration of inelastic electrons as we move away from the spot center. This conclusion is based on several observations. Firstly, the tails are observed at all temperatures for all substrates investigated (Al, Cu, Si). Duke et. al. [55] have shown that the electrons scattered off plasmons should also spread into beams having the same directions as the elastic beams, but with broader distributions and being considerably weaker. Lagally et. al.[53] have shown that for electrons with energies very close to the retarding voltage, the lensing effect of the grids will be very large as seen in Fig. 2.6. This has been confirmed with measurements on our own LEED optics. It is thought to be unlikely that the angular divergence in the incoming beam is large enough (or has the shape) to cause the tails in the outgoing beams. These tails introduce an uncertainty in estimates of the shape and size of the elastically scattered beams. Assuming the beam profiles are a mix of elastic and inelastic electrons, it is hard to determine a cut-off or a lineshape. But what can be used is the half-width of the beam since the effects discussed above only influence the tails, and to a lesser extent the center part of the beam. We have used this half-width to estimate the total beam width as two times the half width. From measurements of this halfwidth it has been found to vary as approximately as $\frac{A}{\sqrt{E}} + B$

Our troubles with the grid optics do not end with the lensing effects. As is seen on Fig. 2.5b, the grids also produce a Moirré pattern on the image. This pattern varies strongly with energy, and Fourier analysis shows that it consists of many different periods. The origin of this pattern can easily be understood. The grid wires deflect about 8% of the electrons passing through the grid[50] because the electrons pass close by or hit the wires. This will superimpose a pattern on

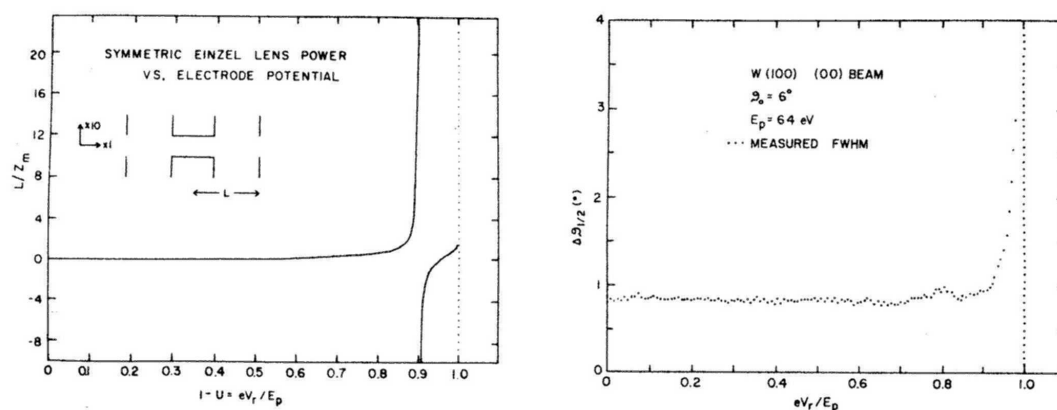


Figure 2.6: Computer simulation and experimental verification of grid lensing effect by Lagally et al.[53]

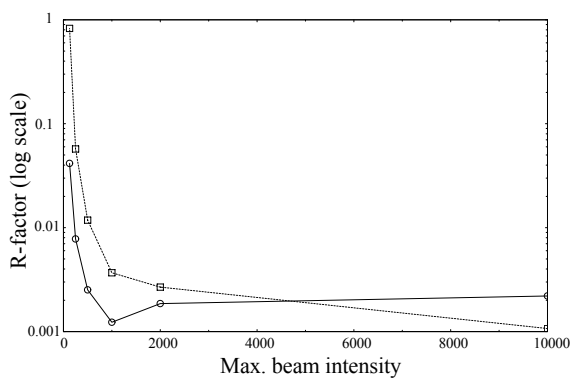


Figure 2.7: Theoretically calculated series of LEED images are analyzed as ordinary experimentally obtained images would be to obtain $I(V)$ curves. Circles connected by a solid line represent the R-factor comparison between symmetry equivalent beams as a function of maximum beam intensity from images distorted by a Morrié pattern. Squares connected by a broken line represent the R-factor comparison between beams obtained from completely undistorted images and beams obtained from images distorted by a Morrié pattern. R-factors for comparison of symmetry equivalent beams for conventional experimental spectra are in the range of 0.01 - 0.05

the outgoing electron distribution resembling the grid, with some distortion due to the voltage on the wires. After having passed four grids, four such patterns will be superimposed, giving patterns like the one shown in Fig. 2.5b. The good news is that the variation of this pattern is so rapid that it averages out, when obtaining the integrated intensity. This has been confirmed by simulations of the Moirré effect on a computer-generated LEED pattern, which we have carried out. The grids were assumed to be flat, however the correct widths[56] of the grid wires ($25 \mu m$) and spacings between the wires of ($250 \mu m$) was used. The four grids were positioned at the approximate positions of the real circular grids. The grids were randomly moved and rotated parallel to each other. The LEED spots were assumed Gaussian in shape deriving from a number of domains, having an energy dependence of $\frac{1}{\sqrt{E}}$ and a FWHM of 16-20 pixels (the diameter of the full LEED screen was set to 480 pixels) and a broad Gaussian background with FWHM of 100 pixels and maximum intensity of 5000 (out of 65535) was added. The Al(100) diffraction pattern was assumed and the energy range was 50-250eV. Beam intensities were assumed constant. The distortions produced by the Moirré patterns on the I(V) spectra were found to be an order of magnitude less than the observed discrepancies between symmetry-equivalent beams with intensities down to 500, as can be seen in Fig. 2.7.

In fact the biggest distortion is due to the variations of the background, which can have the same symmetry as the beams. To investigate this effect a central symmetric background oscillating radially from the center of the LEED pattern, but isotropic in the angle, was introduced. The results of these simulations are shown in fig 2.8, where it can be seen, that oscillations in the background must have a half-period equal to or smaller than the width of the LEED spots, before the R-factor values reaches problematic levels (comparable to R-factors values of comparison between experiment and theory). It is comforting that the R-factor found by comparing symmetry equivalent beams will reflect distortions both due to the Moirré pattern and the variations of the background as is also seen in Fig. 2.7 and Fig. 2.8.

Following the arguments above, the I(V) curve of a spot is obtained as follows: The center pixel of the spot is found automatically as described previously. The circular area of the spot is defined as $\times 2$ the average halfwidth of the spots as found by using the expression $A \frac{1}{\sqrt{E}} + B$, where A and B are determined by giving the width of the beams at the start energy and the end energy of a beam set. Usually the start radius is set to 12 pixels and the end radius to 10 pixels, however uncertainty in both numbers of several pixels can be allowed for without changing the resulting I(V) curves significantly. A rectangular box with side length ~ 3 times the radius of the spot is defined around the center of the spot. Pixels which lie inside the rectangular box, but *outside* the circular center, are used to obtain

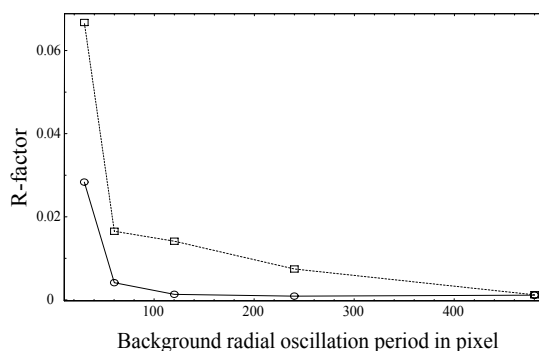


Figure 2.8: Theoretically calculated series of LEED images are analyzed as ordinary experimentally obtained images would be to obtain $I(V)$ curves. Circles connected by a solid line represent the R-factor comparison between symmetry equivalent beams *as a function of the period of a radially oscillating background* from images distorted by a Morrié pattern. Squares connected by a broken line represent the R-factor comparison between beams obtained from completely undistorted images and beams obtained from images distorted by a Morrié pattern. R-factors for comparison of symmetry equivalent beams for conventional experimental spectra are in the range of 0.01 - 0.05

a fit of the background which can be approximated by a plane or a paraboloid. Typically the 'spot' area contains ~ 400 pixels and the 'background' area contains ~ 500 pixels. Using the calculated background, and assuming that it can be extrapolated to the circular center, the integrated intensity of the background inside the circular center can be found. The intensity inside the circular center is summed and the background integral is subtracted.

Range and quality of the $I(V)$ spectra

$I(V)$ spectra are usually measured at 100K, to reduce thermal effects, thus yielding a larger and more precise data set. Measurements are made in the energy range 40-450eV with a step size of 1eV. In a number of cases $I(V)$ spectra are measured both at normal incidence, $\theta = 0^\circ$, and off normal at around $\theta = 10^\circ$, this will be stated for each specific case.

In each set of measurements, the intensities of *all* diffracted beams contained in the solid angle defined by the LEED optics are measured, except for the few beams whose trajectories are blocked by the electron gun and/or its connections, and beams for which the accessible energy range is less than about 30eV.

All steps of the calculations have been thoroughly checked. To further assure the correctness of the obtained $I(V)$ curves, the curves obtained with the new Digital LEED system have been compared to the $I(V)$ curves recorded with the old Video-LEED system of the Århus group. These comparisons show that for the

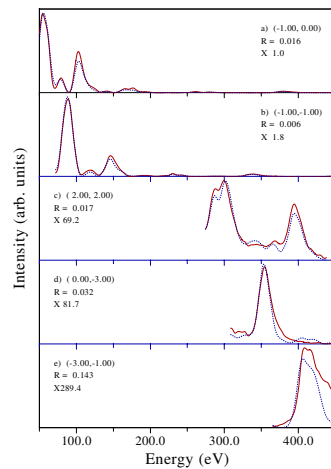


Figure 2.9: $I(V)$ spectra (solid line) (5 out of 7 beams) of Al(100) recorded at $T=300\text{K}$, compared to theoretical calculations (dotted line). As is seen, beams of intensity 70, 80 and 290 times less than the strongest beam can be resolved even at room temperature .

strong beams, the differences as measured by our usual R-factor are of the order or below the R-factor found by comparing symmetry equivalent beams. Comparison of several subsequently recorded spectra also show that R-factors of comparison are an order of magnitude below the R-factors found by comparing symmetry equivalent beams.

The strength of the new digital LEED system is exemplified by noting that the old state-of-the-art video LEED system, used a video camera which was effectively only 5-6bit, and only averaging of many recording $I(V)$ spectra and precise camera gain control enabled measurements with a range of 10-12 bit. The improved sensitivity has enabled the measurement of a larger number of beams over a wider range. One example is given in Fig. 2.9 where a comparison between theory and experiment shows that it is possible to record beams with an integrated intensity at least 250 times weaker than the strongest beam even at room temperature.

2.1.4 Experimental procedures used for alkali-metal systems

The metal crystals were cleaned by cycles of Ar^+ bombardment and annealing to 770K for Al(111) and Al(100), 670K for Al(110) and 900K for Cu(100). Sharp LEED spot with good contrast were obtained for all clean substrates, except for Al(110) where some broadening of the spots along the [100] direction at energies around 70eV was always observed. The 50K lower annealing temperature used for the Al(110) surface resulted in a more well-ordered surface, as it judged by

the quality of the LEED patterns, than obtained in earlier studies by the Århus group of this surface[57]. After Li adsorption experiments, Li was removed by Ar^+ bombardment, rather than by thermal desorption, to minimize possible diffusion of Li into the bulk of the crystal. With this procedure, no evidence of such diffusion was observed in the course of many experiments.

AES measurements taken both before and after completion of a set of LEED measurements indicated that surface contamination of S, C and O was always less than 0.03 ML. Several consecutive I(V) spectra were always recorded and compared in order to check for damage induced by the incident electron beam or for surface contamination.

Optimum development of a given structure was achieved by incremental deposition of the alkali until a maximum was reached in the ratio of integrated intensity in fractional-order and integral-order diffracted beams. As this number is usually quite sensitive to the structural perfection, it is possible to distinguish very small deviations (0.1ML) from the optimal coverage, as was for example found for Li adsorption on Al(100) between 0-0.5ML in a combined LEED and HRCLS study[58].

2.2 Theory of LEED

2.2.1 The LEED pattern

A typical LEED diffraction pattern is depicted in Fig. 2.10. The total wavefield Ψ_{tot} of the incoming and scattered wave satisfies the Schrödinger equation:

$$\left\{ -\frac{\hbar^2}{2m}\nabla^2 + V(\mathbf{r}_{\parallel}, z) \right\} \Psi_{tot} = E\Psi_{tot} \quad (2.1)$$

where \mathbf{r}_{\parallel} is the coordinate parallel to the surface, z is the coordinate along the axis perpendicular to the surface.

When the surface has a periodicity which can be defined by two primitive vectors \mathbf{a}_1 and \mathbf{a}_2 , the potential will also have this periodicity:

$$V(\mathbf{r}_{\parallel} + \mathbf{R}, z) = V(\mathbf{r}_{\parallel}, z); \mathbf{R} = l * \mathbf{a}_1 + m * \mathbf{a}_2; l, m \in Z$$

This means that we can apply Bloch's theorem parallel to the surface: $\Psi_{tot} = e^{i\mathbf{k}_{\parallel}\mathbf{r}_{\parallel}} v_{\mathbf{k}_{\parallel}}(\mathbf{r}_{\parallel}, z)$ where $v_{\mathbf{k}_{\parallel}}(\mathbf{r}_{\parallel} + \mathbf{R}, z) = v_{\mathbf{k}_{\parallel}}(\mathbf{r}_{\parallel}, z)$ has the same period as the potential. The incident electron can to a good approximation be considered as a plane wave $\psi_i = Ae^{i\mathbf{k}_i \cdot \mathbf{r}}$ with a well defined wavevector $\mathbf{k}_i^2 = \frac{2m}{\hbar^2}E$. Such a plane wave inherently fulfills Bloch's theorem. This implies that the scattered wave is also a Bloch wave, since both the total $\Psi_{tot} = \psi_i + \psi_s$ and the incoming wave ψ_i are

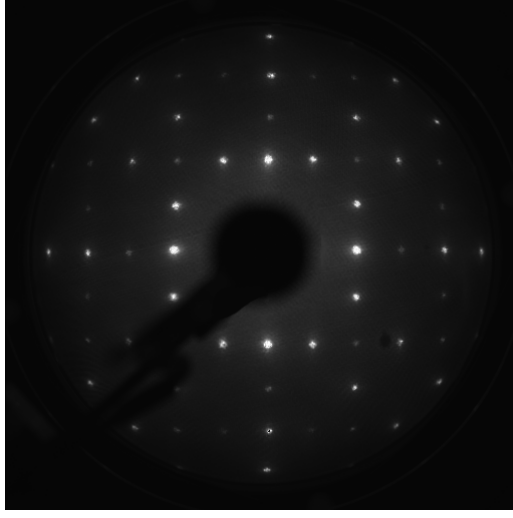


Figure 2.10: Typical LEED diffraction pattern. The example is Si(100)-(2 × 1), T=100K, E=124eV. Note that the picture only contains 256 gray scale nuances are shown, the full 65535 different intensities can not be resolved in grey tones.

Bloch waves, hence $\psi_s = e^{i\mathbf{k}_{\parallel} \cdot \mathbf{r}} u_{\mathbf{k}_{\parallel}}(\mathbf{r}_{\parallel}, z)$ where $u_{\mathbf{k}_{\parallel}}(\mathbf{r}_{\parallel}, z)$ has the same periodicity as the lattice and \mathbf{k}_{\parallel} is the part of \mathbf{k}_i parallel to the surface. $u_{\mathbf{k}_{\parallel}}(\mathbf{r}_{\parallel}, z)$ can be expanded in a Fourier series since it is periodic, which gives for ψ_s :

$$\psi_s = \sum_{\mathbf{g}_{hk}} \alpha_{\mathbf{g}_{hk}}(z, E) e^{i(\mathbf{k}_{\parallel} + \mathbf{g}_{hk}) \cdot \mathbf{r}_{\parallel}}$$

where the sum is over all the reciprocal lattice vectors $\mathbf{g}_{hk} = h\mathbf{a}_1^* + k\mathbf{a}_2^*$; $h, k \in \mathbb{Z}$. The $\alpha_{\mathbf{g}_{hk}}(z, E)$ functions can be determined easily, within a multiplicative constant, by substituting the total wavefield $\psi_s + \psi_i$ into the Schrödinger equation in vacuum (far from the crystal) where the potential vanishes. This gives a solution for outgoing waves of ψ_s given by:

$$\psi_s = \sum_{\mathbf{g}_{hk}} a_{\mathbf{g}_{hk}}(E) e^{i\mathbf{k}_{\mathbf{g}_{hk}}^- \cdot \mathbf{r}}$$

$$(\mathbf{k}_{\mathbf{g}_{hk}}^-)_{\parallel} = \mathbf{k}_{\parallel} + \mathbf{g}_{hk}, (\mathbf{k}_{\mathbf{g}_{hk}}^-)_{\perp} = (-\{\frac{2m}{\hbar^2}E - (\mathbf{k}_{\parallel} + \mathbf{g}_{hk})^2\})^{\frac{1}{2}}$$

We see that the scattered wave and thus the diffraction pattern is completely determined by the reciprocal lattice of the crystal planes. These outgoing plane waves in directions $\mathbf{k}_{\mathbf{g}_{hk}}^-$ are the so-called LEED beams. This derivation did not include rotational symmetry, but it can be derived that the rotational symmetry of the lattice is also exhibited by the intensities of the LEED beams if the incoming beam is parallel to the rotational axis.

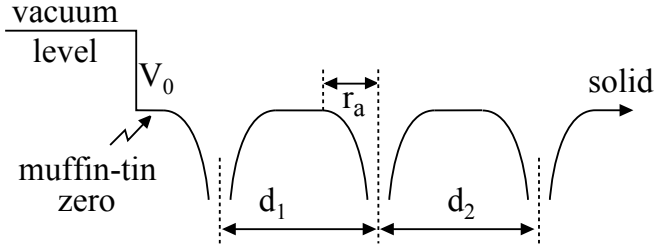


Figure 2.11: Model of potential used in LEED calculations

2.2.2 Multiple scattering theory of LEED

One can now determine the periodicity of the surface from the LEED pattern, but nothing has been learned about the crystal structure perpendicular to the surface, or the arrangement of the atoms within the 2D-unit cell. Inspired by the Bragg condition for interference between waves scattered off crystal planes separated by a distance d , $\lambda = \frac{2d \sin \theta}{n}$ [44], one could perhaps immediately obtain the layer distance by varying $\lambda =$ the wave length of the electrons or $\theta =$ the incidence angle of the electron beam. But once again it must be stressed, that direct methods such as the Bragg condition can not be easily applied in LEED because they assume a first order approximation to scattering. This has led to the development of the multiple scattering theory of LEED, which is derived from a full band-structure calculation using the Greens function method. Continuing the discussion from the previous section, one would like to calculate the $|a_{\mathbf{g}_{hk}}|^2$ of the individual beams as a function of energy. Assuming a model potential of the surface this can be accomplished using the multiple scattering theory.

The model potential used in LEED, depicted schematically in Fig. 2.11, is composed of spherically symmetric muffin-tin band-structure potentials centered around each ion position. For the calculations presented here the potentials are usually taken from self-consistent DFT band-structure calculations of Moruzzi et al. [59] (in the case of Si and Ge the potentials were taken from self-consistent DFT band-structure calculations by N. E. Christensen, IFA). A step of height V_0 at the surface-vacuum interface represents the kinetic energy gained by the electron, due to the dipole layer at the surface and the exchange and correlation with the valence electrons. This step is of the order of 10eV and is taken as a non-reflective, but refractive step positioned at a distance equal to one-half the bulk interlayer spacing above the first layer of atoms. The incident electron energy inside the solid is:

$$E = E_{vac} + V_0 + iV_{im}$$

The imaginary potential V_{im} is introduced to model all inelastic scattering processes such as electron-hole pair production and plasmon excitation. Both V_0 and V_{im} are assumed independent of \mathbf{k}_i and E_{vac} . This assumption is roughly confirmed by jellium calculations of V_0 and V_{im} for low energy electrons[60], although recent work has shown that more elaborate models can explain some inconsistencies in structural determinations[61].

In the following the formalism of scattering matrices is used as found in a number of textbooks [62, 63]. The description presented here is largely based on a review article by S. Y. Tong[64]. The multiple scattering at the various stages of the calculation can be understood by restating the Schrödinger equation in integral form for the situation of an incoming plane wave ψ_i and an outgoing scattered wave:

$$\Psi^+(\mathbf{r}) = \psi_i(\mathbf{r}) + \int G^+(\mathbf{r}, \mathbf{r}')V(\mathbf{r}')\Psi^+(\mathbf{r}')d\mathbf{r}' \quad (2.2)$$

where $G^+(\mathbf{r}, \mathbf{r}')$ is a free-electron propagator or Greens function of the Helmholtz equation calculated in various textbooks [63]. $\Psi^+(\mathbf{r})$ denotes the solution of the Schrödinger equation in this particular scattering picture. The total scattering matrix in real space $T(\mathbf{r}, \mathbf{r}')$ is now defined as:

$$V(\mathbf{r}')\Psi^+(\mathbf{r}') = \int T(\mathbf{r}, \mathbf{r}')\psi_i(\mathbf{r})d\mathbf{r} \quad (2.3)$$

It must be noted that it is really the Fourier transform of T which is of interest in, since the amplitude scattered into beam \mathbf{k}_g from incoming beam \mathbf{k}_i is $\langle \mathbf{k}_g | T(\mathbf{k}_g, \mathbf{k}_i) | \mathbf{k}_i \rangle$, where

$$T(\mathbf{k}, \mathbf{k}_i) = \int e^{-i\mathbf{k}\cdot\mathbf{r}_2} T(\mathbf{r}_2, \mathbf{r}_1) e^{i\mathbf{k}_i\cdot\mathbf{r}_1} d\mathbf{r}_1 d\mathbf{r}_2 \quad (2.4)$$

These amplitudes are exactly the amplitudes $a_{\mathbf{g}}a_{\mathbf{g}}^*$ of the beams discussed in the previous section. Economizing on the notation, Eq. 2.3 can be expressed as $V\Psi^+ = T\psi_i$, and from Eq. 2.2: $\Psi^+ = \psi_i + GV\Psi^+ = \psi_i + GV\psi_i + GVG\Psi^+ + \dots$ thus the following expression is obtained:

$$\begin{aligned} T &= V + VGV + VGVG + \dots = V + VG(V + VGV + \dots) \\ &= V + VGT \Rightarrow T = (I - VG)^{-1}V \end{aligned} \quad (2.5)$$

Since

$$V(\mathbf{r}) = \sum_{\mathbf{R}} v_{\mathbf{R}}(\mathbf{r} - \mathbf{R}) \quad (2.6)$$

where $v_{\mathbf{r}}(\mathbf{r})$ is an individual ion-core potential, an equation similar to equation 2.5 can also be derived for the scattering matrix of the individual ion-cores $t_{\mathbf{R}}(\mathbf{r} - \mathbf{R}, \mathbf{r}' - \mathbf{R})$ given by

$$t_{\mathbf{R}} = v_{\mathbf{R}} + v_{\mathbf{R}}Gv_{\mathbf{R}} + v_{\mathbf{R}}Gv_{\mathbf{R}}v_{\mathbf{R}} + \dots \quad (2.7)$$

By inserting equation 2.6 into equation 2.5 and then splitting the sums up into terms as found on the right side of equation 2.7 it is found that:

$$T = \sum_{\mathbf{R}} t_{\mathbf{R}} + \sum_{\mathbf{R}\mathbf{R}'} t_{\mathbf{R}'} G t_{\mathbf{R}} + \sum_{\mathbf{R}\mathbf{R}'\mathbf{R}''} t_{\mathbf{R}''} G t_{\mathbf{R}'} G t_{\mathbf{R}} + \dots \quad (2.8)$$

The prime in the sums indicates that all terms $t_{\mathbf{R}} G t_{\mathbf{R}}$ which 'propagate' a scattering matrix directly onto itself are excluded. This expression can be understood as the multiple scattering of electron waves between the individual ion cores. The first sum consists of contributions $t_{\mathbf{R}}$ from single scattering off the ion-cores at \mathbf{R} before the wave leaves the crystal. The second sum consists of contributions $t_{\mathbf{R}'} G t_{\mathbf{R}}$ from scattering $t_{\mathbf{R}}$ off the ion-core at \mathbf{R} , propagation G of the scattered wave to all \mathbf{R}' and scattering $t_{\mathbf{R}'}$ again at all \mathbf{R}' before the wave leaves the crystal. The next terms $t_{\mathbf{R}''} G t_{\mathbf{R}'} G t_{\mathbf{R}}$ represents triple-scattering events and so forth.

For the individual ion-core, which is taken to be spherically symmetric, the scattering problem is solved by expanding the total wavefunction in spherical harmonics around the ion-core center:

$$\Psi^+(r, \theta, \phi) = \sum_{l,m} R_l(r) Y_{lm}(\theta, \phi) \quad (2.9)$$

In this manner one is left with solving the radial part of the Schrödinger equation for each l for a spherically symmetric potential. Outside the muffin-tin radius r_a (where $V(r) \equiv 0$) the radial part can be found as $R_l = \beta_l \left[h_l^{(1)}(e^{2i\delta_l} - 1) + 2j_l \right]$. The first term in the brackets can be interpreted as the scattered spherical wave and the second part as an incoming spherical wave (it is the solution to the equation with $V(r) = 0$ for all r). The shape of the potential determines the values of δ_l . It is found that for the potentials and electron energies used in LEED, the phase shifts δ_l go to zero as l increases, thus only a finite number of phase shifts are needed at a given energy.

A scattering matrix for an incoming spherical wave into scattered spherical waves can be defined as $t_{LL'}(k_i) = \delta_{LL'}(e^{2i\delta_l} - 1)/(i2k_i)$ ($L \equiv (l, m)$), which is diagonal since an incoming spherical wave only scatters into an outgoing wave with the same L quantum numbers for a spherically symmetric potential. Now one is left with the somewhat tedious mathematical task of using these ion-core scattering matrices expressed with a spherical basis (l -space) in our $T(\mathbf{k}, \mathbf{k}_i)$ matrices defined in plane wave space (k -space). This can be done and leads to the following expression for T [64]:

$$T(\mathbf{k}', \mathbf{k}) = (4\pi)^2 \sum_{LL'} Y_{L'}(\mathbf{k}') Y_L^*(\mathbf{k}) \left\{ \sum_{\mathbf{R}} e^{i(\mathbf{k}-\mathbf{k}') \cdot \mathbf{R}} [t(k_0)]_{LL} \right. \\ \left. + \sum_{\mathbf{R}} \sum_{\mathbf{R}' \neq \mathbf{R}} e^{i(\mathbf{k} \cdot \mathbf{R}' - \mathbf{k}' \cdot \mathbf{R})} [t(k_0) \mathbf{G}(\mathbf{R} - \mathbf{R}') t(k_0)]_{LL} + \dots \right\}$$

where the matrix $\mathbf{G}(\mathbf{R} - \mathbf{R}') = G_{LL'}(\mathbf{R} - \mathbf{R}')$ consists of the terms in a spherical expansion of the free-electron propagator[64]. The next step is to realize that the sums of the above expression can be separated into two parts: One dealing with multiple scattering within individual Bravais layers of the same kind of atoms, and one dealing with multiple scattering between atoms in different, possibly co-planar Bravais layers. One defines a single Bravais layer electron propagator as $G^{SP}(\mathbf{k}) = \sum_{\mathbf{R} \neq \mathbf{0}} \mathbf{G}(\mathbf{R}) e^{-i\mathbf{k} \cdot \mathbf{R}}$ which sums over all positions in one Bravais layer,

and an interlayer electron propagator $G^{\gamma\beta}(\mathbf{k}_i) = \sum_{\mathbf{R}} G(\mathbf{R} + \mathbf{d}_\gamma - \mathbf{d}_\beta) e^{-i\mathbf{k}_i \cdot (\mathbf{R} + \mathbf{d}_\gamma - \mathbf{d}_\beta)}$ for scattering between layers γ, β positioned at $\mathbf{d}_\gamma, \mathbf{d}_\beta$ from the origin of the crystal[64]:

$$T(\mathbf{k}', \mathbf{k}) = \frac{(4\pi)^2}{A} \sum_{LL'} Y_{L'}(\mathbf{k}') Y_L^*(\mathbf{k}) \left\{ \sum_{\alpha} e^{i(\mathbf{k}_i - \mathbf{k}) \cdot \mathbf{d}_\alpha} \times T_{\alpha}^{LL'}(k) \right\} \sum_{\mathbf{g}} \delta(\mathbf{k}_{\parallel} - \mathbf{k}'_{\parallel} + \mathbf{g}) \quad (2.10)$$

$$T_{\alpha}^{LL'}(k) = \tau_{\alpha}^{LL'}(k) + \sum_{L_1 L_2} \tau_{\alpha}^{LL_2}(k) \sum_{\beta \neq \alpha} G_{L_1 L_2}^{\alpha\beta}(\mathbf{k}_i) T_{\beta}^{L_2 L'}(k)$$

is the scattering matrix for a surface slab consisting of the α Bravais layers. $\tau_{\alpha} = t_{\alpha} (I - G^{SP} t_{\alpha})^{-1}$ is the Bravais layer scattering matrix for the α layer. The sum over \mathbf{g} is the sum over reciprocal lattice vectors and A is the area of the primitive unit cell. The problem has now been reduced to a matrix inversion in l -space of $(\mathbf{I} - \mathbf{G}^{SP} \mathbf{t})$ where \mathbf{G}^{SP} depends on the Bravais lattice and \mathbf{t} depends on the type of atom in the Bravais lattice. If the Bravais layers are separated by such a reasonable distance (larger than $\sim 1\text{\AA}$) that a plane wave expansion between the Bravais layers is warranted without too many terms, then this is preferred because symmetry considerations are more easily taken into account in the plane wave expansion. Since most surfaces possess some kind of symmetry (X -fold rotational symmetry, mirror symmetry) it is obvious that some beams in the interlayer scattering must be identical much in the same way as some of the beams seen in the LEED pattern are the same in case of symmetry. Taking this symmetry into account can greatly reduce the number of beams necessary to obtain converged calculations, saving valuable computational time. It is also possible in the case of the spherical expansion of intralayer multiple scattering to apply symmetry arguments, but this is not done in the LEED program used in this work, except for partitioning of the τ matrices smaller blocks, which is possible due to the inversion symmetry of the Bravais sublattices.

For scattering between layers, one can turn to the plane wave expansion of the electron wave field instead of the spherical waves used for intralayer scattering. In k -space it is natural to split the scattering on the i 'th layer into four separate

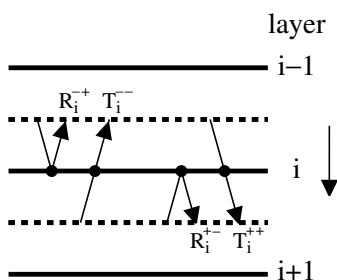


Figure 2.12: Reflection and transition matrices $R_i^{-+}, T_i^{-+}, R_i^{+-}, T_i^{+-}$ in k-space for the i 'th layer

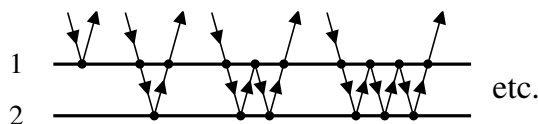


Figure 2.13: Visualization of multiple scattering between two slabs in k-space

components resulting in four different scattering matrices as depicted in Fig. 2.12.

In deriving the T -matrix for a slab of Bravais layers no assumption of the origin of the incoming plane wave was specified. Thus for the $T(\mathbf{k}_1, \mathbf{k}_2)$ matrix describing scattering off *one* slab of Bravais layers the incoming plane wave could originate from the scattering off *another* slab of Bravais layers. With this generalized view of the slab T -matrices and using the propagators between individual layers, which are now simple plane waves, the scattering matrices for the four different scattering components in Fig. 2.12 can be derived. Plane wave multiple scattering between two layers (1 and 2) can be visualized as the multiple scattering processes depicted in Fig. 2.13 giving the expression for R_s^{-+} for the two layers together as:

$$R_s^{-+} = R_1^{-+} + T_1^{-+}(I + R_2^{-+}R_1^{+-} + R_2^{-+}R_1^{+-}R_2^{-+}R_1^{+-} + \dots)R_2^{-+}T_1^{+-} \quad (2.11)$$

$$= R_1^{-+} + T_1^{-+}(I - R_2^{-+}R_1^{+-})^{-1}R_2^{-+}T_1^{+-} \quad (2.12)$$

In the same way the three other parts of the scattering matrix for the combined layers 1 and 2 can be found. These two layers can now be treated as one layer using the combined scattering matrices. This layer can be combined with a third layer and so on. For the bulk crystal this method can be further exploited by noting that in a given direction there will be some kind of stacking period for example an fcc(100) surface will have ABABAB.. stacking. Thus if we combine the two first layers of the bulk the combined AB type slab will be the same as the AB slab of third and fourth layers. This means that in the next step we can simply

combine two slabs of AB layers. Now we have calculated the scattering matrix for an ABAB slab, two of these combine to a ABABABAB slab etc. etc. Using this "layer-doubling" method[54] the reflection matrix for a large bulk crystal can be calculated rapidly.

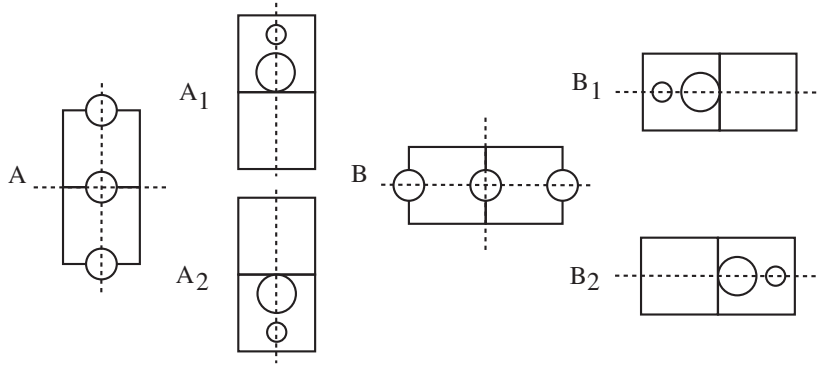


Figure 2.14: Schematic drawing of domains of the Si(100)- (2×1) tilted dimer structure discussed in chapter 8. A and B represent the two different bulk terminations with two mirror planes. A_1 , A_2 , B_1 and B_2 represent the asymmetric dimer domains, which have only one mirror plane. Note that A_1 , A_2 , B_1 and B_2 are connected by 90° rotations.

While most superstructures discussed in this thesis only break the translational symmetry of the substrate, the possibility of structures, which also break either rotational or mirror symmetry, recently had to be taken into account. One example is the Si(100) surface, with a bulk termination symmetry of $p2mm$, which reconstructs into a tilted dimer structure with only pm symmetry, leading to the possibility of four distinct domains on the surface, as seen in Fig. 2.14. The LEED pattern exhibits the full $p4mm$ symmetry, because all four domains usually exists in equal amounts, and thus contribute equally to the LEED pattern. To model such a structure in LEED (assuming that the domains do not interfere) we only need to do a full calculation for one of the domains, as they are connected by symmetry operations. For the example in Fig. 2.14 all four domains A_1 , A_2 , B_1 and B_2 of the tilted dimers are connected by 90° rotations and the same symmetry operations then apply to the LEED beams (at normal incidence). Summing the contributions from the domains to the (I_{hk}) beam in the LEED pattern:

$$(I_{hk})_{LEED} = [(I_{hk})_{A_1} + (I_{hk})_{A_2} + (I_{hk})_{B_1} + (I_{hk})_{B_2}]/4$$

Instead of now calculating the contribution of the I_{hk} beam from each of the four domains, one can note that A_1 is for example connected to A_2 by a 180° rotation which implies that $(I_{hk})_{A_2} = (I_{h\bar{k}})_{A_1}$. Using the same kind of argument for B_1 and B_2 this expression is obtained:

$$(I_{hk})_{LEED} = [(I_{hk})_{A_1} + (I_{h\bar{k}})_{A_1} + (I_{\bar{k}h})_{A_1} + (I_{\bar{k}\bar{h}})_{A_1}]/4$$

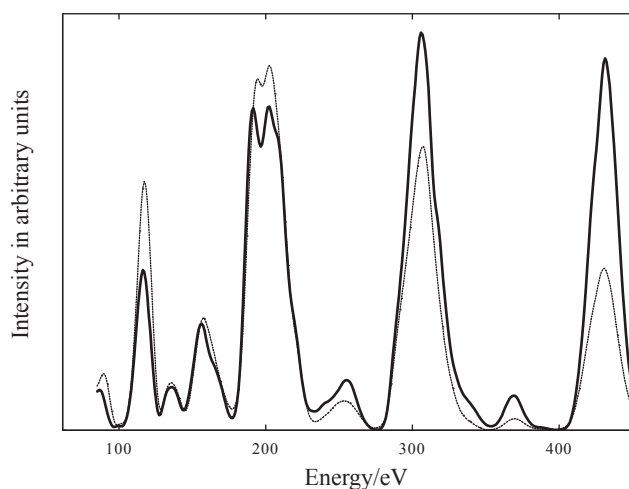


Figure 2.15: Temperature effect on Cu(100) (1,1) beam recorded at 100K (solid line) and 300K (broken line).

which shows that it is only necessary to calculate beams of one of the four domains.

2.2.3 Including thermal atomic vibrations

One improvement of the model has to be included in order to obtain meaningful results. From the comparison of spectra taken at $T=100\text{K}$ and $T=300\text{K}$ for Cu(100) in Fig. 2.2.3, the need to take the thermal vibrations of atoms into account can be seen. In this temperature range the geometric structure does not change significantly for Cu(100) as seen in Table 3.9 in section 3.5. The changes of relative peak intensities observed in the spectra arise from the thermal vibrations of the Cu atoms.

Several approximations to the nature of surface vibrations are needed to be able to include them easily in our multiple scattering calculations. It is assumed that the electrons move so quickly compared to thermal motion of the atoms (typically a factor 10^4) that atoms can be thought of as having displacements unchanged during the process of diffraction. This is the Born-Oppenheimer approximation and corresponds to neglecting loss to phonons. Although the atoms are stationary on the time scale of the electron scattering, they still move very rapidly compared to our measurement times, so that we will only register average displacements. Another approximation is the neglect of correlation between the vibrations of the different atoms in the multiple scattering process. It is not known how much this approximation affects the values obtained for vibrations,

but Pendry [54] has argued that it might not be such a big problem. His argument builds on the assumptions, that correlation only extends between nearest or next-nearest neighbors and that only very few electron multiple scattering paths pass close to the same atoms several times due to the attenuation and strong forward scattering of electrons. Calculations by Duke and Laramore[65] taking correlation into account to the first order seem to agree with the conclusions of Pendry, at least under favorable conditions.

Neglecting correlations, thermal vibrations will only influence the atomic scattering matrices, eg. in a plane wave expansion:

$$t^T(\mathbf{k}_1, \mathbf{k}_2) = t^0(\mathbf{k}_1 \mathbf{k}_2) e^{-\frac{1}{2} \langle \mathbf{u}_{\Delta \mathbf{k}}^2 \rangle_T (\Delta \mathbf{k})^2} \quad (2.13)$$

where \mathbf{u} is the atomic displacement introduced by a Gaussian distribution of thermal vibrations (harmonic approximation), $\Delta \mathbf{k} = \mathbf{k}_1 - \mathbf{k}_2$ and $\langle \mathbf{u}_{\Delta \mathbf{k}}^2 \rangle_T$ is the mean square vibration in the direction $\Delta \mathbf{k}$ at temperature T. The expression for t can be expanded in spherical harmonics and if the vibrations are assumed to be isotropic this will lead to a diagonal form of the t -matrix of the atom, as in the case of no vibrations.

The vibrational amplitudes are defined below by noting that if \mathbf{u} is the displacement of an atom from its node at a given instant, then the time-average displacement is given by $u^2 = u_1^2 + u_2^2 + u_3^2$ ($= 3u_1^2$, for isotropic vibrations) where $u_{1,2,3}$ are the time-average values of the projection of \mathbf{u} on three orthogonal axes [66]. The mean-square vibrational amplitude u^2 can be related to a Debye temperature [66] θ_D via $u^2 = \frac{9\hbar^2 T}{M k_B \theta_D^2} \left(\frac{\theta_D}{4T} + \varphi\left(\frac{\theta_D}{T}\right) \right)$, where the function $\varphi\left(\frac{\theta_D}{T}\right)$ is defined in Ref [66]. However, the vibrational amplitudes u rather than the Debye temperatures θ_D are the direct input to our calculations, and are optimized in the structural refinement. It should be mentioned that LEED is much more sensitive by an order of magnitude to structural than dynamical parameters[8]. Further, it can be observed that changes in structure are reflected mostly in changes in peak positions, while changes in vibrations mostly changes the relative intensities of the peaks. Thus even with a crude approximation to vibrations, the values obtained for structural parameters will probably hold within 0.02Å.

Extending the model to include anisotropic vibrations is also possible[67, 68]. In this work the scheme suggested by W. Moritz and J. Landskron[67] has been used, introducing the probability density function $p(\mathbf{u})$ for harmonic vibrations:

$$p(\mathbf{u}) = \frac{1}{\sqrt{8\pi^3 \langle u_x \rangle^2 \langle u_y \rangle^2 \langle u_z \rangle^2}} \exp \left[-\frac{1}{2} \left(\frac{u_x^2}{\langle u_x^2 \rangle} + \frac{u_y^2}{\langle u_y^2 \rangle} + \frac{u_z^2}{\langle u_z^2 \rangle} \right) \right]$$

where $\langle u_{x,y,z} \rangle^2$ are the mean square displacements in the x-, y-, and z-directions.

The thermally averaged t-matrix can quite generally be expressed as:

$$t^T(\mathbf{k}_1, \mathbf{k}_2) = t^0(\mathbf{k}_1, \mathbf{k}_2) * \int p(\mathbf{u}) e^{i\Delta\mathbf{k}\cdot\mathbf{u}} * u^2 du$$

for single scattering using the probability density. $\int p(\mathbf{u}) e^{i\Delta\mathbf{k}\cdot\mathbf{u}} * u^2 du$ is then expanded in spherical harmonics as was originally done with t^0 , the main difference being that the off-diagonal terms of the t-matrix have to be calculated and used. The LEED program of W. Moritz has been used for implementing anisotropic vibrations, however it should be noted that the R-factor used for optimization is the same as used in our other work.

2.2.4 The Average T-matrix Approximation (ATA)

To model the surfaces of substitutional disordered alloys, the average t-matrix approximation (ATA) has been introduced into LEED[69–71]. Within the ATA approximation, disordered alloys are modelled by an ordered solid in which the atomic scattering matrices are calculated as simple compositional averages between the scattering matrices of the real alloy components. Assuming that the I 'th layer of a surface consists of atom types A and B, the effective t-matrix is given by:

$$t_{ata}^I = c_I t_A + (1 - c_I) t_B \quad (2.14)$$

Here c_I is the concentration of atom A in layer I and t_A is the usual atomic t-matrix for atom type A. This type of approximation has been used extensively in LEED analysis of random alloys, although it is well known that for band structure calculations, ATA gives a poor representation of the alloy local density of states (LDOS)[72].

In fact this approximation is somewhat similar to the one used for treating surface vibrations described above. While ATA treats any open scattering paths where the electron never crosses its own path, closed paths are treated incorrectly. However as was argued for vibrations, closed paths where electrons scatter on the same atom more than once make a comparatively small contribution to the scattering amplitude. Quantitatively this argument has been checked by comparison with the more elaborate coherent potential approximation (CPA)[73], which has been applied successfully to self-consistent electronic structure calculations for bulk alloys[74]. It was shown in ref. [24] for random alloys of the atoms Ni and Pt, which have very different scattering matrices, that very little difference could be found in LEED I/V curves calculated with ATA and CPA respectively. Together with some studies[75, 76] where both I(V) LEED and other techniques sensitive to the surface composition have been shown to give similar results, this gives some confidence in the USE of ATA in LEED.

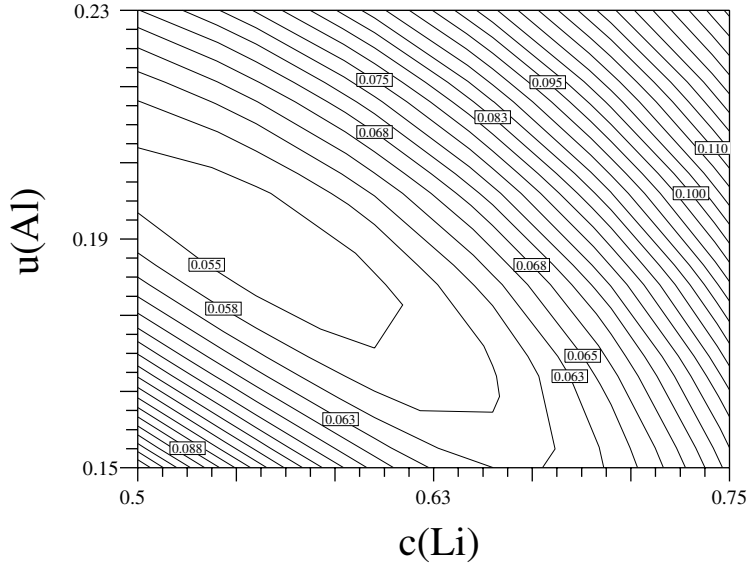


Figure 2.16: Contour plot of the R-factor as a function of Li content of the first layer and vibrations of the Al atoms.

One problem is also the strong correlation between vibrations and the element concentrations used in ATA. Writing out equation 2.14 using 2.13 we get:

$$t_{ata}^I = c_I e^{-\frac{1}{2} \langle \mathbf{u}(\mathbf{A})_{\Delta \mathbf{k}} \rangle_T (\Delta \mathbf{k})^2} t_A^0 + (1 - c_I) e^{-\frac{1}{2} \langle \mathbf{u}(\mathbf{B})_{\Delta \mathbf{k}} \rangle_T (\Delta \mathbf{k})^2} t_B^0$$

In this expression c_I is completely correlated with the the vibrations of atoms A and B for a specific electron energy. The only relief is the fact that the exponential term in the equation for thermal vibrations is energy dependent, while c_I is not. Thus over an extended energy range the three parameters will not be completely correlated. However there are ample reasons for being careful when using ATA. To illustrate this point, the Al(100)-c(2 × 2)-2Li alloy presented in chapter 6 is used as an example. The top layer consists of a c(2 × 2) mixed substitutional layer of Al and Li. The Al content of this layer was then varied adding more Li to the top layer, i.e. the model assumption is that more than 0.5ML Li is substituted into the top layer. A contour plot of the R-factor as a function of first layer Li concentration and Al vibrations of the first layer is shown in Fig. 2.16. It can be seen that these two parameters are strongly correlated, which can be understood as the mixing of the weaker Li scatterer with the Al is being compensated by a decrease in the Al vibrations resulting in a stronger contribution to the scattering from the remaining Al atoms.

2.2.5 Recent developments in LEED theory

The multiple scattering calculations presented here involve matrix inversion so that the method is bound to scale as N^3 , which severely limits the complexity of the structures which can be determined. This problem is of course to some extent diminishing as computer power versus price keeps on growing as Moore's law. It would be possible to develop LEED calculational methods which scaled as N by using finite element methods as has recently been discussed by Pendry[77]. The same author unfortunately finds that while conventional methods scale like αN^3 with a small pre-factor α , the finite element methods scale as βN with a horrendously large pre-factor β making such methods unpractical at present.

Of somewhat more practical use are methods combining multiple scattering theory with some form of kinematical approximation. These methods have been quite important in attempts to tackle for example semi-conductor surface structures and other very complex systems. For some favorable situations it can be argued that multiple scattering plays only a minor role and kinematic calculations can be introduced. Especially successful has been the tensor LEED perturbative approach introduced by Rous and Pendry[78]. This method involves a full dynamical calculation of a single structural model as starting point. Returning to equation 2.8 for T, we displace an atom at position \mathbf{r}_R with scattering matrix t_R by $\delta\mathbf{r}_R$. If we are to retain the atomic position of \mathbf{r}_R a new non-diagonal t-matrix has to be calculated.

$$t'_R = t_R + \delta t_R(\delta\mathbf{r}_R) \quad (2.15)$$

δt_R can quickly be calculated by use of the free electron propagator introduced previously:

$$\delta t_R = G(\delta\mathbf{r}_R)t_R G(-\delta\mathbf{r}_R) - t_R \quad (2.16)$$

Denoting the T matrix of the starting model T_0 and neglecting all terms of order $\delta t_R(\delta\mathbf{r}_R)^2$ and higher:

$$T_{new} = T_0 + (I + T_0 G)\delta t_R(I + GT_0) \quad (2.17)$$

As δt_R is quickly calculated and the expression for the new T-matrix is also easily evaluated this method allows a quick survey of a number of trial structures. Of course, the method is limited by the fact that δt_R is assumed small. The complexity of multiple scattering makes an exact limit difficult to derive for the tensor LEED approximation. However a limit of 0.2-0.5 is noted in literature[79].

Finally it is worth mentioning that direct methods which are also based on the kinematic approximation have been applied to a number of systems with some success. Early attempts by Adams and Landman [80, 81] were inspired by the Patterson function used to directly evaluate X-ray diffraction data

$$P(xyz) = \sum_h \sum_k \sum_l I_{hkl} e^{-2\pi i(hx+ky+lz)} \quad (2.18)$$

where I_{hkl} is the intensity of the hkl reflection. It can be shown[82] that in the case of single scattering, $P(xyz)$ is given by the self-convolution of the real-space scattering potential. Thus peaks found in $P(xyz)$ represent interatomic vectors within the unit cell. The equation for $P(xyz)$ has to be rewritten for LEED as the intensity of the hk beam varies continuously along the l direction

$$P(xyz) = \sum_h \sum_k \left(\int I_{hk}(s) e^{-2\pi i s z} ds \right) e^{-2\pi i (hx+ky)} \quad (2.19)$$

s is the momentum transfer perpendicular to the surface. In the late 70's only very limited data sets were available and only the 00 beam was used for evaluation using the Patterson function. Although Adams and Landman had some limited success the method was abandoned because the approximate treatment of the scattering problem and the limited data set produced unreliable results.

More recently holographic methods have also been used for direct structural determination in LEED. Holographic LEED was originally developed for interpretation of diffuse LEED, but quite recently it was applied with some success with LEED I(V) curves[83]. The basic concept of the holographic method is based on interference between a known reference wave with a unknown object wave which forms the hologram. In LEED the reference wave is identified as the single scattering process of a surface atom (emitter), while the object wave is the subsequently diffracted wave of the reference wave scattered by a nearby atom (scatterer). This is conceptually different to the Patterson methods in which one focusses on the interference between the single scattering waves from both the emitter and the scatterer. Thus instead of the interatomic vectors found by calculation of $P(xyz)$, we now calculate the real-space distribution $B(xyz)$ with respect to the emitter.

$$B(xyz) = \int \int_{k_{\parallel}} \left[\int_{k_{\perp}} K \chi e^{-(ikr - k_{\perp} z)} dk_{\perp} \right] \times e^{ik_{\parallel} * r_{\parallel}} d^2 k_{\parallel} \quad (2.20)$$

$\chi = (I - I_{av})/I_{av}$ is a contrast-enhancing and normalizing function of the measured intensities, while K corrects for the anisotropy of the reference wave, taking the atomic scattering factor of the emitter into account.

Patterson inversion has also reemerged[84], and for both holographic LEED and Patterson LEED it is evident that the larger data sets available nowadays have been a primary improvement over the first attempts. But one must still recognize that the basic single scattering approximation which is inherent in all these methods still presents a major problem, although larger data sets might to some extent have solved the problems of data truncation.

2.3 Application of LEED theory to actual crystal structures

2.3.1 Computation of I(V) curves

The theoretical computation of the I(V) curves proceeds in a hierarchical manner. First the temperature-dependent atomic scattering matrices $t_{ll'}$ of the individual atoms are calculated. These matrices are then used to calculate the scattering matrices $\tau_{LL'}$ of the individual Bravais layers of the crystal sublattices, parallel to the surface. These sublattices are then combined to layers, which are defined in a way that the distance between individual layers is large enough that propagation of electron waves between individual layers using plane waves is computationally feasible (typically larger than 1Å). Finally the scattering matrices of the individual layers $M_{gg'}$ are used to calculate the scattering matrix of the whole crystal $T_{gg'}$.

The precision of the calculations is dependent, inter alia, on the number of phase shifts used in the atomic scattering matrices $t_{ll'}$, which for all atoms were calculated using at least $l_{\max} + 1 = 14$ phase shifts using the band-structure muffin tin potentials mentioned above (the number of phase shifts needed is energy dependent, $l_{\max} + 1$ is the maximum number of phase shifts included at any energy). Test calculations on clean Al(110) show that the intensity calculations were converged to 0.02% when using 22 phase shifts. Convergence levels of 6%, 2%, and 0.1% were found for 10, 14, and 18 phase shifts, respectively. Increasing the number of phase shifts used in the structure determination from 14 to 18 led to changes in the optimum values of the interlayer spacings of the order of 0.002Å and to changes in the optimum values of the rms vibrational amplitudes of order 0.005Å, for the case of Al(110). In these test calculations, stopping criteria for the various lattice summations were set such that errors due to truncation of the sums were $< 0.02\%$.

2.3.2 R-factor analysis of experimental and theoretical spectra

For a given surface structure, the resulting LEED pattern as a function of energy can now be calculated. To quantify the comparison between theory and experiment several reliability factors (R-factors) have been defined. The R-factor used in all LEED I(V) studies described below is a normalized χ^2 function defined [9, 18, 85] as:

$$R = \sum_{hk,i} \left(\frac{I_{hk}^{exp}(E_i) - cI_{hk}^{cal}(E_i)}{\sigma_{hk}(E_i)} \right)^2 \bigg/ \sum_{hk,i} \left(\frac{I_{hk}^{exp}(E_i)}{\sigma_{hk}(E_i)} \right)^2 \quad (2.21)$$

which is a sum over beams hk and energies E_i in terms of the experimental $I_{hk,i}^{exp}$, and calculated intensities $I_{hk,i}^{cal}$, and the root-mean-square experimental uncertainty $\sigma_{hk,i}$ of the beam hk obtained [9] via comparison of measurements for symmetry-equivalent beams:

$$\sigma_{hk,i}^2 = \frac{1}{n_s} \sum_{h'k'} (I_{hk,i}^{exp} - I_{h'k',i}^{exp})^2 \quad (2.22)$$

where $I_{h'k',i}^{exp}$ are the intensities of n_s symmetry-equivalent beams and $I_{hk,i}^{exp}$ is their average. The number of symmetry equivalents is generally too small to give reliable statistics, which finally leads us to replace $\sigma_{hk,i}$ by the mean values over energy of each beam σ_{hk} . For beams with no symmetry equivalents σ_{hk} is found by polynomial fit of all the other beams rms intensity $\langle I_{hk} \rangle$ versus their σ_{hk} . Defining the beam weighting factors

$$w_{hk} = \frac{1}{\sigma_{hk}} \sum_i (I_{hk,i}^{exp})^2 \quad (2.23)$$

our experience shows that one or more beams can occasionally acquire unduly large weights. If this occurs then the beam weight is automatically reduced to $2 \times$ the average weight, to prevent a single beam from dominating the R-factor.

The scaling constant c is determined by the requirement that $\partial R / \partial c = 0$ as:

$$c = \sum_{hk,i} \left(\frac{I_{hk,i}^{ex} I_{hk,i}^{cal}}{\sigma_{hk}^2} \right) / \sum_{hk,i} \left(\frac{I_{hk,i}^{cal}}{\sigma_{hk}} \right)^2 \quad (2.24)$$

Substitution for c in Eqn. 2.21 leads to:

$$R = 1 - \left[\sum_{hk,i} \left(\frac{I_{hk,i}^{ex} I_{hk,i}^{cal}}{\sigma_{hk}} \right) \right]^2 / \sum_{hk,i} \left(\frac{I_{hk,i}^{ex}}{\sigma_{hk}} \right)^2 \sum_{hk,i} \left(\frac{I_{hk,i}^{cal}}{\sigma_{hk}} \right)^2 \quad (2.25)$$

from which it follows that R is bounded by 0 and 1. An estimation of the uncertainties in the best-fit values is obtained from [86]

$$\sigma_j^2 = 0.2 R_{min} / \frac{\partial^2 R}{\partial x_j^2} \quad (2.26)$$

This recipe amounts to equating σ_j with the change Δx_j in the optimum value of x_j that corresponds to a 10% increase in R from R_{min} .

Other R-factors are also commonly used, especially the Pendry R-factor based on the logarithmic derivative:

$$R_P = \frac{\sum_{hk,i} \left(Y_{hk}^{exp}(E_i) - Y_{hk}^{cal}(E_i) \right)^2}{\sum_{hk,i} \left(Y_{hk}^{exp}(E_i) \right)^2 \left(Y_{hk}^{cal}(E_i) \right)^2}$$

$$Y_{hk} = \frac{\frac{d \log(I_{hk})}{dE}}{1 + V_{im}^2 \left(\frac{d \log(I_{hk})}{dE} \right)}$$

The argument for R_p is based on kinematic theory in which the Bragg peaks directly reflect the layer spacings. Although no such simple relation exists for full multiple scattering theory, Pendry[87] nonetheless argued that one could focus on the peak positions and not relative intensities in order to derive the correct structural parameters, even with poor experimental data or poor modelling. The use of logarithmic derivatives of experimental and calculated LEED spectra results in loss of most of the information contained in peak intensity variation for a given diffracted beam, and total loss of the information contained in the differences in intensity between different beams. As is for example shown in this thesis and in previous work of the Århus LEED group peaks differing more a factor of 200 can be fitted quite well even when taken the relative intensities into account. The merit of R_p , for well defined and well measured adsorption systems can be disputed, making the following points. The Pendry R factor is an ad hoc measure of the quality of fit, with no statistical basis. It does not include any explicit measure of the experimental uncertainties, and it contains in its definition V_{im} , one of the parameters to be determined. One should also note that since R_p inherently focus on peak positions, it will be quite insensitive to dynamical parameters such as thermal vibrations and disorder. This can be a good thing as long as only structural parameters are of interest, but as soon as one wants more from the analysis it should be considered whether the Pendry R-factor is the right choice.

2.3.3 Structural refinement

Firstly it can be noted that because of the rapid increase of computer power over price, even the most complex calculations performed in this thesis have been done on a ordinary PC (well alright, a state-of-the-art ordinary PC and with extensive use of optimized BLAS and LAPACK matrix subroutines from Intels MKL library).

The procedure used for obtaining the crystal structure is as follows: First the experimental LEED I(V) curves are compared to a number of possible trial structures that fulfil symmetry requirements, and other information available, for example, coverage. When the correct basic structure has been found, further refinement of both structural and dynamical parameters of the model is carried out using a semi-automatic implementation of an iterative procedure[88], in which the disagreement between experimental and calculated intensities (as measured by the R-factor given above) is minimized as a function of one variable plus v_0 at a time. The procedure contains an inner loop in which the structural variables are optimized iteratively, and an outer loop in which the nonstructural variables are

optimized iteratively. The inner loop is executed automatically in a single computer run, but the outer loop is currently executed manually. The procedure is very efficient by virtue of maximum re-use of intermediate calculations. It is necessary to make the iterative optimization because all parameters are correlated to some extent. In calculations presented in this report all structural and dynamical parameters found in various tables have been optimized as just described unless specifically stated otherwise. Thus usually we have optimized all dynamical parameters of the sublattices, which we also vary structurally.

All plots of experimental vs. theoretical $I(V)$ curves in this work have been constructed using a single, beam-independent, scaling factor between the experimental and calculated spectra. *Thus the good agreement between experiment and theory also includes agreement between the relative intensities of the different beams.* As can be seen throughout this thesis, there is also good agreement within estimated uncertainties between the results of the analysis for $\theta = 0^\circ$ and $\theta \neq 0^\circ$. However, for the case of Li adsorption, the uncertainties in the Li-Al layer-spacing and in the vibrational amplitudes of adsorbed Li are large. These larger uncertainties can probably be attributed to the relatively weak scattering from Li atoms, whose phase shifts are a factor of about 10 smaller than for Al.

The possibility that the Al atoms displaced by alkali atoms in various substitutional structures are re-adsorbed in high symmetry sites has generally been investigated, but found to be incompatible with the measured intensities. It is assumed, therefore as discussed in previous work for Al(111)[8], that the displaced Al atoms are re-adsorbed at surface steps.

Finally let's take the Al(110)- $c(2 \times 2)$ -Na structure presented in section 4.5 as an example. First a preliminary survey was carried out of structural models involving Na atoms adsorbed in on-top, two-fold hollow, two-fold short and long-bridge, and two-fold substitutional sites, compatible with the symmetry of the measured LEED intensities. Although no optimization of the nonstructural parameters was carried out, the results indicated unequivocally that only the two-fold substitutional site warranted further refinement. The R factors for the discarded models were in the range 0.25-0.35 as compared to the value of 0.045 found for the optimal model in the analysis of the normal-incidence data. The possibility that the 0.5 ML of Al atoms displaced by Na atoms are re-adsorbed in high symmetry sites was also investigated, but found to be incompatible with the measured intensities. It is assumed, therefore, that the displaced Al atoms are re-adsorbed at surface steps. A full optimization of all structural and dynamical parameters was carried out for normal incidence $\theta = 0^\circ$ and off-normal incidence $\theta = 10^\circ$. The following structural and dynamical parameters were considered. The spacing between the $c(2 \times 2)$ -Na layer and the $c(2 \times 2)$ -Al layer. The interlayer spacings between the first 6 layers, were also optimized along with rumpling of the 3rd and the 5th layers. The nonstructural variables were the rms vibrational amplitudes of adsorbed

Na atoms, of Al atoms in the first five Al layers including separate amplitudes of inequivalent Al sublattices of the 3rd and 5th layers, of Al atoms in the bulk. Finally V_0 and V_{im} , assumed constant as a function of energy, were optimized.

2.4 HRCLS experiments and analysis

As HRCLS experiments only constitute a minor part of this work the experimental setups and analyzing methods, which have been used are only described very briefly.

2.4.1 Beamlines I311 at the MAXII storage ring and SGM-1 at the ASTRID storage ring

HRCLS experiments were carried out at the SGM-1 beamline at ASTRID and beamline I311 at MAXII.

The SGM-1 beamline is a bending magnet based beamline with a spherical grating monochromator (SGM) constructed locally at our institute. The SGM-1 monochromator has a usable energy range from 30eV to 400eV.

Beamline I311, is an undulator based VUV, soft x-ray beamline. The monochromator is a modified SX-700 type PGM with spherical optics and a movable exit slit. Together with the 38-period, 66 mm period length, $K_{\max} = 4.50$, undulator the photon energy range 30eV to about 1500eV is covered.

2.4.2 Experimental chambers

The experimental setup at the end of beamlines I311 and SGM-1 are very similar. The vacuum chambers are split up in two separate parts connected by an all metal valve. The top parts of the chambers are equipped with sample preparation and analysis tools. The crystal sample can be heated to several 1000K, and cooled to about 100K by liquid nitrogen. Several evaporation sources can be mounted and an ion sputtering gun is used with Ar^+ to clean the crystal. The crystallinity and ordering of the sample can be checked by a LEED optics. The cleanliness of the crystal was checked by recording valence electron spectra and by observing the C-1s and O-1s core-level regions. It is estimated that the surface concentrations of C and O were less than 0.01 ML. The lower parts of both of the vacuum chambers are both equipped with a Scienta SES-200 (200mm mean radius) hemispherical electron analyzer. It is in the lower parts of the chambers that the photon beam enters. The analyzer collect photoelectrons over a solid angle of 8° and is aligned at an angle of 40° to the direction of the photon beam.

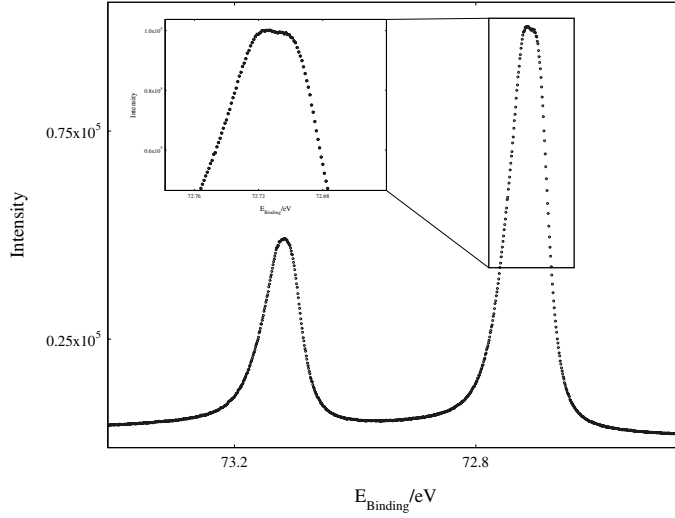


Figure 2.17: Al₂p spectrum of Al(111) recorded at T=100K. Notice that the surface splitting of ~ 30 meV is visible.

The contribution from the experimental equipment to the FWHM of the core-level peaks is determined by a convolution of the broadening due to the monochromator (resolution of the incoming photon beam) and the SCIENTA electron analyzer (resolution of the outgoing electron beam). While the resolution of the Scienta analyzers should in principle be the same for the two beamlines used, the undulator based I311 beamline clearly has the best resolution of the incoming photon beam, due to the larger photon flux. A benchmark resolution for such equipment is then illustrated in Fig. 2.17, where the ~ 30 meV, surface core-level shift of Al(111) at T=100K has been resolved at the I311 beamline.

2.4.3 Numerical analysis of Core-level Spectra

Individual peaks of core-level spectra can be fitted by the theoretical Doniach-Sunjic[89] profile convoluted with a Gaussian lineshape and a background assumed to be a polynomial of zeroth to second order. The Doniach Sunjic profile is given by:

$$D(E) = \frac{\Gamma(1 - \alpha) \cos\left(\frac{\pi}{2}\alpha + (1 - \alpha)a \tan\left(-\frac{E - E_b}{\gamma}\right)\right)}{\left(1 + \frac{(E - E_b)^2}{\gamma^2}\right)^{(1 - \alpha)/2}}$$

This lineshape is derived as a convolution between a Lorentzian $\frac{1}{1 + \left(\frac{E - E_b}{\gamma}\right)^2}$

due to the natural lifetime width of the core-hole and a $\frac{1}{(E-E_b)^{1-\alpha}}$ singularity determined by the screening response of the valence electrons to the core-hole. $D(E)$ is then convoluted with a Gaussian function which represents instrumental broadening and broadening due to such effects as surface disorder be it static or dynamic.

The program used for the fitting is FitXPS2 which uses the Quadratic Tensor Model algorithm of Hanson and Krogh[90], for nonlinear minimization with both simple bounds and linear inequality constraints. The program was written in a combination of Fortran and Visual Basic by David L. Adams[91].

2.4.4 Interpretation of core-level shift

Using core-level shifts to study dynamics and structure of surface systems hinges very much on the ability to interpret the various components found in the spectra. It is highly desirable to do so as CLS probes the local surroundings of a given atomic species and is in this respect complementary to LEED, which probes the periodic structures on the surface. The analysis of core-level spectra is described in an excellent review by N. Mårtensson and A. Nilsson[92] The core-level binding energy is defined as the total energy difference between an ionized (N-1 electron) final-state system and a initial (N electron) system ($E_{ion}(N-1) - E_G(N)$). The chemical shift between two systems A and B can then be expressed as:

$$\Delta E_B = \{E_{ion,A}(N-1) - E_{ion,B}(N-1)\} - \{E_{G,A}(N) - E_{G,B}(N)\} \quad (2.27)$$

ΔE_B is then determined by two energy differences, one relating to the initial states and one relating to the final states. This expression is usually the basis of a treatment of chemical shifts. For some systems, arguments can be made that the shifts are dominated by either initial or final state terms. This has lead to the introduction (often with great ingenuity) of many different approximations explaining the shifts in various other subsets of adsorbate systems. However, especially if the shifts are quite small <40 meV, most of these approximation are not good enough.

Another method, used throughout this work, is to identify the structure and chemical composition completely for one or two coverages of an adsorbate system by for example quantitative LEED and then interpret the HRCLS spectra of these phases. This information can then be used to interpret HRCLS spectra at other coverages, thus obtaining information about for example disordered phases of the system where it is not possible to do so by quantitative LEED.

Finally one can take the full step of turning HRCLS into an independent structural tool by calculation of core-level shifts by ab initio DFT theory. This involves calculating the total energies of the system without a core hole (ground state) and with a core hole placed in various atomic positions (final state). Core holes of Al were in the work presented later modelled by an Al 2p electron excited into the 3p

level in order to keep the system charge neutral. This process is quite reminiscent of quantitative LEED structure determination in that they both are trial-and-error methods. Core-level shifts can be calculated for an arrangement of atoms and if they fit well one achieves some confidence in the model, but the pitfalls are similar to quantitative LEED, and as there are probably at most 3-4 peaks to determine one has to be careful.

Chapter 3

Structure and dynamics of unreconstructed metal surface systems

3.1 Introduction

The primary motivation for the studies presented in this chapter has been to measure the structural and dynamical parameters of a number of simple model systems which have been used as testing grounds for new theoretical and experimental methods. For these systems it is very important to have the most accurate and reliable determination of structural and dynamical parameters possible.

Firstly structural determinations for a few clean surfaces are presented. Most interesting is the quantitative LEED determination of the structural and dynamical parameters of Al(110) as a function of temperature, from 100K to 553K. This work was motivated by recent theoretical calculations by Marzari et al[93], in which a new ab initio theoretical scheme, taking temperature into account, was used for calculating the thermal expansion coefficients and vibrational amplitudes of the clean Al(110) surface. Most noticeable was the finding of a negative thermal expansion coefficient between the first and second layer, which the new LEED results qualitatively confirm.

In the final section of this chapter the structural determination of the Cu(100)-c(2 × 2)-Na phase, a four-fold hollow site chemisorption system is reported. Besides from the fact that DFT calculations have been made for this system, the Cu(100)-Na system has also been used as a testing ground for surface potential energy mapping by Helium Atom Scattering (HAS). Also for this system the present LEED results agree qualitatively with theoretical DFT calculations and predictions from HAS.

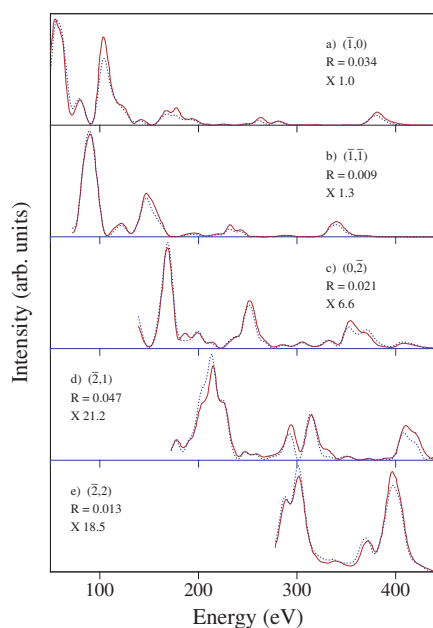


Figure 3.1: Comparison of experimental (solid lines) and calculated (dotted lines) $I(V)$ spectra for clean Al(100) at $\theta = 0^\circ$ for 5 integral-order beams, a)-e). The beam hk indices, R factors, and scale factors are shown in each panel. The calculated spectra were obtained using the best-fit parameter values given in Table 3.1.

3.2 Clean Al(100)

$I(V)$ spectra were measured for a total of 7 symmetry-inequivalent beams. The results of structural analysis for clean Al(100) are listed in Table 3.1. The structure of clean Al(100) is shown to involve small expansions of the first and second interlayer spacings of $2.0 \pm 0.8\%$ and $1.2 \pm 0.7\%$ respectively. This result is in agreement to within estimated uncertainties with the conclusions of earlier studies[94, 95] which reported that the clean Al(100) surface is essentially unrelaxed. In these earlier studies only a single Debye temperature was used to represent the effect of thermal vibrations. In fact the relaxations of the first two interlayer spacings are reduced to $1.6 \pm 1.0\%$ and $0.8 \pm 0.9\%$ respectively if a single vibrational parameter is used in analyzing the data. *A similar trend is found in the analysis of clean Al(110) as will be discussed in the next section.* As can be seen from the results in the table, the vibrations of Al atoms in the first layer are twice as large as for Al atoms in the bulk. The enhanced surface vibrations decay to the bulk value within the first four layers. A plot of experimental $I(V)$ spectra and spectra calculated for the optimum parameter values given in Table 3.1 is shown in Fig. 3.1.

Table 3.1: Best-fit parameter values for clean Al(100). The interlayer spacings are denoted d_{ij} , and the rms vibrational amplitudes are denoted u_i , where the subscripts indicate the layers in question.

θ	0°
d_{12}	$2.06 \pm 0.02 \text{ \AA}$
d_{23}	$2.04 \pm 0.02 \text{ \AA}$
d_{34}	$2.01 \pm 0.02 \text{ \AA}$
u_1	$0.17 \pm 0.02 \text{ \AA}$
u_2	$0.14 \pm 0.02 \text{ \AA}$
u_3	$0.10 \pm 0.02 \text{ \AA}$
u_{bulk}	$0.08 \pm 0.02 \text{ \AA}$
V_{im}	$5.1 \pm 0.08 \text{ eV}$
R	0.021

3.3 Al(110): Temperature dependence of structural and dynamical parameters

3.3.1 Introduction

The Al(110) surface has played an important role in the development of experimental and theoretical methods for the study of surface relaxations. A large contraction, $\Delta d_{12} \sim -10\%$, of the first interlayer spacing was first reported in the pioneering LEED study of Jepsen et al [94] in 1972. A simple physical explanation of the contraction of the first interlayer spacing at open metal surfaces was given by Finnis and Heine [96] in 1974 in terms of the electrostatic interactions between point ions and a smoothed electron charge distribution in the surface Wigner-Sietz cells. The first clear evidence of *multilayer* relaxations was found in 1980 in the calculations of Landman et al [97] using a generalization of the model of Finnis and Heine.

Experimental confirmation of the occurrence of oscillatory, multilayer relaxations for the Al(110) surface came in 1982 from a LEED study [57, 98] carried out in the laboratory of D. L. Adams, and a year later from a LEED study by Noonan and Davis [99], except that these authors found an expansion of the third interlayer spacing as opposed to the contraction found by Nielsen et. al [98]. Near quantitative agreement with the experimental results was obtained shortly afterwards in the calculations of Barnett et al [101] and Ho and Bohnen [102]. These and all subsequent studies [93, 100, 103–109] reported the occurrence of a $- + -$ relaxation sequence, as found by Nielsen et al [98], rather than the $- + +$ sequence found by Noonan and Davis [99].

Very recently, Marzari et al [93] have presented calculations of the temperature

Table 3.2: Relaxations Δd_{12} , Δd_{23} , Δd_{34} , Δd_{45} of the first four interlayer spacings of Al(110) expressed as % deviations from the bulk value. At 100K and 300K the bulk values are 1.4263Å and 1.4318Å, respectively. For the present work, the results of the analysis using layer-dependent and layer-independent ("single u") vibrational amplitudes are both listed.

Method	Ref.	Temp. (°K)	Δd_{12}	Δd_{23}	Δd_{34}	Δd_{45}
LEED	[57, 98]	100	-8.6	5.0	-1.6	0.2
LEED	[99]	300	-8.5	5.5	2.2	1.6
MEIS	[100]	300	-8.5	4.8	-3.9	
LEED	Present	100	-8.1	5.5	-3.8	1.1
LEED	Present	300	-11.2	6.7	-4.0	0.0
LEED	Present (single u)	100	-7.6	4.2	-2.3	0.0
LEED	Present (single u)	300	-9.9	4.3	-2.8	0.0
Theory	[101]	0	-10	4	-3	
Theory	[102]	0	-6.8	3.5	-2.0	1.6
Theory	[93]	0	-7.4	3.8	-2.5	2.0
Theory	[93]	400	-7.1	4.9	-1.1	2.4
Theory	[93]	600	-7.9	5.0	-1.4	1.9

dependence of the surface relaxations and vibrational amplitudes of the Al(110) surface, using a new theoretical approach which takes temperature into account, called ensemble density-functional molecular dynamics (eDFT-MD). Notable features of their results are the observations that the first and second interlayer spacings exhibit *negative* and positive coefficients of thermal expansion, respectively, and that the surface-normal vibrations of second layer atoms are *larger* than those of first layer atoms. Experimental support for the calculated temperature dependence of the interlayer relaxations was stated to be found in the results of a LEED analysis[108]. However the LEED study in question was based on the analysis at each temperature of I(V) spectra for only the (0,0) diffracted beam using kinematic theory. Such an analysis lies so far from the state-of-the-art of surface structure determination via LEED, even in 1993, that its conclusions form a fragile basis for evaluating the results of a new theoretical approach. In view of the continuing interest in the Al(110) surface as a testing ground for new theoretical approaches, and in view of the considerable improvements made to the methodology of LEED over the last 15 years, it seemed to be important to carry out a new LEED study of this system, with a view to providing the basis for a more stringent evaluation of new theories.

Initially new LEED measurements at 100K and 300K were carried out. The structural determination based on the new measurements turned out to agree qualitatively with the theoretical results, in that a negative thermal expansion coefficient was found for the first interlayer spacing. After the publication of these measure-

ments it was decided to carry out a more thorough study measuring LEED spectra at regular intervals in the temperature range between 100K and 553K. Additionally, anisotropic vibrations were introduced to model the surface better at higher temperatures, and to compare with eDFT-MD calculations, which predicted significant vibrational anisotropies, thought to be responsible for the negative thermal expansion coefficient.

The study presented here also compares structure determinations obtained using state-of-the-art versions of two independent experimental methods, LEED and MEIS, *over a significant temperature range*. For the Cu(110) metal surface, comparison between LEED and HEIS studies at a given temperature has been made[110]. This comparison showed that LEED and MEIS results agree reasonably well at low temperatures. This is also confirmed by the studies presented here, but it is also found that the development of structural parameters as a function of temperature differs for LEED and MEIS, leading to a notable disagreement at higher temperatures.

3.3.2 LEED experiment and calculations

Intensity-energy spectra were measured at 100K, 200K, 300K, 373K, 473K and 553K for the clean Al(110) surface in the energy ranges 40-440 eV, 40-440 eV, 40-440 eV, 40-440eV, 40-240 eV and 40-240 eV respectively. Spectra were recorded for 13, 13, 11, 10, 9 and 9 symmetry-inequivalent beams at 100K, 200K, 300K, 373K, 473K and 553K respectively. The shorter energy range at higher temperatures is due to the $e^{-\frac{1}{2}\langle u_{\Delta\mathbf{k}}^2 \rangle_T (\Delta\mathbf{k})^2}$ dependence of the atomic scattering matrix, which leads to an attenuation of the intensity of the LEED spectra as a function of energy and temperature. This results in a shorter energy range and fewer beams at higher temperatures. The lattice constant for Al was taken[111, 112] to be $a(T=100K)_0 = 4.0341\text{\AA}$, $a(T=200K)_0 = 4.0409\text{\AA}$, $a(T=300K)_0 = 4.0493\text{\AA}$, $a(T=373K)_0 = 4.0569\text{\AA}$, $a(T=473K)_0 = 4.0667\text{\AA}$, $a(T=553K)_0 = 4.0754\text{\AA}$. Comparisons of experimental $I(V)$ spectra measured at 100K, 303K, and 473K with spectra calculated for the optimum parameter values are shown in Fig. 3.2.

For the measurements at 100K and 300K calculations were carried out using a maximum of 18 phase shifts. A full optimization of the first four interlayer spacings d_{12} , d_{23} , d_{34} , and d_{45} and the rms vibrational amplitudes u_1 , u_2 , u_3 and u_{bulk} , the inner potential V_0 , and the damping V_{im} was carried out.

In the analysis of the full set of measurements, 14 phase shifts were used (limited by the program used for calculating anisotropic vibrations), but as mentioned in section 2.2.3, increasing the number of phase shifts used in the structure determination from 14 to 18 led to only small changes in the optimum values in the order of 0.002\AA to 0.005\AA , for the case of Al(110). The structural variables con-

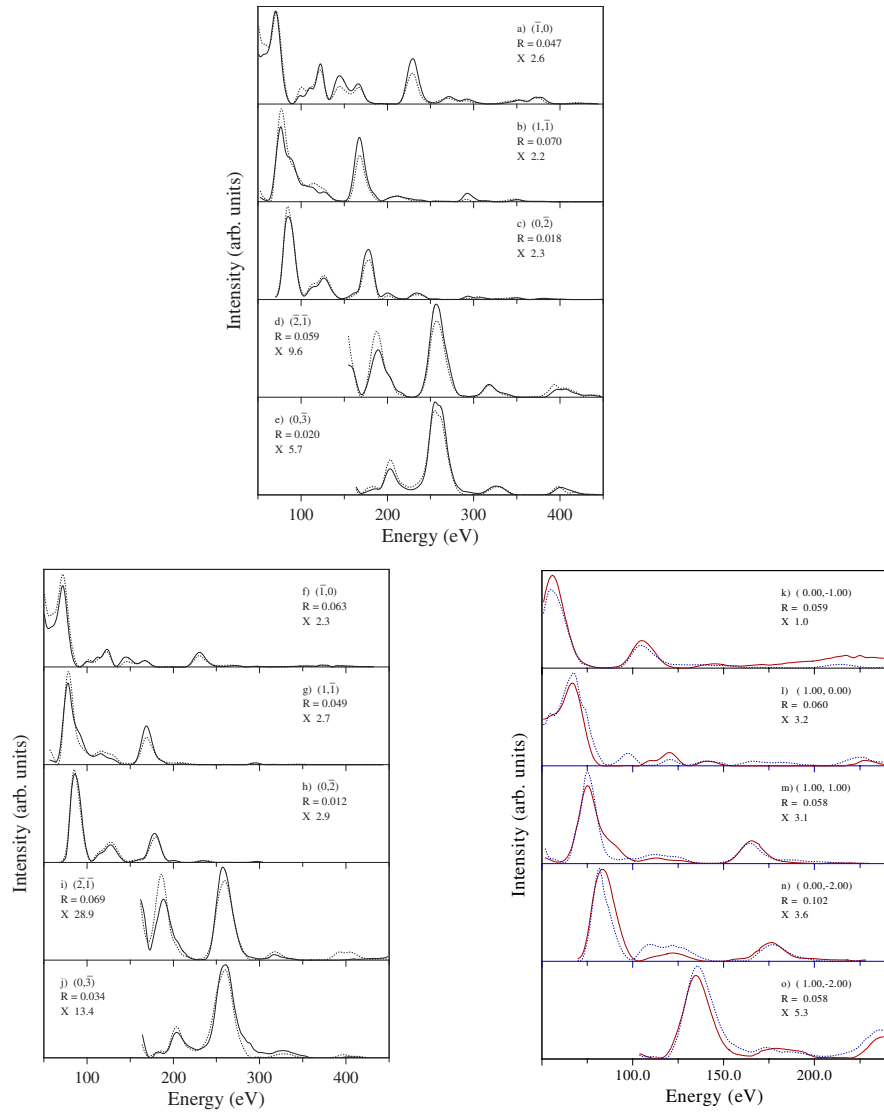


Figure 3.2: Comparison of experimental (solid lines) and calculated (dotted) $I(V)$ spectra, for five of the symmetry-inequivalent diffracted beams used in the analysis at 100K (beams a to e), 300K (beams f to j) and 473K (beams k to o). The beam hk indices, R factors, and scale factors are shown in each panel. The calculated spectra were obtained using the best-fit parameter values as shown on Fig. 3.4, Fig. 3.5 and Fig. 3.6.

Table 3.3: Relaxation of Al(331), comparison between LEED experimental determination[113] and theoretical DFT calculations[27]

	LEED	DFT
Δd_{12}	$-11.7 \pm 2.3\%$	-11.3%
Δd_{23}	$-4.1 \pm 3.1\%$	-6.3%
Δd_{34}	$+10.3 \pm 2.7\%$	$+10.1\%$
Δd_{45}	$-4.8 \pm 4.1\%$	-4.4%
Δd_{56}	$-2.4 \pm 5.3\%$	-1.8%
Δd_{67}	$+0.3 \pm 5.5\%$	$+4.8\%$
Δr_{12}	$-2.8 \pm 3.7\%$	-1.1%
Δr_{23}	$-0.8 \pm 3.5\%$	-2.8%
Δr_{34}	$+0.3 \pm 3.5\%$	$+1.7\%$
Δr_{45}	$+1.0 \pm 4.9\%$	$+0.9\%$
Δr_{56}	$+0.6 \pm 4.9\%$	-1.2%

sisted of the first three interlayer spacings d_{12} , d_{23} , and d_{34} , as relaxation of d_{45} was deemed insignificant after the initial calculations at 100K and 300K.

Two separate structural optimizations were carried out at all temperatures. Initially a full optimization was carried out assuming isotropic vibrations u_1, u_2, u_3 and u_{bulk} . Subsequently a new optimization was carried out allowing anisotropic vibrations $u_{||1}, u_{||2}, u_{||3}, u_{\perp1}, u_{\perp2}, u_{\perp3}$ in the first three layers, using the values for isotropic vibrations as a starting point. Finally the possibility was investigated of introducing full three dimensional anisotropy where the x-direction was defined along the close-packed rows, while the y-direction was defined perpendicular to the close packed rows. However as LEED (at normal incidence) is inherently less sensitive to the parallel plane of the surface, determination of surface parallel vibrations is very difficult, and thus distinguishing x and y vibrations was virtually impossible.

One should realize that surface thermal expansions or contractions are small effects of only a few percent of an interlayer spacing even over a wide temperature range. Inevitably attempts to extract such data is met with the important question - are the measured (or calculated) changes significant?? Answering this question is made difficult by the fact that virtually all surface crystallographic techniques are dominated by systematic errors in both data and modelling. This makes the use of ordinary statistical methods to evaluate the uncertainties very difficult. In the case of LEED two approaches to resolve this issue have been used. Either one invents some new ad-hoc error estimate based on physical arguments, or one attempts to use χ^2 based statistical methods and somehow incorporate the fact that some basic assumptions are not fulfilled. While the Århus LEED group has consistently chosen the latter approach, the error estimates based on physical arguments by

Pendry are more commonly used. A discussion of the pros and quos of these two approaches will not be presented here, although it should be mentioned that both methods yield quite similar error estimates. It must be stressed though that all formulas used for calculation of uncertainties in LEED are only rough estimates.

Another estimate of systematic errors can be obtained by comparing values found using different experimental and theoretical methods. However not all methods share the same precision, thus unreasonable error estimates can be found if poor experimental or theoretical methods are included in such a comparison. Nonetheless one can for example make a comparison between $T=0\text{K}$ DFT calculations of clean surfaces and LEED structural calculations at around $T=100\text{K}$. For LEED measurements the low temperature situation is very favorable as background is low and beam intensities fall off slowly making it possible to record a large data set very reliably. For Al surfaces, DFT and LEED structural determinations have been made for Al(110) and Al(331). As is seen from Table 3.2 and 3.3, comparison between experiments and theory gives some confidence, that for the parameters to which LEED is the most sensitive (perpendicular structural parameters), precision is in the range of 1% to 2% . Unfortunately the same arguments are harder to use at higher temperature where the precision and reliability of theoretical methods is unknown, and the influence of thermal disorder is greater in LEED. However some general observations can be made: LEED is about 10 times less sensitive to vibrational parameters as compared to structural parameters[8]. LEED is very insensitive to lateral disorder, especially for normal incidence, as is indicated by the weak R-factor dependence (leading to large error bars) of such lateral structural and vibrational parameters.

One can further resort to changing the size of the data set to which the model is fitted or changing the complexity of the model used, in order to observe how these changes affect the structural parameters. As is shown in Fig. 3.3 for LEED data recorded at 473K variation of the number of beams results in changes, at least for the first layer distance of less than 1% . As was already indicated in Table 3.4, the approximation used for thermal vibrations does influence structural parameters. It can be seen that the relaxations found here are in general larger than found in older LEED studies. Part of the observed differences can be attributed to the fact that the earlier studies used a single, layer-independent vibrational parameter, as can be judged from the results shown in table 3.4 for analysis of the present data with a single vibrational parameter. Further it was also found in the previous section dealing with clean Al(100), the interlayer spacings depend slightly on the approximation used for thermal vibrations. From these and more tests it is concluded that variations of structural parameters as a function of vibrational parameters is 1% - 2% It can thus be concluded that a precision of at least 1% - 2% is to be expected from LEED, when using the best approximation for vibrations.

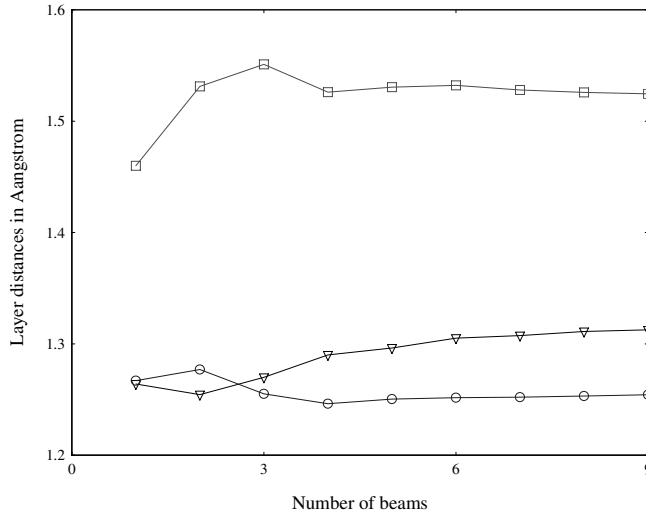


Figure 3.3: Interlayer distances d_{12} , d_{23} and d_{34} as a function of the number of beams involved in the LEED analysis (using isotropic vibrations). Δd_{12} , Δd_{23} and Δd_{34} are denoted by circles, squares and triangles respectively.

3.3.3 Structural results

The results of the initial structure determinations at 100K and 300K are listed in columns 2 and 3 of Table 3.4. Columns 4 and 5 of the table list the corresponding best-fit values obtained using a single, layer-independent vibrational amplitude, for the purpose of comparison with the results of earlier LEED analyses[57, 98, 99].

The results of independent optimizations using isotropic and anisotropic vibrations of the full series of structure determinations at 100K, 200K, 303K, 373K, 473K and 553K, are shown in Fig. 3.4, 3.5 and 3.6 for d_{12} , d_{23} and d_{34} respectively. Error bars are calculated, for the results obtained using anisotropic vibrations, using the methods described in section 2.3.2.

MEIS results deduced from Fig. 5 of ref. [114] are also shown on Fig 3.4, 3.5 and 3.6. In ref.[114] MEIS errors on structural parameters between 1% and 2% are quoted and optimistically values of 1% are used. It is quite unclear how they arrive at these error estimates, as the method used is not discussed in any detail. Finally eDFT-MD simulations[93] are also shown. Results of the optimization of vibrational parameters for isotropic and anisotropic vibrations are shown in Fig. 3.7 and Fig. 3.8.

Table 3.4: Best-fit parameter values for Al(110) at T=100K and 300K. The interlayer spacings are denoted d_{ij} and the rms vibrational amplitudes are denoted u_j , where the subscripts indicate the layers in question. The final two columns give the results of analysis using a single, layer-independent vibrational parameter, for the purpose of comparison with earlier LEED studies.

Temp.	100K	300K	100K	300K
d_{12}	$1.31 \pm 0.03 \text{ \AA}$	$1.27 \pm 0.03 \text{ \AA}$	$1.32 \pm 0.03 \text{ \AA}$	$1.29 \pm 0.03 \text{ \AA}$
d_{23}	$1.51 \pm 0.03 \text{ \AA}$	$1.53 \pm 0.03 \text{ \AA}$	$1.49 \pm 0.03 \text{ \AA}$	$1.49 \pm 0.04 \text{ \AA}$
d_{34}	$1.37 \pm 0.02 \text{ \AA}$	$1.37 \pm 0.03 \text{ \AA}$	$1.39 \pm 0.03 \text{ \AA}$	$1.39 \pm 0.04 \text{ \AA}$
d_{45}	$1.44 \pm 0.02 \text{ \AA}$	$1.43 \pm 0.03 \text{ \AA}$	$1.43 \pm 0.03 \text{ \AA}$	$1.43 \pm 0.04 \text{ \AA}$
u_1	$0.17 \pm 0.04 \text{ \AA}$	$0.25 \pm 0.03 \text{ \AA}$		
u_2	$0.17 \pm 0.08 \text{ \AA}$	$0.29 \pm 0.06 \text{ \AA}$		
u_3	$0.12 \pm 0.04 \text{ \AA}$	$0.18 \pm 0.03 \text{ \AA}$		
u_{bulk}	$0.07 \pm 0.02 \text{ \AA}$	$0.14 \pm 0.01 \text{ \AA}$	$0.09 \pm 0.02 \text{ \AA}$	$0.15 \pm 0.02 \text{ \AA}$
V_{im}	$5.1 \pm 0.8 \text{ eV}$	$5.5 \pm 0.7 \text{ eV}$	$4.2 \pm 1.0 \text{ eV}$	$3.3 \pm 1.2 \text{ eV}$
$R_{\text{exp-theory}}$	0.0376	0.0402	0.0564	0.0790

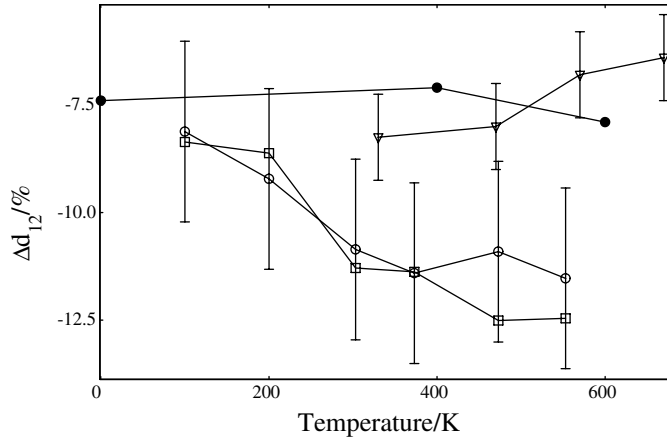


Figure 3.4: Relaxation of the first interlayer spacing Δd_{12} as a function of temperature. LEED results obtained using isotropic vibrations are marked by empty squares. LEED results obtained using anisotropic vibrations are marked by empty circles. MEIS results[114] are marked by empty triangles. eDFT-MD results[93] are marked by filled circles. Uncertainties are given for LEED results using anisotropic vibrations and MEIS results.

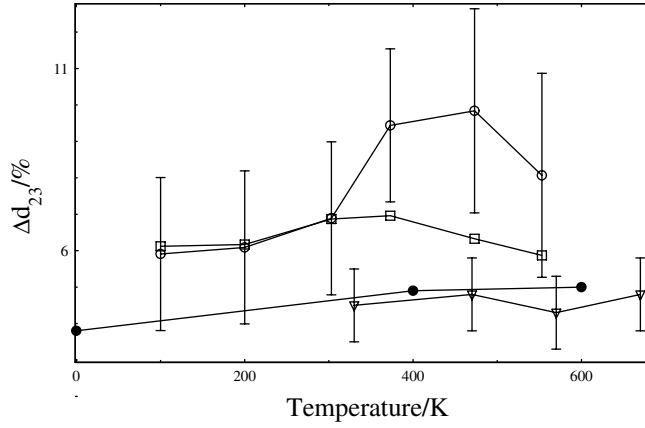


Figure 3.5: Relaxation of the second interlayer spacing Δd_{23} as a function of temperature. LEED results obtained using isotropic vibrations are marked by empty squares. LEED results obtained using anisotropic vibrations are marked by empty circles. MEIS results[114] are marked by empty triangles. eDFT-MD results[93] are marked by filled circles. Uncertainties are given for LEED results using anisotropic vibrations and MEIS results.

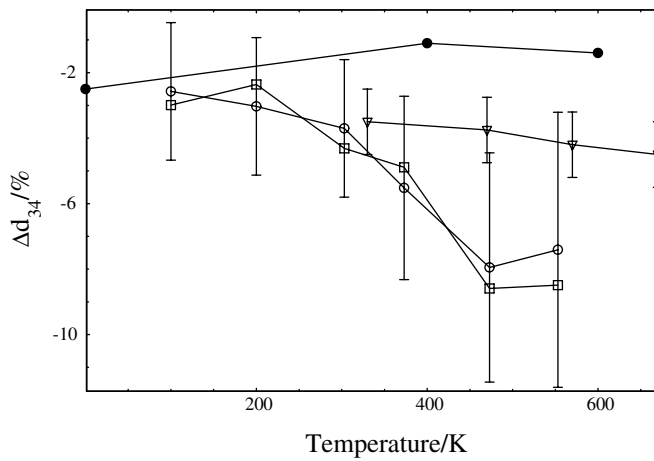


Figure 3.6: Relaxation of the third interlayer spacing Δd_{34} as a function of temperature. LEED results obtained using isotropic vibrations are marked by empty squares. LEED results obtained using anisotropic vibrations are marked by empty circles. MEIS results[114] are marked by empty triangles. eDFT-MD results[93] are marked by filled circles. Uncertainties are given for LEED results using anisotropic vibrations and MEIS results.

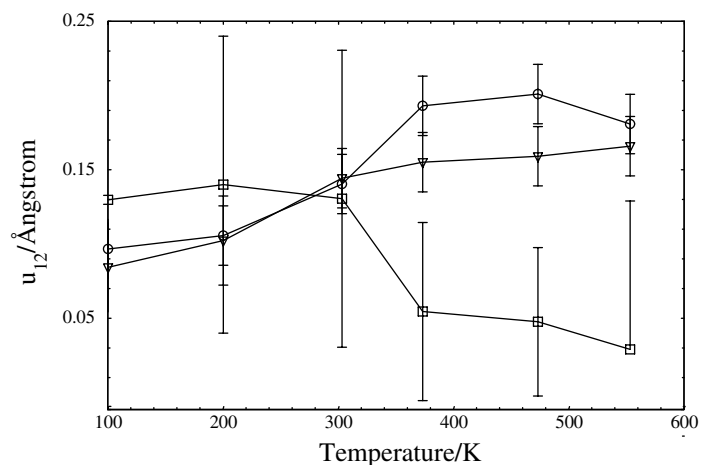


Figure 3.7: First layer isotropic and anisotropic vibrations as a function of temperature obtained from the LEED analysis. Isotropic vibrations u_1 are denoted by triangles, the perpendicular and parallel components $u_{1\perp}$ and $u_{1\parallel}$ are marked by circles and squares respectively.

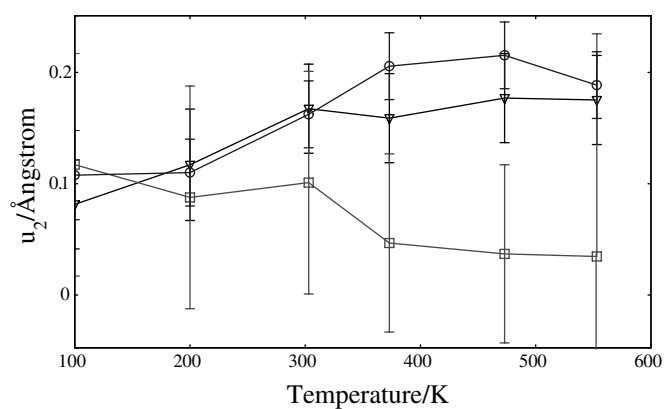


Figure 3.8: Second layer isotropic and anisotropic vibrations as a function of temperature obtained from the LEED analysis. Isotropic vibrations u_2 are denoted by triangles, the perpendicular and parallel components $u_{2\perp}$ and $u_{2\parallel}$ are marked by circles and squares respectively.

3.3.4 Surface thermal expansion coefficients

The surface thermal expansion coefficient between the i 'th and the j 'th layers can be defined as

$$\alpha_{ij} = \frac{\partial \Delta d_{ij}(T)}{\partial T} \simeq \frac{\Delta d_{ij}(T + \Delta T) - \Delta d_{ij}(T)}{\Delta T} \quad (3.1)$$

where $\Delta d_{ij}(T) = 100 * [d_{ij}(T) - d_{bulk}(T)]/d_{bulk}(T)$. In a simple picture one may understand thermal expansion by considering anharmonic terms for a classical oscillator. Using the Boltzmann distribution one finds according to Kittel[115] that the average displacement $\langle x \rangle \propto k_B T$ in a classical model. Assuming then that the surface thermal expansion is linear over the measured temperature range, we can initially fit $\Delta d_{ij}(T)$ to $\Delta d_{ij} = aT + b$, and set $\alpha_{ij} = a$. The results for both LEED, MEIS and eDFT-MD, derived from the relaxation data on fig 3.4, 3.5 and 3.6 are shown in Table 3.5.

As is seen, the linear thermal expansion coefficients found by LEED differ qualitatively from the coefficients found by MEIS. MEIS also consistently predicts smaller layer relaxations compared to LEED. These discrepancies in inter-layer spacing gradually increase as a function of temperature and the disagreements of more than 5% are found at the highest temperatures. With the discussion of the previous section in mind and the observation that improvement of the model assumptions of thermal vibrations in LEED have generally lead to increases in surface expansions and contractions, there is no reason to believe that LEED is overestimating the surface relaxations by several percent. There has been no real possibility to check the systematic errors of the MEIS structural determinations, but clearly some problems can be pointed out. The data set available in MEIS is considerably smaller than the data set available in LEED, in the sense that MEIS relies on various configurations of ion scattering off the surface while LEED as a diffraction technique can be said to probe many different scattering configurations at once. Both structural and vibrational parameters can be strongly correlated in MEIS, and MEIS measurements are more sensitive to lateral disorder than LEED. One should also note that LEED and MEIS measure two different things, LEED samples the periodic crystalline areas of the Al(110) surface, while MEIS measurements will result in an average over perfect areas and various defects (static or thermal). This makes it an open question whether MEIS and LEED determine exactly the same structure on more disordered surfaces. Finally, MEIS measurements should become increasingly unreliable as the temperature goes up, because the scattering configuration gets more diffuse.

It is interesting to compare the present results with the results of eDFT-MD calculations by Marzari et al [93] mentioned above. As can be seen from Table 3.2, the calculations show an increase in the contraction of the first interlayer

Table 3.5: Comparison of linear thermal expansion coefficients of Al(110) measured experimentally by LEED and MEIS and calculated by eDFT-MD

	LEED	MEIS [114]	eDFT-MD [93]
α_{12}	-0.007 K^{-1}	$+0.006 \text{ K}^{-1}$	-0.00006 K^{-1}
α_{23}	$+0.008 \text{ K}^{-1}$	-0.0006 K^{-1}	$+0.002 \text{ K}^{-1}$
α_{34}	-0.013 K^{-1}	-0.003 K^{-1}	$+0.002 \text{ K}^{-1}$

spacing with temperature at temperatures above 400K, and an increase in the expansion of the second interlayer spacing with temperature from 0K. Our results confirm these calculations, although we find that an increase in the contraction of the first interlayer spacing occurs already in the range 100K to 300K, where the calculations show an almost constant value. The linear thermal expansion coefficients have also been derived for the eDFT-MD calculations and are found in Table 3.5. The signs of α_{12} and α_{23} of the calculations agree with LEED measurements, however the sign of α_{34} differs. The relaxations found by eDFT-MD calculations are generally smaller than the values found by LEED, although they converge to some extent at low temperatures.

Recently, temperature dependent LEED structural measurements have also been carried out by Ismael et al[116] on Mg(10 $\bar{1}$ 0), which has the same $- + -$ sequence of relaxations as Al(110). Qualitatively the results for the linear thermal expansion coefficients are remarkably similar to our results for Al(110). The sequence of linear thermal expansion coefficients for Mg(10 $\bar{1}$ 0) is $- + -$ and the absolute value of the negative expansion coefficient α_{34} is larger than the absolute value of α_{12} . This is similar to the findings for Al(110) presented here. For Mg(10 $\bar{1}$ 0), theoretical calculations using the quasiharmonic approximation (QHA) confirmed the $- + -$ sequence of the thermal expansion coefficients, and indicated that the negative thermal expansion was intimately tied to the positive thermal expansion coefficient d_{23} . As was suggested by Ismael et al, and is corroborated by our findings, it seems that *surface thermal expansion coefficients generally follow the pattern of the interlayer relaxations*. The QHA calculations further show that the thermal expansion of the surface could be correlated with the in-plane bulk thermal expansion, as the $- + -$ thermal expansion pattern was only found when this effect was included. Finally Ismael et al, speculated that the $- + -$ thermal expansion pattern could be a volume conservation effect, as the overall thermal expansion of the first seven surface layers followed the bulk thermal expansion. This result is not confirmed by the present finding, as the combined thermal expansion of the first three layers is negative, and no evidence of an expansion was found for d_{45} , when included in the structural determinations at 100K and 300K

Table 3.6: Anisotropic vibrational parameters at comparable temperature for LEED, eDFT-MD [114] and MEIS [114]. In the case of MEIS and eDFT-MD calculations $u_{i\parallel} = (u_{ix} + u_{iy})/2$

Method	Temp	$u_{1\parallel}$ (Å)	$u_{1\perp}$ (Å)	$u_{2\parallel}$ (Å)	$u_{2\perp}$ (Å)
LEED	300K	0.13	0.14	0.10	0.16
LEED	553K	0.03	0.18	0.05	0.19
eDFT-MD	400K	0.16	0.14	0.13	0.19
eDFT-MD	600K	0.22	0.20	0.18	0.24
MEIS	330K	0.16	0.14	0.12	0.12
MEIS	570K	0.22	0.18	0.21	0.21

3.3.5 Anisotropic and isotropic vibrations

As can already be seen from Table 3.4 for the calculations at 100K and 300K, the vibrational amplitudes of Al atoms in the first two layers are about twice as large as for Al atoms in deeper layers both at 100K and 300K. It is also noteworthy that Al atoms in the second layer have larger vibrational amplitudes than Al atoms in the first layer at 300K.

Thermal vibrations as a function of temperature are shown for the first two layers in Fig. 3.7 and 3.8. Numerical values for surface vibrations at various temperatures are shown for LEED, eDFT-MD and MEIS in Table 3.6. Above room temperature we find evidence of anisotropic vibrations in both the first and second layers, in that $u_{1\perp} \simeq u_{2\perp}$ are twice as large as $u_{1\parallel} \simeq u_{2\parallel}$. These trends are qualitatively different from theoretical eDFT-MD calculations, which predict that $u_{2\perp} > u_{1\perp}$, while $u_{2\perp} \simeq u_{1\parallel}$. MEIS results for the measurements of thermal vibrations are rather inconclusive for $u_{1\parallel}$ and $u_{2\parallel}$ as they were strongly correlated. It could only be concluded that they were both enhanced $\sim 10 - 20\%$ with respect to bulk vibrations. MEIS measurements also show that $u_{2\perp} > u_{1\perp}$ at 570K while $u_{1\perp} > u_{2\perp}$ at 330K.

As is evident from comparison of these three methods, some disagreement exists for thermal vibrations. All three methods agree quantitatively on the most easily determined vibrational quantity $u_{1\perp}$, while there is little agreement for $u_{2\perp}$ as is shown in table 3.6. One important point can be deduced with some certainty: $u_{2\perp}$ is strongly enhanced especially at higher temperatures. The enhanced vibrations of second layer Al atoms are explained by Marzari et al by the surface-normal direction providing an "easy" channel for vibrations on the open Al(110) surface. Both LEED and MEIS have difficulties measuring $u_{1\parallel}$ and $u_{2\parallel}$, which is also reflected by the deviations found. The fact that LEED measurements show a drop of $u_{1\parallel}$ and $u_{2\parallel}$ with temperature seems implausible. Although a definite minima in the R-factor is found for both parallel vibrations, the weak R-factor de-

pendence means that other approximations, such as the energy dependence of the inner potential could influence this value. Finally it should be noted that isotropic vibrational parameters found by LEED are almost identical to the values found for the perpendicular component of the anisotropic vibrations, which can be attributed to the weak sensitivity to parallel vibrations.

3.3.6 Bulk vibrational parameters

One puzzling feature of the results is the anomalously low values found for the "bulk" rms vibrations, namely 0.07Å and 0.14Å at 100K and 300K, respectively, as compared to the values of 0.12Å and 0.21Å which can be calculated assuming a Debye model and a Debye temperature[117] of 394K. Since our values apply to atoms in the fourth and deeper layers, it might be concluded that they could be inaccurate because of poorer sensitivity to the deeper layers. However, such a conclusion would be at odds with the relatively small uncertainties in the determined values. Another possible explanation might be errors due to the approximate treatment of vibrations in the LEED analysis, in particular the lack of any treatment of correlated vibrations. As pointed out by Jepsen et al[118], the correlated movement of neighboring atoms for low-frequency phonon modes will reduce thermal disorder. Such an explanation, however, raises the further question of why the effects of correlations are more important for Al than for Cu, since in our analysis of LEED measurements for Cu(100) described below we found bulk vibrations in excellent agreement with values in the literature.

3.4 Cu(100)

I(V) spectra were measured at 100K and 300K for the clean Cu(100) surface. The calculations carried out for comparison with measurements made at 300K used a value[111] for the lattice constant for Cu of $a_0 = 3.6150\text{Å}$. The corresponding calculations carried out for 100K used a value of $a_0 = 3.6044\text{Å}$, derived from measurements[119] of thermal expansion in the range 87K to 773K. Comparison between experimental and calculated I(V) curves is presented in Fig. 3.9, for measurements at 300K.

The present results for the geometry of the clean Cu(100) surface are compared with the results of previous studies in Table 3.7. As can be seen from the results in the table, the geometry of the clean Cu(100) surface corresponds to an almost perfect truncation of a bulk crystal. The spread of values in the table is most probably within the errors of the respective analysis. It is noted, however, that the present analysis shows no evidence for a relaxation of the second interlayer spacing found in the MEIS studies[120, 121] and in an early LEED study[122].

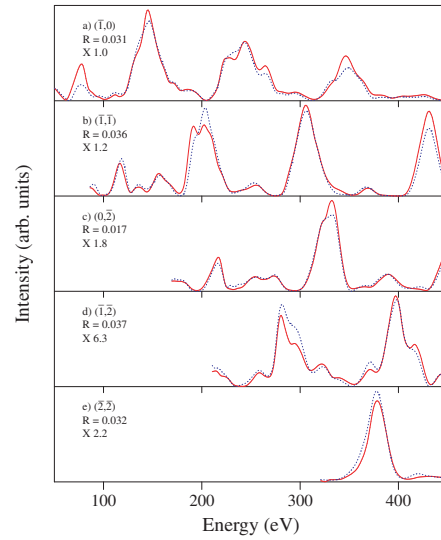


Figure 3.9: Comparison of experimental (solid lines) and calculated (dotted lines) intensity-energy spectra for clean Cu(100) at 100K and $\theta = 0^\circ$ for 5 integral order beams, a)-e). The beam hk indices, R factors, and scale factors are shown in each panel. The calculated spectra were obtained using the best-fit parameter values given in Table 3.9

It is also interesting to compare the dynamical parameters found here with those found in the earlier MEIS studies, as listed in Table 3.8. The values for the (isotropic) bulk vibrations agree to within 0.01\AA , but the values for the surface vibrations found in the MEIS studies are larger than those found here. In the MEIS studies it was found that the vibrations of the first Cu layer are anisotropic, with larger vibrations parallel to the surface than perpendicular to the surface. However, different ratios of parallel to perpendicular amplitudes of 1.55 and 1.08, respectively, were found in the two studies[120, 121]. Perhaps the difference between the present LEED results and the MEIS results lies in the possible error resulting from the assumption of isotropic vibrations in our LEED calculations. As concluded in the previous section, LEED samples mostly the perpendicular component of the vibrational amplitudes. Thus lower average vibrations should be found in this LEED analysis compared to the MEIS analysis, as is in fact the case.

The mean square vibrations (MSVs) determined here for the bulk of a Cu(100) crystal lead to Debye temperatures of $327 \pm 10\text{K}$ and $328 \pm 10\text{K}$ at 100K and 300K, respectively. These results are in remarkable agreement with earlier X-ray diffraction measurements[126], which yield an almost constant bulk Debye temperature of $322 \pm 20\text{K}$ in the range of 100K to 300K. This indicates that the vibrations found in LEED dynamical calculations for Cu have real physical meaning and are

Table 3.7: Relaxations Δd_{12} and Δd_{23} of the first two interlayer spacings expressed as % deviations from the bulk value of 1.81Å of clean Cu(100).

Ref.	LEED					MEIS		Theory
	present	[122]	[123]	[124]	[61]	[120]	[121]	[125]
Δd_{12} (%)	-1.0	-1.1	-1.2	-2.4	-1.7	-2.4	-2.0	-3.0
Δd_{23} (%)	0.0	+1.7	+0.9	+0.4	+0.7	+1	+1.0	+0.1

not just fitting parameters. For comparison it can be noted that the corresponding Debye temperatures for the first Cu layer are 233K and 254K, respectively, based on the vibrations determined at 100K and 300K.

For the surface, MSVs can in principle be calculated from phonon spectra, as measured by Energy Electron Loss Spectroscopy (EELS)[127], for example. Unfortunately, very few calculations of this kind have been made, and until very recently the most advanced took only nearest neighbor and next nearest neighbor interactions into account or used Lennard-Jones potential interactions [127, 128]. Ensemble DFT molecular dynamics calculations[93] have been able to predict MSVs, and this study was discussed in the previous section. Comparison of the MSVs found from quantitative LEED analysis with theoretical calculations is very interesting because MSVs are thermodynamic parameters much like entropy or internal energy. Thus if a model can predict MSVs it might also be able to handle other thermodynamic parameters with some precision.

Table 3.8: Total vibrational amplitudes for Cu atoms in the first layer and in the bulk. The values from Refs.[120] and[121] are calculated from the one-dimensional vibrational amplitudes reported in these articles via $u^2 = u_{\perp}^2 + 2u_{\parallel}^2$.

Ref.	100K		300K		
	present	[121]	present	[120]	[121]
u_1 (Å)	0.120	0.157	0.180	0.264	0.248
u_{bulk} (Å)	0.090	0.095	0.140	0.144	0.147

Finally it should be mentioned that the clean Cu(100) surface has recently been the subject of some controversy as an in-plane lattice reconstruction of 1% was found by LEED for Cu(100)[124]. This result was quite surprising and although investigations of epitaxial growth of Cu on Cu(100) seemed to support these results[129], the result was in clear contradiction with XRD data[130, 131]. Finally last year[61] the discrepancy was resolved by the introduction of an energy dependence of the inner potential in the analysis of low energy electron diffraction.

3.5 Cu(100)-c(2 × 2)-Na

3.5.1 Introduction

The adsorption of Na on the Cu(100) surface has been the subject of interest in several recent experimental and theoretical studies[125, 132, 133]. From a qualitative LEED study[133] it was concluded that a Cu(100)-c(2 × 2)-Na phase is the only ordered phase resulting from the adsorption. The authors of this work also concluded that Na atoms are located in 4-fold sites in the c(2 × 2)-Na structure, but no concrete evidence for this conclusion was given. The x-y dependence of the surface potential for Na adsorbed on Cu(100) at very low coverages, $\theta_{Na} < 0.05$ monolayer (ML), has been determined[132] by helium atom scattering (HAS). A result of this study was the prediction that the four-fold-hollow site is the adsorption site with lowest energy. *Ab initio* DFT calculations have been carried out recently[125] for the structures formed by adsorption of 0.25 ML and 0.5 ML of Li, Na and K on Cu(100), leading to the predictions that while Li adsorption favors a (2 × 1) missing row reconstruction at room temperature, Na and K adsorption does not lead to reconstruction of the Cu substrate. The (2 × 1)-Li reconstruction has been confirmed by an earlier quantitative LEED study[12]. The results of the present work provide a qualitative confirmation of the predictions for the Cu(100)-c(2 × 2)-Na structure by DFT. This study also presents full dynamical LEED I(V) structural determinations at *two* different temperatures for the same adsorbate system.

3.5.2 LEED experiment and calculations

Sharp c(2 × 2) LEED patterns with good contrast were obtained after deposition of 0.5 ML Na, both at 100K and 300K. Further deposition of Na led to a decrease of intensities in fractional and integral order spots and, finally, to a weak (1 × 1) pattern. Optimum development of the c(2 × 2) structure was achieved by incremental deposition of Na until a maximum was reached in the ratio of integrated intensity in fractional order and integral order diffracted beams. By recording several consecutive spectra, it was found that no significant damage to the overlayer system occurred on the time scale of the experiment for adsorption and measurement at 300K. This was not the case, however, for adsorption and measurement at 100K, where the second of two successive sets of measurements showed a small, but significant decrease in the overall intensity of the fractional order beams as compared to the integral order beams. By carrying out measurements with different electron beam currents, it was established that the damage was related to the integrated current to the crystal. Thus the damage was most probably due to the interaction of the incident electron beam with the surface structure. However,

Table 3.9: Best-fit parameter values for Na adsorbed in four-fold hollow sites in the Cu(100)- $c(2 \times 2)$ -Na phase formed by adsorption at 300K. The interlayer spacings are denoted d_{ij} and the rms vibrational amplitudes are denoted u_j , where the subscripts indicate the layers in question. d_{01} is the spacing between the adsorbed Na layer and the first Cu layer. u_0 is the vibrational amplitude of adsorbed Na atoms. The analysis of measurements at both 100K and 300K are shown in the table. The corresponding results for the clean Cu(100)- (1×1) surface are also shown for comparison

Temperature	100K		300K	
Phase	(1×1)	$c(2 \times 2)$ -Na	(1×1)	$c(2 \times 2)$ -Na
d_{01}		$2.37 \pm 0.03 \text{ \AA}$		$2.42 \pm 0.04 \text{ \AA}$
d_{12}	$1.79 \pm 0.01 \text{ \AA}$	$1.80 \pm 0.02 \text{ \AA}$	$1.79 \pm 0.01 \text{ \AA}$	$1.80 \pm 0.02 \text{ \AA}$
d_{23}	$1.81 \pm 0.01 \text{ \AA}$	$1.80 \pm 0.02 \text{ \AA}$	$1.81 \pm 0.01 \text{ \AA}$	$1.81 \pm 0.02 \text{ \AA}$
d_{34}	$1.81 \pm 0.02 \text{ \AA}$	$1.79 \pm 0.03 \text{ \AA}$	$1.81 \pm 0.01 \text{ \AA}$	$1.79 \pm 0.02 \text{ \AA}$
u_0		$0.25 \pm 0.02 \text{ \AA}$		$0.32 \pm 0.02 \text{ \AA}$
u_1	$0.12 \pm 0.01 \text{ \AA}$	$0.13 \pm 0.03 \text{ \AA}$	$0.18 \pm 0.01 \text{ \AA}$	$0.19 \pm 0.02 \text{ \AA}$
u_2	$0.11 \pm 0.01 \text{ \AA}$	$0.11 \pm 0.02 \text{ \AA}$	$0.16 \pm 0.01 \text{ \AA}$	$0.15 \pm 0.01 \text{ \AA}$
u_3	$0.08 \pm 0.01 \text{ \AA}$		$0.13 \pm 0.01 \text{ \AA}$	
u_{bulk}	$0.09 \pm 0.01 \text{ \AA}$	$0.09 \pm 0.02 \text{ \AA}$	$0.14 \pm 0.01 \text{ \AA}$	$0.14 \pm 0.01 \text{ \AA}$
V_{im}	$4.5 \pm 0.7 \text{ eV}$	$4.8 \pm 0.7 \text{ eV}$	$3.4 \pm 0.7 \text{ eV}$	$4.3 \pm 0.8 \text{ eV}$
$R_{\text{exp} - \text{exp}}$	0.007	0.026	0.008	0.023
$R_{\text{exp} - \text{theory}}$	0.031	0.074	0.025	0.046

quantitative analysis of several of the deteriorated spectra showed that the errors in the data due to this beam damage led to changes in the structural parameters that were less than their estimated errors. It is presumed that possible electron-beam damage is annealed out at 300K.

I(V) spectra were measured at 100K and 300K for the $c(2 \times 2)$ -Na phase formed by adsorption at 300K, and were measured at 100K for the $c(2 \times 2)$ -Na phase formed by adsorption at 100K. The latter spectra were virtually identical to those measured at 100K after adsorption at 300K. A full optimization of the fit between experimental intensities and intensities calculated for Na adsorbed in the four-fold hollow site was carried out. The results of the refinement are listed in Table 3.9, together with the results of the LEED analysis for the clean Cu(100) surface. Plots of experimental intensity-energy spectra measured at 100K and spectra calculated for the optimum parameter values given in Table 3.9 can be found in Fig. 3.10 for the Cu(100)- $c(2 \times 2)$ -Na phase formed by adsorption at 300K. Similarly good agreement was obtained in plots (not shown) of experimental and calculated spectra for the Cu(100)- $c(2 \times 2)$ -Na phase formed by adsorption at 100K.

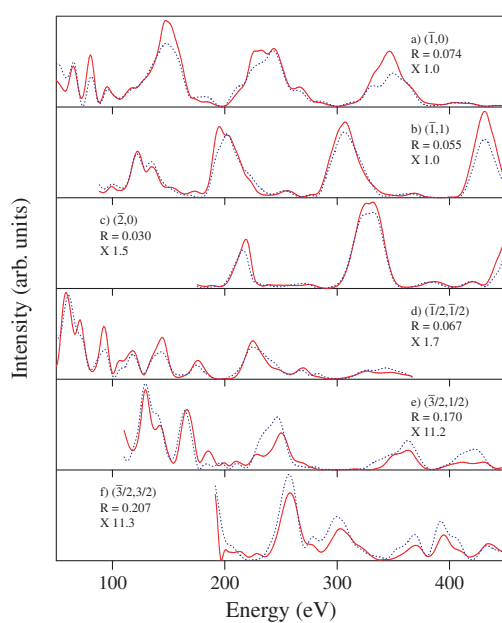


Figure 3.10: Comparison of experimental (solid lines) and calculated (dotted lines) intensity-energy spectra at 100K and $\theta = 0^\circ$ for the Cu(100)- $c(2 \times 2)$ -Na phase formed by adsorption at 300K, for three integral order beams, a)-c), and three fractional order beams, d)-f). The beam hk indices, R factors, and scale factors are shown in each panel. The calculated spectra were obtained using the best-fit parameter values given in Table 3.9

3.5.3 Discussion

Table 3.10: Comparison of interlayer spacings determined here for the Cu(100)- $c(2 \times 2)$ -Na structure with the results of DFT calculations. The first two interlayer spacings in the substrate are given as percentage deviations from the bulk value.

	present	DFT[125]
d_{Na-Cu_1}	$2.37 \pm 0.03 \text{ \AA}$	2.12 \AA
Δd_{12}	$-0.4 \pm 1.1\%$	-4.1%
Δd_{23}	$-0.4 \pm 1.1\%$	-4.0%

The results of this work confirm the prediction of DFT calculations [125] that Na atoms adsorb in four-fold hollow sites on an unreconstructed Cu(100) substrate in the $c(2 \times 2)$ -Na phase. In detail, however, the interlayer spacings determined here differ rather significantly from the theoretical predictions, as can be seen from the listing in Table 3.10. In particular, it is noted that the present work indicates that Na adsorption occurs without significant perturbation of the substrate. It is interesting to compare the present results with previous results[18] for the Ni(100)- $c(2 \times 2)$ -Na structure, where Na atoms also adsorb in four-fold hollow sites. The distance between the Na overlayer and the metal substrate is almost identical in the two structures at room temperature. Also the enhancement of $\sim 40\%$ of the vibrations of first layer Cu atoms with respect to those of bulk atoms is similar to the corresponding enhancement in the case of Ni(100). However, the vibrational amplitudes of the adsorbed Na atoms are considerably larger on Cu(100) than on Ni(100), namely 0.32 \AA versus 0.25 \AA . This leads one to conclude that Na is bound stronger to the Ni(100) surface than the Cu(100) surface.

Chapter 4

Single layer Li and Na surface alloys on Al

4.1 Introduction

The surprising finding of complex substitutional alkali structures on Al(111) by the immiscible Na, K and Rb encouraged the Århus LEED group to expand the studies of alkali-aluminum systems to the more open Al(100) and Al(110) surfaces. In fact a quantitative LEED study on Al(100)[14] had already found that adsorption of 0.5ML Na at room temperature leads to the formation of a Al(100)-c(2 × 2)-Na substitutional surface alloy, indicating that such behavior was not restricted to Al(111). Prior to this work it was also concluded from an unpublished LEED and CLS study by the Århus LEED group[134, 135] that an Al(110)-c(2 × 2)-Na substitutional alloy was probably formed after adsorption of 0.5ML Na at room temperature, but the quality of the LEED data was not satisfactory taking previous studies into account. Qualitative LEED observations combined with CLS measurements indicated that also 0.5ML Li adsorbed at room temperature form a Al(100)-c(2 × 2)-Li surface alloy[58]. Based on this work it was decided to do a more thorough investigation of the structures formed by Li and Na on Al(100) and Al(110).

The adsorption of alkali metals on Al(110) is also of particular interest in that extrapolation of the results of previous studies of alkali metal adsorption on Al surfaces, and previous studies of alkali metal adsorption on fcc(110) metal surfaces, lead to quite different expectations of the adsorption behavior on Al(110). Thus, on the one hand, as noted above, recent studies of alkali metal adsorption[8, 9, 24] on Al(111) at room temperature have shown that the adsorption leads to a reconstruction of the substrate, with alkali atoms located in substitutional sites. On the other hand, small (~ 0.1 monolayer) coverages of alkali metals on Ni, Cu,

Ag, and Pd(110) induce (1×2) , "missing-row" reconstructions[136–138], similar to the intrinsic (1×2) , missing-row reconstructions[139–142] of clean Pt, Ir, and Au(110). It has been suggested [143, 144] that the adsorption of alkali metals on fcc(110) metal surfaces is in general likely to induce missing-row structures, because of the small energy difference between the (1×1) and (1×2) structures for the clean surfaces, and because of the larger binding energy of the alkali atoms in sites of high coordination in the missing rows. The latter suggestion has been confirmed in the case of Cu(110)/K by a photoelectron diffraction study[145].

In addition to the novel findings of substitutional adsorption, a further interesting aspect of alkali metal adsorption on Al surfaces has been the discovery of structural phase transitions as a function of temperature. Thus, as has already been found for adsorption of K and Rb on Al(111), adsorption at around 100K temperature can lead to the formation of very different structures, as compared to the substitutional structures formed at room temperature. At 100K the adsorption of 0.33ML K and Rb also leads to the formation of an Al(111)- $(\sqrt{3} \times \sqrt{3})R30^\circ$ structure, but the alkalis are adsorbed in on-top positions[8, 25]. This can be explained in that the activation energy of vacancy formation is too high for substitutional adsorption to occur at low temperatures[27, 28, 146]. This also means that there is an irreversible phase transition from the low temperature phase to the room temperature phase, as substitutional adsorption is thermodynamically the most stable configuration. As was established by E. Lundgren and J. N. Andersen[147], the alkali-aluminum phase diagram as a function of coverage and temperature can hold even more surprises. For example a Al(100)- $(\sqrt{5} \times \sqrt{5})R27^\circ$ -Na structure forms below room temperature after adsorption of 0.2ML Na at room temperature. It will be shown in this thesis that there is in fact a reversible disorder/order phase transition around 220K leading to the formation of the substitutional Al(100)- $(\sqrt{5} \times \sqrt{5})R27^\circ$ -Na structure below 220K.

As has also been found previously for alkali adsorption on Al(111)[8], the structures at low coverage are very similar for Li and Na adsorption on Al(100) and Al(110) although Li is miscible, while Na is immiscible. Accordingly the structures formed by both Li and Na on Al(100) and Al(110) in the 0.0 to 0.5ML adsorption regime are treated together in this chapter.

In the following, the structures of the Al(100)- $c(2 \times 2)$ -Li, Al(100)- $(\sqrt{5} \times \sqrt{5})R27^\circ$ -Na, Al(110)- $c(2 \times 2)$ -Li, and Al(110)- $c(2 \times 2)$ -Na phases are determined by analysis of extensive LEED data .

Combining LEED and HRCLS measurements the formation dynamics in the coverage regime between 0.0ML - 0.5ML on Al(110) for both Li and Na is studied.

As noted in section 2.3.3, the LEED structural analysis for these Al-alkali systems included tests of all models compatible with the observed symmetry of the LEED intensities. In the following, for brevity, the results are described only

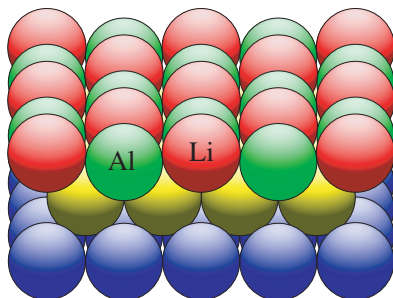


Figure 4.1: Hard-sphere model of the geometry of the Al(100)-c(2 × 2)-Li structure, shown as a central projection on the (211) plane, tilted by 20° with respect to the plane of the paper.

for the final optimal structures.

4.2 Structure of Al(100)-c(2 × 2)-Li

4.2.1 LEED measurements and structural determination

Sharp c(2 × 2) LEED patterns with good contrast were obtained after deposition of 0.5ML Li at 300K. Further deposition of Li led to a decrease in intensity of the fractional-order beams, but no new ordered structures were observed. Measurements for the c(2 × 2)-Li phase were made both at normal incidence and at $\theta = 8.9^\circ$. Measurements were made for a total of 42 symmetry-inequivalent beams (27 integral-order, 15 fractional order).

The optimal geometry was found to consist of Li adsorbed in 4-fold substitutional sites. The structural variables comprised the interlayer spacing between the Li and first Al layer d_{01} , the interlayer spacings between the first 4 Al layers d_{12} , d_{23} , d_{34} and a vertical displacement towards the surface Δr_3 of those atoms in the third Al layer that lie beneath adsorbed Li atoms. The results of the structural analysis for Al(100)-c(2 × 2)-Li with Li adsorbed in substitutional sites are listed in Table 4.1. A hard-sphere model of the Al(100)-c(2 × 2)-Li structure is shown in Fig. 4.1.

Plots of experimental I(V) spectra and spectra calculated for the optimum parameter values given in Table 4.1 are shown in fig 4.2 and 4.3 for $\theta = 0^\circ$ and 8.9° . The overall level of agreement between experiment and theory is regarded as satisfactory, although less definitive than in our other analysis of the surface structures formed by the heavier alkalis. The residual discrepancies between experiment and theory are perhaps due to a less than perfect order in the c(2 × 2)-Li structure, re-

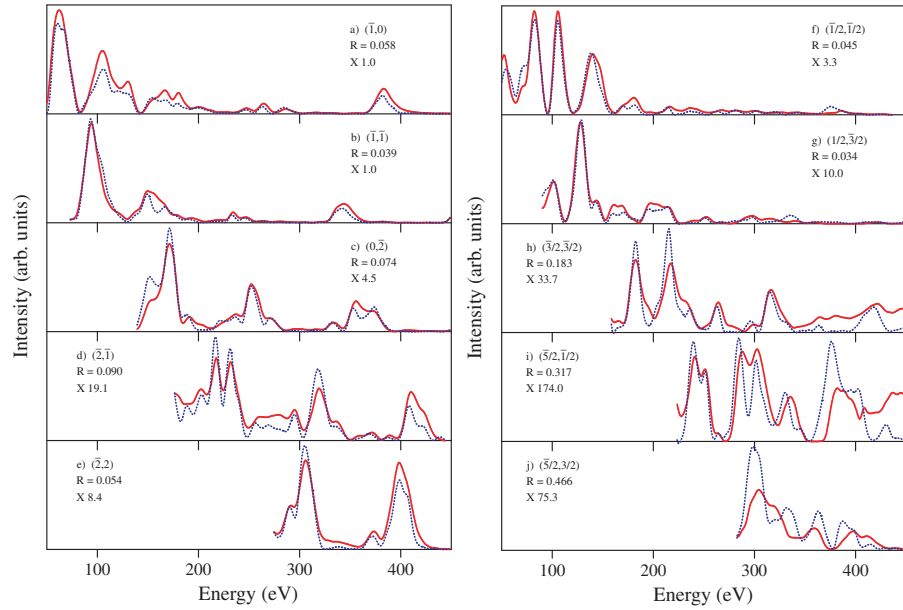


Figure 4.2: Comparison of experimental (solid lines) and calculated (dotted lines) intensity-energy spectra for Al(100)-c(2 × 2)-Li at $\theta = 0^\circ$ for 5 integral-order beams, a)-e), and 5 fractional order beams, f)-j). The beam hk indices, R factors, and scale factors are shown in each panel. The calculated spectra were obtained using the best-fit parameter values given in table 4.1.

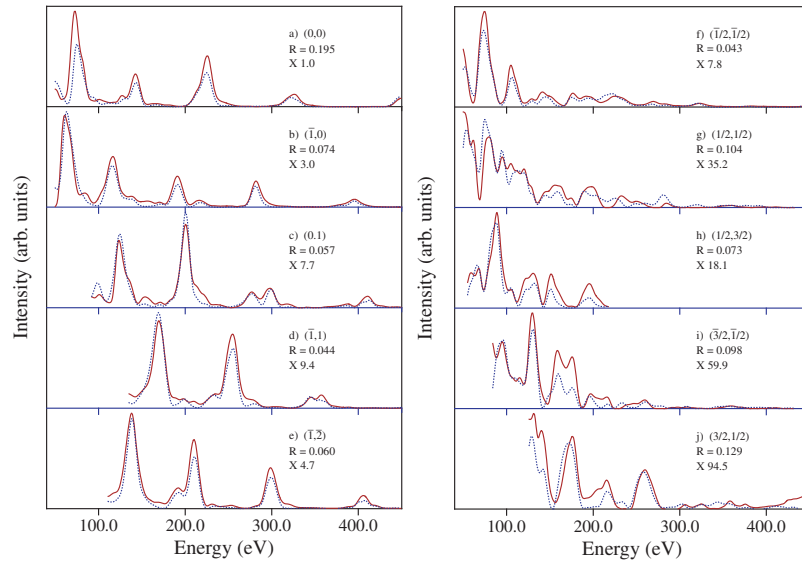


Figure 4.3: Comparison of experimental (solid lines) and calculated (dotted lines) intensity-energy spectra for Al(100)-c(2 × 2)-Li at $\theta = 8.9^\circ$ for 5 integral-order beams, a)-e), and 5 fractional order beams, f)-j). The beam hk indices, R factors, and scale factors are shown in each panel. The calculated spectra were obtained using the best-fit parameter values given in table 4.1.

lated to the onset of multi layer alloy formation prior to the completion of the first layer.

4.2.2 Structural parameters

The spacing d_{01} between the Li layer and the reconstructed Al layer of only $0.32 \pm 0.04 \text{ \AA}$ shows that the Li atoms are close to being perfectly embedded in the Al layer. The hard-sphere radius of the Li atoms is 1.44 \AA , as compared to the bulk (bcc) metallic radius [111] of 1.52 \AA and the Al bulk radius of 1.43 \AA . The Li-Al bond length is 2.87 \AA . It is also interesting to note that the vertical spacing between Al atoms in the first, mixed Al/Li layer and Al atoms in the second layer corresponds to a $-5.8 \pm 1.5\%$ contraction with respect to the bulk interlayer spacing, as can be compared to the $2 \pm 0.8\%$ expansion of the first interlayer spacing in the clean Al(100) surface. The substitutional adsorption of Li in the first Al layer also induces a small ($\Delta r_3 = 0.03 \text{ \AA}$) rumpling of the third Al layer, such that the Al atoms in this layer which are directly beneath Li atoms in the first mixed Al/Li layer are displaced towards the surface. Finally, it is noted that the vibrational amplitudes of Al atoms in the first, mixed Al/Li layer are even larger than is the case for the clean Al(100) surface.

4.2.3 Surface structure vs. bulk alloy

The surface structure of the Al(100)-c(2 × 2)-Li phase, as determined here, is very similar to that of the (100) plane of the metastable Al_3Li bulk alloy. The c(2 × 2)-Li structure is also similar to that of the corresponding Al(100)-c(2 × 2)-Na phase [14], although Na unlike Li is immiscible in Al. This result agrees with previous studies of the submonolayer adsorption of Li on close-packed Al surfaces which have yielded results similar to those found for the heavier alkali metals which are immiscible in Al. The question as to whether the surface structures formed by adsorption of Li have any relation to bulk Al-Li alloys, will be discussed in chapter 6.

4.2.4 Comparison to theoretical calculations

Recent FLAPW calculations by Ohsaki et. al. [148] of the Al(100)-c(2 × 2)-Li phase also favor adsorption in four-fold coordinated substitutional sites. Results of the calculations are presented along with the LEED structural results in Table 4.2. The agreement for structural parameters between the experimental structure determination and the FLAPW results is quite good. Ohsaki et. al. have also calculated the adsorption energy of both the Li and Na c(2 × 2) structures on Al(100). They find that $E(\text{Li})_{ads} = 2.6 \text{ eV}$ and $E(\text{Na})_{ads} = 1.8 \text{ eV}$. Thus the energy

Table 4.1: Best-fit parameter values for clean Al(100) and for Li adsorbed in the substitutional site in the Al(100)-c(2 × 2)-Li structure. The interlayer spacings are denoted d_{ij} and the rms vibrational amplitudes are denoted u_i , where the subscripts indicate the layers in question. d_{01} is the spacing between the adsorbed Li layer and the first Al layer and u_0 is the vibrational amplitude of adsorbed Li atoms. Δr_3 is the rumpling of Al atoms in the third layer. For the c(2 × 2)-Li phase, results are shown of the analysis of measurements at $\theta = 0^\circ$ and 8.9° . The final column gives the weighted means of the results of these two analysis.

	(1 × 1)	c(2 × 2)-Li		
θ	0°	0°	8.9°	weighted mean
d_{01}		$0.35 \pm 0.05 \text{ \AA}$	$0.28 \pm 0.05 \text{ \AA}$	$0.32 \pm 0.04 \text{ \AA}$
d_{12}	$2.06 \pm 0.02 \text{ \AA}$	$1.89 \pm 0.03 \text{ \AA}$	$1.92 \pm 0.05 \text{ \AA}$	$1.90 \pm 0.03 \text{ \AA}$
Δr_3		$0.03 \pm 0.02 \text{ \AA}$	$0.03 \pm 0.02 \text{ \AA}$	$0.03 \pm 0.01 \text{ \AA}$
d_{23}	$2.04 \pm 0.02 \text{ \AA}$	$2.02 \pm 0.03 \text{ \AA}$	$2.01 \pm 0.04 \text{ \AA}$	$2.02 \pm 0.02 \text{ \AA}$
d_{34}	$2.01 \pm 0.02 \text{ \AA}$	$2.02 \pm 0.03 \text{ \AA}$	$2.04 \pm 0.03 \text{ \AA}$	$2.03 \pm 0.02 \text{ \AA}$
u_0		$0.23 \pm 0.09 \text{ \AA}$	$0.24 \pm 0.08 \text{ \AA}$	$0.24 \pm 0.06 \text{ \AA}$
u_1	$0.17 \pm 0.02 \text{ \AA}$	$0.21 \pm 0.02 \text{ \AA}$	$0.27 \pm 0.02 \text{ \AA}$	$0.24 \pm 0.01 \text{ \AA}$
u_2	$0.14 \pm 0.02 \text{ \AA}$	$0.14 \pm 0.03 \text{ \AA}$	$0.19 \pm 0.03 \text{ \AA}$	$0.17 \pm 0.02 \text{ \AA}$
u_3	$0.10 \pm 0.02 \text{ \AA}$	$0.12 \pm 0.03 \text{ \AA}$	$0.14 \pm 0.03 \text{ \AA}$	$0.13 \pm 0.02 \text{ \AA}$
u_{bulk}	$0.08 \pm 0.02 \text{ \AA}$	$0.11 \pm 0.02 \text{ \AA}$	$0.09 \pm 0.02 \text{ \AA}$	$0.10 \pm 0.01 \text{ \AA}$
V_{im}	$5.1 \pm 0.08 \text{ eV}$	$3.1 \pm 0.7 \text{ eV}$	$5.3 \pm 0.08 \text{ eV}$	$4.1 \pm 0.05 \text{ eV}$
R	0.021	0.055	0.073	

Table 4.2: Comparison of the experimental LEED structure determination with theoretical FLAPW-LDA calculations. The distance between the substituted Li and the first Al layer d_{01} and the relaxations of the two first interlayer spacings Δd_{12} and Δd_{23} are given in % relative to the interlayer spacing of bulk Al

	LEED	FLAPW[148]
d_{01} (%)	16.1 ± 2	20.1
Δd_{12} (%)	-5.8 ± 2	-8.7
Δd_{23} (%)	-0.2 ± 1	+2.1

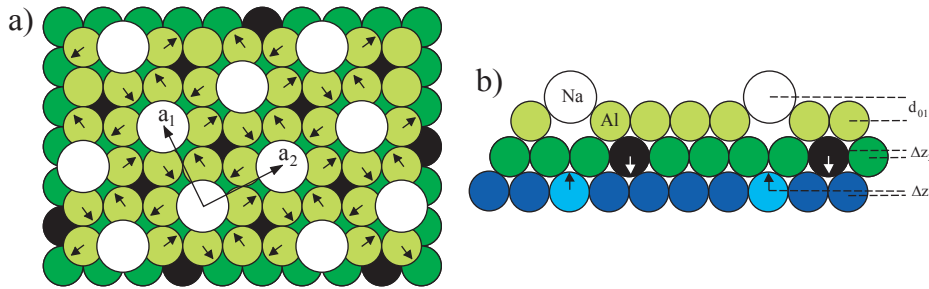


Figure 4.4: a) Top view and b) side view models of the geometry of the unrelaxed $\text{Al}(100)-(\sqrt{5} \times \sqrt{5})R27^\circ\text{-Na}$ structure for the first two surface layers. Symmetry equivalent sublattices are indicated by identical grey tones. Arrows indicate direction of substrate relaxations.

gain of Li adsorption is significantly higher than Na adsorption, indicating that the smaller size allowing Li to alloy almost perfectly into the surface is a more favorable situation.

4.3 Structure of $\text{Al}(100)-(\sqrt{5} \times \sqrt{5})R27^\circ\text{-Na}$

4.3.1 LEED measurements and structural analysis

Adsorption of 0.20ML Na at room temperature on Al(100) results in no apparent changes of the (1×1) LEED pattern, but cooling below 240K leads to the formation of a sharp $\text{Al}(100)-(\sqrt{5} \times \sqrt{5})R27^\circ\text{-Na}$ structure. Details of this disorder/order phase-transition will be presented below. $I(V)$ curves were measured for a total of 22 symmetry-inequivalent beams (6 integral-order, 16 fractional order).

The optimal geometry was found to contain Na atoms adsorbed in 4-fold substitutional sites in a $(\sqrt{5} \times \sqrt{5})R27^\circ$ unit-cell. It is noted that the structure has two domains with a fourfold rotational axis through the Na atoms, but no mirror plane. A model of the unrelaxed $\sqrt{5}$ structure is shown in Fig. 4.4, with arrows marking relaxations of the atoms in the first layer. The radial relaxations of the

Table 4.3: Best fit parameters in cylindrical atomic coordinates (r, Θ, z) and rms vibrational amplitudes (u) in \AA determined for the $\text{Al}(100)-(\sqrt{5} \times \sqrt{5})R27^\circ\text{-Na}$ structure. The $r-\Theta$ axis lies in the surface plane. The z -axis is the outward surface normal. Interlayer spacings d_{ij} are also given. Unit vectors of the chosen $\sqrt{5}$ domain are $a_1(r, \Theta) = (6.3784\text{\AA}, 116.5651^\circ)$, $a_2(r, \Theta) = (6.3784\text{\AA}, 26.5651^\circ)$. The bulk lattice constant at 100 K is $a_0 = 4.0341 \text{\AA}$ and bulk termination surface unit vectors are $a_1(r, \Theta) = (2.8525\text{\AA}, 0^\circ)$ and $a_1(r, \Theta) = (2.8525\text{\AA}, 90^\circ)$. Structural coordinates are only given for symmetry inequivalent sublattices.

Structural par.		Dynamical par.	
	LEED		LEED
d_{01}	$0.91 \pm 0.04 \text{\AA}$	u_0	$0.31 \pm 0.03 \text{\AA}$
r_1	$+3.04 \pm 0.03 \text{\AA}$	u_1	$0.23 \pm 0.02 \text{\AA}$
Θ_1	$1.5^\circ \pm 0.9^\circ$	u_{2a}	$0.14 \pm 0.02 \text{\AA}$
d_{12}	$2.04 \pm 0.03 \text{\AA}$	u_{2b}	$0.14 \pm 0.03 \text{\AA}$
Δz_2	$-0.05 \pm 0.02 \text{\AA}$	u_{3a}	$0.12 \pm 0.02 \text{\AA}$
r_2	$2.83 \pm 0.03 \text{\AA}$	u_{3b}	$0.13 \pm 0.03 \text{\AA}$
Θ_2	$0.2^\circ \pm 0.5^\circ$	u_b	$0.12 \pm 0.03 \text{\AA}$
d_{23}	$1.98 \pm 0.03 \text{\AA}$	V_{im}	$4.1 \pm 1.0 \text{\AA}$
Δz_3	$+0.02 \pm 0.02 \text{\AA}$		
r_3	$2.84 \pm 0.04 \text{\AA}$		
Θ_3	$-0.2^\circ \pm 0.5^\circ$		
R-factor	0.068		

four Al atoms surrounding a Na atoms were immediately introduced. However, the rotation of the four Al atoms around the Na atom, which is also allowed by symmetry, was only introduced after DFT calculations by M. Borg had found such a relaxation to occur.

The four-fold rotational symmetry restricts the relaxations of the surface sublattices and makes it relevant to describe the structure in a right handed cylindrical coordinate system, with origo in the Na atoms (positive angles of rotation are for counter clockwise rotation). The structural variables considered were the Na-Al interlayer distance d_{01} , and the interlayer distances between the first three Al layers d_{12} and d_{23} . Rumpplings of the second and third Al layers Δz_2 and Δz_3 (sense of rumpling noted on Fig. 4.4) and the radial and angular positions $r_1, \Theta_1, r_2, \Theta_2, r_3$ and Θ_3 of Al atoms in the first three Al layers were also varied. $r_1 = 2.85\text{\AA}$ and $\Theta_1 = 0^\circ$ for the unrelaxed surface. Directions of layer relaxations can be inferred from Fig. 4.4. The results of the structural analysis for $\text{Al}(100)-(\sqrt{5} \times \sqrt{5})R27^\circ\text{-Na}$ with Na adsorbed in substitutional sites are listed in Table 4.3. Plots of experimental $I(V)$ spectra and spectra calculated for the optimum parameter values given in Table 4.3 are shown in Fig. 4.5.

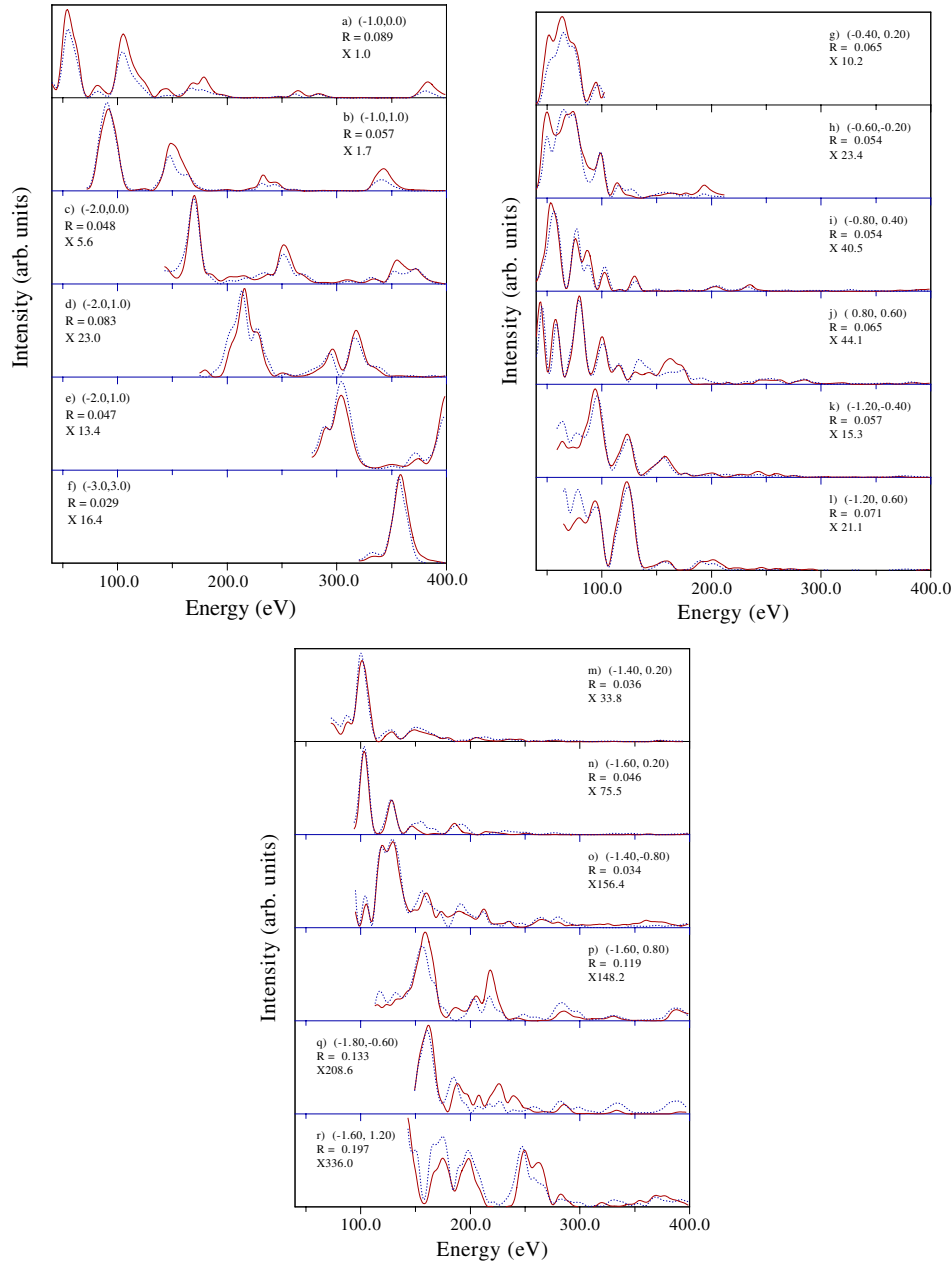


Figure 4.5: Comparison of experimental (solid lines) and calculated (dotted lines) intensity-energy spectra for $\text{Al}(100)-(\sqrt{5} \times \sqrt{5})R27^\circ\text{-Na}$ at $\theta = 0^\circ$ for 6 integral-order beams, a)-f), and 12 fractional order beams, g)-r). The beam hk indices, R factors, and scale factors are shown in each panel. The calculated spectra were obtained using the best-fit parameter values given in table 4.3.

Table 4.4: Comparison of LEED measurements with DFT calculations, changes in substrate structural parameters are given with respect to an unrelaxed Al(110) substrate. Results of DFT calculations are shown for Na in the substitutional $\sqrt{5}$ structure (DFT- $\sqrt{5}$ -Na) and for a hypothetical $\sqrt{5}$ vacancy structure (DFT- $\sqrt{5}$ -Vac).

	LEED	DFT- $\sqrt{5}$ -Na	DFT- $\sqrt{5}$ -Vac
Δz_{01}	$0.91 \pm 0.04 \text{ \AA}$	0.81 \AA	
Δr_1	$+0.19 \pm 0.03 \text{ \AA}$	$+0.23 \text{ \AA}$	$+0.12 \text{ \AA}$
$\Delta \Theta_1$	$-1.5^\circ \pm 0.9^\circ$	-1.7°	-1.0°
Δd_2	$-0.05 \pm 0.02 \text{ \AA}$	-0.07 \AA	-0.08 \AA
Δr_2	$-0.02 \pm 0.03 \text{ \AA}$	-0.06 \AA	-0.05 \AA
$\Delta \Theta_2$	$-0.2^\circ \pm 0.5^\circ$	-0.05°	-0.12°
Δd_3	$+0.02 \pm 0.02 \text{ \AA}$	$+0.03 \text{ \AA}$	
Δr_3	$-0.01 \pm 0.04 \text{ \AA}$	$+0.004 \text{ \AA}$	
$\Delta \Theta_3$	$+0.2^\circ \pm 0.5^\circ$	-0.4°	
R-factor/ E_{ads}	0.068	-1.533eV	

4.3.2 Theoretical calculations and discussion

Following the initial LEED analysis, ab-initio total-energy DFT calculations[149] with a plane-wave basis set and norm-conserving pseudopotentials[150] were performed by M. Borg to determine the structure of lowest energy. This involved calculating the total energies of slabs consisting of 9 layers. For the top layer a substitutional Al/Na layer, a Al layer vacancy layer and a chemisorbed Na layer in on top position on Al(100) were considered, all three structures with a $(\sqrt{5} \times \sqrt{5})R27^\circ$ unit cell. A cut-off energy of 13 Ry and 36 k-points in the irreducible wedge of the Brillouin zone (distributed in accordance with the Monkhorst-Pack scheme[151]) was found sufficient for convergence of the total energy. The exchange-correlation functional was described by a generalized gradient approximation[152]. The total energy was optimized with respect to relaxations of all parameters allowed within the $(\sqrt{5} \times \sqrt{5})R27^\circ$ unit cell in a four-fold rotational symmetry.

From Table 4.4 it can be seen that LEED and DFT results for the Al(100)- $(\sqrt{5} \times \sqrt{5})R27^\circ$ -Na structure agree on a quantitative level. However it is important to note that DFT calculations can not definitively distinguish between substitutional adsorption and chemisorption, as the energy difference is only 0.008eV in favor of the substitutional structure, which is below the estimated precision of the calculation. Plots of the valence electron density are shown on Fig. 4.6. As can be seen from Fig. 4.6c, electron charge is build up in between the Al atoms, by just introducing a vacancy. The charge build up is essentially just increased by the introduction of Na, as seen on Fig. 4.6b. Thus Na seems to donate much of its valence charge to the surface, in good agreement with the Langmuir-Gurney

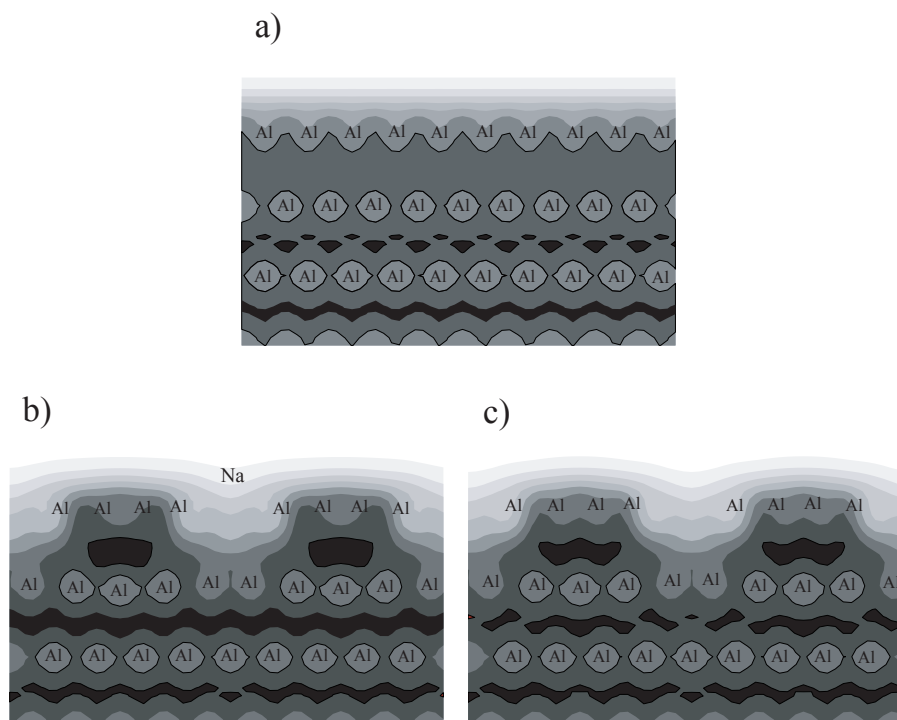


Figure 4.6: Electron density projection of a) the clean $\text{Al}(100)$ surface, b) the $\text{Al}(100)-(\sqrt{5} \times \sqrt{5})R27^\circ\text{-Na}$ and c) a hypothetical $\text{Al}(100)-(\sqrt{5} \times \sqrt{5})R27^\circ$ vacancy structure, respectively. The horizontal direction on the plot is parallel to the surface, while vertical direction is perpendicular to the surface. Note that the electron density has been integrated in the $[100]$ direction giving the appearance of a cubic structure. Atom positions are indicated on the plot, due to the projection along the $[100]$ direction not all atoms are in the same plane parallel to the paper. Black denotes the area of highest electron density, while white denotes the areas of lowest density on the plot.

picture of alkali adsorption.

While the $(\sqrt{5} \times \sqrt{5})R27^\circ$ structure might seem a bit exotic, at least two other substitutional $(\sqrt{5} \times \sqrt{5})R27^\circ$ structure are known, namely $\text{Al}(100)-(\sqrt{5} \times \sqrt{5})R27^\circ\text{-Yb}$ [153] and $\text{Cu}(100)-(\sqrt{5} \times \sqrt{5})R27^\circ\text{-Mg+K}$ [154] (Mg atoms in substitutional sites, K atoms in fourfold hollow sites). Comparison of the structural parameters for these three structures are shown in table 4.5, and the similarities are striking. All three structures exhibit rotations and lateral relaxations in the same directions. From DFT calculations it has further been found that also a pure vacancy $\text{Al}(100)-(\sqrt{5} \times \sqrt{5})R27^\circ$ structure exhibits such relaxations, as is also shown in Table 4.4.

Table 4.5: Cylindrical atomic coordinates (r, Θ, z) determined for the substitutional Al(100)-($\sqrt{5} \times \sqrt{5}$)R27-Na, Al(100)-($\sqrt{5} \times \sqrt{5}$)R27-Yb, Cu(100)-($\sqrt{5} \times \sqrt{5}$)R27-Mg/K structures. The x-y axis lies in the surface plane.

	Al(100)- $\sqrt{5}$ -Na	Al(100)- $\sqrt{5}$ -Yb	Cu(100)- $\sqrt{5}$ -Mg/K
Δz_{01}	$0.91 \pm 0.04 \text{ \AA}$	$0.37 \pm 0.04 \text{ \AA}$	$0.44 \pm 0.05 \text{ \AA}$
r_1	$3.04 \pm 0.03 \text{ \AA}$	$3.36 \pm 0.1 \text{ \AA}$	$2.66 \pm 0.07 \text{ \AA}$
Θ_1	$1.5^\circ \pm 0.9^\circ$	$4.3^\circ \pm 1.7^\circ$	$1.1^\circ \pm 0.4^\circ$

4.3.3 HRCLS and LEED measurements of the order/disorder phase transition

LEED pattern observations were made in the temperature range of 100K to 300K, and it was found that the phase-transition takes place in the narrow temperature range of 245K-215K. To gather further information about the phase transition, HRCLS spectra were measured at beamline I311 at MAX-Lab, as a function of temperature in the neighborhood of the phase transition. Core-level spectra measured at T=100K and at T=260K, which is below and above the transition temperature of the ($\sqrt{5} \times \sqrt{5}$)R27°-Na phase, are shown in Fig. 4.7b and c respectively. Spectra of the clean Al(100) surface is shown in Fig. 4.7a for comparison. Spectra shown here were obtained using a photon energy of 133eV.

For the clean surface, analysis of the spectrum, reveals the presence of two spin-orbit doublets, with $2p_{3/2}$ component of the major doublet due to emission from bulk Al atoms at a binding energy of 72.72 eV and $2p_{3/2}$ component of the minor component due to emission from surface Al atoms shifted by 92 meV to lower binding energy. The spin-orbit splitting is 410 ± 5 meV for each doublet. The FWHM of the bulk components are found to be 61 meV, while the surface components have a FWHM of 98 meV. The spectrum for the ($\sqrt{5} \times \sqrt{5}$)R27°-Na phase at T=100K shown in Fig. 4.7b show three individual doublets, the bulk component, a component shifted 196 meV to lower binding energy, and a poorly resolved component shifted 67meV meV also to lower binding energy. Finally the spectrum measured at 260K, above the ($\sqrt{5} \times \sqrt{5}$)R27°-Na phase transition, contains (at least) three poorly resolved components, the bulk component and components shifted 191 meV and 71 meV to lower binding energy.

In an attempt to understand the core-level measurements, DFT calculations were made by M. Borg of the core-level shifts for both substitutional and chemisorbed structures. As can be seen from Table 4.6 chemical shifts obtained from the experimental Al2p core-level spectra of the Al(100)-($\sqrt{5} \times \sqrt{5}$)R27°-Na structure measured at 100K, match the shifts found by DFT calculations for the substitutional structure. From comparison of Fig. 4.7b and c it is seen that for a temperature of 260K, where the ($\sqrt{5} \times \sqrt{5}$)R27° is gone, the same peaks are probably present,

Table 4.6: Experimentally determined positions (with respect to the bulk component) of the peaks resolved in the $\text{Al}2p$ spectra of the $\text{Al}(100)-(\sqrt{5} \times \sqrt{5})\text{-Na}$ phase at $T=100\text{K}$ and the disordered structure at $T=260\text{K}$. Note that in each Al layer, two inequivalent types of Al atoms can exist, with relative concentration of 1:4. For the first Al layer in the substitutional structure the 1/5ML Al atoms have been substituted by the 1/5ML Na atoms.

	HRLCS T=100K	HRCLS T=260K	DFT-Subst.	DFT-Chem.
$\text{Al}_{1/5}$				-73.3 meV
$\text{Al}_{4/5}$	-196 meV	-191 meV	-192.8 meV	-52.8 meV
$\text{Al}_{1/5}$	-67 meV	-71 meV	-61.3 meV	+40.1 meV
$\text{Al}_{4/5}$	-67 meV	-71 meV	-20.2 meV	+64.4 meV

except that all peaks are considerably broadened.

The $(\sqrt{5} \times \sqrt{5})R27^\circ$ structure can be lifted in (at least) two different ways. Since DFT calculations indicated that substitutional adsorption and chemisorption are almost equally energetically favorable, some of the substitutionally adsorbed Na atoms could become chemisorbed, leading to a disordered array of chemisorbed and substitutionally adsorbed Na atoms. Another possibility is that the Na atoms remain substitutional, but a 2D surface melting of the $(\sqrt{5} \times \sqrt{5})R27^\circ$ structure occurs, where the substitutional Na atoms become mobile.

DFT calculations for the core-level shifts of a hypothetical $(\sqrt{5} \times \sqrt{5})R27^\circ\text{-Na}$ chemisorption structure as shown in Table 4.6 indicate that only very small amounts of chemisorbed Na can be present on the surface, as the calculated shifts are quite incompatible with the experimental spectra on Fig. 4.7c. Chemisorbed Na should result in $\text{Al}2p$ components at higher energies than the Al bulk component and the first layer Al atoms should induce a component shifted only 73 meV to lower binding energy. The growth of such a peak should also result in the reduction of the component due to first layer Al atoms in a substitutional Na configuration.

The experimental spectrum in Fig. 4.7c is most readily explained by a simple 2D crystal/liquid phase-transition where the substitutional Na is still the dominant species in the disordered phase. However instead of being locked in the $(\sqrt{5} \times \sqrt{5})$ crystal structure, the substitutional Na atoms now move about randomly as in a liquid with an average distance quite similar to the distance found in the $(\sqrt{5} \times \sqrt{5})$ structure.

One also finds that the broadening of the -191meV peak of the Al atoms in the first layer is probably not only due to thermal broadening as it is considerably stronger than for the bulk peak. In fact the phase-transition can be monitored by plotting the FWHM of the -191meV peak divided by the FWHM of the bulk peak as a function of temperature, this has been done on Fig. 4.8. From Fig. 4.8 it can also be concluded that the phase-transition is probably a simple first order

transition.

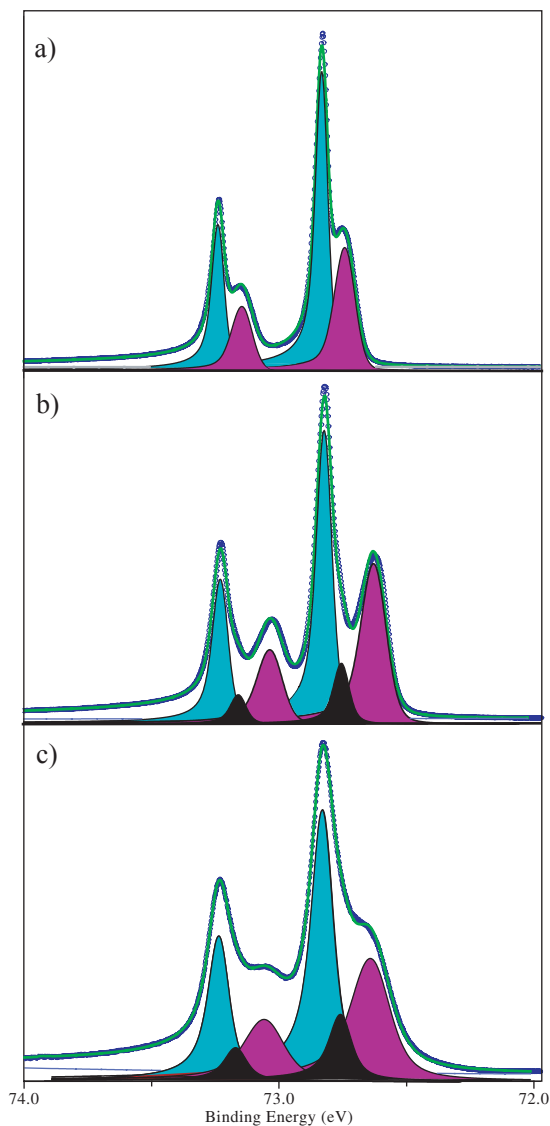


Figure 4.7: Al-2p core-level spectra. a) Clean Al(100). b) $\text{Al}(100)-(\sqrt{5} \times \sqrt{5})R27^\circ\text{-Na}$ (0.2ML Na, T=100K) c) $\text{Al}(100)-(1 \times 1)\text{-Na}$ (0.2ML Na, T=260K). The experimental measurements are shown as small circles. The line through the measurements is the fit to the data. Decomposition of the spectrum for the clean surface in a) indicates the presence of two spin-orbit doublets, corresponding to emission from Al atoms in the bulk (shaded light) and Al atoms in the surface layer. The spectra for $(\sqrt{5} \times \sqrt{5})\text{-Na}$ at T=100K and T=260K both contains the bulk doublet together with a doublet due to emission from Al atoms in the first, mixed Al/Na layer and a small peak due to Al atoms in the second layer.

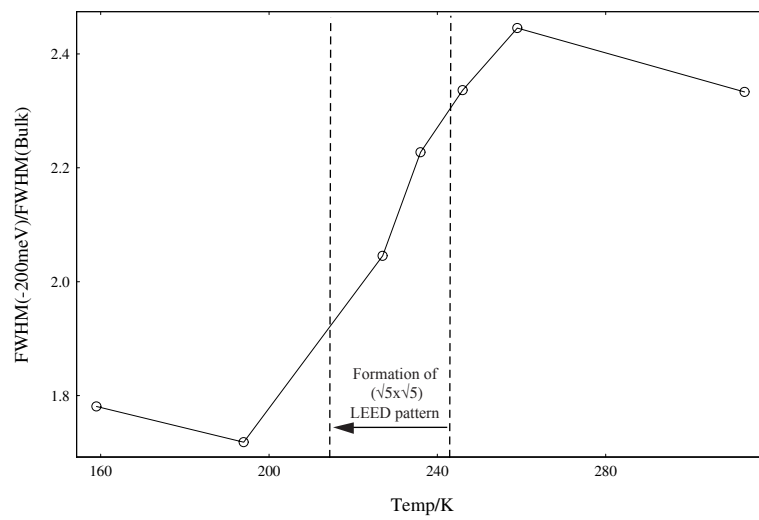


Figure 4.8: FWHM of the peak attributed to the first layer Al atoms in the Al2p spectra of the Al(100)-($\sqrt{5} \times \sqrt{5}$)R27°-Na divided by the FWHM of the bulk peak as a function of temperature across the phase transition

4.4 Structure of Al(110)-c(2 × 2)-Li

4.4.1 LEED measurements and structural analysis

Sharp $c(2 \times 2)$ LEED patterns with good contrast were obtained after deposition of 0.5ML Li at room temperature. $I(V)$ spectra were measured at $\theta = 0^\circ$ and $\theta = 10^\circ$ for a total of 57 symmetry-inequivalent beams (33 integral-order and 24 fractional-order).

The optimal geometry was found to contain Li atoms in 2-fold substitutional sites in a $c(2 \times 2)$ pattern. The structural variables consisted of the Li-Al interlayer spacing d_{01} , the first six interlayer spacings d_{ij} in the Al substrate, and the vertical displacements ('rumpling') Δr_3 and Δr_5 of atoms in the 3rd and the 5th Al layers from their bulk positions. For each of the two rumpled layers, the sense of the rumpling is that Al atoms lying on the axis through adsorbed Na atoms move towards the surface and Al atoms in the second $c(2 \times 2)$ sublattice move towards the bulk, as shown in Fig. 4.9b.

The results of the independent structural refinements for $\theta = 0^\circ$ and at $\theta = 10^\circ$ are listed in Table 4.7. A model of the substitutional $c(2 \times 2)$ -Li structure based on the structural parameters from Table 4.7 is shown in Fig 4.9. It should be noted that the uncertainty on d_{01} is substantially larger at normal incidence than off-normal incidence. This is indeed a bit surprising, however one could imagine that this is a case where one get a better sensitivity to the outmost structural parameters by changing the incidence angle away from normal incidence.

The main feature of the structure is that Li atoms occupy substitutional sites in a reconstructed Al layer. The Li-Al interlayer spacing is 0.38\AA , corresponding to a almost perfect Al-Li substitutional alloy. This can be explained by noting that the Li has a bulk hard-sphere radius of 1.52\AA compared to 1.43\AA for Al - a

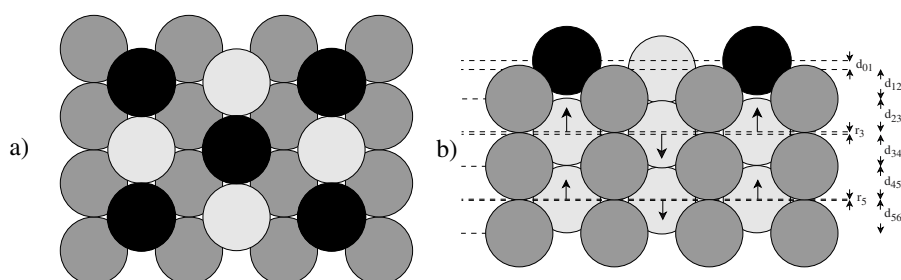


Figure 4.9: Hard-sphere model of the Al(110)- $c(2 \times 2)$ -Li structure as determined by LEED. a) top view. b) side view. Li atoms are shown in black. Al atoms in different layers are shown with different gray tones. Arrows in b) indicate the directions of the atomic displacements in the rumpled third and fifth Al layers.

Table 4.7: Best-fit parameter values for Li adsorbed in two-fold substitutional sites in the Al(110)-c(2 × 2)-Li structure. The interlayer spacings are denoted d_{ij} and the rms vibrational amplitudes are denoted u_j , where the subscripts indicate the layers in question. d_{01} is the spacing between the adsorbed Li layer and the first Al layer and u_0 is the vibrational amplitude of adsorbed Li atoms. The third and fifth Al layers are split into bilayers with vertical splittings denoted by Δr_3 and Δr_5 . Note that the interlayer spacings d_{ij} are given with respect to the outer surfaces of the bilayers.

	$\theta = 0^\circ$	$\theta = 10^\circ$	weighted average
d_{01}	$0.54 \pm 0.2 \text{ \AA}$	$0.37 \pm 0.07 \text{ \AA}$	$0.38 \pm 0.07 \text{ \AA}$
d_{12}	$1.25 \pm 0.02 \text{ \AA}$	$1.25 \pm 0.02 \text{ \AA}$	$1.25 \pm 0.01 \text{ \AA}$
d_{23}	$1.39 \pm 0.02 \text{ \AA}$	$1.40 \pm 0.02 \text{ \AA}$	$1.39 \pm 0.02 \text{ \AA}$
d_{34}	$1.36 \pm 0.03 \text{ \AA}$	$1.35 \pm 0.02 \text{ \AA}$	$1.36 \pm 0.02 \text{ \AA}$
d_{45}	$1.40 \pm 0.03 \text{ \AA}$	$1.40 \pm 0.02 \text{ \AA}$	$1.40 \pm 0.02 \text{ \AA}$
d_{56}	$1.39 \pm 0.03 \text{ \AA}$	$1.40 \pm 0.03 \text{ \AA}$	$1.39 \pm 0.02 \text{ \AA}$
d_{67}	$1.42 \pm 0.04 \text{ \AA}$	$1.41 \pm 0.04 \text{ \AA}$	$1.42 \pm 0.03 \text{ \AA}$
Δr_3	$0.11 \pm 0.02 \text{ \AA}$	$0.11 \pm 0.02 \text{ \AA}$	$0.11 \pm 0.01 \text{ \AA}$
Δr_5	$0.05 \pm 0.03 \text{ \AA}$	$0.05 \pm 0.03 \text{ \AA}$	$0.05 \pm 0.02 \text{ \AA}$
u_0	$0.50 \pm 0.2 \text{ \AA}$	$0.28 \pm 0.1 \text{ \AA}$	$0.35 \pm 0.1 \text{ \AA}$
u_1	$0.18 \pm 0.03 \text{ \AA}$	$0.17 \pm 0.02 \text{ \AA}$	$0.17 \pm 0.02 \text{ \AA}$
u_2	$0.17 \pm 0.04 \text{ \AA}$	$0.15 \pm 0.03 \text{ \AA}$	$0.15 \pm 0.02 \text{ \AA}$
u_3	$0.13 \pm 0.02 \text{ \AA}$	$0.13 \pm 0.02 \text{ \AA}$	$0.13 \pm 0.02 \text{ \AA}$
u_4	$0.09 \pm 0.04 \text{ \AA}$	$0.08 \pm 0.03 \text{ \AA}$	$0.09 \pm 0.03 \text{ \AA}$
u_5	$0.11 \pm 0.04 \text{ \AA}$	$0.07 \pm 0.06 \text{ \AA}$	$0.10 \pm 0.03 \text{ \AA}$
u_{bulk}	$0.09 \pm 0.03 \text{ \AA}$	$0.10 \pm 0.04 \text{ \AA}$	$0.10 \pm 0.02 \text{ \AA}$
V_{im}	$4.2 \pm 0.7 \text{ eV}$	$3.9 \pm 0.7 \text{ eV}$	$4.1 \pm 0.5 \text{ eV}$
R	0.039	0.062	

difference of only 6% . A second notable feature of the structure is the rumpling of both the third and fifth Al layers of 0.11 \AA and 0.05 \AA , respectively.

Plots of some of the experimental I(V) spectra and spectra calculated for the optimum parameter values given in Table 4.10 are shown in Fig. 4.10.

4.4.2 Substitutional adsorption and Al-Li alloy formation

Substitutional adsorption of Li was also found for the Al(100)-c(2 × 2)-Li phase as described in section 4.2.3, where it was noted that the structure is essentially the same as that of the (100) plane of the bulk Al_3Li alloy. Thus it is interesting to consider if the structure of the Al(110)-c(2 × 2)-Li phase found here can be understood similarly. It turns out, however, that the (110) plane of Al_3Li would correspond to an Al(110)-(2 × 1)-Li structure. Nevertheless the present c(2 × 2) structure can be understood in terms of a hypothetical Al_3Li bulk alloy with an

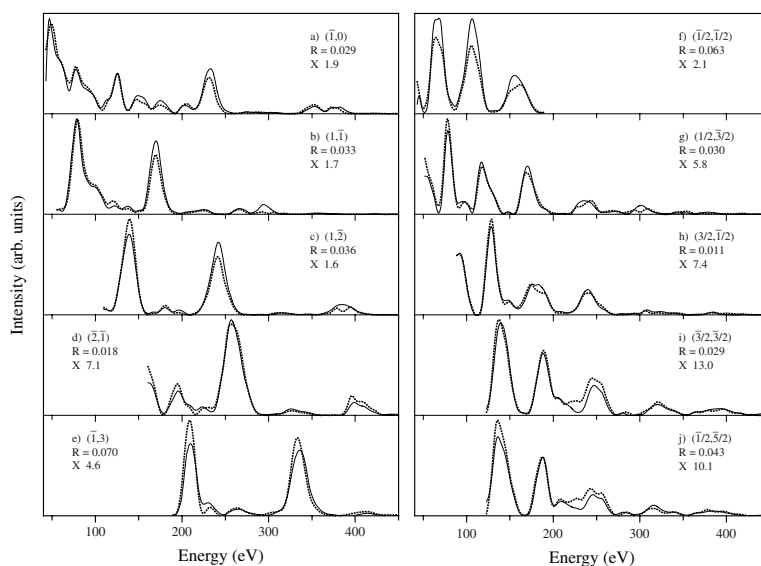


Figure 4.10: Comparison of experimental (solid lines) and calculated (dotted lines) I(V) spectra for Al(110)-c(2 × 2)-Li at $\theta = 0^\circ$ for 5 integral-order beams, a)-e), and 5 fractional order beams, f)-j). The beam hk indices, R factors, and scale factors are shown in each panel. The calculated spectra were obtained using the best-fit parameter values given in Table 4.7 .

Al₃Ti-type structure, whose (110) plane *would* correspond to Al(110)-c(2 × 2)-Li. In Chapter 6 a quantitative LEED analysis of the Al(100)-c(2 × 2)-2Li phase formed by adsorption of Li at elevated temperature reveals the occurrence of a surface alloy with an Al₃Ti-type structure.

4.5 Structure of Al(110)-c(2 × 2)-Na

4.5.1 LEED measurements and structural analysis

The adsorption of 0.5ML Na on Al(110) at room temperature leads to the formation of a sharp c(2 × 2) LEED pattern. As will be discussed in some detail in chapter 7, adsorption of 0.65ML leads to the formation of a disordered (3 × 1) phase followed by a reasonable sharp (4 × 1) phase. The complete adsorption sequence can be followed in reverse order by adsorption of >0.8 ML followed by annealing to 340K, 390K, 410 K, for the (4 × 1), (3 × 1) and c(2 × 2) phases respectively. Desorption of all Na occurs at temperatures greater than 475 K resulting in the restoration of the original (1 × 1) LEED pattern. The method of annealing was used to prepare the c(2 × 2) phase for which LEED I(V) spectra are presented. I(V) spectra were measured for the c(2 × 2)-Na phase at normal incidence, $\theta = 0^\circ$, and $\theta = 10^\circ$. This led to a total of 57 symmetry-inequivalent

Table 4.8: Best-fit parameter values for Na adsorbed in the two-fold substitutional site in the Al(110)-c(2 × 2)-Na structure. The interlayer spacings are denoted d_{ij} and the rms vibrational amplitudes are denoted u_j , where the subscripts indicate the layers in question.

Phase	Clean Al(110)	Al(110)-c(2 × 2)-Na		
Incidence angle	$\theta = 0^\circ$	$\theta = 0^\circ$	$\theta = 10^\circ$	Average
d_{01}		$1.06 \pm 0.03 \text{ \AA}$	$1.05 \pm 0.03 \text{ \AA}$	$1.06 \pm 0.02 \text{ \AA}$
d_{12}	$1.31 \pm 0.03 \text{ \AA}$	$1.28 \pm 0.02 \text{ \AA}$	$1.25 \pm 0.02 \text{ \AA}$	$1.27 \pm 0.01 \text{ \AA}$
d_{23}	$1.51 \pm 0.03 \text{ \AA}$	$1.35 \pm 0.03 \text{ \AA}$	$1.37 \pm 0.03 \text{ \AA}$	$1.36 \pm 0.02 \text{ \AA}$
d_{34}	$1.37 \pm 0.03 \text{ \AA}$	$1.36 \pm 0.03 \text{ \AA}$	$1.35 \pm 0.03 \text{ \AA}$	$1.36 \pm 0.02 \text{ \AA}$
d_{45}	$1.44 \pm 0.02 \text{ \AA}$	$1.38 \pm 0.03 \text{ \AA}$	$1.38 \pm 0.03 \text{ \AA}$	$1.38 \pm 0.02 \text{ \AA}$
d_{56}		$1.40 \pm 0.03 \text{ \AA}$	$1.40 \pm 0.05 \text{ \AA}$	$1.40 \pm 0.03 \text{ \AA}$
d_{67}		$1.42 \pm 0.04 \text{ \AA}$	$1.41 \pm 0.06 \text{ \AA}$	$1.42 \pm 0.03 \text{ \AA}$
Δr_3		$0.15 \pm 0.03 \text{ \AA}$	$0.14 \pm 0.02 \text{ \AA}$	$0.14 \pm 0.02 \text{ \AA}$
Δr_5		$0.06 \pm 0.04 \text{ \AA}$	$0.05 \pm 0.05 \text{ \AA}$	$0.06 \pm 0.03 \text{ \AA}$
u_0		$0.27 \pm 0.04 \text{ \AA}$	$0.27 \pm 0.03 \text{ \AA}$	$0.27 \pm 0.02 \text{ \AA}$
u_1	$0.17 \pm 0.04 \text{ \AA}$	$0.17 \pm 0.04 \text{ \AA}$	$0.17 \pm 0.03 \text{ \AA}$	$0.17 \pm 0.02 \text{ \AA}$
u_2	$0.17 \pm 0.08 \text{ \AA}$	$0.13 \pm 0.04 \text{ \AA}$	$0.13 \pm 0.03 \text{ \AA}$	$0.13 \pm 0.02 \text{ \AA}$
u_{3A}	$0.13 \pm 0.04 \text{ \AA}$	$0.17 \pm 0.04 \text{ \AA}$	$0.14 \pm 0.04 \text{ \AA}$	$0.16 \pm 0.03 \text{ \AA}$
u_{3B}	$0.13 \pm 0.04 \text{ \AA}$	$0.11 \pm 0.04 \text{ \AA}$	$0.09 \pm 0.04 \text{ \AA}$	$0.10 \pm 0.03 \text{ \AA}$
u_4		$0.10 \pm 0.04 \text{ \AA}$	$0.10 \pm 0.04 \text{ \AA}$	$0.10 \pm 0.03 \text{ \AA}$
u_5		$0.11 \pm 0.04 \text{ \AA}$	$0.10 \pm 0.04 \text{ \AA}$	$0.10 \pm 0.03 \text{ \AA}$
u_{bulk}	$0.06 \pm 0.02 \text{ \AA}$	$0.10 \pm 0.04 \text{ \AA}$	$0.15 \pm 0.10 \text{ \AA}$	$0.11 \pm 0.04 \text{ \AA}$
V_{im}	$5.1 \pm 0.7 \text{ eV}$	$4.1 \pm 0.6 \text{ eV}$	$3.2 \pm 0.5 \text{ eV}$	$3.7 \pm 0.4 \text{ eV}$
$R_{\text{exp-theory}}$	0.039	0.045	0.042	

beams (33 integral-order and 24 fractional-order).

The optimal geometry was found to consist of Na atoms adsorbed in 2-fold substitutional sites. A full optimization of the fit between experimental intensities and intensities calculated for this model was carried out. The structural variables consisted of the first seven interlayer spacings d_{ij} and a rumpling Δr_3 and Δr_5 of the 3rd and the 5th Al layers. For each of the two rumpled layers, the sense of the rumpling is that Al atoms lying on the rotation axis through adsorbed Na atoms move towards the surface and Al atoms in the second $c(2 \times 2)$ sublattice move towards the bulk, as shown in Fig. 4.11b. Plots of some of the experimental I(V) spectra and spectra calculated for the optimum parameter values given in Table 4.8 are shown in Figs. 4.12 and 4.13. A model of the substitutional $c(2 \times 2)$ -Na structure constructed using the average values of the structural parameters from the two independent analysis is shown in Fig. 4.11.

The results of the independent refinements for measurements at $\theta = 0^\circ$ and $\theta = 10^\circ$ are listed in Table 4.8, together with the results of the recent LEED analysis for the clean Al(110) surface, found in chapter 3. The main feature of the structure is that Na atoms occupy substitutional sites in a reconstructed Al layer. The Na-Al interlayer spacing is 1.06\AA , corresponding to a hard-sphere radius of 1.62\AA for the adsorbed Na atoms, as compared to the bulk bcc radius of 1.86\AA . A second notable feature of the structure is the large rumpling of the third and fifth Al layers of 0.14\AA and 0.06\AA , respectively.

Separate vibrational amplitudes u_{3a} and u_{3b} were assigned to Al atoms in the two sublattices of the third, rumpled Al layer, where u_{3a} are the amplitudes for Al atoms directly beneath Na atoms. One can observe that the enhanced vibrational amplitudes of the surface layers of the clean Al(110) surface are preserved on adsorption (see table 4.8), as found previously for other alkali/Al adsorption systems [86]. It can also be noted that the vibrational amplitudes of Al atoms in the two

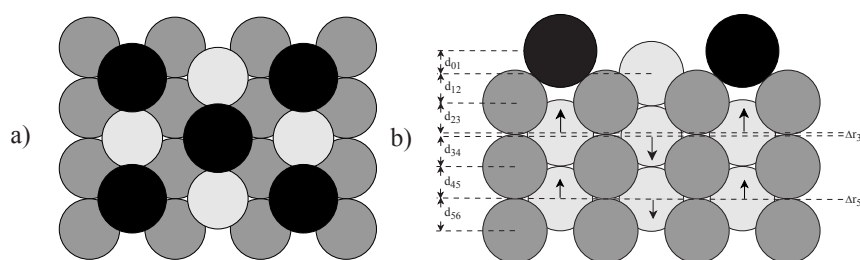


Figure 4.11: Hard-sphere model of the geometry of the Al(110)- $c(2 \times 2)$ -Na structure. a) topview, shown as a projection on the (110) plane; b) sideview, shown as a projection on the $(1\bar{1}0)$ plane. The shading indicates atoms lying in the same planes perpendicular to the plane of the drawings. Black circles indicate the position of Na atoms. Arrows in b) indicate the sense of the rumpling of the third and fifth Al layers. See text.

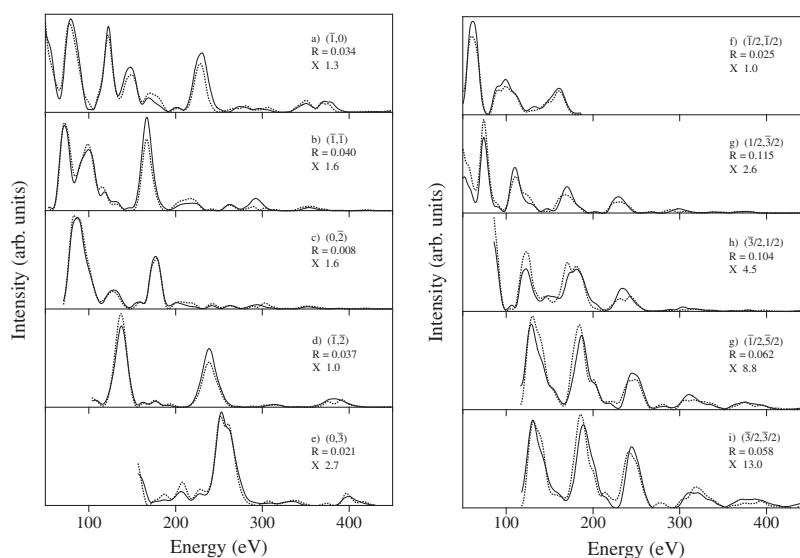


Figure 4.12: Comparison of experimental (solid lines) and calculated (dotted lines) intensity-energy spectra for Al(110)- $c(2 \times 2)$ -Na at $\theta = 0^\circ$ for 5 integral-order beams, a-e), and 5 fractional order beams, f-j). The beam hk indices, R factors, and scale factors are shown in each panel. The calculated spectra were obtained using the best-fit parameter values given in Table 4.8.

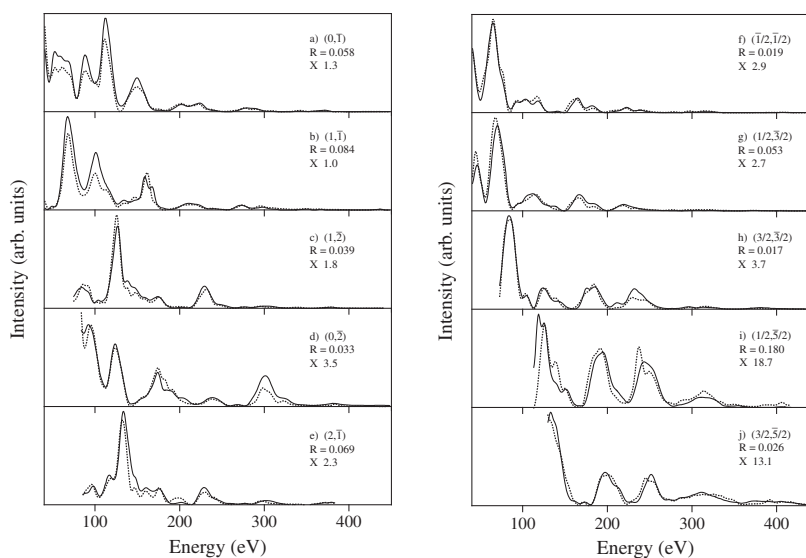


Figure 4.13: Comparison of experimental (solid lines) and calculated (dotted lines) intensity-energy spectra for Al(110)- $c(2 \times 2)$ -Na at $\theta = 10^\circ$ for 5 integral-order beams, a-e), and 5 fractional order beams, f-j). The beam hk indices, R factors, and scale factors are shown in each panel. The calculated spectra were obtained using the best-fit parameter values given in Table 4.8.

sublattices of the ruffled third Al layer differ significantly. The vibrational amplitudes of Al atoms directly beneath Na atoms are enhanced with respect to the remaining Al atoms of this layer.

4.6 Comparison of the $c(2 \times 2)$ Na and Li structures on Al(110)

The results presented here show that the stable binding geometry for 0.5 ML Li or Na adsorbed on Al(110) involves alkali atoms adsorbed in substitutional sites formed by displacement of 0.5 ML Al atoms from the first layer of the substrate. The possibility that the Al atoms displaced by alkali atoms in various substitutional structures are re-adsorbed in high symmetry sites was investigated, but found to be incompatible with the measured intensities. It is assumed, therefore as discussed in previous work for Al(111)[8], that the displaced Al atoms are re-adsorbed at surface steps.

The 0.5ML Li and Na structures on Al(110) are very similar as was also the case for Li and Na on Al(111) and Al(100) for coverages of 0.33ML and 0.5ML respectively. Similar structural features found for Li and Na on Al(110), include the large contraction of the first interlayer spacing and the strong rumpling of the third layer of the substrate.

The adsorption of Na or Li on Al(110) appears to fit the pattern of previous results for the adsorption of alkali metals on Al, rather than the pattern of formation of (1×2) missing row structures as found for adsorption of low coverages of alkali metals on other fcc(110) metal surfaces. In discussing possible reasons for the formation of the substitutional $c(2 \times 2)$ structure, rather than a missing-row structure, it can be noted that the former process can be thought of as occurring in two steps, in which an Al atom is removed from the surface and re-bonded at a surface step, followed by adsorption of a Na or Li atom in the vacancy. Similarly, the latter process can be thought of as a reconstruction of the (1×1) surface to a (1×2) missing-row structure, followed by adsorption of alkali atoms in sites in the troughs of the missing rows. Ab initio[155] calculations of vacancy formation, and effective-medium calculations[144] of the reconstruction energy of the Al(110) surface, indicate that these energies are roughly equal with value of ~ 0.12 eV. This suggests that the energy required for reconstruction of the substrate is not the deciding factor in the choice of adsorption site. It is therefore presumed that the adsorption energy in the substitutional site is larger than the adsorption energy in sites in the troughs of the missing-row structure. In this regard it is interesting to note that the Al(110)- $c(2 \times 2)$ -Na and Al(110)- $c(2 \times 2)$ -Li structures determined here are almost identical to the Au(110)- $c(2 \times 2)$ -K struc-

ture proposed by Ho et al[23] on the basis of ab initio calculations, and later confirmed by an ion-scattering study[156]. Ho et al suggested that K atoms adsorb in the troughs of the intrinsic missing-row structure at low coverage, but form a structure of the kind shown in Fig. 4.11 at higher coverage, in order to minimize the large electrostatic energy associated with K ions sitting in adjacent sites in the missing rows. Ho et al noted further that the fact that Au forms bulk alloys with K suggests that formation of a surface alloy might be energetically feasible. In the light of the present results it is interesting to speculate that the substitutional $c(2 \times 2)$ structure, as formed on Au and Al(110), might in fact be the configuration of lowest energy for the fcc(110) metals that form missing-row structures on adsorption of alkali metals, but that its formation is hindered by an activation energy barrier, which can be overcome at room temperature on Al and Au. In detail, of course, the mechanisms of formations of the Al(110)- $c(2 \times 2)$ -Na/Li and Au(110)- $c(2 \times 2)$ -K structures must be different, in that the formation of the former requires displacement and re-adsorption of 0.5 ML Al atoms, whereas formation of the latter structure requires only a place exchange of Au and K atoms.

4.7 Evolution of the surface structure with Li and Na coverage on Al(110)

4.7.1 CLS reference spectra

The knowledge of the structures of the clean surface and the 0.5ML $c(2 \times 2)$ -Li and $c(2 \times 2)$ -Na phases are used as a basis for interpretation of the corresponding CLS measurements. This in turn enables conclusions to be drawn from CLS measurements concerning the nature of the adsorbed Li and Na phases at coverages less (or greater) than 0.5 ML.

Al-2p core-level spectra measured at 120 K for the clean Al(110) surface, for the $c(2 \times 2)$ -Li phase formed by adsorption of 0.5 ML Li at room temperature and for the $c(2 \times 2)$ -Na phase formed by adsorption of 0.5 ML Na at room temperature are shown in Figs. 4.14a, b and c respectively. Measurements of the Al-2p, the Li-1s and the Na-2p core levels were made at photon energies of 102eV, 132eV and 112eV respectively. All CLS measurements presented in this section were performed at the SGM1 beamline at the storage ring ASTRID.

For the clean surface, analysis of the spectrum, as described in section 2.4.3, reveals the presence of two poorly-resolved spin-orbit doublets, with $2p_{3/2}$ component of the major doublet due to emission from bulk Al atoms at a binding energy of 72.72 eV and $2p_{3/2}$ component of the minor component due to emission from surface Al atoms shifted by 80 meV to lower binding energy. The spin-orbit

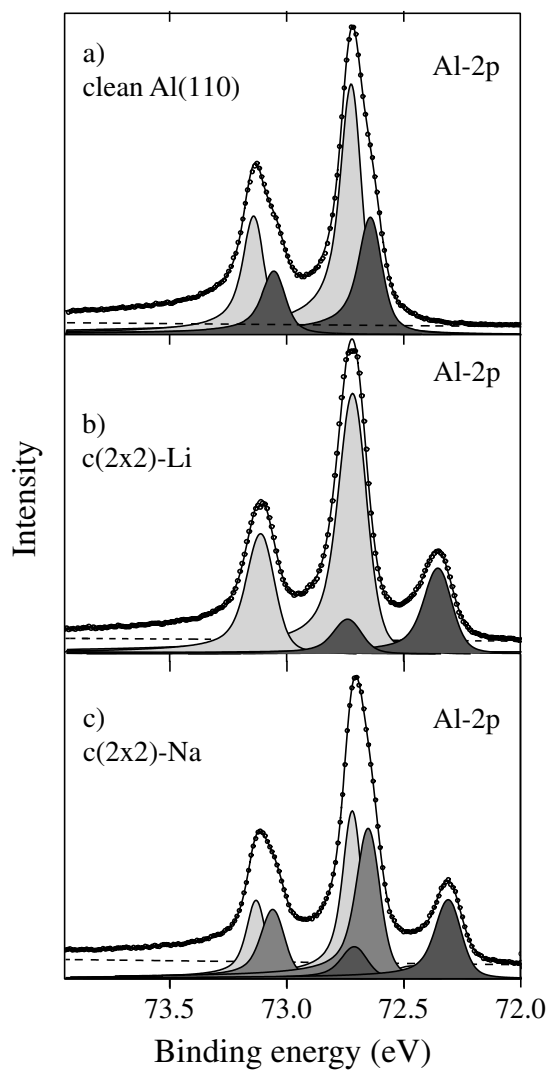


Figure 4.14: Al-2p core-level spectra measured at 120 K. a) clean Al(110). b) $c(2 \times 2)$ -Li. c) $c(2 \times 2)$ -Na. The experimental measurements are shown as small circles. The line through the measurements is the fit to the data. Decomposition of the spectrum for the clean surface in a) indicates the presence of two spin-orbit doublets, corresponding to emission from Al atoms in the bulk (shaded light) and Al atoms in the surface layer. The spectra for $c(2 \times 2)$ -Li and $c(2 \times 2)$ -Na both contains the bulk doublet together with a doublet due to emission from Al atoms in the first, mixed Al/alkali layer. In the $c(2 \times 2)$ -Na spectrum a peak derived from the second Al layer can additionally be resolved.

splitting is 410 meV for each doublet. The spectrum for the $c(2 \times 2)$ -Li phase shown in Fig. 4.14b also contains two spin-orbit doublets with splitting 410 meV, but the surface shift at 80 meV in the spectrum of the clean surface has been replaced by a doublet shifted by 380 meV to lower binding energy. The spectrum for the $c(2 \times 2)$ -Na phase shown in Fig. 4.14c show three individual doublets, the bulk component, and components shifted 402 meV and 73meV meV to lower binding energy.

As described in section 4.4 and section 4.5, LEED analysis of the $c(2 \times 2)$ - Li and $c(2 \times 2)$ - Na phases indicates that they consists of a single type of Li or Na atom adsorbed in two-fold substitutional sites, formed by displacement of 0.5 ML Al atoms from the first layer of the substrate. Accordingly, the structure contains three (counting nearest and next-nearest neighbors) types of Al atoms, namely Al atoms in the first mixed Al/alkali layer, Al atoms in the second layer and Al atoms in the bulk. Thus the second spin-orbit doublet in the Al/Li spectrum of Fig. 4.14b can be interpreted simply as due to the 0.5 ML Al atoms in the mixed Al/Li layer. The fact that the intensity of the second doublet is roughly half that of the surface peak of the clean surface is consistent with this interpretation. The fact that no peak of the second layer can be resolved only indicates that this peak probably lies closer than 50meV to the bulk component. In a similar fashion the spin-orbit doublet in Al/Na the spectrum of Fig. 4.14c shifted by 402meV can be interpreted simply as due to Al atoms in the mixed Al/Na layer, while the doublet shifted 73meV can be attributed to Al atoms in the second layer which have had some of their Al next-nearest neighbors in the top layer substituted for Na. The intensity of the Al/Na layer Al peak is approximately $\frac{1}{2}$ of the intensity of the surface peak of the clean surface also in keeping with the suggested interpretation.

The corresponding Li-1s spectra for the $c(2 \times 2)$ -Li phase, shown in Fig. 4.16b, contains single peaks at 55.54 eV consistent with the occurrence of a single type of alkali atom in the $c(2 \times 2)$ phase. The Na-2p spectra, as shown in Fig. 4.17b, also contain a single broad peak at 30.82 eV indicating the occurrence of a single type of Na. The peak can in fact be fitted with a poorly-resolved spin-orbit doublet, with splitting of 160 ± 10 meV, in agreement with a previous study of Na(110) films[157].

4.7.2 Evolution of the surface structure with Li and Na coverage

The evolution of the surface structure with Li and Na coverage was studied by correlated measurements of the LEED pattern and Li-1s, Na-2p and Al-2p core-level spectra. In the following, the sequence of observed LEED patterns is first described, then the corresponding evolution of the CLS spectra is discussed.

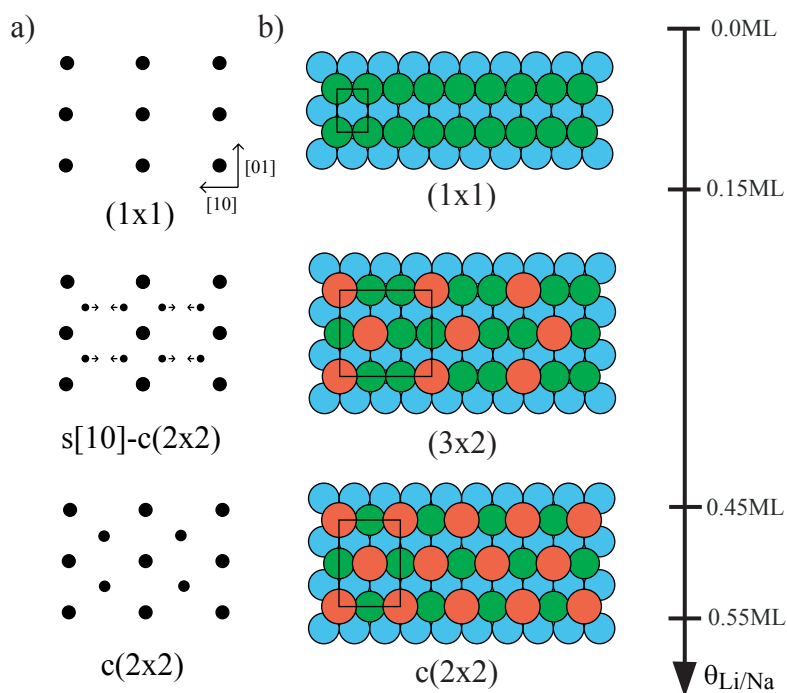


Figure 4.15: a) LEED patterns observed for adsorption of 0-0.5ML Li or Na. b) Real space structures as a function of coverage 0-0.5ML of Li or Na, deduced from LEED and CLS (See text).

LEED patterns

The development of the LEED pattern as a function of coverage is essentially identical for the adsorption of Li and Na on Al(110) in the 0-0.5ML coverage regime. The LEED pattern sequence as a function of coverage of Li or Na is shown schematically in Fig. 4.15a.

At about 0.15ML, the (1×1) pattern of the clean surface begins to be superseded by a very weak $c(2 \times 2)$ pattern in which the fractional-order spots are split along the $[1\bar{1}0]$ direction, but are not noticeably broader than the integral-order spots. The splitting between the spots is about one third of a reciprocal lattice vector in the $[1\bar{1}0]$ direction and remains unchanged until about 0.33 ML coverage, after which the splitting decreases with increasing coverage to give a sharp $c(2 \times 2)$ pattern in a relatively narrow coverage range of 0.45-0.55 ML. The pattern indicates that the alkali structure has a well-ordered, double periodicity in the $[001]$ direction perpendicular to the close-packed rows in the coverage range 0.15-0.55 ML. At about 0.33 ML coverage, the pattern is consistent with the presence of anti-phase domain boundaries with a separation of about three lattice spacings along the close-packed rows in the $[1\bar{1}0]$ direction. The sharpness of the fractional order spots suggests that the domains are quite well ordered with respect

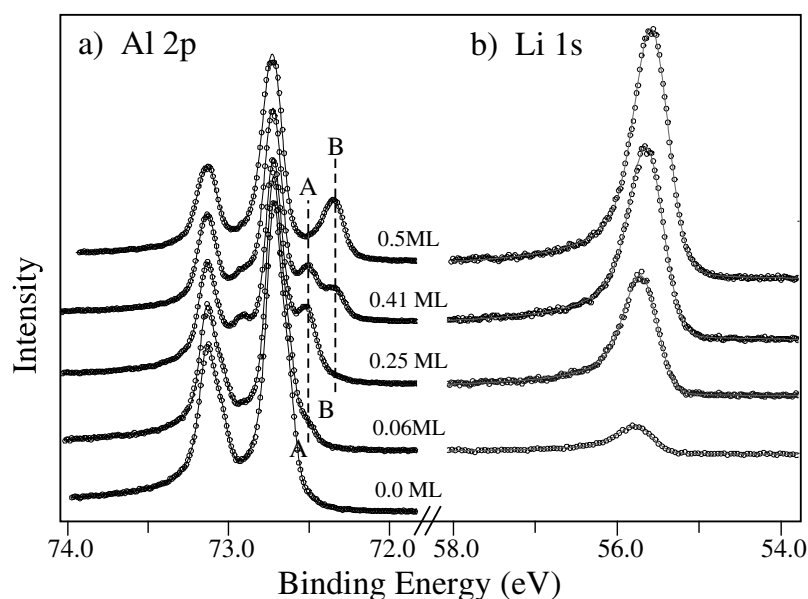


Figure 4.16: Core level spectra as a function of Li coverage after adsorption at room temperature. a) Al 2p. b) Li 1s.

to each other, so that the structure can essentially be regarded as a (3×2) phase, with two alkali atoms per unit cell forming a minimal $c(2 \times 2)$ basis, as shown in Fig. 4.15b. In other words, the structure consists of Al/alkali zig-zag lines two rows wide, separated in the $[1\bar{1}0]$ direction by a row of pure Al atoms. The structure factor associated with the presence of a second alkali atom in the unit cell, at coordinates of $(1/3, 1/2)$, leads to a three-fold increase in intensity of the (observed) $(1/3, 1/2)$ and $(2/3, 1/2)$ spots as compared to the (not observed) $(1/3, 0)$ and $(2/3, 0)$ spots, and largely accounts for the absence of the latter spots. The fact that the spot splitting is essentially unchanged in the coverage range of 0.15-0.33 ML, suggests that the (3×2) phase also forms as islands at coverages below 0.33 ML. At coverages in the range 0.33-0.45 ML, the decrease in spot splitting can be accounted for by an increasing distance between anti-phase boundaries due to growth of the $c(2 \times 2)$ domains in the $[1\bar{1}0]$ direction.

CLS measurements

The development of corresponding Li-1s and Al-2p core-level spectra as a function of Li coverage is illustrated in Fig. 4.16. The development of corresponding Na-2p and Al-2p core-level spectra as a function of Na coverage is illustrated in Fig. 4.17. In the coverage regime between 0.0ML and 0.5ML Li and Na CLS spectra develop quite similarly.

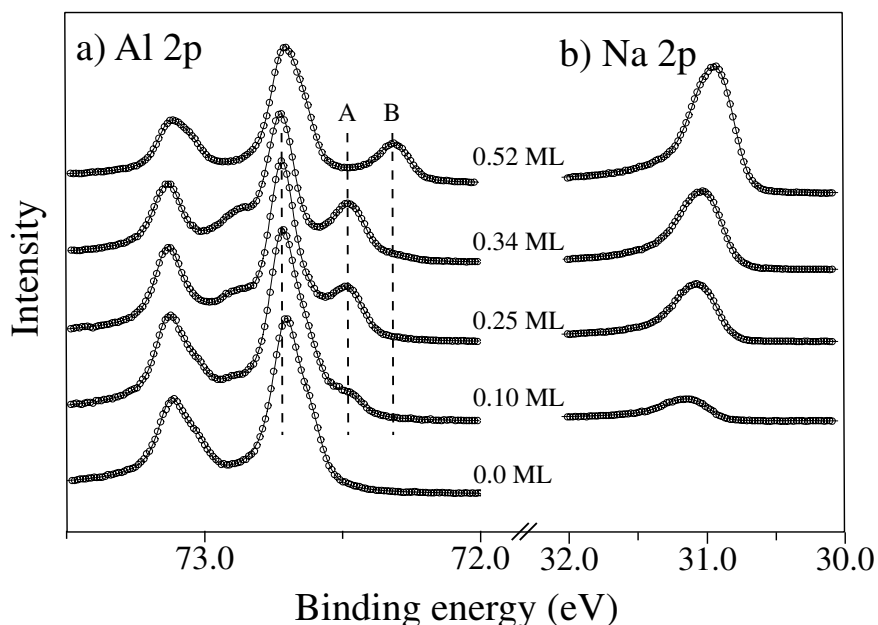


Figure 4.17: Core level spectra as a function of Na coverage after adsorption at room temperature. a) Al 2p. b) Na 2p.

At the lowest coverages, the Li-1s spectra contain a single broad peak at 55.72 eV with FWHM of 610 meV. The binding energy and FWHM of this peak decrease with coverage to 55.54 eV and 540 eV, respectively at 0.5 ML coverage. In the coverage range of 0-0.5 ML, the Al-2p spectra contain two new spin-orbit doublets, with $2p_{3/2}$ components marked as peaks A and B in Fig. 4.16a, with shifts in binding energy to lower energy of 210 meV and 385 meV, respectively, independent of coverage. As can be seen from the spectra in Fig. 4.16a, peak A is present at the lowest Li coverage, and increases with coverage before disappearing at 0.5 ML, whereas peak B first appears at coverages greater than about 0.2 ML.

The development of the CLS in the Na case is rather similar to the Li case. At the lowest coverages, the Na 2p spectra contain a single broad peak at a binding energy of 31.09 eV with a FWHM of 440 meV. The binding energy and FWHM of this peak decrease with coverage to 30.94 eV and 375 meV, respectively, at 0.5 ML coverage. In the coverage range of 0 to 0.5 ML, the Al-2p spectra contain two new spin-orbit doublets, with $2p_{3/2}$ components marked as peaks A and B in Fig. 4.17a, with shifts in binding energy to lower energy of 247 meV and 416 meV, respectively. As can be seen from the figure, peak A is present at the lowest Na coverage, but peak B appears only for coverages greater than about 0.3 ML. In contrast to the Li case a peak at 73 meV is visible at around a coverage of 0.5 ML,

which is approximately at the position of the original surface peak.

From the quantitative LEED analysis of the $c(2 \times 2)$ -Na phase, we know that this phase contains a single kind of Na atom, adsorbed in 2-fold substitutional sites. Thus it is natural to associate peak B with emission from Al atoms in the mixed Al/Na layer. The fact that the binding energy shift of peak A is roughly half that of peak B, and the fact that peak A develops at low coverages before the $c(2 \times 2)$ LEED pattern is first seen, makes it likely that peak A is associated with emission from Al atoms having a single Na nearest-neighbor in an isolated substitutional site, rather than two such neighbors as in the $c(2 \times 2)$ structure.

The most notable difference between the Li and Na CLS spectra is the presence of the second layer Al peak in Al-2p CLS spectra shifted 73meV at around 0.5ML Na indicating that the second layer Al atoms are more affected by the Na substitutional structure than the Li. This can be explained by noting that the alkali in some sense "makes up" for the presence of the vacancy by donating its valence electron to the surface Al atoms and as the Li atoms are positioned closer to the surface this effect is perhaps more pronounced for Li. The same effect can be seen for the first layer Al shift which is also larger for the Na structure. It is thus conceivable that the the alkali contributes little to the core-level shifts compared to the formation of a vacancy.

4.7.3 Summary and discussion

The combination of LEED pattern observations and core-level measurements suggests that the adsorption of Li and Na on Al(110) at low coverages is controlled by repulsive interactions between adsorbed Li atoms along the close-packed rows, and an attractive next-nearest-neighbor interaction perpendicular to the close-packed rows. At coverages below 0.15 ML, Al-2p spectra contain a shifted component (peak A in Fig. 4.16 and Fig. 4.17) which can be attributed to Al atoms with a single alkali nearest-neighbor in a substitutional site. The fact that this component continues to increase in intensity in the coverage range 0.15-0.33 ML where a $c(2 \times 2)$ LEED pattern with split spots is observed, suggests that the occupation by alkali atoms of next-nearest neighbor sites along the close-packed rows is still disfavored. The equivalent description of the LEED pattern as a (3×2) pattern with missing $(h/3,0)$ and $(2h/3,0)$ spots, suggests that the structure consists of single ziz-zag lines of alkali atoms along the $[001]$ direction, forming a minimal $c(2 \times 2)$ arrangement, and separated along the $[1\bar{1}0]$ direction by single rows of Al atoms. At coverages above 0.33 ML, peak A decreases because further adsorption of Li involves occupation of next-nearest-neighbor sites along the close-packed rows. Hence Al atoms acquire a second nearest-neighbor alkali atom. This is signalled by the growth of a second shifted component in Al-2p spectra (peak B in Fig. 4.17 and Fig. 4.16) which can be attributed to Al atoms

with two alkali nearest-neighbors in substitutional sites. The growth of peak B corresponds to the decrease in splitting of the spots in the $c(2 \times 2)$ LEED pattern. Both observations are consistent with the growth of larger $c(2 \times 2)$ domains. The fact that peak B is first observed at coverages below 0.33 ML suggests that some condensation of the zig-zag lines of alkali atoms into larger domains starts to occur at about 0.2 ML coverage.

Chapter 5

Substrate relaxation induced by superstructure formation

5.1 Introduction

For clean, unreconstructed surfaces, the loss of translational symmetry in the surface-normal direction leads to unbalanced forces on the layers of the unrelaxed surface, resulting in vertical and lateral displacements of surface layers[97, 98, 110, 158]. The reduction of translational symmetry parallel to the surface due to the occurrence of a superstructure, formed by reconstruction, adsorption or both, leads quite generally to reconstruction of the substrate. Although the occurrence of the different relaxation phenomena is a simple consequence of the reduction of symmetry due to the creation of a surface and to the occurrence of a superstructure, the details of the relaxations, for example, the question of whether a particular sublattice moves up or down, can only be answered by model calculations.

A considerable structural database of alkali adsorbate structures on aluminum is developing, and it could be interesting to look at some of the very general patterns in the relaxation and reconstruction of the aluminum substrates. As an example the layer rumplings and interlayer relaxations found for the Al(110)-c(2 × 2)-Na and Al(110)-c(2 × 2)-Li substitutional structures are listed in table 5.1. It is quickly realized that the primary reconstruction of the substrate due to adsorption of the alkali in two-fold substitutional sites is accompanied by a secondary reconstruction involving a rumpling of the third and even fifth layers. As can be seen from the table, the strong similarity between the two substitutional alkali structures also extends to the reconstruction and relaxation of the substrate. The similar Au(110)-c(2 × 2)-K two-fold substitutional structure is also listed in table 5.1, as it can be noted that the similarities in substrate relaxations also extends to

Table 5.1: Comparison of substrate reconstruction and intralayer relaxation for Al(110)-c(2 × 2)-Li, Al(110)-c(2 × 2)-Na, and Au(110)-c(2 × 2)-K. Relaxations Δd_{12} , Δd_{23} , Δd_{34} , and Δd_{45} of the first four interlayer spacings are expressed as % deviations from the corresponding bulk values. The interlayer spacings involving rumped layers are defined by taking the nearest distance between the two layers. The vertical separations between the two sublattices of the rumped third and fifth bulk layers, Δr_3 and Δr_5 are also expressed as percentages of the bulk interlayer spacing.

Phase	Al(110)-c(2 × 2)-Li	Al(110)-c(2 × 2)-Na	Au(110)-c(2 × 2)-K	
Method	LEED	LEED	DFT[23]	MEIS[156]
Δd_{12}	-12.4 ± 0.7	-11.2 ± 0.7	-16	-13 ± 3
Δd_{23}	-2.5 ± 1.4	-4.4 ± 1.4	+1.5	-8 ± 5
Δr_3	+7.7 ± 0.7	+10.2 ± 1.4	+7	+8 ± 3
Δd_{34}	-4.6 ± 1.4	-5.2 ± 1.4		
Δd_{45}	-1.8 ± 1.4	-1.4 ± 1.4		
Δr_5	+3.5 ± 1.4	+4.2 ± 2.1		

other metal substrates.

Previously it has also been found for a large majority of clean metal surfaces that for a given plane on a specific crystal type, the same general relaxation pattern would occur regardless of the metal[159]. The contraction of the first interlayer spacing found for many metal surfaces was explained by Finnis and Heine[96] through redistribution of the valence electrons at the surface, and the resulting electrostatic forces. More complex patterns of oscillatory relaxations were also successfully explained using simple electrostatic models of the surface assuming Bravais lattices of valence charged point ions embedded in a neutralizing electron background[88, 102, 160, 161]. Very recently a simple electrostatic model has also been used by Repp et. al.[162] to explain relaxations of NaCl on Cu. They were able to explain the observations that Cl atoms sit on top of the step edges, while the Na ions appear to lie between steps, by considering electrostatic interactions due to the ionic nature of Na⁺ and Cl⁻ and the Smolouchowski charge smoothing effect.

In this chapter the extent to which calculations of *the electrostatic forces on the surface layers of the unrelaxed substrate in a point-ion/frozen background (PIFB) model* can predict trends of relaxation phenomena is discussed. Before describing this model and its consequences, it is worth asking whether there is any utility in such a simple approach when determination of the specific surface structures discussed here is within the grasp of self-consistent, *ab initio* calculations. The first, pragmatic, answer is that the consequences of a simple electrostatic model are trivial to evaluate and, for a number of systems at least, correctly reproduce the relaxations observed experimentally. The second answer is that notwithstanding the success of modern *ab initio* calculations, their results do not always lead to an

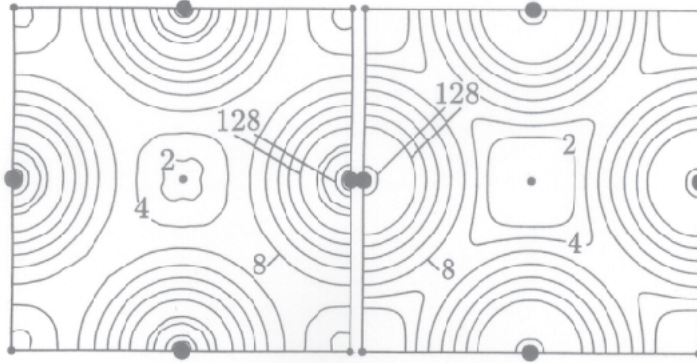


Figure 5.1: Valence charge density obtained by a superposition of the neutral atomic charge densities (left) and self-consistent calculations (right). Large dots marks the positions of the Cl atoms and small dots marks the positions of the Na atoms. Adapted from ref. [163]

increase in physical intuition. As an example, the controversy concerning the ionic or polarized-covalent nature of the adsorption bond in the adsorption of alkali metals on metal surfaces results from different interpretations of virtually identical calculational results. This point is amplified in a nice example of the very similar electron density contours for respectively NaCl and the superposition of atomic charge densities for Na and Cl by J. Bormet et al[163], as shown in Fig. 5.1.

In the following, the PIFB model is described in the form in which it has been used for self-consistent calculation of surface relaxations[160], before discussing the simplified form of the model used here (LF-PIFB model), in which forces on the ions of an unreconstructed substrate are calculated. After showing that the LF-PIFB model gives a good account of clean metal surfaces, its extension to superstructures is described and evaluated.

5.2 The PIFB electrostatic model

The PIFB-model involves calculations of the electrostatic forces between infinite Bravais nets of point-ions, embedded in slabs of neutralizing charge. The Hellmann-Feynmann forces \mathbf{F}_{mn} are calculated using the derivative of the Madelung equation [97, 164] for the electrostatic potential $\Phi(\mathbf{r}_{mn})$ on the ions in the m 'th slab due to the ions in the n 'th slab:

$$\mathbf{F}_{mn} = (F_{mn}(x), F_{mn}(y), F_{mn}(z)) = -\nabla\Phi(\mathbf{r}_{mn}) * Z_m \quad (5.1)$$

$$\Phi(\mathbf{r}_{mn}) = \frac{2\pi Z_n}{A_n} \sum_{\mathbf{g}_n \neq \mathbf{0}} g_n^{-1} e^{-g_n |z_{mn}|} \cos(g_{xn} x_{nm} + g_{yn} y_{nm})$$

⇒

$$F_{mn}(x) = \frac{2\pi Z_m Z_n}{A_n} \sum_{\mathbf{g}_n \neq \mathbf{0}} \frac{g_{xn}}{g_n} e^{-g_n |z_{mn}|} \sin(g_{xn} x_{nm} + g_{yn} y_{nm}) \quad (5.2)$$

$$F_{mn}(z) = \frac{2\pi Z_m Z_n}{A_n} \sum_{\mathbf{g}_n \neq \mathbf{0}} \frac{z_{mn}}{|z_{mn}|} e^{-g_n |z_{mn}|} \cos(g_{xn} x_{nm} + g_{yn} y_{nm}) \quad (5.3)$$

$F_{mn}(y)$ is not shown as it is quite similar to $F_{mn}(x)$. $\mathbf{r}_{mn} = (x_{mn}, y_{mn}, z_{mn})$ is a vector extending from an origin in the n th bravias plane to the nearest point in the m th bravais plane, the x-y plane is chosen parallel to the surface, and the z axis is chosen to be along the outward surface normal. The summation is over the reciprocal lattice vectors \mathbf{g}_n , of the n th plane. A_n and Z_n are the area of the primitive unit mesh and valence charge respectively of the n th layer.

In addition to the ion-ion interaction between different slabs described above, there are in general self-energy terms due to possible displacement of the ion lattice from the center of the slab[160].

$$F_{mm}(z) = 2\Delta_m/d_m$$

d_m is the width of the m'th slab and Δ_m is the displacement of the m'th layer from its bulk position.

5.3 Applications of the PIFB model to clean metal surfaces

For the interlayer relaxations of clean, unreconstructed surfaces the utility of the PIFB-approximation was first demonstrated in the self-consistent calculations of Landman et al[97, 101]. Landman and coworkers went on to show that electrostatics was the mechanism behind the general trends of the relaxations i.e. the order of expansion and contractions of the surface layers. Rearrangement of electric charge due to movement of the layers was responsible for the finer details of these relaxations. This is shown in table 5.2, where relaxations of Al(110) have been calculated by potential energy minimization of a range of different potentials with increasing complexity. In general it was found that a pure electrostatic model would overestimate the relaxations especially in the deeper layers.

A version of the PIFB model, including one adjustable parameter, which weights relative contributions of the interaction energy between different slabs and the slab self-energy, was later used by Jiang et al[161] to predict the relaxations of a number of open Fe and Al surfaces.

In the course of their ab initio total-energy calculation for Al(110), Ho and Bohnen [102], pointed out that the trends of the relaxations could be explained in

Table 5.2: Experimentally determined multilayer relaxations of Al(110) compared to various theoretical methods. LF-PIFB results are obtained using forces of the unrelaxed crystal, as described in this work. PIFB results are obtained by a potential energy minimization assuming a point ion / frozen background model. DLH results are obtained by a potential energy minimization assuming a PIFB model with a dipole-layer. A 1D treatment of the electron response to the ion movement has been included in the DLHSB0 model, and finally the DLHSB model takes electron response in 3D into account. eDFT-MD and DFT results from full ab initio calculations also included for comparison.

Method:	LEED	LF-PIFB	PIFB	DLH	DLHSB0	DLHSB	eDFT-MD	DFT
Ref:	Present	Present	[101]	[101]	[101]	[101]	[93]	[102]
Δd_{12}	-8.1 ± 2	-8.0	-26	-12	-14	-10	-7.5	-6.8
Δd_{23}	$+5.5 \pm 2$	+1.1	+16	+8	+9	+4	+4.5	+3.5
Δd_{34}	-3.8 ± 1	-0.1	-8	-4	-2	-3	-2.0	-2.0

terms of the electrostatic forces on the layers of the *unrelaxed* surface. This model, called LF-PIFB here, was later used by D.L.Adams[88] to predict the trends of the relaxations, both vertical and lateral, for the Al(210) surface, and it is the further evaluation of this model and its extension to superstructure systems that is the point of this chapter.

In the previous work for clean surfaces [88, 97] the full set of equations for a surface on a infinite bulk was much simplified due to the fact that only one surface species existed and there was no superstructures present, thus $\mathbf{g}_n = \mathbf{g}$ and $Z_n = Z$ for all n. Introducing \mathbf{v} as the projection of the shortest distance between two layers on the xy plane and d as the smallest distance between adjacent ion planes, the following analytical expressions for the total force $\mathbf{F}_m = (F_m(x), F_m(y), F_m(z))$, on an ion in the m'th layer due to the ions in the other layers can be found[88]:

$$F_m(z) = \frac{4\pi Z^2}{A} \sum_{\mathbf{g} \neq \mathbf{0}} \text{Re} \left[e^{-mgd} e^{-i\mathbf{m}\mathbf{g}\cdot\mathbf{v}} / (1 - e^{-gd} e^{-i\mathbf{g}\cdot\mathbf{v}}) \right] \quad (5.4)$$

$$F_m(x) = \frac{4\pi Z^2}{A} \sum_{\mathbf{g} \neq \mathbf{0}} \text{Im} \left[\frac{g_x}{g} e^{-mgd} e^{-i\mathbf{m}\mathbf{g}\cdot\mathbf{v}} / (1 - e^{-gd} e^{-i\mathbf{g}\cdot\mathbf{v}}) \right] \quad (5.5)$$

with a similar expression for $F_m(y)$ as for $F_m(x)$. Using equations 5.4 and 5.5, it is possible to analytically deduce a number of general trends for clean surfaces. For example the signs of the force components on a given layer are governed by the phase factors $e^{-i\mathbf{m}\mathbf{g}\cdot\mathbf{v}}$. For a surface with bulk repeat period of p layers where $e^{ip\mathbf{g}\cdot\mathbf{v}} = 1$ it follows that $e^{-i\mathbf{m}\mathbf{g}\cdot\mathbf{v}} = e^{-i(m+p)\mathbf{g}\cdot\mathbf{v}}$, and the signs of the forces are periodic with periodicity p. This for example predicts a $- + -$ sequence of relaxations for the fcc(110) surface with an ABABA stacking.

The application of the LF-PIFB model to clean surfaces is further demonstrated here. It must be emphasized again that the simplified LF-PIFB version of

Table 5.3: Comparison of experimentally-determined reconstructions and relaxations for the fcc(110) surfaces with calculations using the LF-PIFB model. Interlayer relaxations Δd_{ij} , are given with respect to the bulk interlayer distance. For all fcc(110) metal surfaces the forces predicted by the LF-PIFB model are identical besides from a multiplicative constant as seen from equations 5.2 and 5.3. Thus only relaxations of Al(110) are given, however relaxations of Ag,Cu,Pd and Ni can be found by multiplying the relaxations found for Al by $\frac{Z_X^{Al}}{Z_{Al}^{Al}} X$ being Ag,Cu,Pd and Ni.

	Al(110)	Ag(110)	Cu(110)	Pd(110)	Ni(110)	Al(110)
Layer	Exp.	Exp.[165]	Exp.[110]	Exp.[166]	Exp.[167]	LF-PIFB
Δd_{12}	-8.1 ± 2.1	-5.7 ± 2	-8.5 ± 0.6	-5.7 ± 2.0	-8.7 ± 0.5	-8.0
Δd_{23}	$+5.5 \pm 2.1$	$+2.2 \pm 2$	$+2.3 \pm 0.8$	$+0.5 \pm 2.0$	$+3.0 \pm 0.6$	+1.1
Δd_{34}	-3.8 ± 1.4		-0.9 ± 0.9		-0.5 ± 0.7	-0.1
Δd_{45}	$+1.1 \pm 1.4$		-0.8 ± 0.8			+0.0

the PIFB model used here does not attempt to find structures of minimum energy by a self-consistent variation of the geometry. Rather the assumption is made that the *trends* of the relaxations can be determined by calculations of forces on the unrelaxed substrate. Considering that the relaxations of the substrate atoms are usually a minor perturbation in the order of 10% of the lattice constant, it is relevant to use a first order approximation for the relaxations, assuming that *substrate relaxations are linear proportional with the forces on the unrelaxed surface*. As was found in the work by Landman et al [101] described above, the redistribution of the electron charge due to the presence of the surface seems to contribute less than the potential energy change from the ion-ion interaction of atoms at the surface, in determining the trends (expansion vs. contraction etc.) of surface relaxations.

Since forces are assumed linear proportional to the surface relaxation, a constant of proportionality has to be introduced. As only trends and not actual magnitudes of the relaxations are of interest, the calculated forces are arbitrarily normalized by the same constant. The constant is found by assuming a perfect agreement for the relaxation of the first interlayer distance of Al(110). Four tables for the comparison between experimental values and LF-PIFB predictions for the fcc(110), fcc(210), fcc(311) and several bcc Fe surfaces are given in tables 5.3, 5.4, 5.5 and 5.6. As is seen the LF-PIFB model is able to predict the signs of all relaxations correctly, while the magnitude of a specific expansion may be incorrect.

Table 5.4: Comparison of experimentally-determined reconstructions and relaxations for the fcc(210) surfaces with calculations using the LF-PIFB model. Interlayer relaxations Δd_{ij} , are given with respect to the bulk interlayer distance. For all fcc(210) metal surfaces the forces predicted by the LF-PIFB model are identical besides from a multiplicative constant as seen from equations 5.2 and 5.3. Thus only relaxations of Al(210) are given, however relaxations of Cu and Pt can be found by multiplying the relaxations found for Al by by $\frac{Z_X^2 A_{Al}}{Z_{Al}^2 A_X}$ X being Cu or Pt.

	Al(210)	Cu(210)	Pt(210)	Al(210)
Layer i	Exp.[88]	Exp.[168]	Exp. [169]	LF-PIFB
Δd_{12}	-15.5 ± 2	-5.7 ± 5	-23 ± 4	-15.5
Δd_{23}	-0.8 ± 3	-6.0 ± 5	-12 ± 4	-3.0
Δd_{34}	$+8.9 \pm 3$	$+6.8 \pm 4$	$+4 \pm 7$	+1.5
Δd_{45}	-4.4 ± 4	-3.7 ± 5	-4 ± 7	-0.3
Δd_{56}	-1.2 ± 5	-0.5 ± 4		+0.1

Table 5.5: Comparison of experimentally-determined reconstructions and relaxations for the fcc(311) surfaces of Al, Cu, Ni, Rh, Pb with calculations using the LF-PIFB model. Interlayer relaxations Δd_{ij} are given with respect to the bulk interlayer distance. For all fcc(311) metal surfaces the forces predicted by the LF-PIFB model are identical besides from a multiplicative constant as seen from equations 5.2 and 5.3. Thus only relaxations of Al(311) are given, however relaxations of Cu,Ni,Rh and Pb can be found by multiplying the relaxations found for Al by by $\frac{Z_X^2 A_{Al}}{Z_{Al}^2 A_X}$ X being Cu,Ni,Rh or Pb.

	Al(311)	Cu(311)	Ni(311)	Rh(311)	Pb(311)	Al(311)
Layer i	Exp.[167]	Exp.[170]	Exp. [171]	Exp.[172]	Exp.[173]	LF-PIFB
Δd_{12}	-13.3 ± 1	-7.3 ± 3	-15.9 ± 1	-14.5 ± 2	-14.1 ± 2	-11.9
Δd_{23}	$+8.8 \pm 2$	$+3.7 \pm 1$	4.1 ± 2	$+4.9 \pm 2$	-2.0 ± 2	+1.9

Table 5.6: Comparison of experimentally-determined reconstructions and relaxations for the bcc Fe(111), Fe(211), Fe(310) and Fe(210) surfaces with calculations using the LF-PIFB model. Inter-layer relaxations Δd_{ij} , are given with respect to the bulk interlayer distance.

	Fe(111)		Fe(211)	
Layer i	Exp.[174]	LF-PIFB	Exp.[175]	LF-PIFB
Δd_{12}	-16.9 ± 3	-15.4	-10.4 ± 3	-10.3
Δd_{23}	-9.8 ± 3	-4.7	$+5.4 \pm 3$	+1.8
Δd_{34}	$+4.2 \pm 4$	+2.7	-1.3 ± 3	-0.3
Δd_{45}	-2.2 ± 4	-0.3		
	Fe(310)		Fe(210)	
Layer i	Exp.[176]	LF-PIFB	Exp.[177]	LF-PIFB
Δd_{12}	-16.1 ± 3	-15.3	-22.0 ± 5	-20.9
Δd_{23}	$+12.6 \pm 3$	-0.1	-11.0 ± 5	-14.5
Δd_{34}	-4.0 ± 4	+0.6	$+17.0 \pm 5$	+7.0
Δd_{45}			-4.8 ± 5	+1.7

5.4 Extending the model to reconstructions and adsorbate structures

With the success for clean surfaces in mind it would be interesting to test the LF-PIFB model for more complex adsorbate systems including several elements and possible reconstruction of the surface. By the nature of the model it is not possible of course to calculate the basic reconstruction (on-top, substitutional etc.), but assuming a basic reconstruction it would be interesting to see if one could successfully predict rumpling and lateral relaxation of the substrate induced by the adsorbate. In this respect the alkali - alkali adsorption systems are well suited because the predictive power of the model can easily be tested on the considerable number of known surface structures. Relying on essentially no adjustable parameters it is shown below that the trends of the relaxation of a number of alkali/aluminum adsorbate systems can be predicted. Further it is shown for the important fcc(110) missing row reconstruction on Pt, Ir and Au that one can successfully predict the trends of relaxations of this surface.

The extension of the model to systems containing a superstructure and several atomic species seems straight forward. However, at the outset of this work, it was not obvious that the relaxation trends predicted by the LF-PIFB model would not be very dependent on the precise, perhaps unknown, position of adsorbate atoms. Also the choice of the different valence charges chosen for different atomic species could influence the results. Clearly the model will only have some utility if the predicted trends are rather independent of the precise geometry of the superstructure and valency of the constituents.

Returning to the Madelung equation 5.1, it already distinguishes between different surface unit cells (reciprocal vectors g_n and area of the primitive unit cell A_n) and ionic charges (Z_n) for different layers. In the following, ionic charges of $Z_{alkali} = 1$, $Z_{Pt} = 2$ and $Z_{Al} = 3$ were assumed. Numerical computation of the forces on a specific layer is straight forward, and demands no real insight into symmetry, only the basic structural parameters are needed. One proceeds by calculating the quickly converging sums of equations 5.2 and 5.3 for all other layers regardless of position, unit cell and charge. A calculation for the third Al layer of the Al(110)-c(2 × 2)-Na could for example include, the Na c(2 × 2) layer, followed by the first Al c(2 × 2) layer, followed by a second layer Al lattice with a (1 × 1) unit cell and followed by a contribution from bulk Al(110).

The simple analytical expressions for the total forces 5.5 and 5.4, which assume $\mathbf{g}_n = \mathbf{g}$, $\mathbf{A}_n = \mathbf{A}$ and $Z_n = Z$ for all n are no longer valid. But new analytical expressions can be derived, for bulk and superstructure layers, by splitting up into sums over integral and fractional order \mathbf{g} 's. Consider a system consisting of a selvedge of N_s superstructure layers on a perfect substrate. The electrostatic force

$F_m(xyz)$ on the m 'th layer is given by the sum of contributions from the bulk and selvedge layers as: $F_m(xyz) = F_m^{(S)}(xyz) + F_m^{(B)}(xyz)$, the system origin is set to be on an atom in the first selvedge layer. The contribution from bulk layers $F_m^{(B)}(xyz)$ to the forces on layer m is obtained by simple modification of Eqs. 5.5 and 5.4. The contribution from the selvedge layers to the forces on sublattice l of layer m is given by:

$$F_l^{(S)}(z) = \sum_{n \neq m}^{N_s} \text{sgn}(m-n) c_{mn} \sum_{\mathbf{g} \neq \mathbf{0}} e^{-g|d_m-d_n|} \cos [\mathbf{g} \cdot (\mathbf{v}_m + \mathbf{w}_l - \mathbf{v}_n)] \quad (5.6)$$

$$F_l^{(S)}(x) = \sum_{n \neq m}^N c_{mn} \sum_{\mathbf{g} \neq \mathbf{0}} (g_x/g) e^{-g|d_m-d_n|} \sin [\mathbf{g} \cdot (\mathbf{v}_m + \mathbf{w}_l - \mathbf{v}_n)] \quad (5.7)$$

with an equation similar to Eq. 5.7 for $F_l^{(S)}(y)$. In these equations, $c_{mn} = 4\pi Z_m Z_n / A_n$ and \mathbf{w}_l is a parallel shift vector from the origin of layer m to the l 'th sublattice. The vector \mathbf{r}_m from the origin to layer m has components d_m and \mathbf{v}_m along the surface normal and in the xy plane, respectively. The summations are over the reciprocal-net vectors \mathbf{g} of layer n , which include fractional-order vectors with respect to the reciprocal net of the substrate.

For each system one can in fact just examine the contributions to the forces on a given bulk layer due to the superstructure layers, since only these forces can lead to a reconstruction of a bulk layer. It can be shown that the *signs* of the reconstructive displacements follow analytically from the equations of the forces independent of the magnitude of the charge and the vertical position of the selvedge layers. The trends are however dependent on the sites occupied by the atoms in the selvedge layers. One example of such an analytical solution for Al(110)-c(2 × 2)-Na is given in section 5.4.2, while some other examples are briefly mentioned.

When a selvedge layer is split up into several subplanes, these sublattices can also affect each other, leading to lateral motion. This is as opposed to a bulk layer, where the net forces of the sublattices on each other is zero. For structures with high symmetry or small unit cells, such interactions often cancel due to symmetry. For example, in the case of the Al(111)-($\sqrt{3} \times \sqrt{3}$)-Rb substitutional structure, the first Al layer contains two ($\sqrt{3} \times \sqrt{3}$) sublattices, as opposed to the three ($\sqrt{3} \times \sqrt{3}$) sublattices of a bulk layer. However the net forces on the two sublattices must cancel, since a relative displacement would break symmetry. But there are systems, such as the Al(100)-($\sqrt{5} \times \sqrt{5}$)R27°-Na structure discussed in section 4.3, where it is necessary to calculate the forces between co-planar sublattices. This is not possible using equations 5.2 and 5.3 as the sums do not converge for co-planar layers. The problem can be resolved by splitting up the sums of the original 2D Madelung equation for 2D slabs up into two new sums which do converge.

For a two dimensional lattice the potential in the plane is given by equation B8 of ref. [164] (excluding constant term due to Laplace) and setting $n=1$ and $m=2$:

$$\Phi(\mathbf{r}, 0) = \frac{1}{\sqrt{\pi}} \left\{ \frac{1}{A_m} \sum_{\mathbf{g} \neq \mathbf{0}} \exp(2\pi i \mathbf{g} \cdot \mathbf{r}) \frac{\Gamma[\frac{1}{2}, \pi^2 \mathbf{g}^2 / \omega]}{|\mathbf{g}|} + \sum_l \frac{\Gamma[\frac{1}{2}, \omega(\mathbf{r} - \mathbf{r}_l)^2]}{|\mathbf{r} - \mathbf{r}_l|} \right\}$$

ω has been introduced in order to split up the original expression into two rapidly converging series. ω should be taken equal to π times the inverse square of the nearest-neighbor distance for rapid convergence. $\Gamma(v, x)$ is the incomplete gamma function. Analytically deriving the forces from this expression is rather tedious, and one can instead choose the computational approach of simply numerically calculating the derivative to obtain the forces.

In the following we examine the consequences of the PIFB model for some specific systems. We emphasize again that the intention of the analysis is to determine the trends in the relaxations of the substrate due to the existence of a superstructure. For all of the systems discussed below, *the predicted signs of the reconstructive displacements are the same as those found experimentally*. The magnitudes of the reconstructive displacements and the interlayer relaxations are given by numerical calculations of equations 5.6 and 5.7, including the contributions of bulk layers to the forces. For the adsorption systems, the experimentally-determined positions of the adsorbed layer was normally used, however only the basic symmetry of the adsorbate is relevant. The calculated forces *for each system* are arbitrarily multiplied by 2.865 to produce displacements in Ångströms.

It should be noted that in subsequent figures, only the directions of the *reconstructive displacements* are shown. The additional vertical displacements common to all the sublattices of a layer are not shown. However, the interlayer relaxations are listed in tables of numerical values for relaxations.

5.4.1 Ir, Au, Pt(110)-(1x2) missing row reconstruction

The extension to superstructures without adding several ionic species (a reconstructed clean surface) will be considered as a first step. Presented here, is the important missing-row model[139] of the fcc(110)-(1 × 2) surface found for Ir, Au and Pt. As shown in Fig. 5.2, the unrelaxed structure consists of a (1 × 2) (“missing-row”) layer, $m = 1$, followed by bulk layers. It follows from symmetry that the only possible relaxation for layer $m = 2$ is an equal and opposite lateral displacement of the two sublattices along the [001] direction. Similarly, it follows that the only possible relaxation for layer $m = 3$ is a vertical displacement of the two sublattices in the surface-normal direction. The sequence of relaxations repeats with the bulk repeat periodicity in the surface-normal direction of 2 layers. It follows analytically from the LF-PIFB model that the lateral displacements in the

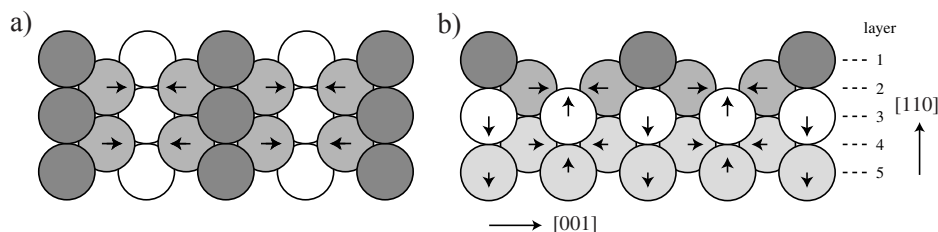


Figure 5.2: a) Top and b) side view of the Pt(110)-(1 \times 2)-missing row structure shown as a projections on the (1 $\bar{1}$ 0) and (110) planes respectively. Arrows indicate the directions of forces due to the missing-row layer, as calculated in the LF-PIFB model, and as found experimentally.

first and third bulk layers consist of an equal and opposite movement of Pt atoms in the two (1 \times 2) sublattices *towards* the missing row. It follows similarly that the vertical displacements in the second and fourth bulk layers are such that Pt atoms directly beneath Pt atoms in the surface (1 \times 2) layer move inwards, whereas the other Pt atoms move outwards. Numerical values of substrate relaxation based on the basic missing row reconstruction are given in Table 5.7.

5.4.2 Al(110)-c(2 \times 2)-Na and Al(110)-c(2 \times 2)-Li

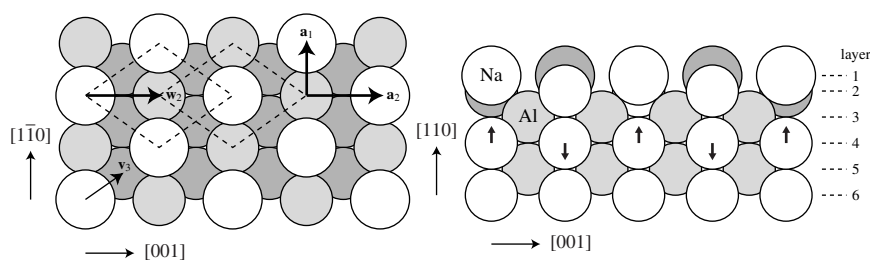


Figure 5.3: Model of the Al(110)-c(2 \times 2)-Na structure shown a) from the top, and b) from the side as a projection on the (1 $\bar{1}$ 0) plane. The basis vectors \mathbf{a}_1 and \mathbf{a}_2 of bulk layers are shown in a). The bulk layers can be decomposed into two c(2 \times 2) sublattices, shown as dotted lines in a), with parallel shift vectors $\mathbf{w}_1 = 0$ and $\mathbf{w}_2 = \mathbf{a}_2$ with respect to the layer origins. Arrows in b) indicate the directions of forces due to the two selvedge layers, as calculated in the LF-PIFB model, and as found experimentally. Note that the forces due to bulk layers give rise to additional vertical displacements, not shown in the figure, which are the same for each sublattice of a bulk layer.

As sketched in Fig. 5.3, the unrelaxed structure consists of a c(2 \times 2)-alkali layer, $m = 1$, with alkali atoms in substitutional sites, followed by a c(2 \times 2)-Al

Table 5.7: Comparison of experimentally-determined reconstructions and relaxations for fcc(110)-(1 × 2) - missing row with calculations using the LF-PIFB model. As for the clean surfaces the relaxations of the three different metals predicted by the LF-PIFB model will be identical except for a multiplicative constant. Thus the relaxations are only shown for Pt. Interlayer relaxations Δd_{ij} , defined with respect to the outer surfaces of rumpled layers, are given with respect to the bulk interlayer distance. Layer rumpling Δr_i is the vertical spacing between the two subplanes in a rumpled layer, also given with respect to the bulk interlayer distance. Lateral displacements Δa_i are given with respect to the nearest-neighbor distance along the [001] direction. Note that the directional properties of the displacements Δr_i and Δa_i are correctly predicted by the model.

	Au(110)	Ir(110)	Pt(110)	
	Exp.[33]	Exp.[178]	Exp.[139]	LF-PIFB
Δd_{12}	-20.1	-12.3	-18.5	-14.1
Δa_2	+4.9	+2.6	+3.3	+13.5
Δd_{23}	-6.3	-11.6	-24.2	-27.2
$ \Delta r_3 $	+16.7	+16.9	+23.1	+30.1
Δd_{34}	-6.3	-6.0	-20.3	-13.2
Δa_4			+6.1	+1.7
Δd_{45}			+0.9	+1.7
$ \Delta r_5 $				+3.1

(Au) layer, followed by bulk Al (Au) layers. For this system, the net forces leading to lateral displacements within the bulk layers are zero due to mirror plane symmetry. Similarly, vertical displacements are only possible for alternate layers $m = 4, 6$, etc. It can be derived that the difference in the forces on the two sublattices ($l = 1, 2$ and $\mathbf{w}_1 = 0$, $\mathbf{w}_2 = \mathbf{a}_2$) of such bulk layers due to the $c(2 \times 2)$ -alkali, substrate selvage layers is given by Eq. 5.6 as:

$$F_{l=1}^{(S)}(z) - F_{l=2}^{(S)}(z) = \sum_{n=1}^2 2c_{nm} \sum_{h \geq 0, k} e^{-g_{hk}^{l} d_{mn}}, \quad (5.8)$$

where $c_{1m} = 2\pi(Z_{alkali}Z_{substrate}/A_b)$ and $c_{2m} = 2\pi(Z_{substrate}^2/A_b)$, and A_b is the area of the bulk unit cell. In Eq. 5.8, the summation over reciprocal lattice vectors has been separated into a summation over integral-order vectors $\mathbf{g}_{hk} = h\mathbf{a}_1^* + k\mathbf{a}_2^*$ and fractional-order vectors $\mathbf{g}_{hk}^{l} = \mathbf{g}_{hk} + (1/2)(\mathbf{a}_1^* + \mathbf{a}_2^*)$. For each $c(2 \times 2)$ selvage layer, the summations over integral-order vectors are equal in magnitude, and thus cancel, whereas the fractional-order vectors give equal and opposite contributions to the forces on the two sublattices, leading to a rumpling (Δr) of bulk layers with $m = 4, 6$, etc. Since the summation in Eq. 5.8 is positive, it follows that the first sublattice with $\mathbf{w}_1 = 0$ moves *outwards* relative to the second sublattice. Thus, as indicated by the arrows in Fig. 5.3b, Al (Au) atoms lying directly beneath alkali atoms move outwards towards the alkali atoms. Numerical values

Table 5.8: Comparison of experimentally-determined reconstructions and relaxations for Al(110)-c(2 × 2)-alkali surface structures with calculations using the PIFB model. Interlayer relaxations Δd_{ij} , defined with respect to the outer surfaces of rumpled layers, are given with respect to the bulk interlayer distance. Layer rumpling Δr_i is the vertical spacing between the two subplanes in a rumpled layer, also given with respect to the bulk interlayer distance. Note that the directional properties of the displacements Δr_i are correctly predicted by the model.

	Al(110)-c(2 × 2)-Na		Al(110)-c(2 × 2)-Li	
	Exp.	LF-PIFB	Exp.	LF-PIFB
Δd_{12}	-11.2	-11.2	-12.4	-38.5
Δd_{23}	-4.4	-34.1	-2.5	-22.6
$ \Delta r_3 $	+10.2	+22.5	+7.7	+15.8
Δd_{34}	-5.2	-7.8	-4.6	-7.1
Δd_{45}	-1.4	-0.5	-1.8	-0.4
$ \Delta r_5 $	+4.2	+0.5	+3.5	+0.5

of substrate relaxation based on the basic substitutional c(2 × 2) reconstruction are given in Table 5.8.

5.4.3 Al(111)-(2 × 2)-Rb

Relaxations of the Al(111)-(2 × 2)-Rb structure formed by adsorption of Rb on Al(111) at low temperature[13], found experimentally and derived numerically by the LF-PIFB model are given in Table 5.9. The unrelaxed structure, as sketched for the (2 × 2) phases in fig 5.4, consists of a (2 × 2) layer ($m = 1$), with alkali atoms in on-top sites, followed by bulk layers. For the (2 × 2) structures, considerations of symmetry show that both vertical displacements (Δr) and radial, lateral displacements (Δa) along {121} directions are possible in layers $m = 2, 3$, and 4. As in the case of the Al(110)-c(2 × 2)-alkali structure discussed above, the signs of the reconstructive displacements follow analytically from the LF-PIFB model. Thus it can be shown, for example, that the (2 × 2) sublattice in the first bulk layer, with Al atoms directly beneath adsorbed alkali atoms, moves inwards, whereas Al atoms in the remaining sublattices move outwards. For the (2 × 2) structures, it can be shown that lateral displacements are zero in the first bulk layer ($m = 2$), whereas in the second bulk layer ($m = 3$), the three Al atoms lying closest to a rotational axis through adsorbed alkali atoms move radially away from the axis along {121} directions in the surface plane, and vertically inwards, whereas Al atoms in the fourth sublattice move vertically outwards.

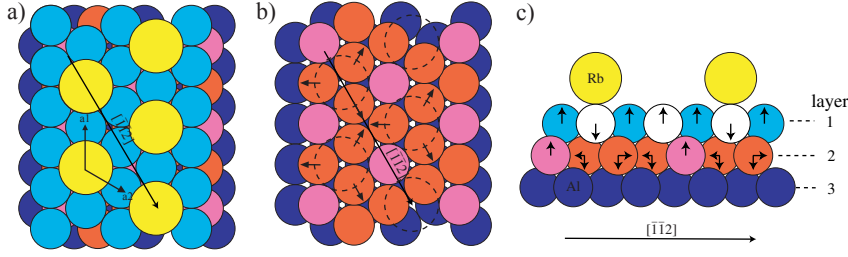


Figure 5.4: a) Top view of the Al(111)-(2×2)-Rb structure. b) Top view of the Al(111)-(2×2)-Rb structure, where the Rb atoms and the first layer Al atoms have been removed to show the direction of the forces on the second Al layer. c) Side view of the Al(111)-(2×2)-Rb structure shown as a projection on the (1 $\bar{1}$ 0) plane. The direction parallel to the side view projection in c) is indicated on a) and b). On b) and c) arrows indicate the directions of forces due to the Rb layer, as calculated in the LF-PIFB model, and as found experimentally. Note that the lateral displacements Δa_2 in the second bulk layer are of equal magnitude along surface {121} directions. The shorter horizontal arrows represent the projections of these displacements on the (1 $\bar{1}$ 0) plane.

Table 5.9: Comparison of experimentally-determined reconstructions and relaxations for Al(111)-(2×2)-Rb with calculations using the LF-PIFB model. Interlayer relaxations Δd_{ij} , defined with respect to the outer surfaces of rumpled layers, are given with respect to the bulk interlayer distance. Layer rumpling Δr_i is the vertical spacing between the two subplanes in a rumpled layer, also given with respect to the bulk interlayer distance. Lateral displacements Δa_i are given with respect to the bulk nearest-neighbor distance in c) and to the nearest-neighbor distance along the [001] direction in d). Note that the directional properties of the displacements Δr_i and Δa_i are in all cases correctly predicted by the model.

	Al(111)-(2×2)-Rb	
	Exp.[13]	LF-PIFB
Δd_{12}	-6.9	-7.2
$ \Delta r_2 $	+9.4	+4.6
$ \Delta a_2 $	+0.4	+0.0
Δd_{23}	-0.9	-0.04
$ \Delta r_3 $	+1.5	+0.1
$ \Delta a_3 $	+0.9	+0.05

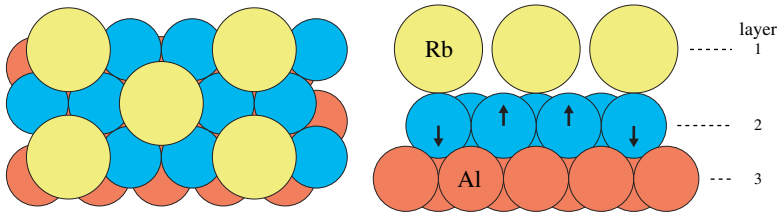


Figure 5.5: a) Top and b) side view of the Al(111)-($\sqrt{3} \times \sqrt{3}$)-Rb structure shown as projections on the (111) and (1 $\bar{1}$ 0) planes respectively. Arrows indicate the directions of forces due to the Rb layer, as calculated in the LF-PIFB model, and as found experimentally.

Table 5.10: Comparison of experimentally-determined reconstructions and relaxations for Al(111)- $(\sqrt{3} \times \sqrt{3})R30^\circ$ -alkali with calculations using the LF-PIFB model. Interlayer relaxations Δd_{ij} , defined with respect to the outer surfaces of rumpled layers, are given with respect to the bulk interlayer distance. Layer rumpling Δr_i is the vertical spacing between the two subplanes in a rumpled layer, also given with respect to the bulk interlayer distance. Note that the directional properties of the displacement Δr_2 is correctly predicted by the model.

	Al/K		Al/Rb		Al/Cs	
	Exp.[179]	LF-PIFB	Exp.[86]	LF-PIFB	Exp.[8]	LF-PIFB
Δd_{12}	-6.4	-4.6	-5.7	-5.1	-6.2	-5.6
$ \Delta r_2 $	+12.6	+2.3	+11.4	+2.6	+12.5	+2.9
Δd_{23}	-0.1	-0.01				

5.4.4 Al(111)- $(\sqrt{3} \times \sqrt{3})R30^\circ$ -K, Rb, Cs

Similar $(\sqrt{3} \times \sqrt{3})R30^\circ$ -K, Rb, Cs structures are formed by adsorption of K, Rb, and Cs on Al(111) at low temperature [8]. The unrelaxed structures, as sketched in Fig 5.5, consist of a $(\sqrt{3} \times \sqrt{3})R30^\circ$ layer ($m = 1$), with alkali atoms in on-top sites, followed by bulk layers. Considerations of symmetry show that vertical displacements between bulk sublattices are possible in layer $m = 2$, and that radial, lateral displacements along $\{121\}$ directions can occur in layers $m = 3, 4$. This sequence repeats with the bulk repeat period of three layers in the surface-normal direction. As in the case of the Al(110)- $c(2 \times 2)$ -Na structure discussed above, the signs of the reconstructive displacements follow analytically from the LF-PIFB model. For both systems, the $(\sqrt{3} \times \sqrt{3})R30^\circ$ sublattice in the first bulk layer, with Al atoms directly beneath adsorbed alkali atoms, moves inwards, whereas Al atoms in the remaining sublattices move outwards. Numerical values of substrate relaxation based on the basic on-top $(\sqrt{3} \times \sqrt{3})R30^\circ$ structure are given in Table 5.10.

5.5 Limitations of the LF-PIFB model

It should be noted, that the LF-PIFB model fails for a few close-packed fcc(111) and (100) surfaces where the relaxations are relatively small. These surfaces have often proved to be difficult to model even in *ab initio* calculations [180], presumably due to a delicate balance of competing effects. In regard to the work presented here the most important exception to the PIFB approximation is the Al(100) surface, where an expansion of the first interlayer spacing exists, in contradiction with the original Finnis and Heine argument. This also results in a situation where the relaxations of a hypothetical vacancy $\sqrt{5}$ structure discussed in section 4.3 in regard to the Al(100)- $(\sqrt{5} \times \sqrt{5})R27^\circ$ -Na structure, is not predicted

correctly, while the effect of the alkali on the substrate is predicted correctly. The problem is the interaction of the co-planar Al sublattices in the layer containing the vacancy, where a contraction around the vacancy is predicted instead of an expansion. One could perhaps conclude from this example that the LF-PIFB model fails for reconstructions involving the few substrates where it also fails in the clean unreconstructed case. However the model can apparently still work for these surfaces if the relaxations are induced by for example a simple alkali adsorbate.

5.6 Summary and discussion

The LF-PIFB model successfully predicts the trends of the observed reconstructive displacements and interlayer relaxations of bulk layers for the particular systems discussed here, suggesting that electrostatic forces play an important role in producing these displacements. In summary, it has been shown that a simple electrostatic model can qualitatively explain the relaxations and rumpings for a number of alkali-aluminum adsorbate systems, and further an example has been given of a reconstructed clean metal system where this model also works. Since it has already been shown that this model can qualitatively explain the relaxations of virtually all clean metal surfaces measured so far, it can be concluded that the simple electrostatic model can be applied to a significant range of systems with confidence. Further development towards implementing electrostatic models for semiconductors or metal-oxides is possible[181, 182]. So called shell model calculations are based on an ionic crystal model assuming formal (integral) ionic charges and dominating pairwise interionic potentials. Besides from the long-range Coulomb interactions short range interactions can be modelled using Buckingham potentials $V(r) = Ae^{-r/\rho} - C/r^6$ which includes a van der Waals term $-C/r^6$ modelling the interionic correlations and a short-range potential resulting from Pauli exclusion principle. This type of model has been applied with success to explain relaxations around vacancies in metal-oxides. The variable parameters A, r, ρ are usually derived from fitting experimental measurements or full ab initio calculations. The shell model can be seen as an extension of our simple electrostatic model, however it is not known how important these extra assumptions are (beyond introducing positive ionic charges), in order to successfully derive trends for (for example) metal-oxides.

Chapter 6

Al-Li multilayer surface alloys

The miscible and immiscible alkalis Li and Na behave very similarly for single layer alkali structures, but the situation at higher coverages is quite different. While it is energetically favorable for Li to form subsurface alkali-aluminum alloys, several layers of Na can only be accommodated by thin film growth on top of the surface.

6.1 An unusual Al(100)- $c(2 \times 2)$ -2Li multilayer alloy

6.1.1 Introduction

In the present chapter the occurrence of a novel type of surface alloy formation is introduced, namely the formation of a well ordered surface alloy between two metals, Al and Li, but where the structure of the surface alloy does not occur in the bulk, although the stoichiometry is that of a known Al-Li bulk alloy. The result is obtained by analysis of LEED data and confirmed by total-energy calculations, which in turn lead to the novel prediction that the surface of a bulk Al_3Li alloy will similarly deviate from the bulk geometry.

As already discussed in chapter 1, studies of the submonolayer adsorption of Li on close-packed Al surfaces have yielded results similar to those found for the heavier alkali metals which are immiscible in Al. It has therefore been an open question as to whether the surface structures formed by adsorption of Li have any relation to bulk Al-Li alloys. For the adsorption of Li on Al(100), it was found in section 4.2, that adsorption of 0.5 ML of Li at room temperature, leads to the formation of a $c(2 \times 2)$ -Li structure, in which Li atoms substitute 0.5 ML Al atoms in the first layer. High-resolution core-level spectroscopy (CLS) measurements have shown that adsorption of 1 ML of Li at room temperature

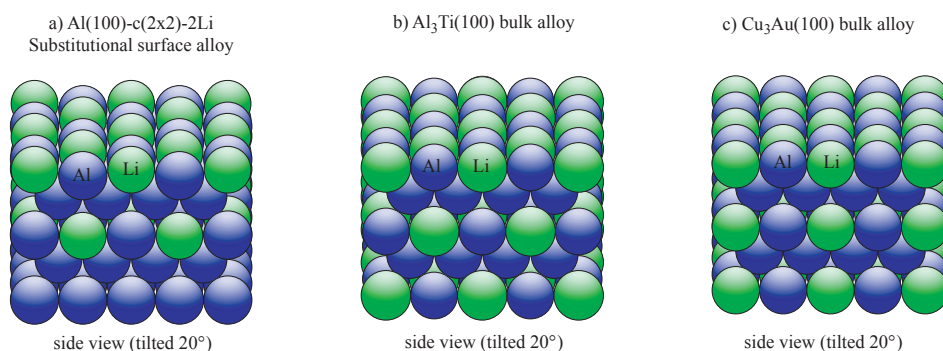


Figure 6.1: a) hard-sphere model of the $\text{Al}(100)\text{-}c(2 \times 2)\text{-}2\text{Li}$ structure, shown as a central projection on the (110) plane, in a side view tilted by 20° with respect to the plane of the paper. Li atoms are shown in green, Al atoms are shown in blue. b) corresponding model of the Al_3Ti bulk alloy. c) corresponding model of the Cu_3Au bulk alloy. Note that in the Cu_3Au -type structure of bulk Al_3Li , Li atoms in every other layer lie directly beneath each other.

leads to the formation of a three-layer surface alloy[58], containing a mixed Al/Li layer, followed by a pure Al layer, followed by a second mixed Al/Li layer. LEED pattern observations indicate that the translational symmetry of this phase is also $c(2 \times 2)$, but that the $c(2 \times 2)\text{-}2\text{Li}$ phase formed by adsorption of 1 ML Li at room temperature is much less well-ordered than the $c(2 \times 2)\text{-Li}$ phase formed by adsorption of 0.5ML Li at room temperature. Based on the bulk Al/Li phase diagram, it was suggested that the structure of the $c(2 \times 2)\text{-}2\text{Li}$ phase probably corresponded to the first three layers of the metastable bulk Al_3Li alloy.

It is shown here that a well ordered $c(2 \times 2)\text{-}2\text{Li}$ phase can actually be prepared by adsorption at temperatures in the range 380 to 440 K. A LEED analysis confirms the basic three-layer model suggested by CLS measurements. However, it is found quite unexpectedly that the structure does not correspond to the first three layers of the bulk Al_3Li alloy but rather to the first three layers of the bulk Al_3Ti structure. This conclusion has been confirmed by total-energy calculations, which in turn lead to the prediction of an unexpected surface structure for the bulk Al_3Li alloy.

In the following the LEED experiment and analysis is first described, then the density-functional theory (DFT) calculations of total energy carried out by M. Borg and J. Andersen.

6.1.2 LEED measurements and structural determination

Sets of $I(V)$ spectra were measured after adsorption of $\sim 1\text{ML}$ of Li at temperatures in the range 300 K - 480 K in steps of 20 K. Adsorption of $> 1\text{ML}$ of Li led to no further change in the intensity spectra. The optimal $\text{Al}(100)\text{-}c(2 \times 2)\text{-}2\text{Li}$

Table 6.1: Structural parameters determined by LEED and DFT calculations for the Al(100)-c(2 × 2)-2Li phase. DFT calculations for a hypothetical Al(100)-c(2 × 2)-3Li phase are also included. Layers a and b of the stacking sequence are both c(2 × 2) substitutional Al/Li layers. However in the b layers the Al and Li atoms have switched places compared to the a layers. Δd_1 , Δd_3 , and Δd_5 are the vertical separations between Li and Al atoms in mixed and rumpled first, third and fifth layers, where positive values correspond to Li atom positions being closer to the surface than Al. d_{ij} are the vertical separations between the outer surfaces of the i 'th and j 'th layers.

Method:	LEED	DFT calculations	
Structure:	Al ₃ Ti	Al ₃ Ti	Cu ₃ Au
Stacking:	ba	ba	aa
Parameter			
Δd_1	0.38 ± 0.04 Å	0.322 Å	0.241 Å
d_{12}	1.82 ± 0.01 Å	1.85 Å	1.89 Å
d_{23}	1.95 ± 0.02 Å	1.98 Å	2.01 Å
Δd_3	-0.04 ± 0.04 Å	0.007 Å	0.012 Å
d_{34}	2.02 ± 0.02 Å	1.98 Å	2.01 Å
E_{ads}		-4.56 eV	-4.45 eV

Method:	DFT calculations			
Structure:	Al ₃ Ti/Cu ₃ Au	Al ₃ Ti	Cu ₃ Au/Al ₃ Ti	Cu ₃ Au
Stacking:	baa	bab	aab	aaa
Parameter				
Δd_1	0.312 Å	0.312 Å	0.248 Å	0.225 Å
d_{12}	1.84 Å	1.84 Å	1.89 Å	1.89 Å
d_{23}	1.97 Å	1.97 Å	2.00 Å	2.00 Å
Δd_3	-0.199 Å	0.029 Å	0.038 Å	-0.014 Å
d_{34}	2.00 Å	2.00 Å	2.01 Å	2.00 Å
Δd_5	0.091 Å	-0.029 Å	-0.002 Å	0.017 Å
E_{ads}	-6.79 eV	-6.65 eV	-6.64 eV	-6.66 eV

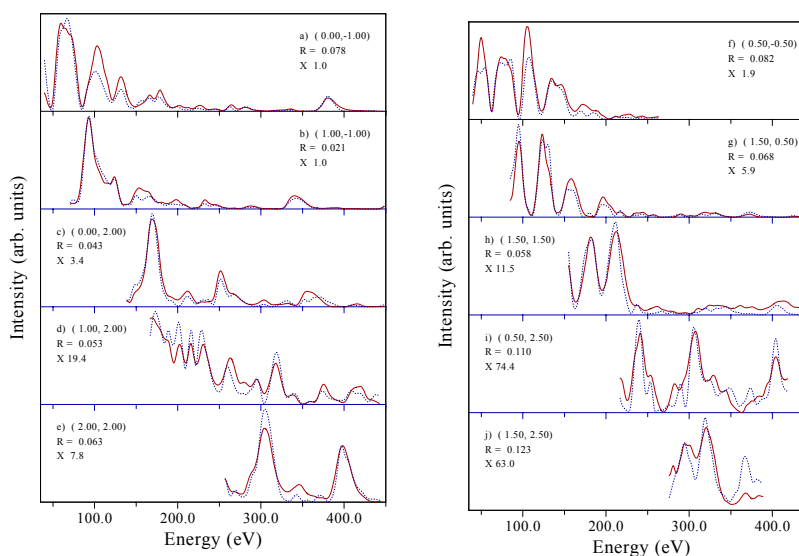


Figure 6.2: Comparison of experimental (solid lines) and calculated (dotted lines) intensity-energy spectra for Al(100)- $c(2 \times 2)$ -2Li at $\theta = 0^\circ$ for five integral-order and five fractional order beams, a)-e) and f)-j) respectively. The beam hk indices, R factors, and scale factors are shown in each panel. The calculated spectra were obtained using the best-fit parameter values given in table 6.1.

2Li structure, as judged by the relative intensity of fractional and integral-order beams, was found to form in a temperature range between 380 K to 440 K. After averaging symmetry-equivalent beams, the data sets contained 7 integral-order and 5 fractional-order symmetry-inequivalent beams.

Refinement of all structural and nonstructural parameters in the first four surface layers was performed for two different, three-layer, surface alloy structures with Cu_3Au -type and the Al_3Ti -type geometries respectively as sketched in Fig. 6.1. The Al_3Ti -type structure gave a significantly better agreement between experimental and calculated intensity spectra, yielding $R = 0.053$ as compared to $R = 0.135$ for the Cu_3Au -type structure expected for bulk Al_3Li . The detailed results of the structure determination are given in table 6.1. Plots of a subset of the experimental intensity spectra and spectra calculated for the optimum parameter values given in table 6.1 are shown in Fig. 6.2.

The degree of ordering of the alloy structure was investigated by carrying out LEED analysis using the sets of $I(V)$ spectra measured for different deposition temperatures. In these analysis, intensities were calculated using the averaged t -matrix approximation (ATA) for a structure with a perfect $c(2 \times 2)$ -Li first layer, but with different Li concentrations in the second and deeper layers. Variation of the concentration in the first layer was not considered, due to the relatively large displacement of 0.4 Å between the Al and Li atoms in the first layer. It was found

that the LEED intensities were incompatible with non-zero concentrations of Li in the 2nd layer for all deposition temperatures between 330K to 450K. However the LEED analysis indicated that the Li concentration in the third layer increases with deposition temperature, with a concentration of 0.35ML at 330K, reaching 0.5ML at deposition temperatures above 380K, where the $c(2 \times 2)$ -Li structure appears to be perfectly developed. The possibility of randomly distributed Li in the fourth layer was also investigated, but it was found that non-zero Li concentrations resulted in a increase of the R -factor. Finally, a structure in which both the third and fifth layers consisted of mixed $c(2 \times 2)$ -Al/Li layers was also investigated, as discussed below.

6.1.3 DFT calculations

Following the LEED analysis, ab-initio total-energy DFT calculations[149] with a plane-wave basis set and norm-conserving pseudopotentials[150] were performed to determine the structure of lowest energy by M.Borg. This involved calculating the total energies of Al(100) slabs consisting of 9 layers, where the first and third (and fifth) layers had a mixed, Al/Li $c(2 \times 2)$ structure. A cut-off energy of 13 Ry and 36 k-points in the irreducible wedge of the Brillouin zone (distributed in accordance with the Monkhorst-Pack scheme[151]) was found sufficient for convergence of the total energy. The exchange-correlation functional was described by a generalized gradient approximation[152]. For the Al_3Ti and Cu_3Au structural models considered here, the total energy was optimized with respect to relaxations of all parameters allowed within the $c(2 \times 2)$ unit cell in a four-fold rotational and mirror symmetry, in accordance with the symmetry of the observed LEED pattern.

6.1.4 Discussion

For a three-layer surface alloy, the DFT calculations clearly confirm the LEED results in that the Al_3Ti -type alloy is more stable than the Cu_3Au -type by $\sim 0.1\text{eV}$ per unit cell. The structural parameters found by DFT calculations in fact agree quantitatively with the LEED results, as can be seen from the comparison of determined structural parameters in Table 6.1. It is interesting to note that the Al_3Ti -type structure is energetically favored regardless of the extent to which Li atoms in the first layer are relaxed out of the plane. It seems likely therefore that the preference for the Al_3Ti -type surface has to do with the nature of the Al-Li bonding rather than being a consequence of the extra degrees of freedom introduced by the loss of symmetry at the surface. It has been shown previously for the AlLi and Al_3Li bulk alloys that Al-Al bonds are strengthened by donation of a Li valence electron[183, 184]. The substitutional Li atoms in the first layer of an Al_3Ti -type or Cu_3Au -type structure have only 8 nearest-neighbor Al atoms to receive their

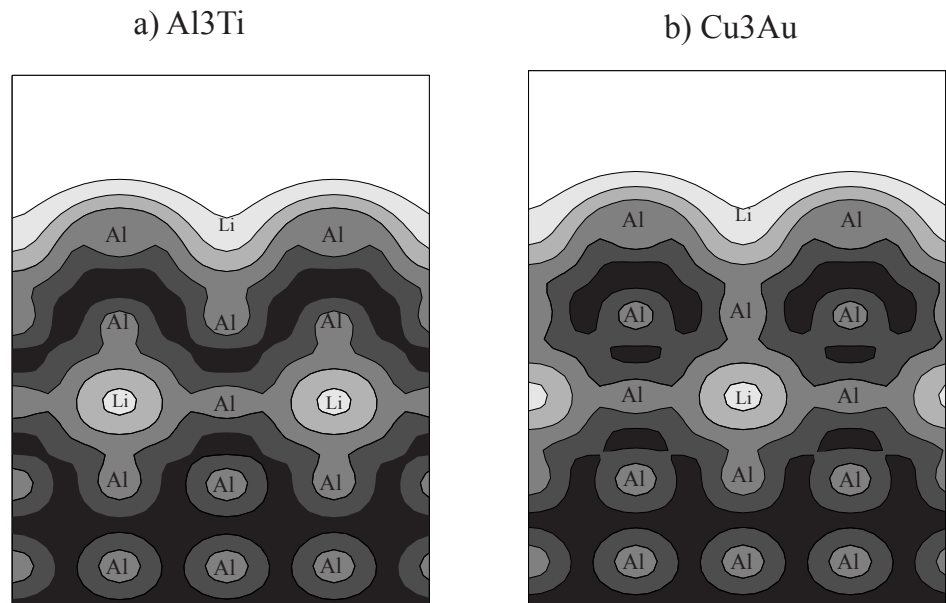


Figure 6.3: Electron density projection of a) Al₃Ti-type and b) Cu₃Au-type structures respectively. The horizontal direction on the plot is parallel to the surface, while vertical direction is perpendicular to the surface. Note that the electron density has been integrated in the [100] direction giving the appearance of a cubic structure. Atom positions are indicated on the plot, due to the projection along the [100] direction not all atoms are in the same plane parallel to the paper. Black denotes the area of highest electron density, while white denotes the areas of lowest density on the plot. The enhanced electron density of the Al-Al bindings between the second and third layer of the Al₃Ti-type structure, should be noted.

valence charge, as opposed to twelve nearest-neighbors in the bulk. However, in the Al_3Ti -type structure, these Li atoms can donate charge to a next-nearest-neighbor Al atom in the third layer, that is not present in the Al_3Li -type structure. A further strengthening of Al-Al bonds in this way is suggested by an additional pile-up of charge found in electron density projections of the third layer in the Al_3Ti structure, as shown in Fig.6.3

In view of the agreement between the LEED and DFT studies of the three-layer surface alloy, it was of obvious interest to investigate the further development of the structure with depth. DFT calculations for a five layer $\text{Al}(100)\text{-}c(2 \times 2)\text{-}3\text{Li}$ alloy show that the five layer alloy reverts to an Cu_3Au stacking, but preserves the Al_3Ti structure at the surface! The stacking sequence of the mixed Al/Li layers is thus baa, as opposed to aaa for Al_3Li . The adsorption energies and structural parameters of the four possible stacking sequences of mixed $c(2 \times 2)$ layers are given in Table 6.1. It is interesting to note that in the most energetically favorable baa structure there is a large rumpling (-0.2\AA) of the third layer, which is not present in the three layer surface alloy. Finally, it is noted that further DFT calculations of the bulk Al_3Li alloy for structures of the Al_3Ti -type and Cu_3Au -type confirm the conclusions of Freeman et. al.[183], that the Cu_3Au -type structure is energetically favored. The energies of formation per atom[183] are found to be $\Delta H_f = -0.098\text{eV}$ for the Cu_3Au -type and $\Delta H_f = -0.082\text{eV}$ for the Al_3Ti -type. However, the *surface* structure of Al_3Li is predicted to have a stacking fault, such that it consists of a three-layer Al_3Ti structure on a Cu_3Au -type bulk. A surface three-layer Al_3Ti -type structure is favored by about 0.1eV per unit cell compared to a pure Cu_3Au -type crystal.

At the present time the fascinating theoretical predictions for the surface structure of bulk Al_3Li and the structure of a five-layer surface alloy await experimental confirmation. In the case of the surface alloy, test calculations indicate that a LEED structure analysis would be marginal because of lack of sensitivity at this depth, unless a significant rumpling ($\sim 0.2\text{\AA}$) of the third layer occurred, as predicted for the five layer alloy by DFT. However, attempts to prepare such an alloy to date indicate that diffusion of Li into the bulk occurs rather than growth of a third mixed Al/Li layer.

6.2 Al(110)-Li multi layer structures

6.2.1 Introduction

The formation of a $c(2 \times 2)$ -Li phase by adsorption of 0.5ML Li at room temperature was described in section 4.4 . This structure consisted of 0.5ML Li atoms adsorbed in two-fold substitutional sites on the Al(110) surface. In this section

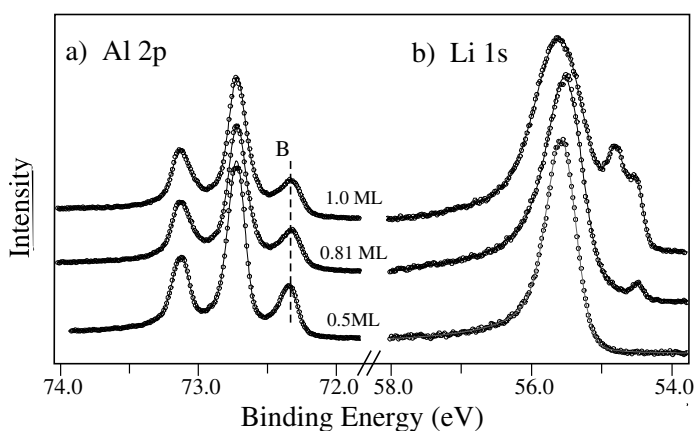


Figure 6.4: Core level spectra as a function of Li coverage after adsorption at room temperature. a) Al 2p. b) Li 1s.

the structures found at higher Li coverages are described

6.2.2 CLS and LEED pattern observations of multi layer structures

The evolution of the surface structure with Li coverage above 0.5ML was studied by correlated measurements of the LEED pattern and Li-1s and Al-2p core-level spectra.

The fractional-order spots in the $c(2 \times 2)$ LEED pattern, start to split along the [001] direction at a coverage of about 0.55ML Li, suggesting the occurrence of antiphase boundaries in the direction perpendicular to the close-packed rows. The LEED pattern gradually approaches a (2×1) periodicity. However the fractional-order spots weaken and finally disappear at 1 ML coverage, such that the (2×1) structure is never fully realized.

At coverages above 0.5 ML, Al-2p spectra are essentially unchanged with increasing coverage as can be seen in Fig. 6.4a. However, as can be seen in Fig. 6.4b, new features develop with coverage in the Li-1s spectra. At coverages above 0.5 ML the main peak broadens and a second peak at a binding energy of 54.48 eV is observed. At 1 ML coverage a third peak at a binding energy of 54.77 eV is also observed. The two new peaks are markedly narrower than the main peak, with FWHM of 250 and 350 meV, respectively, as compared to the FWHM of the main peak of 900 MeV at 1 ML coverage. These results are similar to those found for Li adsorption on Al(100), where at higher coverage, a second narrow peak was observed in the Li-1s spectrum [58], and attributed to the formation of a

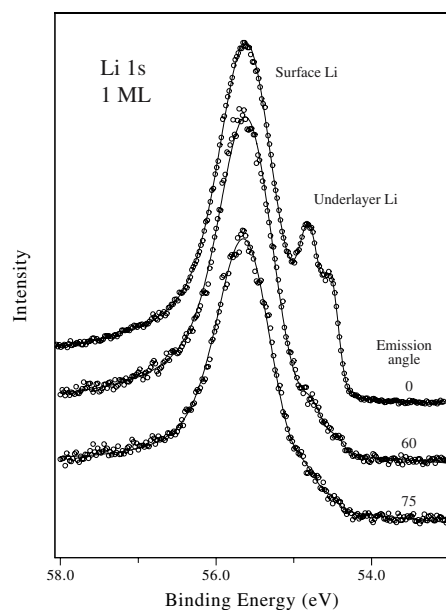


Figure 6.5: Li-1s spectra taken after adsorption of 1 ML Li at room temperature measured at 120 K for emission angles of 0° , 60° and 75° . Note the attenuation of the two narrow peaks at lower binding energy with increasing emission angle.

Li underlayer.

To investigate this possibility for Li adsorption on Al(110), measurements of Li-1s spectra for a coverage of 1 ML were made as a function of photon energy and emission angle. These measurements suggest that the two new peaks in the Li-1s spectra are in fact due to emission from Li atoms beneath the surface. This can be seen from the results shown in Fig. 6.5, where the strong attenuation of the two new peaks at higher emission angles can be seen. Thus core-level measurements at coverages above 0.5 ML suggest that further adsorption occurs in the form of one or more underlayers. At the same time the LEED pattern suggests that the surface structure moves in the direction of (2×1) periodicity, but becomes increasingly less well-ordered. Although the detailed structure is not known in this range of coverage, it is tempting to speculate that a transition occurs from a surface alloy with Al_3Ti -type structure to a surface alloy with the known Cu_3Au -type structure of bulk Al_3Li , as LEED measurements of an unreconstructed Cu_3Au -type (110) crystal would show a (2×1) diffraction pattern.

6.2.3 Segregation on $\text{Al}_{81.3}\text{Li}_{12.7}$ (110) versus adsorption of Li on Al(110)

It is interesting to compare the present results with those obtained by Kim et al [185] in a study of segregation of Li to the (110) surface of a dilute Al-Li alloy with 12.7 at. % Li. These authors found that annealing to 400-450 K after sputtering at room temperature led to the formation of a $c(2 \times 2)$ LEED pattern. Further annealing resulted in a weak (2×1) pattern. The coverage of the optimal $c(2 \times 2)$ structure was judged to be 0.5 ML from AES, which suggests that the $c(2 \times 2)$ structure found by segregation was similar to the substitutional structure found by adsorption in this study. The (2×1) structure found by further annealing is estimated to correspond to a surface Li concentration of 0.71 ± 0.2 ML, and could correspond to the phase formed at higher coverages in our adsorption experiments.

Chapter 7

Na multilayer surface structures on Al(110)

7.1 Introduction

The prospect of growing alkali structures several layers thick on Al surfaces at room temperature is (among other things) limited by the melting point of alkali metals $T(\text{Li})_{\text{melt}} = 453\text{K}$, $T(\text{Na})_{\text{melt}} = 371\text{K}$, $T(\text{K})_{\text{melt}} = 337\text{K}$, $T(\text{Rb})_{\text{melt}} = 312\text{K}$ and $T(\text{Cs})_{\text{melt}} = 302\text{K}$, which indicates that for K,Rb and Cs room temperature growth will probably saturate at submonolayer coverages, while it might be possible for Na and Li. As discussed in the introductory chapter previous studies on Al(111) found that saturation occurred at a coverage of 0.5ML Na in the form of a Na-Al-Na sandwich structure. But as will be shown below it is possible to go beyond 0.5ML on Al(110), although it has not been established whether thin films many layers thick can be formed.

As shown schematically in Fig. 7.1, phases of periodicity (3×2) , $c(2 \times 2)$, (3×1) , (4×1) , and (2×1) are formed sequentially with increasing coverage. However, only the $c(2 \times 2)$ and (4×1) phases are sufficiently well-ordered that their detailed structures can be determined by LEED. It was shown in section 4.5 that the $c(2 \times 2)$ phase is a single-layer surface alloy in which Na atoms occupy two-fold, substitutional sites formed by displacement of 0.5 ML Al atoms from the first layer of the substrate. In this chapter it is shown that the (4×1) phase contains 0.25 ML Na atoms in two-fold substitutional sites and 0.5 ML Na atoms chemisorbed in low-symmetry sites on the first Al layer. Based on the LEED structure determinations for the $c(2 \times 2)$ and (4×1) phases, and on CLS measurements as a function of Na coverage, models are proposed for the structures of the less well-ordered (3×1) , and (2×1) phases.

In the following, the LEED analysis for the (4×1) phase is described, and the

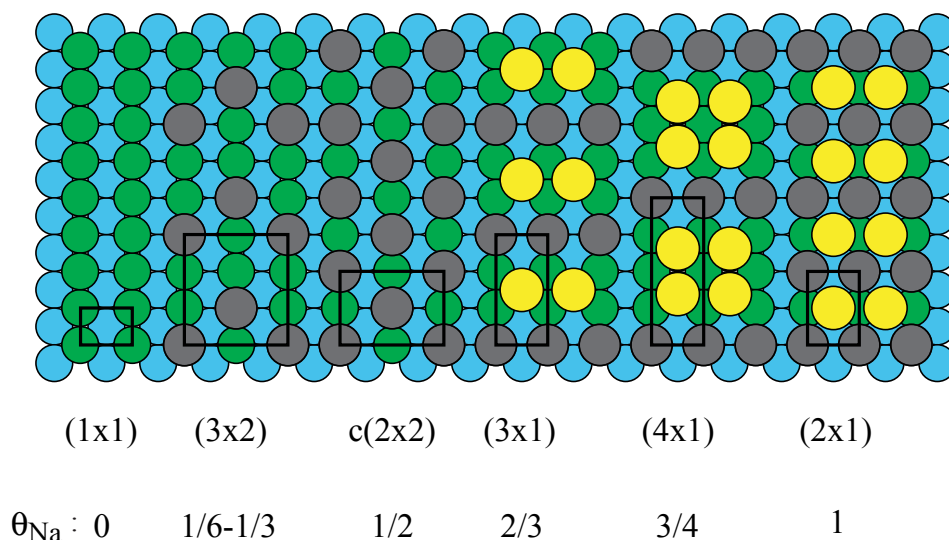


Figure 7.1: The adsorbed phases formed by adsorption of Na on Al(110) and schematic models of their structures as a function of Na coverage θ_{Na} . The unit cell for each phase is marked on the figure. Al atoms are shown in grey. Substitutionally adsorbed Na atoms are shown in dark grey. Chemisorbed Na atoms are shown in light grey.

determined structure is briefly compared with that of the $c(2 \times 2)$ phase. Core-level spectra for the $c(2 \times 2)$ and (4×1) phases are also shown, with a view to identifying the spectral features associated with the new surface structures. The evolution of CLS spectra as a function of Na coverage is described and correlation of the CLS measurements with LEED pattern observations is used to propose structural models for the (3×1) , and (2×1) phases.

7.2 Structure of Al(110)- (4×1) -Na.

7.2.1 LEED measurements and structural determination

Sharp (4×1) LEED patterns with good contrast were obtained after deposition of ~ 0.8 ML Na at room temperature and subsequent brief annealing to ~ 380 K to partially desorb Na. Optimal development of the (4×1) -Na phase was achieved by carrying out measurements of $I(V)$ spectra after successively annealing for 2 mins at increasing temperatures in the range 370–390 K until the ratio of integrated intensity in $I(V)$ spectra for fractional-order and integral-order beams reached a maximum. The structure could also be formed by adsorption of ~ 0.75 ML Na at room temperature. However, since the structure occurs in a narrow coverage range, it proved to be easier to prepare it by annealing.

Table 7.1: Atomic coordinates (xyz) and rms vibrational amplitudes (u) in Å determined for the (4×1) -Na structure. The x and y axes lies in the surface plane along the $[\bar{1}10]$ and $[001]$ directions, respectively. The z - axis is the outward surface normal. Interlayer spacings d_{ij} are also given. The bulk lattice constant at 100 K is $a_0 = 4.0341$ Å.

Layer	Atom	x	y	z	d_{ij}	u
1	Na	3.95 ± 0.08	$a_0/2$	2.09 ± 0.03		0.30 ± 0.03
	Na	-3.95 ± 0.08	$a_0/2$	2.09 ± 0.03		0.30 ± 0.03
	Na	0	0	1.01 ± 0.03		0.28 ± 0.05
	Al	$\sqrt{2}a_0$	0	0.10 ± 0.03		0.18 ± 0.03
	Al	2.86 ± 0.09	0	0		0.16 ± 0.04
	Al	-2.86 ± 0.09	0	0		0.16 ± 0.04
						1.27 ± 0.03
2	Al	1.41 ± 0.09	$a_0/2$	-1.27 ± 0.03		0.15 ± 0.05
	Al	-1.41 ± 0.09	$a_0/2$	-1.27 ± 0.03		0.15 ± 0.05
	Al	4.29 ± 0.09	$a_0/2$	-1.30 ± 0.03		0.16 ± 0.04
	Al	-4.29 ± 0.09	$a_0/2$	-1.30 ± 0.03		0.16 ± 0.04
						1.40 ± 0.03
3	Al	0	0	-2.69 ± 0.03		0.13 ± 0.06
	Al	2.81 ± 0.10	0	-2.75 ± 0.03		0.11 ± 0.05
	Al	-2.81 ± 0.10	0	-2.75 ± 0.03		0.11 ± 0.05
	Al	$\sqrt{2}a_0$	0	-2.76 ± 0.03		0.11 ± 0.05
						1.38 ± 0.03
bulk	Al					0.12 ± 0.06

positions displaced by $\pm 0.33 \text{ \AA}$ from the two sites of four-fold coordination in the unit cell.

It is interesting to note that the $c(2 \times 2)$ -Na phase, as shown schematically in Fig. 7.1, contains 0.5 ML Na atoms in substitutional sites [186]. Thus the addition of a further 0.25 ML Na in going from the $c(2 \times 2)$ phase to the (4×1) phase causes a partial lifting of the reconstruction of the substrate. This is discussed further below.

The structural parameters of clean Al(110), and the Al(110)-(4 × 1)-Na and Al(110)- $c(2 \times 2)$ -Na phases are compared in Table 7.3. It can be noted that the contraction of the first interlayer spacing in the clean Al(110) surface is retained on adsorption of Na, whereas the expansion of the second interlayer spacing is converted to a contraction in the adsorbed phases. It can also be noted that the rumpling of substrate layers induced by the adsorption of Na extends further into the bulk for the $c(2 \times 2)$ -Na phase than for the (4×1) -Na phase. As for the $c(2 \times 2)$ -Na phase relaxations of the substrate can be explained by the LF-PIFB model, discussed in chapter 5.

One can compare the structure of the (4×1) phase to the multilayer Na-Al-Na sandwich alloy found on Al(111) after adsorption of 0.5ML Na[26], shown in chapter 1. Ignoring the sandwiched Al atoms for a moment this structure is also composed of a chemisorbed Na layer on top of a substitutional Na/Al layer. Interestingly the nearest neighbor distance of 3.52 \AA between the two chemisorbed Na atoms of the (4×1) structure is identical to the nearest neighbor distance between the two types of Na in the (2×2) structure and only 4% less than in bulk bcc Na. This indicates that in both cases Na atoms are trying to arrange themselves in bcc Na-Na bonds. As can also be seen the distance between the chemisorbed and the substitutional Na atoms in the (4×1) structure is considerably larger than the nearest neighbor Na distance or even the Na bcc lattice constant of 4.23 \AA . This might explain why intermixed Al exists only for the Al(111)- (2×2) -Na phase, as the intermixed Al probably act to screen this denser Na structure.

Nearest neighbor distances between the substitutional Na and the Al surface atoms are 3.06 \AA and 3.03 \AA for the $c(2 \times 2)$ and (4×1) structures respectively. These two values are quite similar and also compare well with the nearest neighbor distance of 3.06 \AA found for the Al(100)- $c(2 \times 2)$ -Na substitutional structure [14]. This is perhaps surprising in that Na atoms on the Al(100) surface have four Al nearest neighbors while they on Al(110) have only two. Thus to some extent the Na atom positions are not determined by their coordination to the Al atoms or the presence of additional Na atoms. The Al-Na distances for substitutionally adsorbed Na in the Al(111)- $(\sqrt{3} \times \sqrt{3})R30$ -Na structure and for the Al(111)- (2×2) -Na sandwich structure are somewhat larger at 3.21 \AA and 3.17 \AA respectively.

A structure very similar to the Al(110)- (4×1) -Na found in this study has been found for Li adsorption on Cu(110)[187]. For adsorption of roughly 0.75ML Li

Table 7.2: Nearest neighbor distances between various atoms in the Al(111)-(2 × 2)-Na and Al(110)-(4 × 1)-Na structures. Na_c denotes chemisorbed Na atoms, Na_s denotes substitutional Na atoms and Al simply denotes the closest Al atom.

Distance	Al(111)-(2 × 2)-Na	Al(110)-(4 × 1)-Na
$d_{Na_c-Na_s}$ (Å)	3.52	4.56
$d_{Na_c-Na_c}$ (Å)		3.52
d_{Na_c-Al} (Å)	3.22	3.11
d_{Na_s-Al} (Å)	3.17	3.03

Table 7.3: Comparison of structural parameters for the clean Al(110) surface, and the Al(110)-c(2 × 2)-Na and Al(110)-(4 × 1)-Na phases. Vertical separations ("rumpling") between Al sublattices in the j 'th layer are denoted Δr_j . Interlayer spacings between the outer surfaces of the i 'th and j 'th layers are denoted d_{ij} .

Phase	(1 × 1)	c(2 × 2)	(4 × 1)
$d_{Na_2Na_1}$ (Å)			1.08
$d_{Na_rAl_1}$ (Å)		1.06	1.01
Δr_1 (Å)			0.10
d_{12} (Å)	1.31	1.27	1.27
Δr_2 (Å)			0.03
d_{23} (Å)	1.51	1.36	1.40
Δr_3 (Å)		0.14	0.06
d_{34} (Å)	1.37	1.36	1.38
Δr_4 (Å)			0.01
d_{45} (Å)	1.44	1.38	1.41
Δr_5 (Å)		0.06	0.02

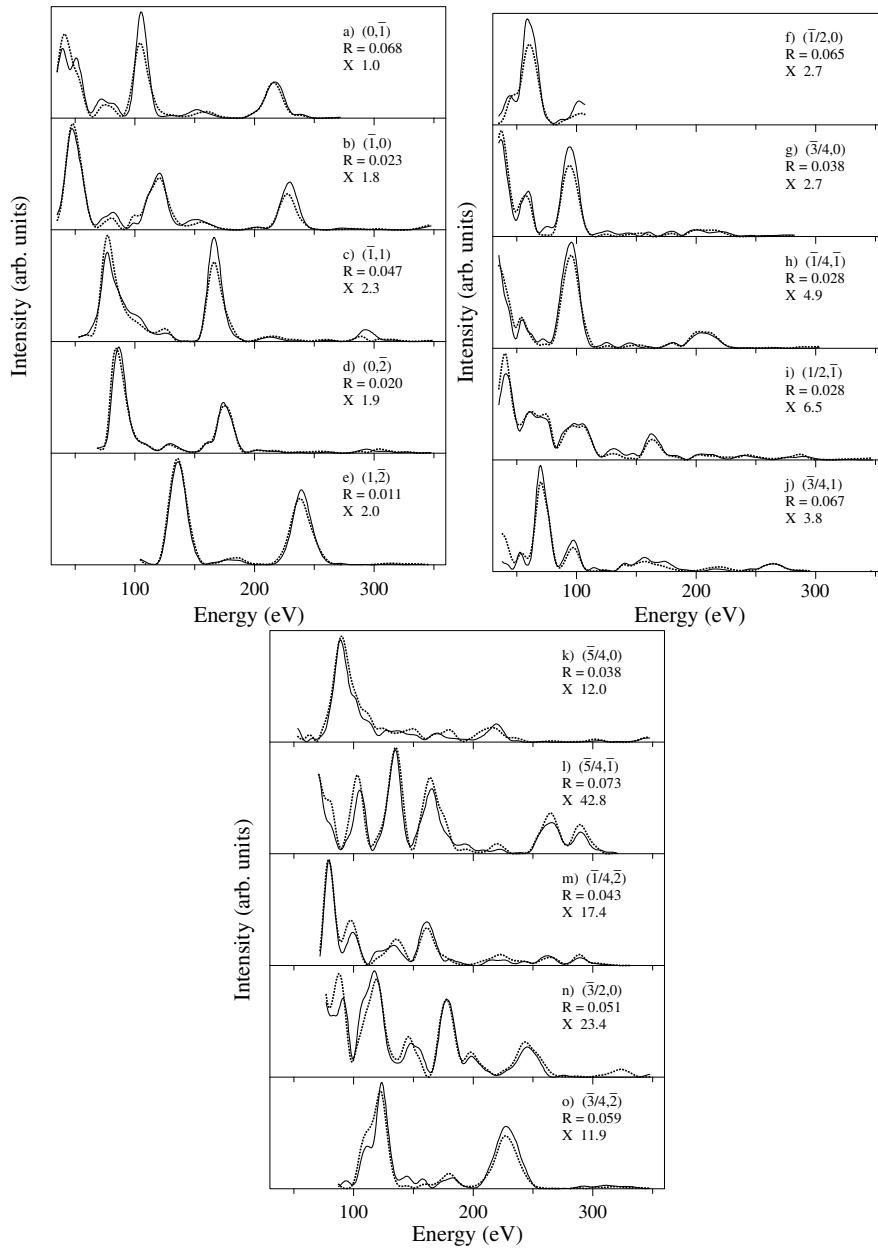


Figure 7.3: Comparison of experimental (solid lines) and calculated (dotted lines) intensity-energy spectra for $\text{Al}(110)\text{-(}4 \times 1\text{)-Na}$ for 5 integral-order beams a) to e) and 10 fractional-order beams f) to o). The beam hk indices, R factors, and scale factors are shown in each panel. The calculated spectra were obtained using the best-fit parameter values given in Table 7.1

at room temperature on Cu(110) a Cu(110)- (4×1) -Li structure formed which also consisted of 0.25ML Li adsorbed in two-fold substitutional sites, and 0.5ML Li chemisorbed in the troughs between the close packed layers. The Li-Li nearest neighbor distance of the chemisorbed Li was determined to $12\% \pm 7\%$ less than the nearest neighbor distance of bulk bcc Li, as compared to $4\% \pm 3\%$ less for the Na-Na nearest neighbor distances mentioned earlier. A rumpling of the first layer Cu atoms similar to the rumpling of the corresponding Al atoms is also found.

A quantitative LEED and HRCLS study has shown that it was possible to exchange the 0.25ML chemisorbed Na atoms of the Al(111)- (2×2) -Na structure with a heavier alkali, forming a ternary surface alloy[188]. It is quite conceivable that by adsorption of 0.25ML of Na on Al(110) followed by 0.25 or 0.5ML of a heavier alkali, one could form a (4×1) ternary structure on Al(110).

7.2.2 CLS measurements for the $c(2 \times 2)$ -Na and (4×1) -Na phases

CLS measurements for clean Al(110), Al(110)- $c(2 \times 2)$ -Na and Al(110)- (4×1) -Na are shown in Fig. 7.4 a, b and c respectively. Measurements of the Al-2p and the Na-2p core levels were made at photon energies of 102eV and 112eV respectively.

The Al-2p spectrum from the clean surface shown in Fig. 7.4a contains two spin-orbit doublets. The main doublet with $2p_{3/2}$ component at 72.72 eV is due to emission from bulk Al atoms, and the second doublet shifted by -80 meV is due to emission from surface Al atoms.

The corresponding spectrum from the $c(2 \times 2)$ -Na phase, shown in Fig. 7.4b, contains three spin-orbit doublets. In addition to the bulk doublet, shifted doublets occur at -69 meV and -410 meV with respect to the bulk doublet. Based on the structure determined in section 4.5 by quantitative LEED for the Al(110)- $c(2 \times 2)$ -Na phase, the component at -410 meV can be attributed to emission from Al atoms having two Na atoms as nearest-neighbors in the first, mixed Al/Na layer. The shift found here is similar to the shifts of -500 meV, -490 meV, and -385 meV found respectively for the Al(100)- $c(2 \times 2)$ -Na [189], Al(100)- $c(2 \times 2)$ -Li [58], and Al(110)- $c(2 \times 2)$ -Li phases where Na and Li are also adsorbed substitutionally. The component at -69 meV in the spectrum of Fig. 7.4b can be attributed to emission from Al atoms in the second layer.

Finally, the spectrum from the (4×1) -Na phase in Fig. 7.4c also contains three spin-orbit doublets. In addition to the bulk doublet, shifted doublets occur at -66 meV and -328 meV. From the models shown in Figs. 7.1 and 7.2 it can be seen that two of the three Al atoms in the (4×1) unit cell of the first layer are in equivalent positions. These atoms have one substitutionally-adsorbed Na and

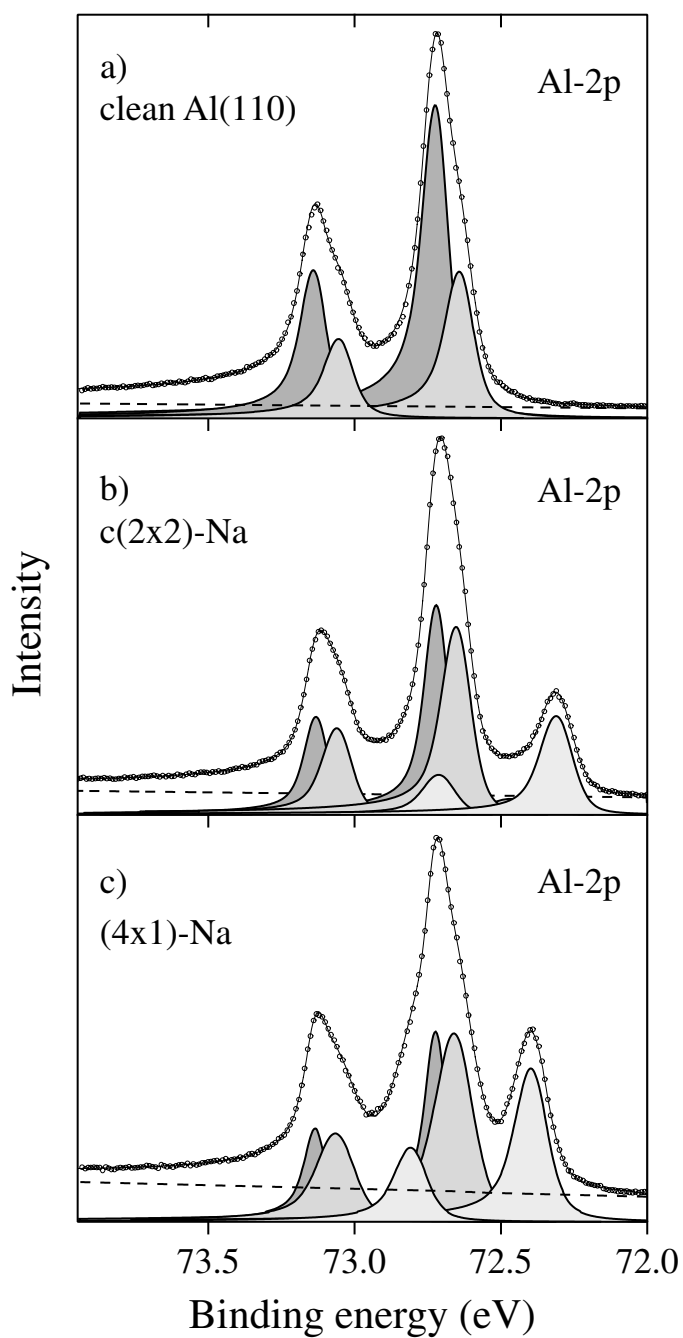


Figure 7.4: Al-2p spectra measured at 120 K for a) the clean Al(110) surface, b) the $c(2 \times 2)$ -Na phase, and c) the (4×1) -Na phase. The experimental measurements are shown as small circles. The line through the measurements is the fit to the data. The resolved spin-orbit doublets in each spectrum are shaded with the same gray tone. Bulk components are shaded in the darkest gray.

two chemisorbed Na atoms as nearest neighbors. The third Al atom in the unit cell has four chemisorbed Na nearest neighbors. Thus the shifted component at -328 meV can be attributed to unresolved contributions from the two types of Al atoms. The component at -66 meV in the spectrum of Fig. 7.4c can again be attributed to emission from Al atoms in the second layer.

7.3 Evolution of the surface structure with Na coverage

Extending the discussion of section 4.7, the evolution of the surface structure with Na coverage was studied by correlated measurements of the LEED pattern and Na-2p and Al-2p core-level spectra. The sequence of observed LEED patterns is briefly described, then the corresponding evolution of the CLS spectra is discussed.

7.3.1 LEED Patterns

With increasing coverage a (3×1) pattern forms at about 0.66 ML. However, this is always found to contain a weak, superimposed $c(2 \times 2)$ pattern. It has not been possible to develop a perfect (3×1) phase. At 0.75ML a (4×1) phase forms with sharp fractional order spots, although some very weak streaks along the $[\bar{1}10]$ direction were present. Adsorption of more than 0.75ML Na leads to a split-spot (2×1) pattern, where the splitting is in the $[\bar{1}10]$ direction. The complete adsorption sequence can be reversed by annealing to 340K, 390K, 410 K, for the (4×1) , (3×1) and $c(2 \times 2)$ phases respectively after adsorption of >0.8 ML. Desorption of all Na occurs at temperatures greater than 475 K resulting in the restoration of the original (1×1) LEED pattern.

7.3.2 CLS measurements

The integrated intensity in Na-2p spectra is shown as a function of coverage in Fig. 7.5. A distinct change of slope coincident with the occurrence of the (2×1) phase can be seen at a coverage of 1 ML Na, suggesting that a distinct, second layer of adsorbed Na begins to be formed.

The evolution of Na-2p and Al-2p core-level spectra with Na coverage is shown in Fig. 7.6.

At coverages in the range 0–0.75 ML, Na-2p spectra contain a single broad peak, as shown in Fig. 7.6a, which could indicate the occurrence of a single type of adsorbed Na. However, it is known from the LEED structure determination that

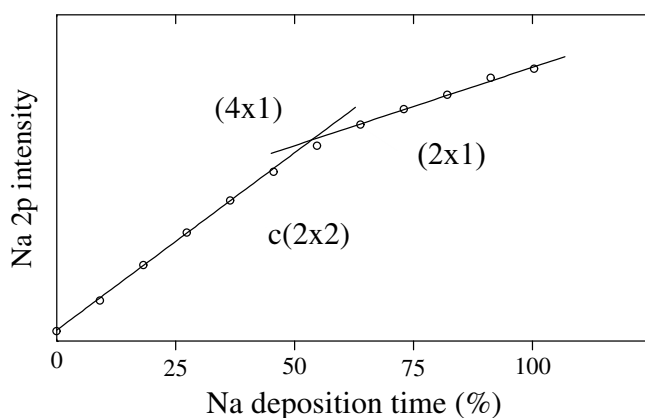


Figure 7.5: Integrated area in Na-2p spectra as a function of coverage. 100% indicates the maximum amount of Na adsorbed.

in fact two types of Na are present at coverages of about 0.75ML. It is assumed that the energy difference in the Na core-levels between the two types of Na is not large enough to be resolved due to the large FWHM of these components. The peak can in fact be fitted with a poorly-resolved spin-orbit doublet, with a splitting of 160 ± 10 meV, in agreement with a previous study of Na(110) films [157], and with FWHM's of ~ 300 meV for the two components. The $2p_{3/2}$ component shifts in energy from 30.99 eV at 0.1 ML to 30.68 eV at 0.75 ML. At coverages above 0.75 ML, the Na-2p peak splits into two spin-orbit doublets with $2p_{3/2}$ components at 30.84 eV and 30.41 eV, indicating the existence of Na atoms in two very different binding configurations. Thus, taken in conjunction with the change in slope of the uptake curve in Fig. 7.5, this spectrum can be attributed to the growth of a distinct second layer of adsorbed Na atoms.

In contrast to the monotonic evolution of the Na-2p spectra in the coverage range of 0–0.75 ML, the Al-2p spectra show quite dramatic changes with Na coverage, as can be seen in Fig. 7.6b.

As already noted, peak B can be attributed to emission from Al atoms with two substitutionally-adsorbed Na nearest neighbors. Assuming that the chemical shift induced by the number of nearest neighbors is roughly additive [190], then the smaller shift of peak A relative to peak B can be understood if peak A is due to emission from Al atoms having a single, substitutionally-adsorbed Na nearest neighbor.

In the coverage range 0.5–0.75 ML, peak B decreases in intensity and is replaced by a new doublet (peak C in the figure), with a binding energy which decreases with coverage from a shift of -272 meV at 0.59 ML to -328 meV at 0.75 ML. From the model shown in Fig. 7.1, it can be seen that the proposed structure of the (3×1) phase is simpler than that of the (4×1) phase, in that the

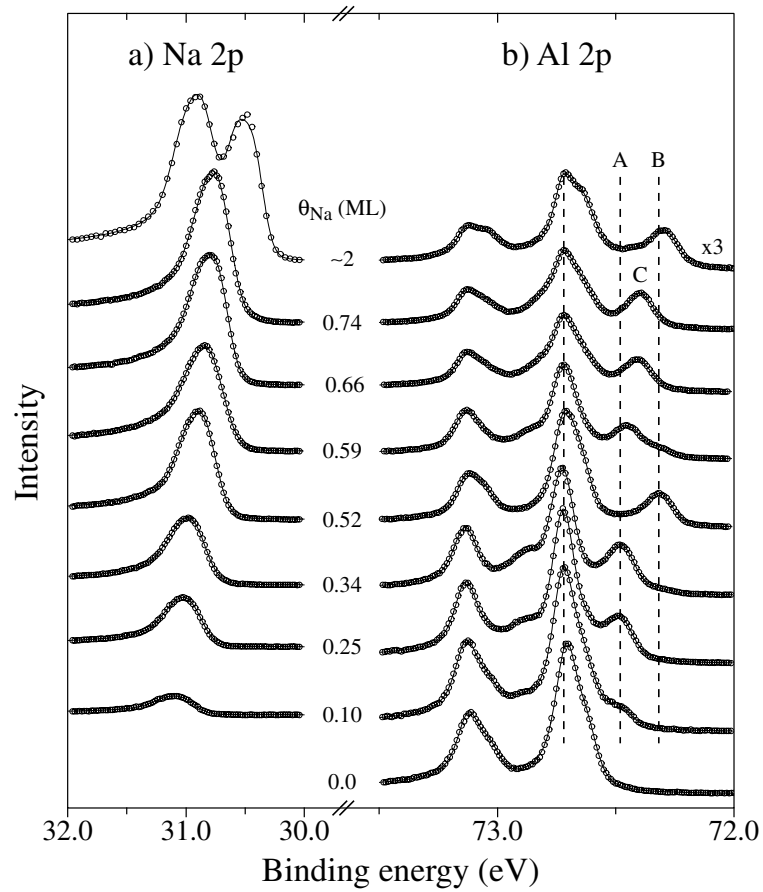


Figure 7.6: Core level spectra measured at 120 K as a function of Na coverage after adsorption at room temperature. a) Na 2p. b) Al 2p. The experimental measurements are shown as small circles. The line through the measurements is the fit to the data.

(3×1) unit cell contains only a single type of Al atom, having one substitutional and two chemisorbed Na atoms as neighbors. Thus peak C in the Al-2p spectrum for a coverage of 0.66 ML can be attributed to emission from such atoms. The minor shift to lower binding energy of peak C can then probably be attributed to the effect of an increasing proportion of chemisorbed Na atoms in the coverage range of 0.59–0.75 ML.

Finally, at Na coverages greater than 1 ML, where the LEED pattern indicates that a poorly-ordered (2×1) phase is formed, peak C is replaced by a doublet shifted by -430 meV, which is to say with a binding energy close to that of peak B. This suggests that Al atoms in the first layer again have two substitutionally-adsorbed Na atoms as nearest neighbors, as in the $c(2 \times 2)$ phase.

7.3.3 Discussion

Correlation of LEED pattern observations with CLS measurements suggests that Na adsorption at coverages in the range 0.5–0.66 ML, a (3×1) phase is formed, containing both substitutionally-adsorbed and chemisorbed Na atoms. This phase co-exists with the $c(2 \times 2)$ phase. After formation of the well-ordered (4×1) phase at a coverage of 0.75 ML, further adsorption leads to the formation of a poorly-ordered (2×1) phase, in which Al atoms have two substitutionally-adsorbed Na atoms as nearest neighbors, as in the $c(2 \times 2)$ phase.

It is interesting to note that the transition from the $c(2 \times 2)$ phase to the (4×1) phase involves a partial lifting of the reconstruction of the substrate. On the assumption that the formation of the $c(2 \times 2)$ phase involves the re-adsorption of 0.5 ML displaced Al atoms at surface steps, it follows that the formation of the (3×1) and (4×1) phases involves the reverse process, namely that Al atoms migrate back from the steps into the growing structures. A similar conclusion was reached previously concerning the transition from the $(\sqrt{3} \times \sqrt{3})$ -Na phase to the (2×2) -Na phase on Al(111). However, the Al(110)– (4×1) –Na phase differs from the Al(111)– (2×2) –Na phase in that the displaced 0.25 ML Al atoms are presumably re-adsorbed at steps rather than being incorporated in the (4×1) –Na structure.

A further novel feature of the present system is that adsorption of 1 ML Na, which leads to the formation of a poorly-ordered (2×1) –Na phase, reinstates the reconstruction of the substrate present in the $c(2 \times 2)$ –Na phase, once again requiring a re-adsorption of displaced Al atoms. Finally one can note that the desorption of the Na corresponding to the (2×1) phase occurs at around 380K, which is very close to the melting point of bulk Na.

Chapter 8

Silicon and germanium surface structures

8.1 Introduction

The results for Si and Ge presented here should be regarded as 'work in progress' and results are only preliminary. In switching from metal to semiconductor substrates it was thought to be necessary to establish a benchmark for the level of agreement between theory and experiment the Århus group could expect from quantitative LEED, as the agreement found by other authors in previous studies [191], was not as good as found for clean metal surfaces. Although a number of very good reasons for this will be given below, they are still just a testament to our inability to prepare and model Si and Ge sufficiently well. At the start of the work presented here, several ways of making further progress were considered. One could investigate how various preparation techniques would affect the I(V) spectra, and whether some of these spectra would agree better with theory than others after a full optimization of structural parameters. It would also be possible to record a considerably larger data set using our new LEED systems. Finally we could improve the precision of the theoretical calculations by including more phase-shifts and allowing a larger number of beams used for calculation of inter-layer scattering.

One could of course ask why bother at all, agreement between LEED theory and experiment for these clean surfaces is still reasonable, and one should perhaps instead progress to more complex systems. While this is in some sense true, several points should be made. Firstly, the unsatisfactory agreement between theory and experiment is also reflected in the uncertainties in various structural parameters. As LEED is a trial-and-error method, lack of agreement between theory and experiment also leaves room open for speculation that the structural

determination is incomplete or in fact wrong. Secondly, it is quite common that the agreement gets worse for adsorbate structures compared to the clean surface, and this could lead to serious problems in determining more complex structures. Finally it should be noted that the structural models found for the clean semiconductor surfaces are often used as a starting point for interpretation of experimental results on more complex systems. Building results on results is of course necessary to make scientific progress, but this approach can have similarities to building a house of cards, and in this case the structural determinations correspond to the bottom cards.

A typical relaxation on Si surfaces is the formation of Si dimers as depicted in Fig. 8.1 which reduce the number of dangling bonds per surface atom from two in the bulk-truncated geometry to one for each of the Si dimer atoms. This typically lowers the surface energy by about 1eV per dimer[192]. It has also been found[192–197] that the dimers are tilted, with one of the dimer atoms closer to the surface than the other. The tilting of the dimers is thought to be energetically favorable because the half-filled bands of the dangling bonds of a symmetric dimer rearrange themselves into a more filled band (related to the Si atom away from the surface) and a more empty band (related to the Si atom close to the surface), lowering the surface energy by 0.1eV per dimer[156, 192, 195, 197]. While dimers have been observed, by both STM[193] and quantitative LEED studies[198], already back in the 80's, experimental evidence of *tilted* dimers has been more difficult to come by. Indirect evidence of the presence of tilted dimers on the clean Si(100)-(2 × 1) has been found by PES[195] and STM studies[156], which both indicated that the Si(100)-(2 × 1) surface is nonmetallic. With symmetric dimers the Si(100) surface should become metallic, as the bands associated with the dangling bonds are half-filled. PES measurements[195] also identified two different types of Si surface atoms attributed to the two Si atoms in the tilted dimer.

Early quantitative LEED studies could not give any convincing evidence for the existence of tilted dimers as the overall agreement between theory and experiment was not so good [198]. This could perhaps be attributed to the use of very few beams and very few phase shifts in the theoretical calculations. However, miserable agreement found between different experimental data sets also indicated problems in preparation and measurements. A more recent study using data sets obtained from two different groups[191] resulted in somewhat more convincing results. Although the agreement between experimental data sets was still not too good, the structural parameters from the LEED analysis of the two data sets were in surprisingly good agreement.

Only symmetric dimers have usually been observed by STM surface topography [156, 193], but this has been explained[197] by noting that the energy barrier for reversing the tilt is only about 0.1eV. Thus it is thought that at room temperature dimers are flipping back and forth all the time leaving in average symmetric

dimers for STM to see. This has to some extent been confirmed by STM studies at low temperatures[196]. Why a tilted dimer is then found by LEED which also averages over vibrational configurations is perhaps difficult to understand.

Theoretically some controversy over this issue also exists as for example discussed by Tang et. al.[199]who notes that several theoretical calculations have found the symmetric dimer to be the most favorable, in contrast to the theoretical work mentioned above which found the tilted dimer to be energetically favorable.

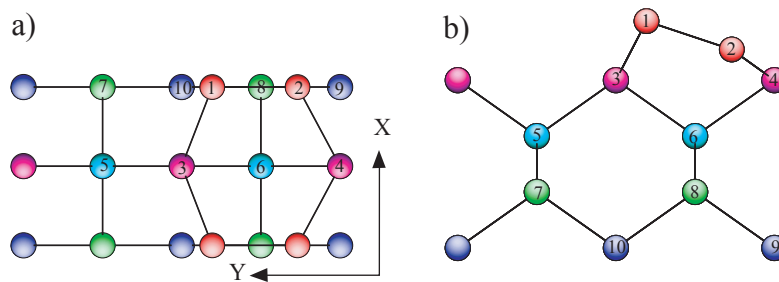


Figure 8.1: Hard-sphere model of the Si(100)-(2 × 1) dimer structure a) top view. b) side view. Numbers on the Si atoms refer to the numbering of Table 8.1

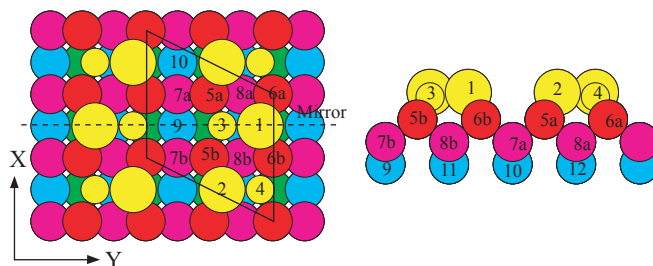


Figure 8.2: Model of the Ge(100)-c(4 × 2) alternating dimer structure a) top view. b) side view. Numbers on the Ge atoms refer to the numbering of Table 8.4. Unit-cell, axis and mirror line for this domain and as used in Table 8.4 are indicated.

8.2 Structural determination of Si(100)-(2 × 1)

8.2.1 Preparation of the Si(100) surface

Defects relating to the the presence of carbon and oxygen can exist on a Si(100) surface. On a standard silicon wafer in free air, a thick amorphous silicon-oxide film will have formed on top of the pure silicon. Carbon related defects exist throughout bulk silicon and also at the surface.

The silicon-oxide film can easily be removed by heating to about 1070K where oxygen desorbs. It is believed that carbon can not be desorbed. However it can be driven into the bulk of the silicon crystal by heating the crystal to 1300-1400K, where all traces of C at the surface disappear.

Despite the large number of studies of Si(100) there is no real consensus on how to prepare this surface. One can separate the many different preparation methods into roughly three categories[200]: Conventional sputtering and annealing, pure annealing and, finally, chemical etching prior to the introduction of the sample into vacuum followed by low temperature annealing in vacuum. Conventional sputtering and annealing have been used especially in early studies of Si surfaces, however it was later claimed that sputtering leaves defects on the Si(100) surface which can not be annealed away. In fact a STM study[201] found that defects due to ion bombardment can be completely removed by annealing to 1400K.

Pure annealing is recommended by Swartzentruber et. al[200], after the recipe:

- Outgas the sample holder and sample below the temperature at which the surface oxide is removed ($T=870\text{K}$), until the pressure stays in the 10^{-10}Torr range.
- Raise the sample temperature rapidly to 1520K and hold for 1-2 min. The pressure must stay at or below the 10^{-9}Torr range.
- Cool slowly at rates of $< 2^\circ/\text{s}$ from $\sim 1220^\circ$ to room temperature.

The surface quality obtained using this method was checked by STM[200] and a typical clean surface area is shown in Fig. 8.3.

Chemical etching is used in industry to clean Si surfaces, since annealing large wafers to temperature close to the melting point of Si is very problematic. This can lead not only to mechanical strain in the wafer, but it will also change designed impurity concentrations. For surface science, the etching method of A. Ishizaka and Y. Shiraki[202] has been applied in a significant number of studies. This method involves four main steps:

- Degreasing using methyl alcohol
- Boiling in HNO_3
- Boiling in NH_4OH
- Boiling in HCl

The treatment in principle leaves the surface without any carbon related defects and forms a thin protecting silicon oxide film on the surface[202]. Swartzentruber et. al. also tested this method and found that large SiC clusters formed on the

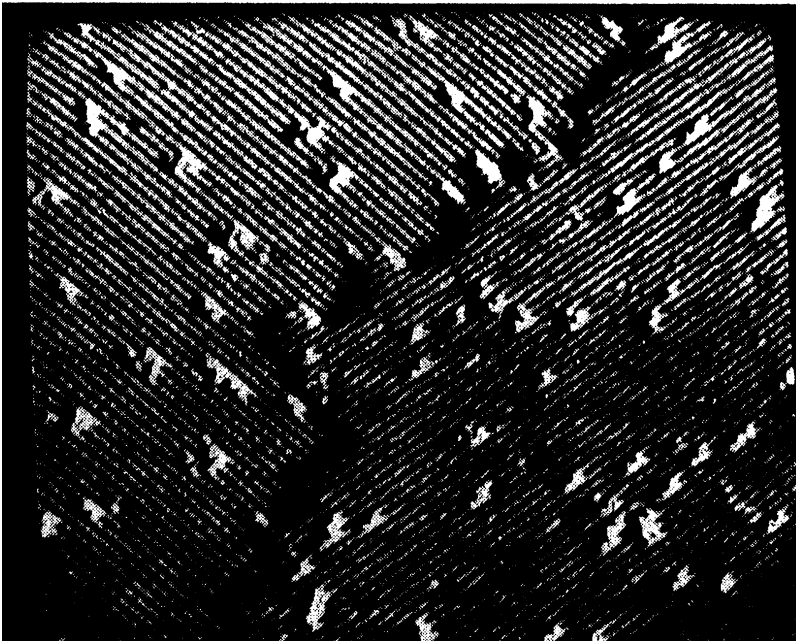


Figure 8.3: STM image $500 \times 400 \text{ \AA}$ from ref. [200] of the clean Si(100) surface after preparation using the method recommended by Swartzentruber et. al[200]

surface, between quite perfect Si domains. These SiC clusters proved impossible to remove by annealing. Speaking in favor of the etching methods is the fact that some authors[195, 203, 204], using this method, have been able to obtain the $c(4 \times 2)$ reconstruction, found below $T=200\text{K}$ for Ge(100), also on Si(100) at low temperatures. This could indicate that these Si(100) surfaces are especially well ordered, as the $c(4 \times 2)$ structure has a larger unit cell than the (2×1) structure.

All samples used in the present work were cut from the same n-type Si(100) wafer doped with phosphor for a resistance of $1\Omega\text{cm}$. The wafer was aligned and polished to within $\pm 0.5^\circ$ of the (100) plane.

Essentially all three methods of preparation have been attempted during our studies and a comparison of $I(V)$ curves measured using each of the three methods is shown in Fig. 8.4, Fig. 8.5 and Fig. 8.6. In all three cases the surface cleanliness was checked with AES, and no traces of either oxygen or carbon were found. It should be noted that carbon was not removed from the surface by the Ishizaka etching procedure when applied in this work. Therefore crystal had to be annealed to high temperatures to remove the carbon. The etching did however seem to leave only a very thin layer of SiO_2 , making the initial preparation of the surface easier.

The comparison of $I(V)$ curves recorded after the use of these three different preparation methods, clearly indicates that the specific surface preparation influences the structure as obtained by LEED. This was also assumed to be the reason

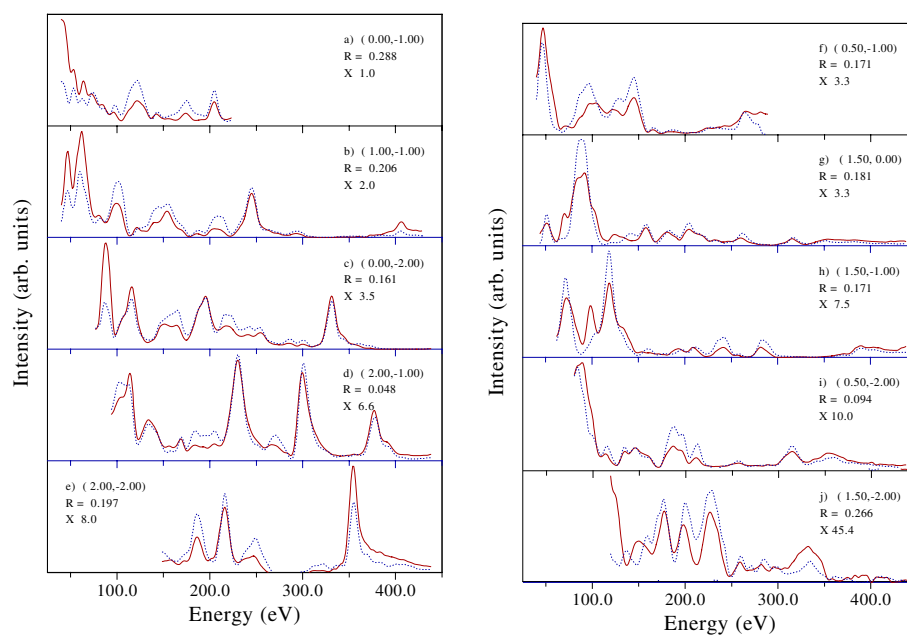


Figure 8.4: Comparison between experimental I(V) spectra obtained using the Ishizaka etching[202] followed by annealing (solid line) and the pure Swartzentruber[200] annealing procedure (broken line). The total R-factor for comparison between the two experimental data set was 0.17

for the discrepancies between the experimental I(V) curves used in ref. [191]. However the point is emphasized in this study as pieces of the same wafer have been used for all experiments, and the experiments have been carried out with the same experimental equipment.

It was never possible to detect any $c(4 \times 2)$ structure at low temperature. However upon cooling to $T=100\text{K}$ streaks reminiscent of a $c(4 \times 2)$ pattern could be found, when using the preparation method of Swartzentruber et. al. The LEED spots were sharp and background low for all spectra measured at 100K, indicating that at least short range order was good.

8.2.2 LEED experiment and structural determination

I(V) curves of the $\text{Si}(100)-(2 \times 1)$ structure recorded at 100K after preparation by the annealing procedure of Schwartzentruber et. al were used for the structure determination. I(V) curves obtained after the etching procedure of Ishizaka[202], have also been used for structural optimization, for comparison with the results from the I(V) curves obtained after the Schwartzentruber preparation.

A total of 22 symmetry-inequivalent beams were recorded. Significant beam damage occurred as a function of the total electron dose on the surface. This

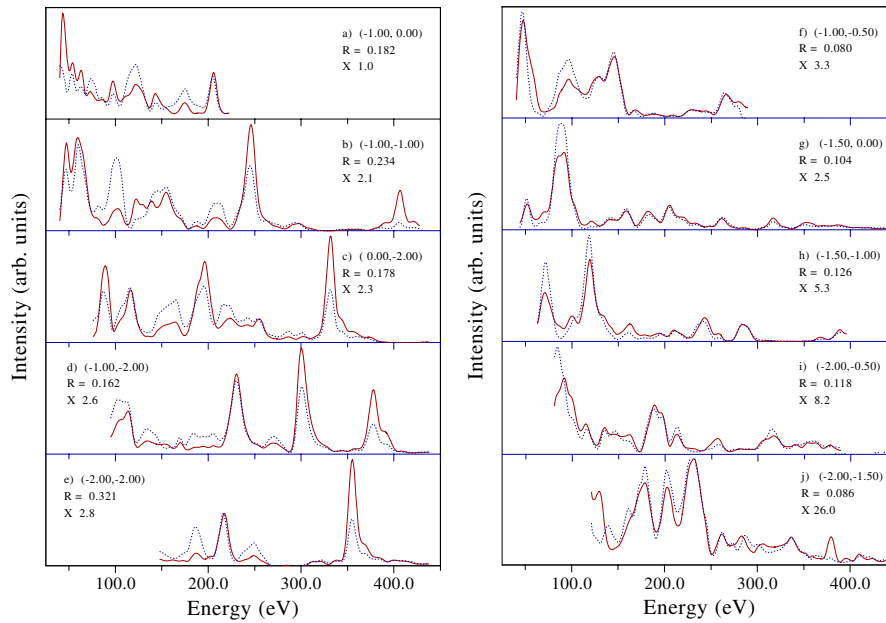


Figure 8.5: Comparison between experimental I(V) spectra obtained by sputtering with 1keV Ar^+ ions followed by annealing (solid line) and the pure Swartzentruber[200] annealing procedure (broken line). The total R-factor for comparison between the two experimental data set was 0.19

damage could be reduced to levels where the comparison between two LEED spectra recorded back-to-back would result in R-factors below R-factors found for comparison of symmetry-equivalent beams. Beam damage was reduced by lowering the beam current to an absolute minimum while raising the exposure time of the CCD chip, in order to still acquire high quality images. This approach works, because the largest period of time during recording is not used for exposure of the CCD chip, but rather for read-out of the CCD chip.

As starting models both the structural model of H. Over et. al.[191] and bulk terminated Si were chosen. Optimization of both models lead to a tilted dimer model as the optimal model. The tilted dimer structure only has one mirror plane, thus four different (2×1) domains will be present on the surface connected by 90° rotations. All parameters free to move in the first 5 layers, subject to the constraint of the mirror-plane symmetry, were relaxed. Comparison of experimental I(V) curves with I(V) curves obtained by use of the parameters listed in table 8.1 are shown in Fig. 8.7. A full optimization of the fit between experimental intensities obtained by the Schwartzentruber preparation and intensities calculated for the tilted dimer model shown schematically in Fig. 8.1 was carried out, with results listed below in Table 8.1.

As is quite evident from visual inspection of Fig. 8.7 and noting the final R-

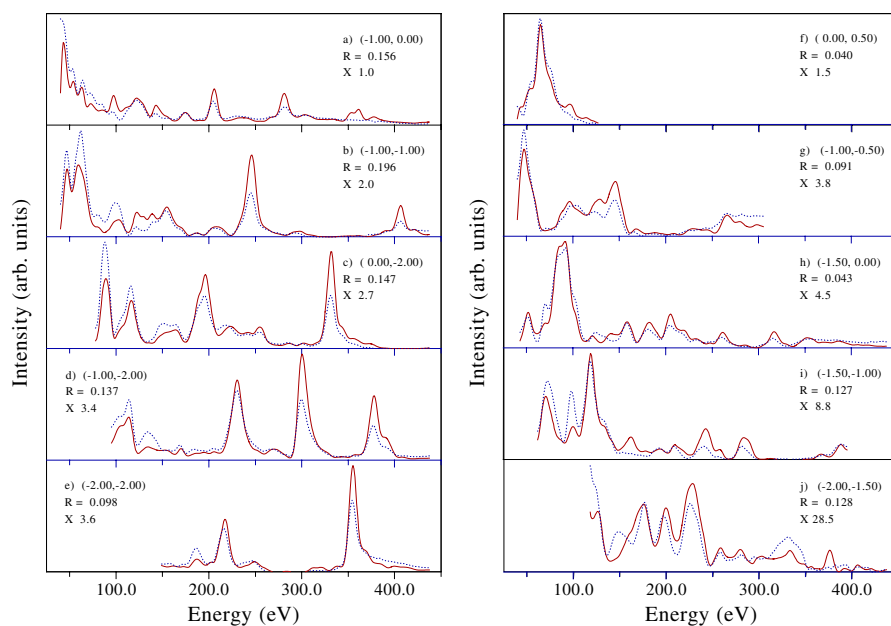


Figure 8.6: Comparison between experimental $I(V)$ spectra obtained by sputtering with 1keV Ar^+ ions followed by annealing (solid line) and using the Ishizaka etching[202] followed by annealing (broken line). The total R-factor for comparison between the two experimental data set was 0.12

Table 8.1: Atomic coordinates (xyz) and rms vibrational amplitudes (u) in \AA determined for the $\text{Si}(100)-(2 \times 1)$ structure, after preparation suggested the Schwartzentruber et. al. The x and y axes are denoted on Fig. 8.1. The z -axis is the outward surface normal. Parameters which have not been varied due to symmetry considerations are marked with a *. The origin in z is placed in the center of atom 4, while the origin of x and y is placed in atom 5. The bulk lattice constant at 100 K is $a_0 = 3.84 \text{\AA}$.

Atom	x (\AA)	y (\AA)	z (\AA)	u (\AA)
1	1.92*	2.49 ± 0.27	-1.36 ± 0.09	0.32 ± 0.08
2	1.92*	4.79 ± 0.18	-0.73 ± 0.06	0.25 ± 0.07
3	0.00*	3.73 ± 0.09	-0.01 ± 0.05	0.12 ± 0.06
4	0.00*	1.87 ± 0.1	0.00*	0.04 ± 0.06
5	0.00*	0.00*	1.22 ± 0.05	0.15 ± 0.06
6	0.00*	3.82 ± 0.1	1.53 ± 0.05	0.20 ± 0.06
7	1.92*	0.06 ± 0.1	2.59 ± 0.05	0.07 ± 0.06
8	1.92*	3.81 ± 0.1	2.90 ± 0.05	0.13 ± 0.06
9	1.92*	5.74 ± 0.1	4.08 ± 0.05	0.001
10	1.92*	1.83 ± 0.1	4.07 ± 0.05	0.002

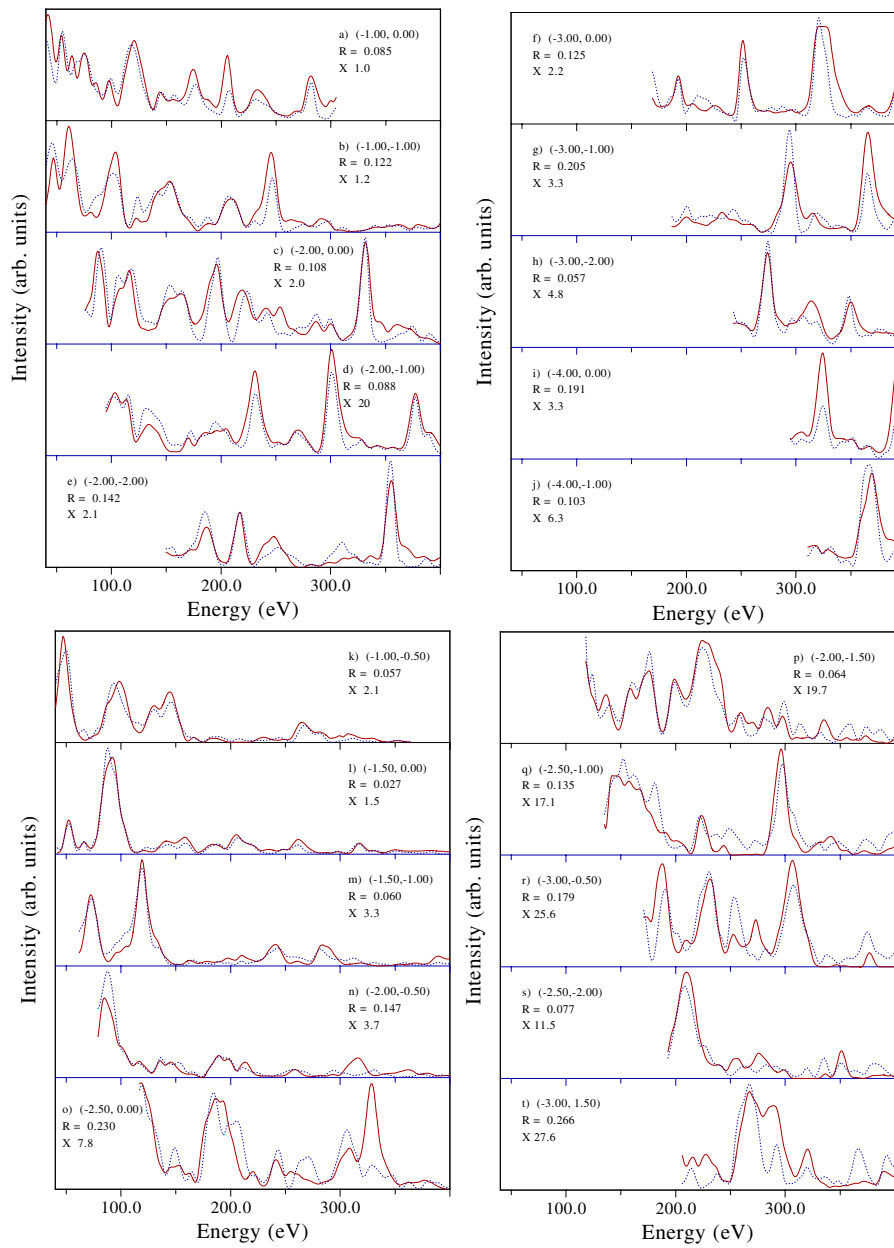


Figure 8.7: Comparison of experimental (solid lines) and calculated (dotted lines) intensity-energy spectra for Si(100)-(2 × 1) for 10 integral-order beams a) to j) and 10 fractional-order beams k) to t). The beam hk indices, R factors, and scale factors are shown in each panel. The calculated spectra were obtained using the best-fit parameter values given in Table 8.1

Table 8.2: Atomic coordinates (yz) in Å for the Si(100)-(2 × 1) structure determined by individual optimizations of four separate LEED data set, and from a DFT calculation. The LEED (A) spectra was obtained after preparation by the Schwartzentruber annealing method. The LEED (B) spectra was obtained after preparation by the etching procedure of Ishizaka. The LEED (C) spectra was obtained after preparation by sputtering and annealing to 1530K. The LEED (D) spectra was obtained after preparation by an etching procedure fairly similar to the procedure of Ishizaka.

Method:	LEED (A)		LEED (B)		LEED (C)		LEED (D)		DFT	
Ref.:	Present		Present		[191]		[191]		[191, 197]	
Atom	y	z	y	z	y	z	y	z	y	z
1	2.49	0.00	2.14	0.00	2.66	0.00	2.63	0.00	2.38	0.00
2	4.79	0.63	4.98	0.47	4.73	0.69	4.79	0.73	4.53	0.60
3	1.87	1.35	2.03	1.20	2.23	1.43	2.10	1.47	2.02	1.35
4	5.60	1.36	5.72	1.20	5.71	1.44	5.61	1.47	5.61	1.40
5	0.00	2.58	0.00	2.58	0.00	2.63	0.00	2.70	0.00	2.62
6	3.82	2.89	3.82	2.89	3.84	3.01	3.84	3.06	3.84	2.92
7	0.06	3.95	0.06	3.95	0.00	4.08	0.00	4.11	0.00	4.02
8	3.81	4.26	3.81	4.26	3.84	4.34	3.84	4.37	3.84	4.24
9	1.83	5.43	1.83	5.43	1.84	5.57	1.75	5.61	1.88	5.48
10	5.74	5.44	5.74	5.44	5.83	5.61	5.92	5.65	5.67	5.48

Table 8.3: Vibrational amplitudes of the first 10 Atoms in Å for the Si(100)-(2 × 1) structure determined by individual optimizations of three separate LEED data set.

Method:	LEED (A)	LEED (C)	LEED (D)
Ref.:	Present	[191]	[191]
Atom	u (Å)	u Å	u Å
1	0.32	0.18	0.20
2	0.25	0.16	0.15
3	0.12	0.15	0.16
4	0.04	0.07	0.07
5	0.15	0.10	0.09
6	0.20	0.09	0.09

factor of 0.09, agreement between theory and experiment is not as good as was found for our previous studies of clean aluminum surfaces. One explanation for the discrepancies could be that the underlying assumption of large domains of Si dimers tilted in the same direction is incorrect. As has been found for the similar Ge(100)-(2 × 1) reconstruction[205, 206], one could imagine that the Si dimers are tilted in many different configurations inside a domain. One way to deal with this is to adsorb atomic hydrogen on the surface, which effectively lifts the tilting of the dimers[207], and should hence leave a more well ordered surface. Alternatively to this explanation various defects on the Si(100) surface, as found for example by Schwartzentruber et. al.[200], could cause the discrepancies. Finally it is quite possible that the model assumptions of the theoretical calculations are not as good for the cases of Si and Ge, as for Al and other metals.

A full optimization of the fit between experimental intensities obtained after the Izihara etching procedure and intensities calculated for the tilted dimer model was also carried out. Although the I(V) spectra resulting after the Izihara etching procedure were quite different from the I(V) spectra obtained after pure annealing as seen on Fig. 8.4, the R-Factor for comparison between theory and experiment after the new optimization was as low as 0.11, as compared to the R-factor of 0.09 found for the I(V) spectra obtained after pure annealing. As shown in Table 8.2 and 8.3, however, significantly different structural and dynamical parameters were obtained. Especially the top most Si atom of the dimer is strongly affected.

Comparison of LEED structural determinations for Si(100) using our two data sets with structural determinations by H. Over et. al.[191] for two data sets is presented in Table 8.2 and 8.3. Although agreement is qualitatively quite good noticeable differences exist. The dimers found in this study are closer to the surface than the dimers found by H. Over et al, and the tilt angle (14°) found here is also smaller than the angle (15°-17°) found by H. Over et. al. In fact most interlayer spacings have decreased in the present work as compared to work by H. Over et. al. It can further be noted that the structural determinations presented in this work are in good agreement with DFT calculations of the structure also presented in Table 8.2. In fact the agreement between our structural parameters and the DFT calculations are better than for the parameters determined by H. Over et. al.

8.3 Structural determination of Ge(100)-c(4 × 2)

8.3.1 Introduction

One motivation for studying Ge is the choice of the Ge(100) surface as a model system for comparison to the very similar Si(100) surface. Like Si(100), the clean

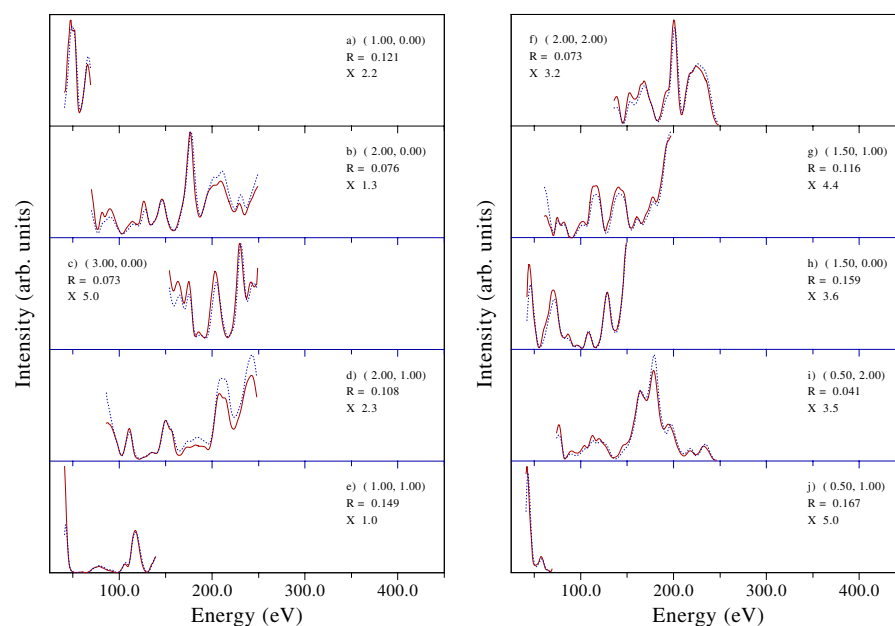


Figure 8.8: Comparison between experimental I(V) spectra of the Ge(100)-c(4 × 2) structures measured in Munich (solid line) and Aarhus (broken line).

Ge(100) forms a (2 × 1) tilted dimer reconstruction at room temperature[205, 206]. Unlike Si where a c(4 × 2) has only been found in some experiments[195, 203, 204], a c(4 × 2) structure can readily be formed on the clean Ge(100) surface below T=200K[208].

Previous structural determinations of the Ge(100)-c(4 × 2) phase are limited to a one surface X-ray diffraction study[209] which led to a model for the Ge(100)-c(4 × 2) structure. However this study was not without problems, especially due to the instability of the Ge surface. Ge(100) is quite reactive and as SXRD is time demanding (it takes a long time to record a sufficient number reflections), the surface may deteriorate significantly during the experiment.

8.3.2 LEED experiment and structural determination

Ge crystals used in the experiments presented here were cut from an Eagle-Picher Technologies n-type germanium wafer. The wafer was orientated to within $\pm 0.1^\circ$, and had a resistivity of $< 0.4 \Omega \text{cm}$. Preparing the Ge(100) surface is quite easy compared to Si(100). This is mainly because Ge does not contain the C defects that Si does. Thus one needs only remove the oxide film on the Ge(100) surface to end up with a clean surface. The usual procedure was to perform several cycles of sputtering with 1keV Ar^+ ions and annealing to 870K of the Ge(100) surface, which leads to a well-ordered clean surface.

Table 8.4: Atomic coordinates (xyz) and rms vibrational amplitudes (u) in Å determined for the Ge(100)-c(4 × 2) structure. The x and y axes lies in the surface plane along the $[\bar{1}10]$ and $[001]$ directions, respectively. The z - axis is the outward surface normal. Parameters which have not been varied due to symmetry considerations are marked with a *. The origin is placed at the position of atom 3 in Fig. 8.2. The bulk lattice constant at 100 K is $a_0 = 4.00$ Å. Superstructure lattice vectors are $\mathbf{a}_1 = (2a_0, 0.00)$, $\mathbf{a}_2 = (-a_0, 2a_0)$

Atom	x (Å)	y (Å)	z (Å)	u (Å)
1	0.00*	2.39	-0.84	0.19
2	-4.00*	-0.36	-0.85	0.19
3	0.00*	0.00*	0.00*	0.15
4	-4.00*	2.07	0.00	0.15
5a	2.00	-0.70	0.79	0.06
6a	2.00	3.21	0.79	0.09
7a	2.00	-2.80	1.77	0.10
8a	2.00	1.09	2.08	0.11
9	0.00	-2.80	2.98	0.13
10	4.00	-2.80	2.98	0.13
11	0.00	1.04	3.23	0.10
12	4.00	1.04	3.23	0.10

Upon cooling to 100K the LEED pattern resulting from the clean Ge(100) surface displayed a sharp c(4 × 2) pattern. I(V) spectra were recorded for 36 symmetry inequivalent beams. Beam damage was induced by the electron beam. However as in the case of Si(100), it was minimized by reducing the electron beam current. The reproducibility of the Ge(100)-c(4 × 2) structure can be demonstrated by comparison to an unpublished data set of the same structure obtained previously by W.Moritz and co-workers shown in Fig. 8.8. This indicates that the Ge(100)-c(4 × 2) structure is much less sensitive to the crystal sample or preparation procedure than is Si(100).

The c(4 × 2) structure is thought to consist of tilted dimers with alternating up and down configuration perpendicular and parallel to the direction of the dimer as depicted in Fig. 8.2. Structural determinations have been carried out both with the alternating dimer model as a starting point, and with bulk terminated Ge(100) as a starting point. Both optimizations converged towards similar structural parameters. The addition of Ge ad-atoms on top of the alternating dimer structure (as on Si(111)-(7 × 7)) was also attempted, but the presence of such atoms did not improve the agreement between theory and experiment. The best agreement at present has been obtained for the alternating dimer model. Unlike the SXRD study[209] where p2mm symmetry was assumed, it was assumed that each domain has only mirror plane symmetry across the axis shown on Fig. 8.2. There

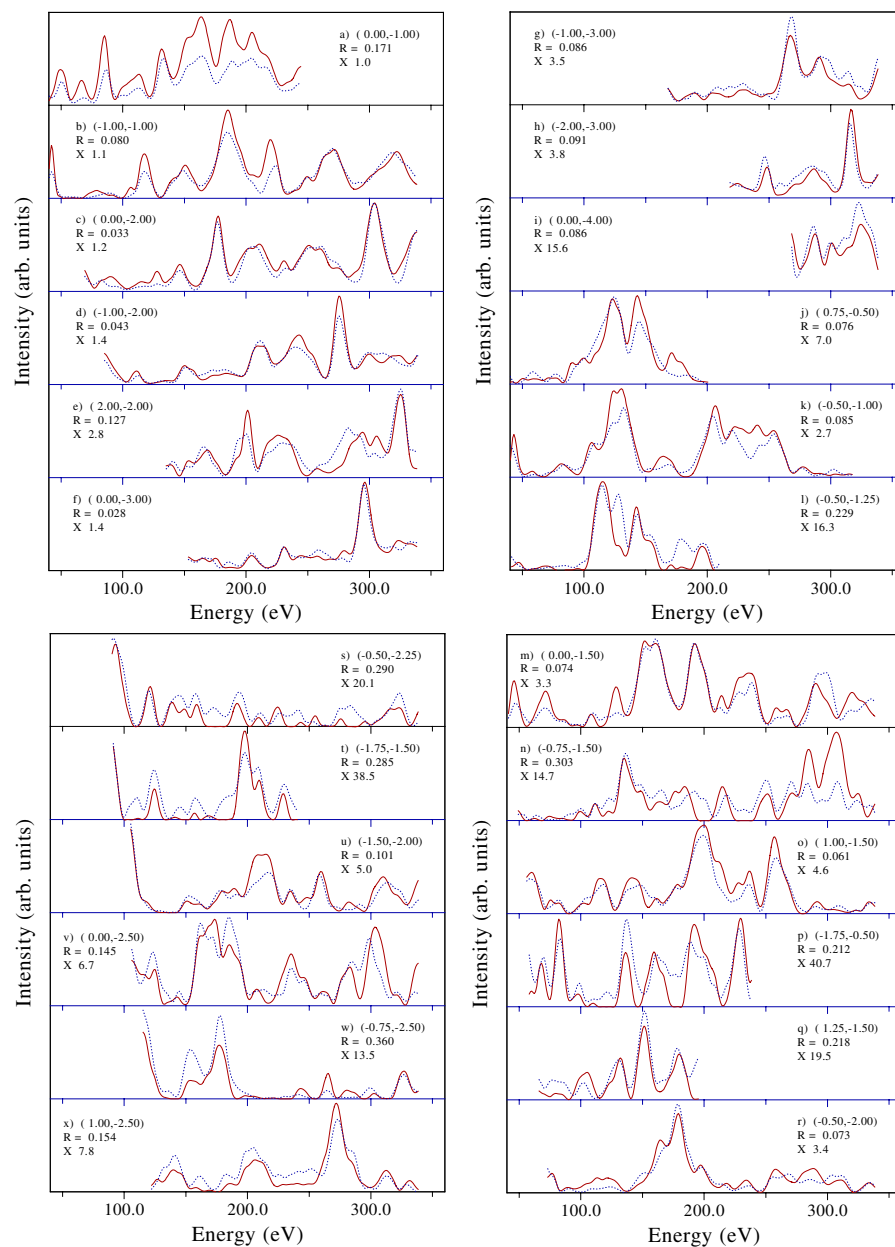


Figure 8.9: Comparison of experimental (solid lines) and calculated (dotted lines) intensity-energy spectra for Ge(100)-c(4×2). The beam hk indices, R factors, and scale factors are shown in each panel. The calculated spectra were obtained using the best-fit parameter values given in Table 8.4

Table 8.5: Atomic coordinates (yz) in Å for the Ge(100)-c(4 × 2) structure determined by LEED, SXRD and MD-DFT calculations.

Method:	LEED		SXRD		MD-DFT	
Ref:	Present		[209]		[210]	
Atom	y(Å)	z(Å)	y(Å)	z(Å)	y(Å)	z(Å)
1	2.39	-0.84	2.41	-0.84	0.90	-0.59
2	-0.36	-0.85	-0.41	-0.84	0.58	-0.60
3	0.0	0.0	0.0	0.0	0.0	0.00
4	2.07	0.00	1.60	0.00	2.03	0.01
5a	-0.70	0.79	-1.10	0.82	-0.87	0.90
6a	3.21	0.79	2.90	0.82	2.94	0.90

are actually quite a number of structural parameters which can be varied. Atoms 1 - 4 in Fig. 8.2 are allowed to move free in z and y, but must remain fixed in x due to symmetry. Atoms 5a and 5b can move *together* both in x, y and z, such that they move in an identical fashion in y and z, while they can move exactly opposite to each other in the x direction. The same movements are allowed for 6a with 6b, 7a with 7b and 8a with 8b. Atoms 9 - 12 obey the same rules of movements as atoms 1 - 4. It should be noted that the optimization process is not finished at present for this structure as convergence has not been reached.

Structural parameters optimized at present for this model are presented in table 8.4, and comparison of theoretical and experimental I(V) curves assuming these parameters are shown in Fig. 8.9 At present an R-factor of 0.12 has been obtained, which is considered unsatisfactory at least compared to previous studies on metal surfaces. Although results of the structural refinement is only preliminary it is still of some concern that agreement between theory and experiment for the LEED spectra are so bad. For the Si(100)-(2 × 1) structure the measured spectra were questionable and there was evidence of disorder even on a very short length scale, which could explain the disagreement between theory and experiment. Both these concerns are however of less importance for the Ge(100)-c(4 × 2) structure. It has been demonstrated here that there is good agreement between two independent experimental data set, and it has also been argued that the c(4 × 2) structure exists when the surface is quite defect free. This could lead one to suspect that a significant structural feature is missing or that the model potential used in the LEED calculations is not as good enough for Ge.

A comparison of structural models obtained from our LEED measurements, SXRD measurements[209] and ab initio molecular dynamics DFT calculations[210] are presented in table 8.5. It can be seen that agreement between the SXRD and the preliminary LEED structural determinations is quite good. The agreement with DFT calculations is also quite reasonable.

8.4 Na adsorption on Si(100) and Ge(100)

8.4.1 Introduction

As discussed in ref. [40, 211, 212] for example, alkali adsorption on Si(100) has been the subject of a large number of studies, but there are still some outstanding problems. For Na adsorption, no structures are known on this surface with any certainty, and even the coverage dependence on various crystal phases is not completely documented. After adsorption of about half the saturation coverage of Na at room temperature a Si(100)-(4 × 1)-Na LEED pattern forms, which at higher coverages changes to a Si(100)-(2 × 1)-Na pattern up until saturation. The saturation coverage has been the subject of some controversy as values ranging from 0.5ML to 1.0ML have been obtained.

There have been a number of attempts to determine the Na adsorption site(s) and various simple possibilities which have been considered[213] are shown in Fig. 8.10. A quantitative LEED study of the Si(100)-(2 × 1)-Na phase has been performed[213], but the results were not satisfactory, since it was not possible to distinguish between a model with 0.5ML Na in pedestal sites and a model with 0.5ML Na in the pedestal site and 0.5ML Na in valley bridge sites.

Results of a recent theoretical ab initio study[214] of the structures of Na on Si(100) as a function of coverage show that at a coverage of 0.25ML the pedestal site is energetically favorable, at 0.5ML a combination of the pedestal and the cave site is most favorable, while at 0.75ML a combination of two hollow site Na atoms with a pedestal site Na atoms is the most favorable. At 1.0ML Na the combination of two hollow site and two pedestal site Na atoms is the most favorable.

Photoemission studies[215] favor a model where the (4 × 1) LEED pattern forms at 0.33ML and only one kind of Na exists on the surface, while (at least) two kinds of Na exists at higher coverages.

The sequence of LEED patterns found for adsorption of Na at room temperature on Ge(100) are completely identical to the sequence on Si(100)[216]. For the Ge(100)-(2 × 1)-Na structure found at saturation coverage SXRD measurements[212] indicate that the Na atoms are positioned at cave and valley bridge sites. However the cave site Na atoms are strongly disordered within the surface plane and have been modelled in split positions parallel to the dimers. The disorder could also explain some of the discrepancies found between previous studies[212], perhaps even for other Si(100), Ge(100) alkali studies.

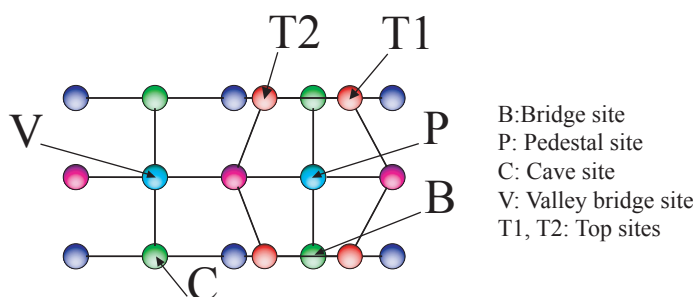


Figure 8.10: Various high symmetry adsorption sites in the (2×1) unit cell.

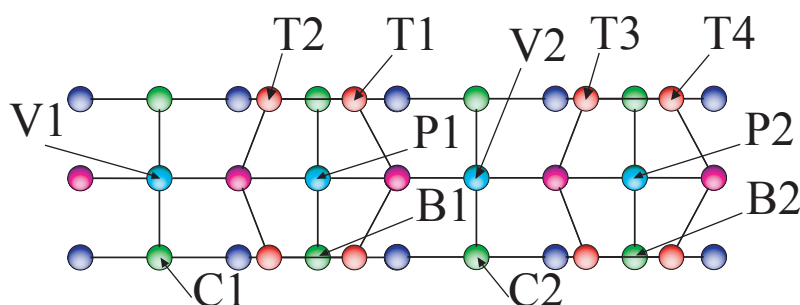


Figure 8.11: Various high symmetry adsorption sites in the (4×1) unit cell. B1,B2 are bridge sites, P1,P2 are pedestal sites, C1,C2 are cave sites, V1,V2 are valley bridge sites and T1 -T4 are Top sites

8.4.2 LEED experiment and structural determination

Na adsorption on Si(100)

LEED I(V) spectra were recorded at $T=100\text{K}$ for the adsorption of Na at room temperature. Measurements were performed for the Si(100)- (2×1) -Na phase at saturation coverage and the Si(100)- (4×1) -Na phase found at approximately half the saturation coverage. The optimally-developed Si(100)- (4×1) -Na structure was found with the help of comparison between integral order beams and the fractional order beams belonging only to the (4×1) pattern, as described for alkalis adsorption on metal surfaces in section 2.1.4 .

The Na coverage for the Si(100)- (2×1) -Na structure could be anything between 0.5ML and 1.0ML (one or two Na atoms per (2×1) unit cell). All models with one or two Na atoms in the high symmetry sites noted on Fig. 8.10 were investigated. It turns out that best agreement in this preliminary survey was obtained with a model containing one Na atom in the pedestal site and one Na atom in the valley bridge site.

Plots of some of the experimental I(V) spectra and spectra calculated for the best parameter values at present given in Table 8.6 are shown in Fig.8.12 for a

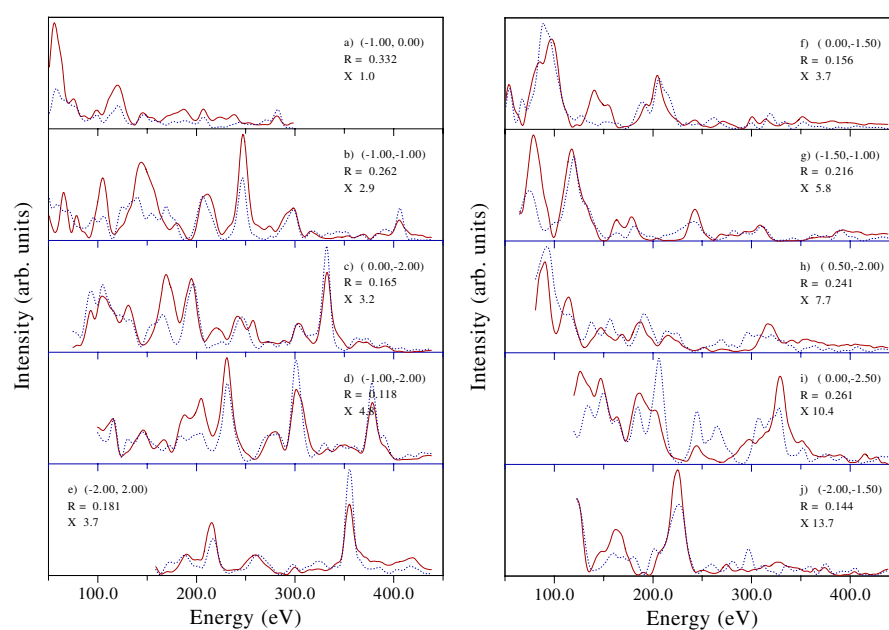


Figure 8.12: Comparison of experimental (solid lines) and calculated (dotted lines) intensity-energy spectra for Si(100)-(2 × 1)-Na for 5 integral-order beams a) to e) and 5 fractional-order beams f) to j). The beam hk indices, R factors, and scale factors are shown in each panel. The calculated spectra were obtained using the best-fit parameter values given in Table 8.6, for a model with one Na atom in the pedestal site and on Na atom in the valley bridge site.

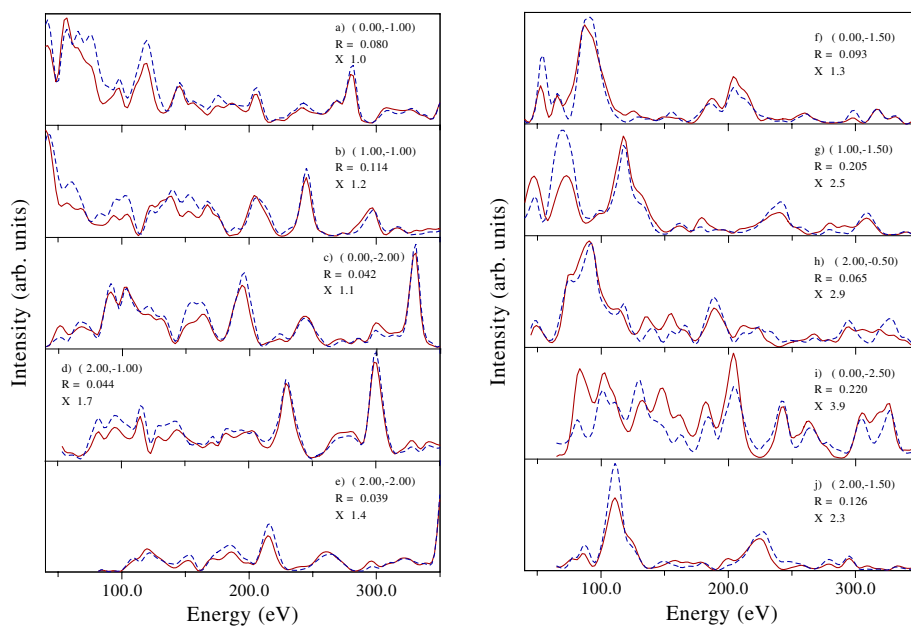


Figure 8.13: Comparison between theoretical $I(V)$ spectra of the $\text{Si}(100)-(2 \times 1)\text{-Na}$ structures with one Na atom in the pedestal site (solid line) and with an additional Na atom in the valley bridge site (broken line).

model containing one Na atom in the pedestal site and one Na atom in the valley bridge site. This model was however not significantly better than the model with just one Na atom in the pedestal site. The problem at of distinguishing between the two models is related to the fact that the agreement with experimental data is poor. As can be seen on Fig. 8.13 a comparison between the $I(V)$ spectra calculated with one and two Na atoms in the unit cell show that they agree considerably better than do the $I(V)$ spectra of the best theoretical model with experimental data shown in Fig. 8.12.

The Na coverage for the $\text{Si}(100)-(4 \times 1)\text{-Na}$ structure could also be anything between 0.25ML and 0.5ML (one or two Na atoms per (4×1) unit cell). All models with one or two Na atoms in the high symmetry sites noted on Fig. 8.11 were investigated. It turns out that best agreement in this preliminary survey was obtained with a model containing one Na atom in the pedestal site P1 and one Na atom in the adjacent valley bridge site V1. However the position of the Na atom parallel to the dimers was very uncertain, and almost equally good agreement was obtained when the second Na atom was positioned in the V2 or P2 sites.

Plots of some of the experimental $I(V)$ spectra and spectra calculated for the best parameter values at present given in Table 8.6 for a model with one Na atom in the pedestal site P1 and one in the valley bridge site V1 are shown in Fig. 8.14.

Table 8.6: Atomic coordinates (xyz) and rms vibrational amplitudes (u) in Å determined for the Si(100)-(2 × 1)-Na structure for a model containing one Na atom in the pedestal site and one Na atom in the valley bridge site as denoted on Fig. 8.10. The x and y axes are denoted on Fig. 8.1. Na atoms are denoted by A and B, while Si atoms are numbered 1-6. The z - axis is the outward surface normal. Parameters which have not been varied due to symmetry considerations are marked with a *. The origin was placed in the center of atom 4. The bulk lattice constant at 100 K is $a_0 = 3.84$ Å.

Atom	x (Å)	y (Å)	z (Å)	u (Å)
A	0.00*	-1.41	-2.34	0.41
B	0.00*	2.18	-2.34	0.45
1	1.92*	3.17	-1.35	0.32
2	1.92*	0.38	-0.62	0.25
3	0.00*	3.57	-0.01	0.12
4	0.00*	0.00*	0.00*	0.04
5	0.00*	5.71	1.22	0.13
6	0.00*	1.81	1.52	0.19

Table 8.7: Atomic coordinates (xyz) and rms vibrational amplitudes (u) in Å determined for the Si(100)-(4 × 1)-Na structure for a model with one Na atom in the pedestal site P1 and one in the valley bridge site V1 as denoted on Fig. 8.11. The x and y axes are denoted on Fig 8.1. Na atoms are denoted by A and B, while Si atoms are numbered 1-8. The z - axis is the outward surface normal. Parameters which have not been varied due to symmetry considerations are marked with a *. The origin is placed in the center of atom 4. The bulk lattice constant at 100 K is $a_0 = 3.84$ Å.

Atom	x (Å)	y (Å)	z (Å)	u (Å)
A	0.00*	1.92	-2.98	0.50
B	0.00*	-1.92	-1.67	0.55
1	1.92*	2.88	-1.46	0.29
2	1.92*	-4.63	-1.39	0.29
3	1.92*	0.09	-1.32	0.29
4	1.92*	-7.11	-0.79	0.29
5	0.00*	-7.65	-0.01	0.12
6	0.00*	0.00*	0.00*	0.12
7	0.00*	-3.93	0.04	0.05
8	0.00*	3.65	0.05	0.05

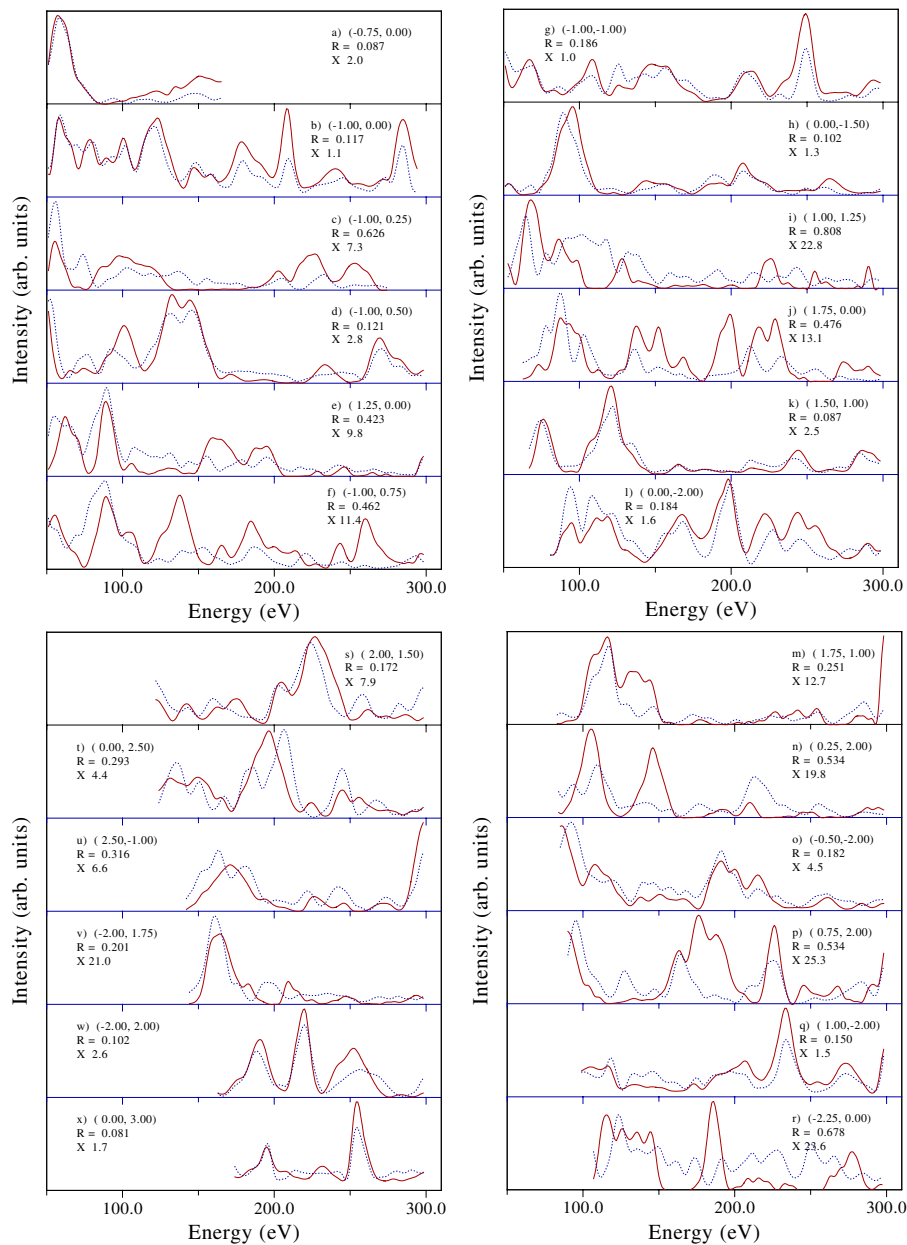


Figure 8.14: Comparison of experimental (solid lines) and calculated (dotted lines) intensity-energy spectra for Si(100)-(4x1)-Na. The beam hk indices, R factors, and scale factors are shown in each panel. The calculated spectra were obtained using the best-fit parameter values given in Table 8.7 for a model with one Na atom in the pedestal site P1 and one in the valley bridge site V1

Na adsorption on Ge(100)

Adsorption of Na on Ge(100) leads to the same sequences of LEED patterns as found for adsorption of Na on Si(100). Measurements were performed of the Ge(100)-(2 × 1)-Na at saturation coverage and the Ge(100)-(4 × 1)-Na structure found at approximately half the saturation coverage.

In the case of Ge(100), Na was also adsorbed at T=100K on the c(4 × 2) reconstruction. Adsorption of small amounts of Na did not change the c(4 × 2) LEED pattern. But quite interestingly, the c(4 × 2) LEED pattern changed into the (4 × 1) LEED pattern at about the same coverage as was the case for adsorption at room temperature. Further adsorption lead also to the formation of a (2 × 1) structure as was the case for adsorption at room temperature. I(V) spectra recorded for the Ge(100)-(4 × 1)-Na phase formed by adsorption at room temperature and at T=100K are shown in Fig. 8.13. As can be clearly seen, the two structures are identical.

At present only very few attempts have been made to solve these structures which have mostly focussed on structural models similar to the ones found for Na adsorption on Si(100), adapted to the bulk Ge unit-cell. However, very poor agreement has been found when trying out these models. The preliminary conclusion is then that significant differences must exist between the structures formed by Na on Si(100) and Ge(100) although the sequence of LEED patterns as a function of coverage are very similar. As mentioned in the introduction, this could be a result of Na disorder as found by SXRD studies of the same structure[212]. However comparison of theoretical I(V) spectra calculated with Na in various configurations have clearly indicated that the wrong positioning of Na can not alone be responsible for the disagreements between theory and experiment. Including more Na atoms or changing their positions simply does not alter the spectra nearly enough to make up for the disagreement. It is concluded that significant changes in relaxations of the Ge(100) substrate are probably necessary.

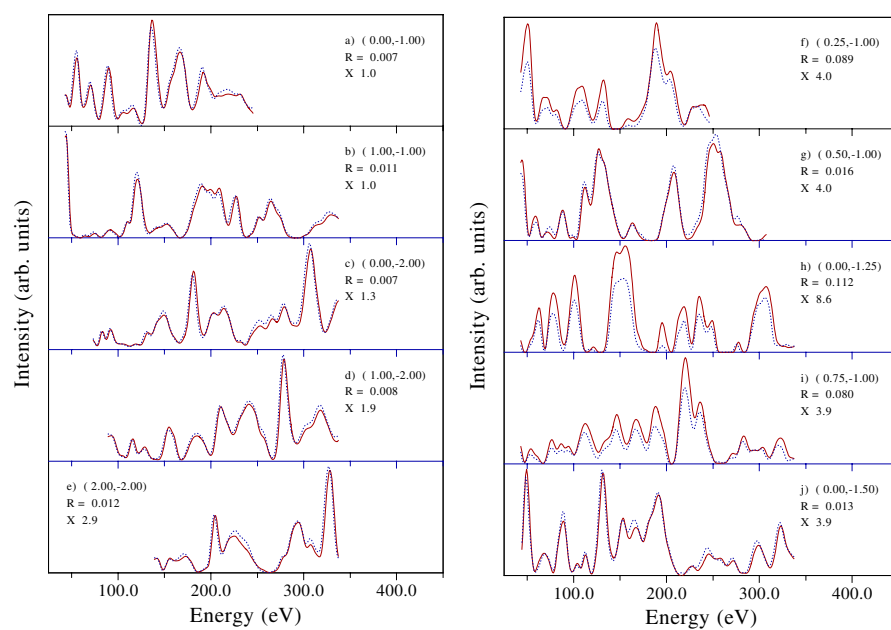


Figure 8.15: Comparison between experimental I(V) spectra of the Ge(100)-(4 × 1)-Na structures obtained by adsorption of one half the saturation coverage of Na at 300K (solid line) and 100K (broken line).

Chapter 9

Summary and conclusion

This thesis deals with a considerable number of crystallographic studies of clean and alkali covered solid surfaces. Most of the experimental work have been carried out using a new digital LEED system, constructed during the first one half year of the Ph.D. study. Information about the structures was obtained from the recorded LEED spectra by a full dynamical quantum mechanical simulation of the LEED process for a large number of possible models. The precision of the structural parameters of the final models are of the order of $1/100$ Ångstrom. While the LEED studies mostly deal with ordered crystalline surfaces, HRCLS has been used to study disordered phases as well.

The most notable component of the new experimental digital LEED system is a 16 bit Princeton CCD camera, which allows for the recording of images of a very high quality. This has made it possible to obtain larger sets of data, as weaker parts of the diffraction pattern can be resolved. The quality of the data has also been significantly improved. Finally the damage of the surface due to the electron beam can be reduced, as a lower electron dose can be used to obtain the LEED images.

The structural and dynamical parameters of several clean metal surfaces have been determined. Most noticeable is the study of Al(110) as a function of temperature in the range of 100K to 553K. In qualitative agreement with a theoretical eDFT-MD study[93], a negative thermal expansion coefficient is found between the first and second Al layers. In fact a $- + -$ sequence of thermal expansion coefficients are found for the first three interlayer spacings. A similar sequence has been found for Mg(1010)[116]. In both cases the sequence is identical to the sequence of interlayer relaxations.

An analysis of LEED intensities measured for the clean Cu(100) surface confirms previous reports of a small contraction of the first layer spacing, but does not show an expansion of the second layer spacing as found in MEIS studies and in a previous LEED study. Bulk Debye temperatures found in this study are in

remarkably good agreement with previous X-ray studies.

The surface structure of the Cu(100)-c(2 × 2)-Na phase formed by adsorption of one-half monolayer Na on Cu(100) has also been determined by quantitative LEED measurements both at T=100K and T=300K. Na atoms occupy four-fold hollow sites on an essentially unperturbed substrate for adsorption at both 100K and 300K.

The structures formed by adsorption of Li and Na on Al(100) and Al(110) have been investigated in some detail.

The adsorption of 0.5 ML Li at room temperature on Al(100) leads to the formation of an Al(100)-c(2 × 2)-Li phase. The structure is found by quantitative LEED to be a binary surface alloy, in which Li atoms occupy 4-fold coordinate substitutional sites formed by displacing every second Al atom in the first layer of the substrate. The surface structure is very similar to both the (100) plane of the metastable, bulk Al₃Li alloy and to the surface structure of the Al(100)-c(2 × 2)-Na phase formed by adsorption of 0.5ML Na at room temperature[14].

The adsorption of 0.2ML Na at room temperature followed by cooling below 250K leads to a reversible phase-transition from a disordered Na layer to an ordered Al(100)-($\sqrt{5} \times \sqrt{5}$)R^o27-Na structure. This structure has been determined by quantitative LEED to be a surface alloy with Na in four-fold coordinated substitutional sites. The structure and phase transition was further investigated by HRCLS and DFT calculations. It was concluded that it was a first order 2D crystal/liquid phase-transition, where the substitutional Na atoms become mobile.

Adsorption of 0.5ML Li or Na at room temperature on Al(110) resulted in the formation of quite similar Al(110)-c(2 × 2)-Li(Na) phases, which were studied by quantitative LEED. Both the Li and the Na structures have the alkali positioned in two-fold coordinated substitutional sites in the first Al layer. Both structures displayed similar significant substrate relaxation five layers deep. The coverage range of 0.0-0.5ML was also investigated using HRCLS and qualitative LEED observations, establishing an asymmetric growth mode, in the two directions perpendicular and parallel to the close-packed rows. The alkali atoms were found to be substitutionally adsorbed in the whole coverage range.

A considerable structural database of alkali adsorbate structures on aluminum is developing, and some general patterns in the relaxation and reconstruction of the alkali-aluminum surface systems have been found. The primary reconstruction of the substrate due to the substitutional adsorption of the alkali is accompanied by a secondary reconstruction involving interlayer relaxations, rumpings and lateral motion, which can extend several layers into the substrate. The strong similarity between many alkali structures also extends to the reconstruction and relaxation of the substrate. It is found that the trends of these secondary relaxations can be predicted for a number of alkali - aluminum system by calculations of the electrostatic forces on the surface layers of the unrelaxed substrate in a point-ion/frozen

background (LF-PIFB) model. This model has previously been successfully used to predict the trends of relaxations of clean metal surfaces.

By adsorption of 1 ML Li on Al(100) at temperatures in the range of 380K to 440K an unusual multilayer surface alloy is formed. It has been shown by analysis of LEED data that the first three layers consist of a mixed Al/Li layer, followed by a pure Al layer, followed by a second, mixed Al/Li layer. Thus the alloy has the same layer-by-layer stoichiometry as the (100) surface of the metastable Al_3Li bulk alloy. However, the relative orientation of the two mixed layers is the same as that in the Al_3Ti -type structure, rather than the Cu_3Au -type structure of Al_3Li . These findings have been confirmed by total-energy calculations, which lead further to the prediction that the bulk Al_3Li alloy has a faulted, Al_3Ti -type surface on a Cu_3Au -type bulk.

Adsorption of more than 0.5ML Na on Al(110) leads to the formation of a number of new structures. A disordered (3×1) structure forms at 0.65ML followed by a well ordered (4×1) structure at 0.75ML. It is shown by quantitative analysis of extensive LEED data that the (4×1) structure consist of 0.5ML Na chemisorbed in a layer above 0.25ML substitutional adsorbed Na. Thus 0.25ML Al atoms are reinserted into the surface as compared to the $c(2 \times 2)$ structure. Further Na adsorption, signified by a disordered (2×1) LEED pattern, is shown to induce another massive rearrangement of surface Al atoms, and a very thin Na film can be formed on top of a strongly intermixed Na-Al layer.

In preliminary studies, the structures of the $\text{Si}(100)-(2 \times 1)$ and the $\text{Ge}(100)-c(4 \times 2)$ phases at $T=100\text{K}$ have been determined by quantitative LEED. The main feature of both structures is the tilted dimer. While the dimers all have the same alignment for the $\text{Si}(100)-(2 \times 1)$, the dimers are aligned in a alternating fashion in the $\text{Ge}(100)-c(4 \times 2)$ structure.

Finally the $\text{Si}(100)-(2 \times 1)\text{-Na}$, $\text{Si}(100)-(4 \times 1)\text{-Na}$, $\text{Ge}(100)-(2 \times 1)\text{-Na}$ and $\text{Ge}(100)-(4 \times 1)\text{-Na}$ phases are briefly discussed based on LEED measurements and an initial structural survey of structural models.

Although quantitative structural determination by LEED dates back 30 years, one should understand that because of the computational demands of the technique, the possibilities of quantitative LEED is intimately connected with the available computer power. While all calculations presented in this thesis have been carried out on a quite ordinary PC, it is not more than 15 years ago that even the most simple structures could only be solved using expensive mainframes and supercomputers. It is thus quite possible that the huge amount of important structural and dynamical information already obtained using LEED is only the humble beginning of what will be revealed in coming years as new and powerful computers become available.

Bibliography

- [1] L. C. Feldman, J. W. Mayer (Eds.), *Fundamentals of Surface and Thin Film Analysis*, North-Holland, New York, 1986. 1.1
- [2] I. Langmuir, K. H. Kingdon, *Phys. Rev.* 21 (1923) 380. 1.4
- [3] J. B. Taylor, I. Langmuir, *Phys. Rev.* 44 (1933) 423. 1.4
- [4] J. Topping, *Proc. Roy. Soc.* 67. 1.4
- [5] R. W. Gurney, *Phys. Rev.* 47 (1935) 479. 1.4
- [6] N. D. Lang, A. R. Williams, *Phys. Rev. B* 18 (1978) 616. 1.4
- [7] S. A. Lindgren, L. Walldén, J. Rundgren, P. Westrin, J. Neve, *Phys. Rev. B* 28 (1983) 6707. 1.4
- [8] D. L. Adams, *Appl. Phys.* 62 (1996) 123. 1.4, 1.5, 2.2.3, 2.3.3, 3.3.2, 4.1, 4.6, 5.10, 5.4.4
- [9] M. M. Nielsen, S. V. Christensen, D. L. Adams, *Phys. Rev. B.* 54 (1996) 17902. 1.4, 2.3.2, 2.3.2, 4.1
- [10] A. Neumann, S. L. M. Schroeder, K. Christmann, *Phys. Rev. B* 51 (1995) 17007. 1.4
- [11] H. Tochihara, S. Mizuno, *Surf. Sci.* 287/288 (1993) 423. 1.4
- [12] S. Mizuno, H. Tochihara, T. Kawamura, *Surf. Sci.* 292 (1993) L811. 1.4, 3.5.1
- [13] M. M. Nielsen, J. Burchhardt, D. L. Adams, J. N. Andersen, *Phys. Rev. B* 58 (1998) 12655. 1.4, 5.4.3, 5.9
- [14] W. Berndt, D. Weick, C. Stampfl, A. M. Bradshaw, M. Scheffler, *Surf. Sci* 330 (1995) 182. 1.4, 4.1, 4.2.3, 7.2.1, 9

- [15] D. Fisher, S. Chandavarker, I. Collins, R. D. Diehl, P. Kaukasoina, M. Lindroos, Phys. Rev. Lett. 68 (1992) 2786. 1.4
- [16] H. Over, H. Bludau, M. Skottke-Klein, G. Ertl, W. Moritz, C. T. Campbell, Phys. Rev. B 45 (1992) 8638. 1.4
- [17] U. Muschiol, P. Bayer, K. Heinz, W. Oed, J. B. Pendry, Surf. Sci. 275 (1992) 185. 1.4
- [18] M. M. Nielsen, J. Burchhardt, D. L. Adams, Phys. Rev. B 50 (1994) 7851. 1.4, 2.3.2, 3.5.3
- [19] J. Burchhardt, E. Lundgren, M. M. Nielsen, J. N. Andersen, D. L. Adams, Surf. Rev. Lett. 3 (1996) 1339. 1.4
- [20] R. D. Diehl, R. McGrath, Surf. Sci. Rep. 23 (1996) 72. 1.4
- [21] C. Stampfl, M. Scheffler, Surf. Rev. Lett. 2 (1995) 317. 1.4
- [22] H. Brune, J. Wintterlin, R. J. Behm, G. Ertl, Phys. Rev. B 51 (1995) 13592. 1.4
- [23] A. Hohlfeld, K. Horn., Surf. Sci. 211 (1989) 844. 1.3, 4.6, 5.1
- [24] A. Schmalz, S. Aminpirooz, L. Becker, J. Haase, J. Neuegebauer, M. Scheffler, D. R. Batchelor, D. L. Adams, E. Bøgh, Phys. Rev. Lett. 67 (1991) 2163. 1.5, 1.5, 2.2.4, 4.1
- [25] J. N. Andersen, E. Lundgren, R. Nyholm, M. Quarford, Surf. Sci. 289 (1993) 307. 1.5, 4.1
- [26] J. Burchhardt, M. M. Nielsen, D. L. Adams, E. Lundgren, J. N. Andersen, C. Stampfl, M. Scheffler, A. Schmalz, S. Aminpirooz, J. Haase, Phys. Rev. Lett. 74 (1995) 1617. 1.5, 1.5, 7.2.1
- [27] J. S. Nelson, P. J. Feibelman, Phys. Rev. Lett. 68 (1992) 2188. 1.5, 3.3, 4.1
- [28] C. Stampfl, M. Scheffler, Surf. Sci. 319 (1994) L23. 1.5, 4.1
- [29] D.M.Gruen, A. Krauss, M. H. Mendelsohn, S. Susman, J. Nucl. Mater. 111. 1.6
- [30] P. G. Partridge, Int. Materials Rev. 35 (1990) 37. 1.6
- [31] A. Septier, F. Sabary, J. C. Dudek, H. Bergeret, B. Leblond, Nucl. Instr. Methods Phys. Res. A 304 (1991) 392. 1.6

- [32] C.-S. Tsao, T.-L. Lin, *J. Appl. Cryst.* 32 (1999) 426. 1.6
- [33] C. Moreau, A. Allouche, E. Knystautas, *J. Appl. Phys.* 58 (1985) 4582. 1.6, 5.7
- [34] M. Sluiter, D. de Fontaine, X.-Q. Guo, R. Podloucky, A. Freeman, *Phys. Rev. B* 42 (1990) 10460. 1.6
- [35] X.-Q. Guo, R. Podloucky, A. Freeman, *Phys. Rev. B* 40 (1989) 2793. 1.6
- [36] S. M. Sze, *Semiconductor Devices*, John Wiley and Sons, New York, 1985. 1.7
- [37] F. Schäffler, *Semicond. Sci. Technol.* 12 (1997) 1515. 1.7
- [38] K. Y. Takayanagi, M. Tanishiro, M. Takahashi, S. Takahashi, *Surf. Sci.* 164 (1985) 367. 1.9, 1.7
- [39] H. P. Bonzel, A. M. Bradshaw, G. Ertl (Eds.), *Physics and Chemistry of Alkali Metal Adsorption*, Elsevier, Amsterdam, 1989. 1.7
- [40] F. Flores, *Surf. Rev. and Lett.* 2 (1995) 513. 1.7, 8.4.1
- [41] C. J. Davisson, L. H. Germer, *Nature* 119 (1927) 558. 1.8.1
- [42] C. J. Davisson, L. H. Germer, *Phys. Rev.* 29 (1927) 908. 1.8.1
- [43] C. J. Davisson, L. H. Germer, *Phys. Rev.* 30 (1927) 705. 1.8.1
- [44] N. W. Ashcroft, N. D. Mermin, *Solid State Physics*, Saunders College Publishing, 1976. 1.8.1, 2.2.2
- [45] S. Hüfner, *Photoelectron Spectroscopy*, Springer-Verlag, Berlin, 1995. 1.8.2
- [46] K. Siegbahn, C. Nordling, A. Fahlman, R. Nordberg, K. Hamrin, J. Hedman, G. Johansson, T. Bergmark, S. E. Karlson, J. Lindgren, B. Lindberg, *Nova Acta Regiae Soc. sci. Ups.* 20. 1.8.2
- [47] SAES Getters, Milan, Italy. 2.1.1
- [48] D. L. Adams, S. P. Andersen, J. Burchhardt, *The Structure of Surfaces III*, Springer, Berlin, 1991, p. 156. 2.1.2, 2.1.2

- [49] J. Burchhardt, Low energy electron diffraction studies of alkali metal adsorption on metal surfaces: Na and k adsorption on al(111) and k adsorption on pd(100), Ph.D. thesis, Institute of Physics and Astronomy, Aarhus University (1996). [2.1.3](#)
- [50] Omicron, SPECTALEED Optics and Electron Gun User's Guide, version 3.3 Edition (October 1997). [2.1.3](#), [2.1.3](#)
- [51] H. J. D. Wolf, W. Moritz, Surf. Sci. 77 (1978) 265. [2.1.3](#)
- [52] Unertl (Ed.), Handbook of Surface Science, Vol. 2, 1992, Ch. 6. [2.1.3](#)
- [53] M. G. Lagally, J. A. Martin, Rev. Sci. Instrum. 54 (1983) 1273. [2.1.3](#), [2.1.3](#), [2.6](#)
- [54] J. B. Pendry, Low Energy Electron Diffraction, Academic Press, London, 1974. [2.1.3](#), [2.2.2](#), [2.2.3](#)
- [55] C. B. Duke, U. Landman, Phys. Rev. B 6 (1972) 2956. [2.1.3](#)
- [56] Omicron - Private Communication. [2.1.3](#)
- [57] J. N. Andersen, H. B. Nielsen, L. Petersen, D. L. Adams, J. Phys. C 17 (1984) 173. [2.1.4](#), [3.3.1](#), [3.2](#), [3.3.3](#)
- [58] J. H. Petersen, C. Søndergaard, S. V. Hoffmann, A. Mikkelsen, D. L. Adams, Surf. Sci. 437 (1999) 317. [2.1.4](#), [4.1](#), [6.1.1](#), [6.2.2](#), [7.2.2](#)
- [59] V. L. Moruzzi, J. F. Janak, A. R. Williams, Calculated Electronic Properties of Metals, Pergamon, New York, 1978. [2.2.2](#)
- [60] B. I. Lundqvist, Phys. Stat. sol. 32 (1963) 273. [2.2.2](#)
- [61] S. Walter, V. Blum, L. Hammer, S. Müller, K. Heinz, M. Giesen, Surf. Sci. 458 (2000) 155. [2.2.2](#), [3.7](#), [3.4](#)
- [62] L. I. Schiff, Quantum Mechanics, McGRAW-HILL, Singapore, 1968. [2.2.2](#)
- [63] J. J. Sakurai, Modern Quantum Mechanics, Addison-Wesley, Reading, 1994. [2.2.2](#), [2.2.2](#)
- [64] S. Y. Tong, Prog. in Surf. Sci. 7 (1975) 1. [2.2.2](#), [2.2.2](#)
- [65] C. B. Duke, G. E. Laramore, Phys. Rev. B 2 (1970) 4765. [2.2.3](#)

- [66] A. Guinier, X-Ray Diffraction, W. H. Freeman and Company, San Francisco, 1963. [2.2.3](#)
- [67] W. Moritz, J. Landskron, Surf. Sci. 337 (1995) 278. [2.2.3](#)
- [68] V. Fritzsche, Phys. Rev. B 50 (1994) 1922. [2.2.3](#)
- [69] Y. Gauthier, Y. Joly, R. Baudoing, J. Rundgren, Phys. Rev. B 31 (1985) 6216. [2.2.4](#)
- [70] F. Jona, K. O. Legg, H. shih, D. W. Jepsen, P. M. Marcus, Phys. Rev. Lett. 40 (1978) 1466. [2.2.4](#)
- [71] R. Doll, M. Kottcke, K. Heinz, Phys. Rev. B 48 (1993) 1973. [2.2.4](#)
- [72] B.L.Gyorffy, G.M.Stocks, Electrons in disordered metals and metallic surfaces, Plenum, New York, 1979. [2.2.4](#)
- [73] S. Crampin, P. Rous, Surf. Sci. and Lett. 244. [2.2.4](#)
- [74] B. Winter, G.M.Stocks, Phys. Rev. B 27 (1982) 882. [2.2.4](#)
- [75] M. Sporn, E. Platzgummer, S. Forsthuber, M. Schmid, W. Hofer, P. Varga, Surf. Sci. 416 (1998) 423. [2.2.4](#)
- [76] E. Platzgummer, M. Sporn, R. Koller, M. Schmid, W. Hofer, P. Varga, Surf. Sci. 419 (1999) 236. [2.2.4](#)
- [77] J. B. Pendry, Surf. Rev. and Lett 4 (1997) 901. [2.2.5](#)
- [78] P.J.Rous, J. Pendry, Surf. Sci. 219 (1991) 355. [2.2.5](#)
- [79] K. Heinz, Rep. Prog. Phys. 58 (1995) 637. [2.2.5](#)
- [80] D. L. Adams, U. Landman, Characterization of Metal Surfaces, Academic, New York, 1977, p. 211. [2.2.5](#)
- [81] D. L. Adams, U. Landman, Phys. Rev. B 15 (1977) 3775. [2.2.5](#)
- [82] A.L.Patterson, Phys. Rev. 46 (1934) 372. [2.2.5](#)
- [83] K. Reuter, J. Bernhardt, H. Wedler, J. Schardt, U. Starke, K. Heinz, Phys. Rev. Lett. 79 (1997) 4818. [2.2.5](#)
- [84] C. Y. Chang, Z. C. Lin, Y. C. Chou, C. M. Wei, Phys. Rev. Lett. 83 (1999) 2580. [2.2.5](#)

- [85] J. Burchhardt, M. M. Nielsen, D. L. Adams, E. Lundgren, J. N. Andersen, Phys. Rev. B 50 (1994) 4718. [2.3.2](#)
- [86] M. M. Nielsen, J. Burchhardt, D. L. Adams, E. Lundgren, J. N. Andersen, Phys. Rev. Lett. 72 (1994) 3370. [2.3.2](#), [4.5.1](#), [5.10](#)
- [87] J. Pendry, J. Phys. C: Solid St. Phys. 13 (1980) 937. [2.3.2](#)
- [88] D. L. Adams, V. Jensen, X. F. Sun, J. H. Vollesen, Phys. Rev. B 38 (1988) 7913. [2.3.3](#), [5.1](#), [5.3](#), [5.3](#), [5.4](#)
- [89] S. Doniach, M. Sunjic, J. Phys. C 3 (1970) 285. [2.4.3](#)
- [90] R. J. Hanson, F. T. Krogh, ACM Trans. Math. Softw. 18 (1992) 115. [2.4.3](#)
- [91] D. L. Adams, J. N. Andersen, in preparation. The program FitXPS used to fit XPS spectra with the convolution of a Doniach-Sunjic line form and a Gaussian is available from the author at <ftp://boopic.ifa.au.dk/pub/fitxps/>. [2.4.3](#)
- [92] N. Mårtensson, A. Nilsson, J. of Elec. Spec. and Rel. Phen. 75 (1995) 209. [2.4.4](#)
- [93] N. Marzari, D. Vanderbilt, A. D. Vita, M. C. Payne, Phys. Rev. Lett. 82 (1999) 3296. [3.1](#), [3.3.1](#), [3.2](#), [3.3.3](#), [3.4](#), [3.5](#), [3.6](#), [3.3.4](#), [3.5](#), [3.4](#), [5.2](#), [9](#)
- [94] D. W. Jepsen, P. M. Marcus, F. Jona, Phys. Rev. B 5 (1972) 3933. [3.2](#), [3.3.1](#)
- [95] M. A. V. Hove, S. Y. Tong, N. Stoner, Surf. Sci. 54 (1976) 259. [3.2](#)
- [96] M. W. Finnis, V. Heine, J. Phys. F 17 (1974) L37. [3.3.1](#), [5.1](#)
- [97] U. Landman, R. N. Hill, M. Mostoller, Phys. Rev. B 21 (1980) 448. [3.3.1](#), [5.1](#), [5.2](#), [5.3](#), [5.3](#)
- [98] H. B. Nielsen, J. N. Andersen, L. Petersen, D. L. Adams, J. Phys. C 15 (1982) L1113. [3.3.1](#), [3.2](#), [3.3.3](#), [5.1](#)
- [99] J. R. Noonan, H. L. Davis, Phys. Rev. B 29 (1984) 4349. [3.3.1](#), [3.2](#), [3.3.3](#)
- [100] B. W. Busch, T. Gustafsson, Surf. Sci. 415 (1998) L1074. [3.3.1](#), [3.2](#)
- [101] R. N. Barnett, U. Landman, C. L. Cleveland, Phys. Rev. B 28 (1983) 1685. [3.3.1](#), [3.2](#), [5.3](#), [5.2](#), [5.3](#)

- [102] K. M. Ho, K. P. Bohnen, Phys. Rev. B 32 (1985) 3446. [3.3.1](#), [3.2](#), [5.1](#), [5.3](#), [5.2](#)
- [103] S. P. Chen, A. F. Voter, D. J. Srolovitz, Phys. Rev. Lett. 57 (1986) 1308. [3.3.1](#)
- [104] A. G. Eguiluz, Phys. Rev. B 35 (1987) 5473. [3.3.1](#)
- [105] T. Ning, Q. Yu, Y. Ye, Surf. Sci. 206 (1988) L857. [3.3.1](#)
- [106] J. R. Smith, A. Banerjea, Phys. Rev. B 37 (1988) 10411. [3.3.1](#)
- [107] P. D. Ditlevsen, J. K. Nørskov, Surf. Sci. 254 (1991) 261. [3.3.1](#)
- [108] H. Göbel, P. V. Blanckenhagen, Phys. Rev. B 47 (1993) 2378. [3.3.1](#)
- [109] J.-H. Cho, Ismail, Z. Zhang, E. W. Plummer, Phys. Rev. B 59 (1999) 1677. [3.3.1](#)
- [110] D. L. Adams, H. B. Nielsen, J. N. Andersen, I. Stensgaard, R. Feidenhans'l, J. E. Sørensen, Phys. Rev. Lett. 49 (1982) 669. [3.3.1](#), [5.1](#), [5.3](#)
- [111] A. Taylor, B. J. Kagle, Crystallographic Data on Metal and Alloy Structures, Dover, New York, 1963. [3.3.2](#), [3.4](#), [4.2.2](#)
- [112] D. F. Gibbons, Phys. Rev. 112 (1958) 136. [3.3.2](#)
- [113] D. L. Adams, C. S. rensen, Surf. Sci. 166 (1986) 495. [3.3](#)
- [114] B. W. Busch, T. Gustafsson, Phys. Rev. B 61 (2000) 16097. [3.3.3](#), [3.4](#), [3.5](#), [3.6](#), [3.5](#), [3.6](#)
- [115] C. Kittel, Introduction to Solid State Physics (5th edition), John Wiley and Sons, New York, 1976, p. 142. [3.3.4](#)
- [116] Ismail, E. W. Plummer, M. Lazzeri, S. de Gironcoli, Phys. Rev. B 63 (2001) 233401. [3.3.4](#), [9](#)
- [117] K. A. Gschneider, Solid State Physics 16 (1964) 275. [3.3.6](#)
- [118] J. A. Strozier, D. W. Jepsen, F. Jona, Surface Physics of Materials, Academic Press, New York, 1975. [3.3.6](#)
- [119] F. C. Nix, D. MacNair, Phys. Rev. 60 (1941) 597. [3.4](#)
- [120] Q. T. Tiang, P. Fenter, T. Gustafsson, Phys. Rev. B 44 (1991) 5773. [3.4](#), [3.4](#), [3.7](#), [3.8](#)

- [121] D. E. Fowler, J. V. Barth, Phys. Rev. B 52 (1995) 2117. 3.4, 3.4, 3.7, 3.8
- [122] H. L. Davis, J. R. Noonan, J. Vac. Sci. Technol 20 (1982) 842. 3.4, 3.7
- [123] D. M. Lind, F. B. Dunning, G. K. Walters, H. L. Davis, Phys. Rev. B 35 (1987) 9037. 3.7
- [124] S. Müller, A.Klinne, M. Kottcke, R. Metzler, P. Bayer, L. Hammer, K. Heinz, Phys. Rev. Lett 75 (1995) 2859. 3.7, 3.4
- [125] S. Quassowski, K. Hermann, Surf. Rev. and Lett. 4 (1997) 1209. 3.7, 3.5.1, 3.10, 3.5.3
- [126] P. A. Flinn, G. M. McManus, J. A. Rayne, Phys. Rev. 123 (1961) 809. 3.4
- [127] H. Ibach, D.L.Mills, Electron Energy Loss Spectroscopy and surface vibrations, Academic Press, New York, 1982. 3.4
- [128] R. F. Wallis, Prog. in Surf. Sci. 4 (1973) 233. 3.4
- [129] J. Fassbender, U. May, B. Schirmer, R. M. Jungbut, B. Hillebrands, G. Güntherodt, Phys. Rev. Lett. 75 (1995) 4476. 3.4
- [130] A. Baddorf, A.K.Swan, J. Wendelken, Phys. Rev. Lett. 76 (1996) 3658. 3.4
- [131] I. K. Robinson, W. Moritz, F. Jona, M. V. Hove, Phys. Rev. Lett. 76 (1996) 3659. 3.4
- [132] A. P. Graham, F. Hofmann, J. P. Toennies, L. Y. Chen, S. C. Ying, Phys. Rev. Lett. 78 (1997) 3900. 3.5.1
- [133] S. Mizuno, H. Tochihara, T. Kawamura, Phys. Rev. B 50 (1994) 17540. 3.5.1
- [134] S. V. Christensen, Some geometrical and catalytic aspects of alkali metal adsorption, Ph.D. thesis, Institute of Physics and Astronomy, Aarhus University (1996). 4.1
- [135] M. M. Nielsen, Structures of alkali covered aluminium surfaces studied by low energy electron diffraction, Ph.D. thesis, Institute of Physics and Astronomy, Aarhus University (1996). 4.1
- [136] B. E. Haydon, K. C. Prince, P. J. Davie, G. Paolucci, A. M. Bradshaw, Solid State Commun. 4 (1983) 325. 4.1

- [137] R. J. Behm, *Physics and Chemistry of Alkali Metal Adsorption*, Elsevier, Amsterdam, 1989, p. 111. [4.1](#)
- [138] C. J. Barnes, M. Lindroos, D. J. Holmes, D. A. King, *Physics and Chemistry of Alkali Metal Adsorption*, Elsevier, Amsterdam, 1989, p. 129. [4.1](#)
- [139] E. C. Sowa, M. A. V. Hove, D. L. Adams, *Surf. Sci.* 199 (1988) 174. [4.1](#), [5.4.1](#), [5.7](#)
- [140] P. Fery, W. Moritz, D. Wolf, *Phys. Rev. B* 38 (1988) 7275. [4.1](#)
- [141] C. M. Chan, M. A. V. Hove, W. H. Weinberg, E. D. Williams, *Surf. Sci.* 91 (1980) 440. [4.1](#)
- [142] W. Moritz, D. Wolf, *Surf. Sci.* 88 (1979) L29. [4.1](#)
- [143] K. W. Jacobsen, J. K. Nørskov, *Phys. Rev. Lett.* 60 (1988) 2496. [4.1](#)
- [144] O. B. Christensen, K. W. Jacobsen, *Phys. Rev. B* 45 (1992) 6893. [4.1](#), [4.6](#)
- [145] P. Hofmann, S. Bao, K. M. Schindler, O. Schaff, M. Polcik, V. Fritzche, A. M. Bradshaw, R. Davis, D. P. Woodruff, *Surf. Sci.* 319 (1994) L7. [4.1](#)
- [146] C. Stampfl, M. Scheffler, H. Over, J. Burchhardt, M. M. Nielsen, D. L. Adams, W. Moritz, *Phys. Rev. Lett.* 69 (1992) 1532. [4.1](#)
- [147] E. Lundgren, *Alkali metal adsorption on metals studied by high resolution core level spectroscopy and low energy electron diffraction*, Ph.D. thesis, Institute of Physics, Lund University (1996). [4.1](#)
- [148] I. Ohsaki, T. Oguchi, *Jour. Phys. Soc. Jap.* 69 (2000) 2192. [4.2.4](#), [4.2](#)
- [149] J. N. M. Bockstedte, A. Kley, M. Scheffler, *Comp. Phys. Commun.* 107 (1997) 187. [4.3.2](#), [6.1.3](#)
- [150] M. Fuchs, M. Scheffler, *Comput. Phys. Commun.* 119 (1999) 67. [4.3.2](#), [6.1.3](#)
- [151] H. J. Monkhorst, J. D. Pack, *Phys. Rev. B* 8 (1999) 5747. [4.3.2](#), [6.1.3](#)
- [152] J. P. Perdew, K. Burke, M. Ernzerhof, *Phys. Rev. Lett.* 77 (1996) 18. [4.3.2](#), [6.1.3](#)
- [153] R. Fasel, M. Giere, H. Bludau, P. Aebi, J. Osterwalder, L. Schlapbach, *Surf. Sci.* 374 (1997) 104. [4.3.2](#)

- [154] M.-S. Chen, S. Mizuno, H. Tochihara, Surf. Sci. . 4.3.2
- [155] R. Stumpf, M. Scheffler, Phys. Rev. B 53 (1996) 4958. 4.6
- [156] P. Häberle, T. Gustafsson, Phys. Rev. B 40 (1989) 8218. 4.6, 5.1, 8.1
- [157] D. M. Riffe, G. K. Wertheim, P. H. Citrin, Phys. Rev. Lett. 67 (1991) 116. 4.7.1, 7.3.2
- [158] J. Sokolov, F. Jona, P. M. Marcus, Solid State Commun. 48 (1983) 739. 5.1
- [159] F. Jona, P. M. Marcus, The structure of surfaces II, Vol. 11 of Springer seires in surface science, Springer-Verlag, Berlin, 1987, p. 90. 5.1
- [160] U. Landman, R. N. Hill, M. Mostoller, Phys. Rev. B 21 (1980) 448. 5.1, 5.1, 5.2
- [161] P. Jiang, P. M. Marcus, F. Jona, Solid State Commun. 59 (1986) 275. 5.1, 5.3
- [162] J. Repp, S. Fölsch, G. Meyer, K.-H. Rieder, Phys. Rev. Lett. 86 (2001) 252. 5.1
- [163] J. Bornet, J. Neugebauer, M. Scheffler, Phys. Rev. B 49 (1994) 17242. 5.1, 5.1
- [164] M. P. Tosi, Solid State Physics Vol. 16, AP, New York, 1964, p. 1. 5.2, 5.4
- [165] H. L. Davis, J. R. Noonan, Surf. Sci. 126 (1983) 245. 5.3
- [166] R. D. Diehl, M. Lindroos, A. Kearsley, C. J. Barnes, D. A. King, J. Phys. C 18 (1985) 4069. 5.3
- [167] J. R. Noonan, H. L. Davis, W. Erley, Surf. Sci. 152. 5.3, 5.5
- [168] Y. P. Guo, K. C. Tan, A. T. S. Wee, C. H. A. Huan, Surf. Rev. and Lett. 6 (1999) 819. 5.4
- [169] X.-G. Zhang, M. A. V. Hove, G. A. Somorjai, P. J. Rous, D. Tobin, A. Gonis, J. M. MacLaren, K. Heinz, M. Michl, H. Lindner, K. Müller, M. Ehsasi, J. H. Block, Phys. Rev. Lett 67 (1991) 1298. 5.4
- [170] P. R. Watson, K. A. R. Mitchell, Surf. Sci. 203 (1988) 323. 5.5
- [171] D. L. Adams, W. T. Moore, K. A. R. Mitchell, Surf. Sci. 149 (1985) 407. 5.5

- [172] S. Liepold, N. Elbel, M. Michl, W. Nichtl-Pecher, K. Heinz, K. Müller, Surf. Sci. 240 (1990) 81. [5.5](#)
- [173] Y. S. Li, F. Jona, P. M. Marcus, Phys. Rev. B 44 (1991) 8267. [5.5](#)
- [174] J. Sokolov, F. Jona, P. M. Marcus, Phys. Rev. B 33 (1986) 1397. [5.6](#)
- [175] J. Sokolov, H. D. Shih, U. Bardi, F. Jona, P. M. Marcus, J. Phys. C 17 (1984) 371. [5.6](#)
- [176] J. Sokolov, F. Jona, P. M. Marcus, Phys. Rev. B 29 (1984) 5402. [5.6](#)
- [177] J. Sokolov, F. Jona, P. M. Marcus, Phys. Rev. B 31 (1985) 1929. [5.6](#)
- [178] C.-M-Chan, M. A. V. Hove, Surf. Sci. 171 (1986) 226. [5.7](#)
- [179] C. Stampfl, M. Scheffler, H. Over, J. Burchhardt, M. M. Nielsen, D. L. Adams, W. Moritz, Phys. Rev. B 49 (1992) 4959. [5.10](#)
- [180] M. Methfessel, D. Hennig, M. Scheffler, Phys. Rev. B 46 (1992) 4816. [5.5](#)
- [181] H. Donnerberg, M. Exner, Phys. Rev. B 49 (1994) 3746. [5.6](#)
- [182] P. W. M. Jacobs, E. A. Kotomin, R. I. Eglitis, J. Phys.: Condens. Matter 12 (2000) 569. [5.6](#)
- [183] X.-Q. Guo, R. Podloucky, J.-H. Xu, A. Freeman, Phys. Rev. B 41 (1990) 12432. [6.1.4](#)
- [184] N. E. Christensen, Phys. Rev. B 32 (1985) 207. [6.1.4](#)
- [185] J. W. Kim, Y. K. Kim, S. Kim, Surf. Sci. 375 (1997) L392. [6.2.3](#)
- [186] A. Mikkelsen, S. V. Hoffmann, J. Jiruse, D. L. Adams, Phys. Rev. B 61 (2000) 13988. [7.2.1](#)
- [187] S. Mizuno, H. Jiang, H. Tochiyara, Surf. Rev. and Lett. 4 (1997) 1221. [7.2.1](#)
- [188] S. V. Christensen, J. Nerlov, K. Nielsen, J. Burchhardt, M. M. Nielsen, D. L. Adams, Phys. Rev. Lett. 76 (1996) 1892. [7.2.1](#)
- [189] J. N. Andersen, M. Quarford, R. Nyholm, J. J. van Acker, E. Lundgren, Phys. Rev. Lett. 68 (1992) 94. [7.2.2](#)
- [190] A. Nilsson, B. Eriksson, N. Mårtensson, J. N. Andersen, J. Onsgaard, Phys. Rev. B 38 (1988) 10357. [7.3.2](#)

- [191] H. Over, J. Wasserfall, J. Ranke, W. Sawitzki, C. Ambiatello, W. Moritz, Phys. Rev. B 55 (1997) 4731. [8.1](#), [8.2.1](#), [8.2.2](#), [8.2](#), [8.3](#), [8.2.2](#)
- [192] D. J. Chadi, Phys. Rev. Lett 43 (1979) 43. [8.1](#)
- [193] R. M. Tromp, R. J. Hamers, J. E. Demuth, Phys. Rev. Lett 55 (1985) 1303. [8.1](#)
- [194] R. E. Schlier, H. E. Farnsworth, J. Chem. Phys. 30 (1959) 917. [8.1](#)
- [195] E. L. C. J. Karlsson, Y.-C. Chao, R. I. G. Uhrberg, Phys. Rev. Lett. 69 (1992) 1588. [8.1](#), [8.2.1](#), [8.3.1](#)
- [196] R. A. Wolkow, Phys. Rev. Lett. 68 (1992) 2636. [8.1](#)
- [197] J. Dabrowski, M. Scheffler, Appl. Surf. Sci. 56. [8.1](#), [8.2](#)
- [198] W. S. Yang, F. Jona, P. M. Marcus, Phys. Rev. B 28 (1983) 2049. [8.1](#)
- [199] S. Tang, A. J. Freeman, B. Delley, Phys. Rev. B 45 (1992) 1776. [8.1](#)
- [200] B. S. Swartzentruber, Y. W. Mo, M. B. Webb, M. G. Lagally, J. Vac. Sci. Technol. A 7 (1989) 2901. [8.2.1](#), [8.3](#), [8.4](#), [8.5](#), [8.2.2](#)
- [201] H. J. W. Zandvliet, H. B. Elswijk, E. J. van Loenen, I. S. T. Tsong, Phys. Rev. B 46 (1992) 7581. [8.2.1](#)
- [202] A. Ishizaka, Y. Shiraki, J. Electrochem. Soc. 133 (1986) 666. [8.2.1](#), [8.4](#), [8.2.2](#), [8.6](#)
- [203] T. Tabata, T. Aruga, Y. Murata, Surf. Sci. 179 (1987) L63. [8.2.1](#), [8.3.1](#)
- [204] Y.-C. Chao, L. S. O. Johansson, R. I. G. Uhrberg, Surf. Sci. 391 (1997) 237. [8.2.1](#), [8.3.1](#)
- [205] R. Rossmann, H. L. Meyerheim, V. Jahns, J. Wever, W. Moritz, D. Wolf, D. Dornisch, H. Schulz, Surf. Sci. 279 (1992) 199. [8.2.2](#), [8.3.1](#)
- [206] X. Torrelles, H. A. van der Vegt, V. H. Etgens, P. Fajardo, J. Alvarez, S. Ferrer, Surf. Sci. 364 (1996) 242. [8.2.2](#), [8.3.1](#)
- [207] E. M. Lauridsen, J. Baker, M. Nielsen, R. Feidenhans'l, G. Falkenberg, O. Bunk, J. H. Zeysing, R. L. Johnson, Surf. Sci. 453 (2000) 18. [8.2.2](#)
- [208] S.D.Kevan, Phys. Rev. B 32 (1985) 2344. [8.3.1](#)

-
- [209] S. Ferrer, X. Torrelles, V. H. Etgens, H. A. van der Vegt, P. Fajardo, Phys. Rev. Lett. 75 (1995) 1771. [8.3.1](#), [8.3.2](#), [8.5](#), [8.3.2](#)
- [210] M. Needels, M. C. Payne, J. D. Joannopoulos, Phys. Rev. Lett. 58 (1987) 1765. [8.5](#), [8.3.2](#)
- [211] H.L.Meyerheim, W. Moritz, Appl. Phys. A 67 (1998) 645. [8.4.1](#)
- [212] H.L.Meyerheim, R.Sawitzki, W. Moritz, Phys. Rev. B 52 (1995) 16830. [8.4.1](#), [8.4.2](#)
- [213] C. Wei, H. Huand, S.Y.Tong, G. Glander, M.B.Webb, Phys. Rev. B 42 (1990) 11284. [8.4.1](#)
- [214] P.Gravila, P.F.Meier, Phys. Rev. B 59 (1998) 2449. [8.4.1](#)
- [215] Y.-C. Chao, L. S. O. Johansson, R. I. G. Uhrberg, Phys. Rev. B 55 (1997) 7198. [8.4.1](#)
- [216] L. S. B. Naydenov, Surf. Sci. 370 (1997) 155. [8.4.1](#)